Improved engine wall models for Large Eddy Simulation (LES)

by

Chalearmpol Plengsaard

A dissertation submitted in partial fulfillment of the requirements for the degree of

Doctor of Philosophy

(Mechanical Engineering)

at the

University of Wisconsin-Madison

2013

Date of final oral examination: 05/29/13

The dissertation is approved by the following members of the Final Oral Committee:

Christopher J. Rutland, Professor, Mechanical Engineering

Rolf D. Reitz, Professor, Mechanical Engineering

Jaal B. Ghandhi, Professor, Mechanical Engineering

Mario F. Trujillo, Assistant Professor, Mechanical Engineering

Riccardo Bonazza, Professor, Engineering Physics

Abstract

Improved wall models for Large Eddy Simulation (LES) are presented in this research. The classical Werner-Wengle (WW) wall shear stress model is used along with near-wall sub-grid scale viscosity. A sub-grid scale turbulent kinetic energy is employed in a model for the eddy viscosity. To gain better heat flux results, a modified classical variable-density wall heat transfer model is also used. Because no experimental wall shear stress results are available in engines, the fully turbulent developed flow in a square duct is chosen to validate the new wall models. The model constants in the new wall models are set to 0.01 and 0.8, respectively and are kept constant throughout the investigation. The resulting time- and spatially-averaged velocity and temperature wall functions from the new wall models match well with the law-of-the-wall experimental data at Re = 50,000. In order to study the effect of hot air impinging walls, jet impingement on a flat plate is also tested with the new wall models. The jet Reynolds number is equal to 21,000 and a fixed jet-to-plate spacing of H/D = 2.0. As predicted by the new wall models, the time-averaged skin friction coefficient agrees well with experimental data, while the computed Nusselt number agrees fairly well when r/D > 2.0.

Additionally, the model is validated using experimental data from a Caterpillar engine operated with conventional diesel combustion. Sixteen different operating engine conditions are simulated. The majority of the predicted heat flux results from each thermocouple location follow similar trends when compared with experimental data. The magnitude of peak heat fluxes as predicted by the new wall models is in the range of typical measured values in diesel combustion, while most heat flux results from previous LES wall models are over-predicted. The new wall models generate more accurate predictions and agree better with experimental data.

Acknowledgements

First, I would like to express my sincere gratitude to Professor Christopher J. Rutland for being a wonderful advisor. I am truly grateful for his great support, guidance and patience during the past six years at the Engine Research Center (ERC) at the University of Wisconsin-Madison.

Further, I would like to thank my committee members Professors Rolf D. Reitz, Jaal B. Ghandhi, Mario F. Trujillo, and Riccardo Bonazza for their invaluable suggestions during my research.

Additionally, I would like to acknowledge Dr. Randy Hessel, Dr. Sage Kokjohn, Adam B. Dempsey, Benjamin Cantrell, Dr. Terry Hendricks, Dr. Youngchul Ra, Dr. Siddhartha Banerjee, Jian Gong, Noah Van Dam, Martin Wissink, and Dr. Yuxin Zhang for their time, helpful suggestions, and friendship. I would like to thank the ERC Computer System Administrator Joshua Leach for all of his help.

Finally, I would like to thank all my family, especially my father and mother, for their love and support.

Funding support for this work was provided by the Department of Energy Promotion, Thailand, Kasetsart University, Thailand, and Caterpillar Inc.

Table of Contents

List of Figures

List of tables

Nomenclature

Acronyms

CFD	Computational Fluid Dynamics
DSM	Dynamic Structure Model
EGR	Exhaust Gas Recirculation
HRR	Heat Release Rate
IVC	Intake Valve Closing
LES	Large Eddy Simulation
ATDC	After top dead center
WW	Werner-Wengle wall model
LW	Law-of-the-wall
RANS	Reynolds Averaged Navier Stoke
CAT	Caterpillar Engine
MCDC	Mixing Controlled Direct Chemistry
DNS	Direct Numerical Simulation
CA	Crank Angle
TDC	Top Dead Center
TKE	Turbulent Kinetic Energy
SOI	Start of Injection
SGS	Sub-Grid Scale
NOx	Oxides of Nitrogen
DI	Direct Injection
IMEP	Indicated Mean Effective Pressure (bar)

Non-dimensional parameters

Re Reynolds Number

Nu Nusselt Number

f Friction Factor

Chapter 1 Introduction

1.1 Overview

In recent years, there has been an increasing demand for improved advanced internal combustion engines in terms of engine efficiency. This fact suggests a need for more accurate predictions of thermal conditions, in particular, the gas temperatures inside the combustion chamber. Better thermal predictions would help to improve engine efficiency. Moreover, the thermal conditions inside combustion chambers are strongly dependent on wall heat transfer. Higher heat loss from the in-cylinder gases to the walls reduces the average in-cylinder gas temperature, pressure, and work transferred to piston (Heywood, 1988). Therefore, the changes in gas temperature due to wall heat transfer have an impact on engine efficiency. An accurate prediction of heat transfer through combustion chamber walls is a prerequisite for understanding the thermal condition within the engine cylinders.

Engine wall heat transfer is one of the important issues in the study of internal combustion engines. Analysis of engine wall heat transfer is among the most complex engineering topics, because these mechanisms are related to the turbulent motion, the combustion process in cylinders, and the thermal boundary layer near walls. During the engine operating cycles, the unsteady and transient behavior of the turbulent motion inside engine cylinders causes a variation of heat fluxes between fluids and walls. In-cylinder heat fluxes oscillate between a few MW/m^2 during combustion and near-zero or negative values during intake (Heywood, 1988). The large pressure and temperature variations during the engine cycle make the in-cylinder the boundary layer compressible. The very steep temperature gradients which develop near wall surfaces during combustion produce highly inhomogeneous temperature

distributions and create strong local changes in heat flux. All of these factors contribute to highly unsteady and non-uniform phenomena in engine wall heat transfer.

Apart from experimental study, the increase in computational power in recent decades has made the use of engine simulations with computational fluid dynamics (CFD) more practical. The current multi-dimensional CFD tools have become sufficiently mature to employ for engine research i.e., a KIVA engine code (Jhavar et al., 2006; Hu et al., 2007). In a multi-dimensional approach, the three-dimensional governing equations of mass, momentum and energy conservation are solved together with the turbulence model in core regions. To save computational time, all engine simulations rely on a wall model to represent the details of the near-wall flow and to provide wall boundary conditions for the bulk flow governing equations. The schematic of multi-dimensional CFD model in a combustion chamber is shown in Figure1.1

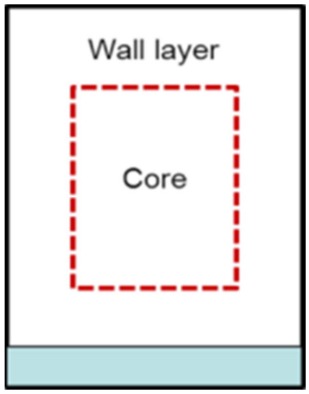

Figure 1.1 Schematic of multi-dimensional CFD model in a combustion chamber.

These engine wall models are used without solving the full governing equations. The inner wall layers are computed based on the solution of a simplified set of momentum and thermal boundary layer equations which are known as wall functions. These functions represent the behavior of all flow variables in the near-wall regions (Borman et al., 1987). In particular, the

wall functions employ the local information of the mean flow in the computational cells at the combustion chamber walls. The velocity wall functions are used to calculate wall shear stress, while temperature wall functions supply wall heat flux at the boundary for engine CFD simulation.

However, most of the wall models which are published in the literature rely on the information from traditional Reynolds Averaged Navier-Stokes (RANS) turbulence modeling (RANS-based wall models). In RANS, the three-dimensional, time-dependent Navier-Stokes equations are ensemble-averaged. Only mean flow parameters are solved numerically, so the ensemble-average results are obtained. This averaging tends to remove important small-scale turbulent structures from flow fields. This affects the local information regarding heat flux distribution near walls. These heat flux results from RANS-based wall models may not provide more flow structure and may not be useful when more detailed spatial thermal information is needed.

Recently, many reports have shown that Large Eddy Simulation (LES) provides significant advantages over RANS techniques in engine CFD simulations (Jhavar et al., 2006; Hu et al., 2007; Rutland, 2011). One observation is that LES can be used to study cycle-to-cycle variability, and it can produce more detailed local information and more accurate results (Rutland, 2011). Also, LES helps in understanding the interactions between in-cylinder flows and fuel-air mixing, which is critical to controlling transient operations and maintaining good combustion characteristics (Banerjee et al., 2012).

In LES, the mean flow equations are derived from local-volume-average Navier-Stokes equations. Then, the flow field is separated into large-scale (grid size, or filtered-scale), and small-scale or sub-grid scale motion by filtering local flow variables. For example, in LES, the

instantaneous velocity is composed of the filtered velocity and the sub-grid scale velocity. Since the large-scale motions, which contain most of the kinetic energy of flow, are directly solved in the governing equations, more local flow structures can be resolved by the nature of LES averaging. This is a different concept from the traditional RANS model in which mean flow equations come from ensemble-average processes. Therefore, LES techniques appear to be a better way to perform highly unsteady engine flows in comparison to the RANS approach. However, in order to provide accurate boundary conditions, the local information of wall models should be consistent with turbulent modeling. Therefore, LES-based wall models are needed when the turbulence model is switched from RANS to LES. In other words, new wall shear stress and wall heat transfer models should rely on information from LES turbulence modeling in the core flow. The results of wall shear stress and wall heat flux from LES wall models would provide more local distribution near walls after obtaining information from the LES turbulence approach.

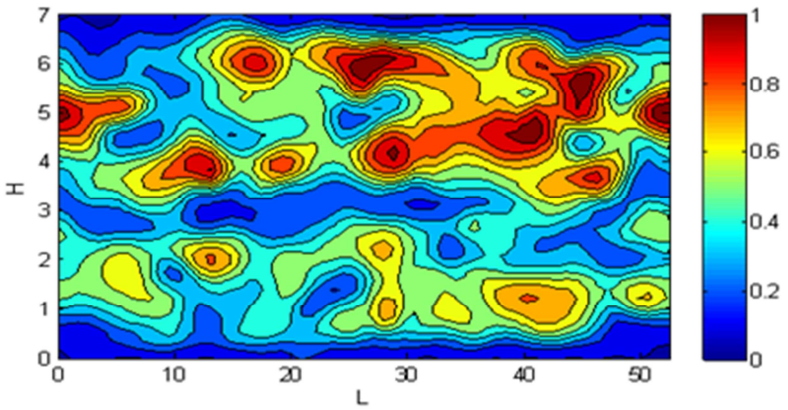

Figure 1.2 Contour plot of wall heat fluxes from a LES-based wall model in a square duct.

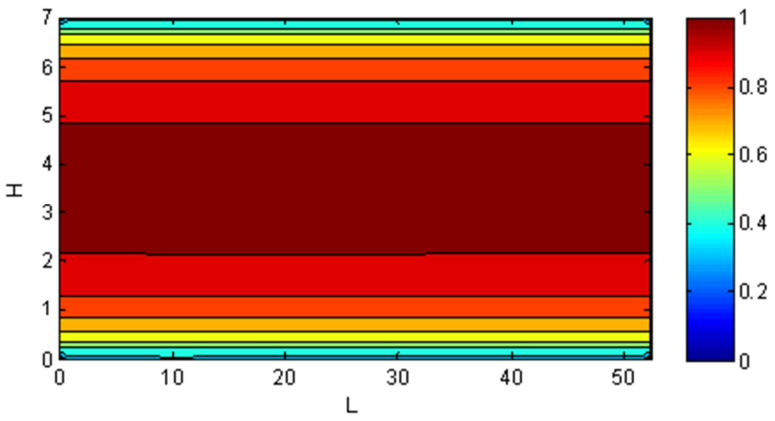

Figure 1.3 Contour plot of wall heat fluxes from a RANS-based wall model in a square duct.

Figures 1.2 and 1.3 show the contour plots of simulations of wall heat flux in a square duct with constant wall temperature, which are normalized by the maximum local wall heat flux values. Comparisons were made between RANS techniques and LES methods. It is clear that LES can capture more detail of the local flux results than RANS, and this is the motivation for this research.

1.2 Objective and Method to Approach

The objective of this research is to improve engine wall models for LES. The new wall models will be able to predict more accurate heat flux results and to capture more detailed local information near walls. This information may help engine designers to understand the detailed local information of thermal conditions within the combustion chambers. Also, the detailed calculation of emissions can be investigated based on this local thermal information. In the present study, LES models are used to simulate turbulent motions along with the KIVA engine code. This code solves the unsteady three-dimensional compressible Navier-Stokes equations

coupled to the LES turbulence model. For model testing, improved wall models will be used as boundary conditions for simulations.

1.3 Organization of a dissertation

The remainder of this dissertation is organized as follows. First, the mechanism of engine wall boundary layers is investigated and key physics associated with wall shear stress and wall heat transfer models are identified. Next, improved wall shear stress and wall heat transfer models are presented. For model validation, comparisons are made with existing experimental data of channel flows, i.e., a square duct flow. The model constants are justified from these comparisons and are used throughout the investigation. In order to study the effect from hot air impinging walls, the jet impingement on a flat plate are also tested with new wall models. Also, the heat flux results from the new wall models are compared with available experimental data from conventional diesel engines. Moreover, results from the traditional RANS turbulence technique are included and compared to the LES results. Finally, the conclusions from the improvements are summarized.

Chapter 2 Literature review

2.1 Structure of near wall flows

In turbulent wall flows, there are three regions which are characterized by their distance from the wall: the very thin viscous sub-layer near the wall, the overlap region, and the outer turbulent layer. In the viscous layers closest to the wall, the turbulent structure is influenced by the viscous shear stress and laminar or molecular viscosity of the fluid (White, 2003). The laminar viscosity of fluid enforces the no-slip boundary condition and causes turbulent velocity fluctuations to vanish at the wall. The flows are close to laminar in this region. In the outer flow regions, the turbulent or Reynolds stress is dominant and there is significant mixing and randomness of the flow. The turbulent eddy viscosity is defined in these outer flow regions. Moreover, there is an intermediate region called the overlap region (logarithmic region), where both viscous shear stress and turbulent shear stress are important.

The character of the flow within the viscous and outer flow region is completely different. The viscous shear stress is dominant within the viscous sub-layer, while the turbulent shear stress is dominant in the outer flow region. This creates a problem with different length scales between the near wall region and the rest of the flow, and leads to the definition of a near-wall velocity scale, i.e., friction velocity (u_*), given as

$$u_* = \sqrt{\frac{\tau_w}{\rho}} \tag{2.1}$$

The term ρ is the density of fluid and τ_w is the wall shear stress. Note that this friction velocity has dimensions $\{LT^{-1}\}$, but it is not actually a flow velocity.

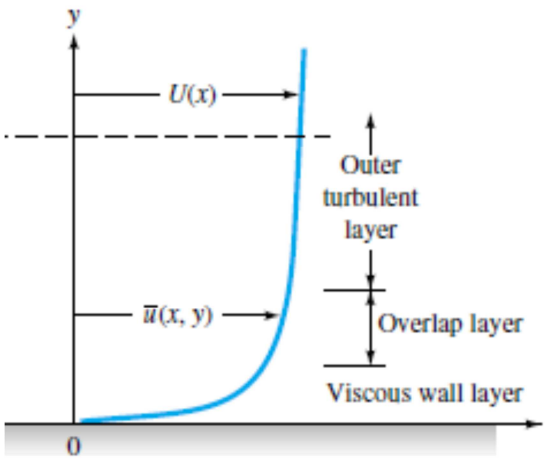

Figure 2.1 A turbulent velocity profile (White, 2003).

In engines, there are many complicated phenomena which make boundary layer flows near walls difficult to analyze. Turbulent motions which are generated during the intake process are convected and diffused into wall regions (Jenning, 1991). The interaction between large scale bulk flow motions and production from mean shear flow produces a high level of turbulence within the boundary layer. As a result, the flow field near walls strongly depends on turbulent motions within the core flow.

Moreover, the operating cycles in engines occur within the order of a few hundred milliseconds. In-cylinder pressure changes by a factor of fifty during the compression stroke and gas temperature increases by a factor of three during the combustion period. These variations of in-cylinder gas conditions during a cycle are very high and make in-cylinder boundary layers highly unsteady and compressible. The high temperature gradients, which are developed during the combustion period, produce steep density and fluid property gradients near walls. Also, engine boundary layers can be highly three-dimensional due to the complex motions, such as tumbling and swirling motion, which are produced by the intake flow during a cycle. Therefore,

in summary, engine boundary layer mechanisms usually undergo highly unsteady, compressible and three-dimensional flows, and it is crucial for engineers and scientists to understand and predict these mechanisms.

However, it has become more feasible to simulate engine wall bounded flows using computational fluid dynamics (CFD) due to the dramatic increase in computational power in recent decades. Since the boundary layer thickness in combustion chambers of engines is thin (Heywood, 1984), the computational grids near walls must be quite fine to capture engine boundary layer mechanisms. There are many investigations of near-wall mesh requirements for CFD simulations in the literature. Chapman (1974), who worked in the aeronautical field, was the first researcher to propose the number of grid points which should be scaled as $Re^{1.8}$ in near-wall regions. It is impossible to resolve near-wall dynamics behavior directly in high Reynolds flows, because it requires a huge computational expense. In order to resolve all scales in the boundary layers, the first grid point should be located at about the dimensionless distance from the wall $y^+ = 1$ (Jenning,1991). Therefore, a large number of computational cells are needed to satisfy this condition. Moreover, Jennings and Morel (1990) proposed the use of separate computational zones in wall regions to provide fine grid resolution in boundary layers. However, this approach required additional computational effort and encountered problems with matching solutions between the wall regions and the outer flows.

To avoid the use of a large number of grid points near walls, wall models are generally used in engine CFD simulations. The most common wall models rely on a set of wall functions. The full governing equations of mass, momentum, energy, and species along with a turbulence model are solved within core regions or outer layer regions, while wall models act like the boundary conditions. These wall functions are based on solutions of near wall flows, which are

derived from an analysis of flow and thermal physics inside the turbulent boundary layers. In particular, using wall functions, the first grid points might be placed in the logarithmic layer. This leads to a reduction in the number of cells in the boundary layers. Because the character of wall functions is universal, and the form of correlations between the wall and the outer edge of the logarithmic layer is invariant, these wall functions can apply to many flow conditions. To understand wall models in more detail, the conventional wall models are first reviewed in the next section.

2.2 Conventional law-of-the-wall overview

Application of dimensional and scale analysis leads to the well-known law-of-the-wall which can be written in the following form

Viscous layer:

$$u^+ = y^+ \quad , y^+ \leq 11.81 \tag{2.2}$$

Log-layer:

$$u^+ = \frac{1}{\kappa}\ln(y^+) + B \quad , y^+ > 11.81 \tag{2.3}$$

The linear profile in the viscous layer can be applied until y^+ equal to 11.81, which was determined from experiments measuring viscous layer thickness (Hinze, 1975). The term κ= 0.4327 and B=5.5 (Amsden et al., 1989) and the term u^+ and y^+ are defined as

$$u^+ = \frac{U}{u_*} \tag{2.4}$$

$$y^+ = \frac{\rho y u_*}{\mu} = \frac{y u_*}{\nu} \tag{2.5}$$

The term U is the magnitude of the gas velocity parallel to the wall. Also, the information of fluid properties such as fluid density ρ and viscosity ν from wall cells is employed in the above wall functions. The law-of-the-wall profiles are shown in Figure 2.2.

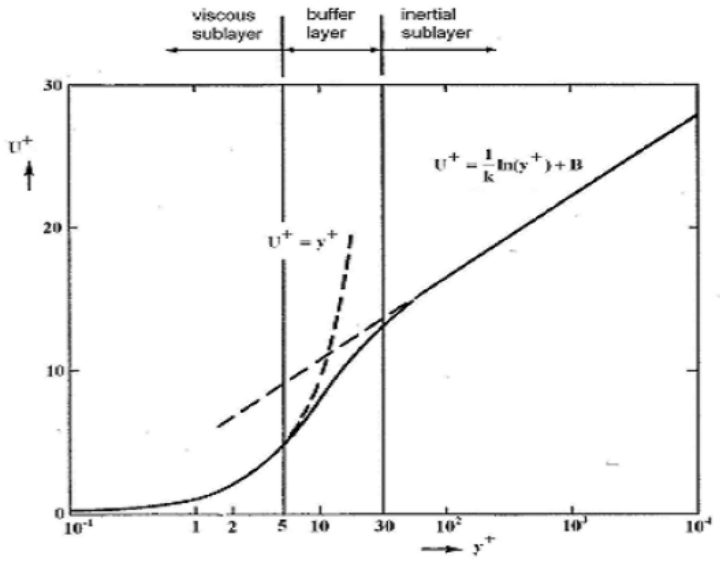

Figure 2.2 Law-of-the-wall profiles (White, 2003)

In CFD models, wall functions use Eqs (2.2-2.5) to determine local wall shear stress on wall surfaces. The wall shear stress is applied as a boundary condition on the momentum equation parallel to the surface at these nodes. For three dimensional flows, there are two velocity components parallel to each wall surface. This makes two components of the wall shear stress for use as boundary conditions on the momentum equations.

Another modification for developing velocity wall functions to apply for general application of CFD simulations is to deal with a new expression of friction velocity. Launder and

Spalding (1974) proposed alternative relations to define a friction velocity by replacing the velocity scale with new scales by

$$u_\tau = C_\mu^{0.25}(tke)^{0.5} \tag{2.6}$$

The term C_μ is 0.09 and the term tke represents the turbulent kinetic energy at the grid cell nearest to the wall. Chieng et al. (1980) found that the friction velocities, u_τ and u_*, are approximately the same for equilibrium boundary layer flow, which was proven using the standard RANS techniques.

In the KIVA engine code, the local wall shear stress is calculated using information from law-of-the-wall velocity conditions to provide boundary conditions for the momentum equations (Amsden et al., 1989). To avoid the iterative solution for unknown friction velocity, the profiles of velocity near the walls are assumed. In particular, a linear profile is assumed in the viscous sub-layer and a 1/7 power law velocity profile is assumed in the logarithmic region. The closed forms of the velocity wall function are only dependent on the magnitude of gas velocity near walls and are rewritten by

Viscous layer

$$u^+ = \left(\frac{yU}{\nu}\right)^{\frac{1}{2}} \quad , \frac{yU}{\nu} \le R_c \tag{2.7}$$

Log-layer

$$u^+ = \frac{1}{\kappa}\ln\left\{c_{lw}\left(\frac{yU}{\nu}\right)^{\frac{7}{8}}\right\} + B \quad , \frac{yU}{\nu} > R_c \tag{2.8}$$

The term $\frac{yU}{\nu}$ represents Reynolds number, which is based on the gas velocity relative to the wall. The transition R_c is equivalent to 114 and the constant c_{lw} is approximately 0.15.

In thermal analysis, the Reynolds analogy between the momentum boundary layer and the thermal boundary layer is applied. In the viscous layer, the fluid slows down and behaves like a laminar flow in which thermal energy transport is by molecular diffusion, while in the log-layer, the effect from turbulent eddies is included. The thermal law of the wall is given by (Kays, 1994)

Viscous layer

$$T^+ = \Pr y^+ \quad , y^+ \le y_{cr}^+ \tag{2.9}$$

Log-layer

$$T^+ = 2.44 \Pr_t \ln\left(\frac{y^+}{13.2}\right) + 13.2 \Pr \quad , y^+ > y_{cr}^+ \tag{2.10}$$

The non-dimensional temperature term T^+ is defined as

$$T^+ = \frac{T - T_w}{T_*} \tag{2.11}$$

The friction temperature is determined by (Bradshaw et al., 1995)

$$T_* = \frac{q_w}{\rho c_p u_*} \tag{2.12}$$

The term q_w is the wall heat flux, c_p is the constant pressure specific heat of the gas, Pr is fluid Prantl number and Pr_t is turbulent Prantl number. A y_{cr}^+ critical value depends on fluid Prantl number (Kays, 1994). The critical value is chosen as 13.2 for air. (Pr = 0.71). The turbulent Prantl number is assumed close to 1.0 in the fully turbulent region. In general, the thermal law of the wall is used to determine local wall heat flux on each surface and these flux results are applied as boundary conditions on the energy equation.

Table 2.1 Comparisons of thermal law-of-the-wall and engine conditions

(Borman et al.,1987)

Thermal law-of-the-wall conditions	Engine conditions
2D flow	3D core flow complicated
Steady	Unsteady
Incompressible	Compressible, low Mach number
Uniform pressure gradient	Pressure waves
Uniform surface temperature	Non-uniform surface temperature
No chemical effects	Chemical reactions
No spray effects	Two-phase effects

In engines, there is some issue when the thermal law-of-the-wall is used in engine applications. The boundary layers in engines have strong fluid density changes due to temperature variations. This leads to different physics between traditional incompressible boundary layers and in-cylinder boundary layers. The many differences between traditional temperature wall function from law-of-the-wall and engine conditions can be summarized in Table 2.1. The traditional temperature wall functions which are currently mentioned before are

derived with the assumptions of steady, incompressible, and fully developed flows. Some of these assumptions are questionable when applied to engine flows, because the in-cylinder gas density varies significantly due to piston motion and combustion.

The unsteadiness and chemical heat release may invalidate the Reynolds analogy. Also, the assumptions of the traditional temperature wall function rely on a constant value of turbulent Prandtl number across the boundary layer while recent experimental results from literature have revealed that the turbulent Prandtl number increases in the boundary layer (Han et al., 1997). This increased Prandtl number affects wall heat transfer predictions.

Therefore, in conclusion, the traditional temperature wall function from the law-of-the-wall may not work when applied in engine simulations. This temperature wall function needs to be modified for representing wall modeling in engines.

2.3 In-cylinder heat transfer and wall heat transfer models

The in-depth research on heat transfer in internal combustion engines has developed for many decades. In theory, heat flux through combustion chamber walls is mainly due to gas-phase convection, fuel film conduction, and high-temperature gas and soot radiation (Han et al., 1997). However, the gas-phase convective heat transfer is the major concern in this research.

The results of experimental measurements such as diesel engines and spark ignition engines have been published by many researchers. In diesel engines, the first attempts were made by Annand (1963) and Woschni (1967). The motoring investigation from Duo (1973) and both motoring and firing conditions of Huber (1990) were reported in the literature. Spark ignition engines both motoring and firing conditions have also been studied by Overbye et al., (1967) and Alkidas et al., (1980). All the above experimental studies focus on measuring the heat fluxes at

various locations on the cylinder head, on the liner and on the piston head including the detailed information of in-cylinder field and the thermal boundary layers.

In the area of computational methods, numerous mathematical heat transfer models have been proposed and can be roughly divided into many groups based on the spatial resolution as follows. (Borman et al., 1987)

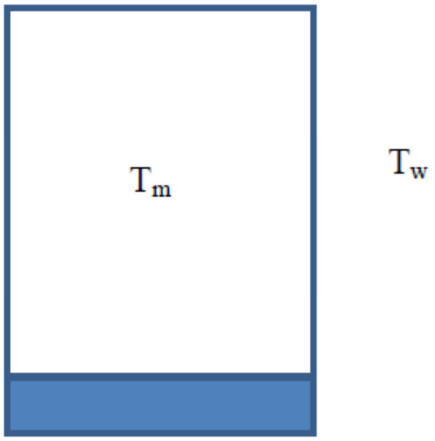

Figure 2.3 Global heat transfer model

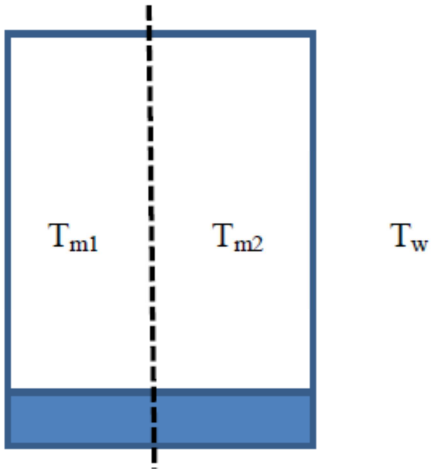

Figure 2.4 Zonal heat transfer model

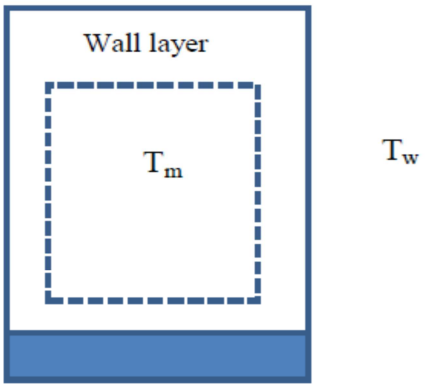

Figure 2.5 One-dimensional model

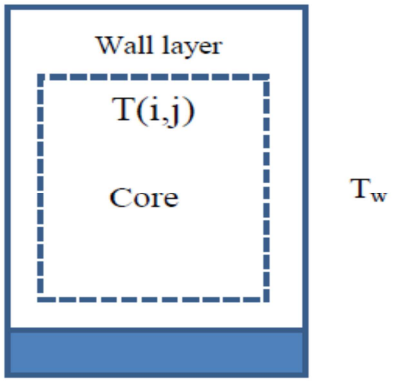

Figure 2.6 Multi-dimensional model

1. Global (one-zone) model
2. Zonal (multi-zone) model
3. One dimensional model
4. Multi-dimensional model

As mentioned before, this present work focuses on in-cylinder convective heat transfer between gas-phase and the walls, thus the radiation heat transfer model is excluded from reports. The radiation terms are sometimes included within the convective heat coefficient in the global model (Borman et al., 1987).

First, the empirical correlation with a dimensionless number as parameters is called the global heat transfer model or one zone model (Woschni, 1967 and Annand, 1970) as displayed in Figure 2.3. These models employ correlations to calculate overall heat transfer coefficients, which are assumed to be the same for all cylinder heat transfer surfaces, and a quasi-steady assumption is applied. However, since the information of spatial variation of heat-flux, temperature, and flow field cannot be provided by this approach and the global models are also strongly dependent on the empirical constants, the practical range of these models is limited within the conditions upon which the correlation is derived. These models are appropriate for engineering applications in which only global quantities are needed.

Table 2.2 Global heat transfer correlations (dimensional form)

Author	Correlation
Nusselt (1923)	$h_1 = c_1 p^{0.67} T^{0.33} (1+1.24u_p)$
Eichelberg (1939)	$h_2 = c_2 p^{0.50} T^{0.50} u_p^{0.33}$
Annand (1963)	$h_3 = c_3 p^{0.7} L^{-0.3} T^{-1.0} u_p^{0.7}$
Woschni (1967)	$h_4 = c_4 p^{0.8} L^{-0.2} T^{-0.35} u_4^{0.8}$
Hohenberg (1979)	$h_5 = c_5 p^{0.8} L^{-0.2} T^{-0.40} \left(u_p + 1.4\right)^{0.8} V_{inst}^{-0.06}$
Chang (2004)	$h_6 = c_6 p^{0.8} L^{-0.2} T^{-0.73} u_6^{0.8}$

Table 2.2 lists the global engine cylinder heat transfer correlations in dimensional form which are referred in the literature. The symbols in Table 2.2 are defined as follows: h is the convective heat transfer coefficient, p is in-cylinder pressure, T is cylinder gas temperature, u_p is the piston velocity, u_4 is unsteady velocity term, u_6 is the modified unsteady velocity term from

the original Woschni (1967) model , L is the characteristic length, and V_{inst} is the instantaneous cylinder volume.

Figure 2.4 shows the schematic of the zonal heat transfer models studied by Krieger et al. (1966) and Poulos et al. (1983). In these models, the in-cylinder combustion chamber was divided into an unburned and a burned zone. Each zone has its own values of heat transfer coefficient for the calculation of heat fluxes. However, using a similar manner as the global model, these models cannot provide local information of thermal condition within the combustion chamber.

One-dimensional heat transfer models were proposed by Isshiki et al. (1970) and Yang et al. (1989) as shown in Figure 2.5. The core regions and near wall layers were separated within these one-dimensional models. In the boundary layer near walls, heat fluxes were calculated directly by solving an energy equation without using a heat transfer coefficient, while the core region was considered a global region with uniform properties without spatial distinction. Compared to global and zonal models, one-dimensional heat transfer models can provide more physics of thermal boundary layers. However, in-cylinder core regions for internal combustion engines cannot be considered globally because there are local changes in the core region due to turbulence, swirling, tumbling and combustion effects. Therefore, to predict better wall heat flux results, multi-dimensional models for core regions including one dimensional heat transfer model are needed.

Figure 2.6 demonstrates a schematic of the multi-dimensional models of core flows and wall layers. In these models, conservation equations of mass, energy, momentum and species are solved for multi-dimensional core regions while the wall models are generally used within wall-layers. Since the mechanisms of wall-layers are similar to the physics within the thermal

boundary layer, the heat flux solutions based on the assumptions of the thermal boundary layer are obtained without solving the full governing equations.

In general, the analysis for the formulation of wall heat transfer model is initiated from the one-dimensional energy equation across the boundary layer which is described below in equation (2.13).

$$\underbrace{c_p \rho \frac{\partial T}{\partial t}}_{unsteady} + \underbrace{c_p \rho v \frac{\partial T}{\partial y}}_{convection} = \underbrace{\frac{\partial}{\partial y}\left[(k + k_t) \frac{\partial T}{\partial y} \right]}_{conduction} + \underbrace{\frac{dP}{dt}}_{work} + \underbrace{\rho Q}_{combustion} \tag{2.13}$$

In the classical wall heat transfer model developed by Launder and Spalding (1974), the unsteady term, the convection term, the work term, and combustion term from equation (2.13) were neglected. This model was based on the assumptions of incompressible flows and constant density and viscosity across thermal boundary layers. The thermal conductivity of fluid and the turbulent Prandtl number variation were not considered in this work. However, it is confirmed from many reports that heat flux results from this simple model under-predicted heat flux (Reitz 1991; Han et al., 1997; Park et al., 2009; Rakopoulos et al., 2010). The constant density assumptions from this model are not valid in engine flows. More advanced wall heat transfer models are needed.

Yang and Martin (1988) demonstrated wall heat transfer by using linearized techniques to avoid nonlinear terms in the governing equations. The unsteady one dimensional energy equation of a turbulent boundary layer was solved by using the empirical correlation of turbulent thermal conductivity. Also, the influence of unsteadiness and compressibility were tested in these studies. Only motored engine results were shown in these reports. It was also shown that the turbulent

thermal conductivity involved the characteristic length which was dependent on friction velocity. The results can match with experimental data by tuning friction velocity.

Improvement of engine heat transfer predictions using the modified wall function were followed by Huh et al. (1990). The pressure work term in the equations (2.13) was added in the formulation of the wall heat flux, and it was found that this pressure work is strongly dependent on the peak value of heat flux results. Moreover, Reitz (1991) applied the Lagrangian transformation to the temperature law-of-the-wall and turbulence boundary conditions. He also studied the effects of unsteadiness and gas compressibility on wall heat flux calculations. However, there are some limits when a Lagrangian transformation is employed. Kojima and Nishiwaki (1994) presented the increased the number of nodes near walls. Only the conservation of momentum and energy equations were solved while neglecting the equations of the turbulent kinetic energy and dissipation rate. They also employed the law-of-the-wall heat transfer in their model.

A compressible version of the Launder and Spalding model was introduced by AngelBerger et al. (1997). This model takes into account the variation of the gas density and viscosity within the boundary layer. Han et al., (1997) also proposed a model which was derived from the one-dimensional energy equation and which included thermodynamic variations of gas density and the increase of the turbulent Prandtl number across the boundary layers. They employed data from the incompressible flow assumption and statistics curve fitting to obtain the final equation of the wall heat fluxes. The valid region of these wall heat transfer models was extended by Ra et al., (2006), and the effects of small y+ were included. Because there is a steep temperature gradient between the wall and the first computational nodes next to the wall, Nijeweme (2001) used a reference temperature, which is a mean value between the wall

temperature and the temperature of the first node off from the wall, to calculate the gas density inside the wall function formulation. Park et al. (2009) presented a wall heat transfer model using full variation of physical properties. This model requires model constants which are tuned along with engine data.

To compare all previous heat transfer models, the final equations of wall heat flux are summarized in Table 2.3

Table 2.3 Comparisons of previous wall heat transfer models

Model	Wall heat flux	Valid region
Launder & Spalding (1974)	$q_w = \frac{\rho u_* c_p (T - T_w)}{\Pr\, y^+}$	$y^+ \le 11.63$
	$q_w = \frac{\rho u_* c_p (T - T_w)}{\Pr_t \left(\frac{1}{\kappa} \ln\left(E y^+\right) + P\left(\frac{\sigma_\theta}{\rho_{\theta,t}} \right) \right)}$	$y^+ > 11.63$
Huh et al. (1990)	$q_w = \frac{\rho u_* c_p (T - T_w) - 0.5 \frac{dP}{dt} \frac{\nu}{u_*} \Pr \left(y^+\right)^2}{\Pr\, y^+}$	$y^+ \le 13.20$
	$q_w = \frac{\rho u_* c_p (T - T_w) - \frac{dP}{dt} \frac{\nu}{u_*} \left(87.12 \Pr + 2.195 y^+ - 28.989\right)}{13.2 \Pr + 2.195 \ln\left(y^+\right) - 5.66}$	$y^+ > 13.20$
Angelberger et al. (1997)	$q_w = \frac{\rho u_* c_p T \ln\left(\frac{T}{T_w} \right)}{\Pr\, y^+}$	$y^+ \le 11.63$

	$q_w = \frac{\rho u_* c_p T \ln\left(\frac{T}{T_w}\right)}{\mathrm{Pr}_t\left(\frac{1}{\kappa}\ln(Ey^+) + P\left(\frac{\sigma_\theta}{\rho_{\theta,t}}\right)\right)}$	$y^+ > 11.63$
Han et al. (1997) and Ra et al. (2006)	$q_W = \frac{\rho u_* c_p T \ln(\frac{T}{T_W})}{\left\{7.483 \arctan(0.0935 y^+)\right\}}$	$y^+ \le 40.0$
	$q_w = \frac{\rho u_* c_p T \ln\left(\frac{T}{T_w}\right)}{2.1\ln(y^+) + 2.5}$	$y^+ > 40$
Rakopoulos et al. (2010)	$q_w = \frac{\rho u_* c_p T \ln\left(\frac{T}{T_w}\right) - \frac{dP}{dt}\frac{\nu}{u_*}\left(\frac{y^+ - 40}{0.4767 + \frac{1}{\mathrm{Pr}}} + 117.31\right)}{\frac{1}{0.4767}\left(\ln\left(y^+ + \frac{1}{0.4767\,\mathrm{Pr}}\right) - \ln\left(40 + \frac{1}{0.4767\,\mathrm{Pr}}\right)\right) + 10.2384}$	*All* y^+

However, most of previous wall heat transfer models were based on the traditional RANS techniques. The results from these methods cannot provide a detailed distribution of instantaneous heat fluxes. Therefore, previous wall heat transfer models have drawbacks and limits when more detailed spatial thermal information is needed.

2.4 Wall shear stress model in LES

The treatment of the wall boundary conditions is important, especially when accurate predictions of wall shear stress are required. In LES wall-bounded flows, an ill-posed problem may occur when uniform filtering is applied in the near-wall region, because the filter width may cross over the wall boundary (Schmidt, 2003). Also, it is impossible to directly resolve all scale

motions in the boundary layer since it requires a huge computational effort. Therefore, wall models are generally used to simulate flow structure near walls.

A good prediction of the wall model in LES should provide results in the local sense and should agree with law of the wall in the mean. Many LES wall models have been proposed in the literature and can be broadly classified into several groups as follows.

2.4.1 Equilibrium Laws

Equilibrium laws assume a constant stress near the walls. In particular, the inner layer is bypassed and the velocity at the first grid point in the outer layer is assumed to satisfy a logarithmic profile. With this approach, the wall model provides a set of boundary conditions to the outer flow LES in the form of wall shear stress. This methodology was first employed in a channel flow simulation by Schumann (1975). In this model, only the values of the streamwise and spanwise components of wall shear stress are calculated at the wall. At the first off-wall velocity nodes, the model assumed zero velocity condition in the wall normal direction and proposed a linear relation between instantaneous streamwise velocity and instantaneous wall shear stress as follow

$$\tau_{12,w} = \frac{\langle \tau_w \rangle}{\langle \tilde{u}(x, y_p, z) \rangle} \tilde{u}(x, y_p, z) \tag{2.14}$$

$$\tau_{32,w} = \nu \frac{\tilde{w}(x, y_p, z)}{y_p} \tag{2.15}$$

$$\tilde{v}_p = 0 \tag{2.16}$$

The term ν is kinematic viscosity, y_p is the distance between the wall and the first-wall node, and $\tilde{u}$ and $\tilde{w}$ are the resolved streamwise and spanwise velocities, respectively. The symbol $\langle\cdot\rangle$ is a time average over a plane parallel to the wall. However, this model is limited in use because the mean wall shear stress $\langle\tau_W\rangle$, which is approximately equal to the driving pressure gradient for a channel flow, must be known first. To overcome this issue, the modification of Grotzbach (1987) may be used, in which the mean velocity between the wall and the first LES grid point is assumed to satisfy a logarithmic law of the wall as

$$\left\langle \tilde{u}(x, y_p, z) \right\rangle = u_* \left[\frac{1}{\kappa} \ln\left(\frac{y_p u_*}{\nu} \right) + B \right] \tag{2.17}$$

$$\left\langle \tau_w \right\rangle = \rho u_*^2 \tag{2.18}$$

The term u_* is the friction velocity, κ is the Von Karman constant, and B is the value of the log law intercept. The model used the iterative process to solve for the friction velocity u_* and obtain the wall shear stress. Hence, a priori knowledge of the mean wall shear stress is not necessary. Moreover, to incorporate more physics in the wall model, the shifted model by Piomelli (1989) proposed a wall model which includes the inclination of near wall structures. He formulated the model according to the fact that the local wall shear stress is related not to the local near-wall parallel velocity, but to the near-wall velocity at the location shifted downstream by the optimal streamwise displacement. The shifted correlation model is written as

$$\tau_{12,w} = \frac{\left\langle \tau_w \right\rangle}{\left\langle \tilde{u}(x, y_p, z) \right\rangle} \tilde{u}\left(x + \Delta_s, y_p, z\right) \tag{2.19}$$

$$\tau_{32,w} = \frac{\langle \tau_w \rangle}{\langle \tilde{u}(x, y_p, z) \rangle} \tilde{w}(x + \Delta_s, y_p, z) \tag{2.20}$$

$$\Delta_s = y_p \cot 8^\circ \,, 30 < y^+ < 50 \tag{2.21}$$

$$\Delta_s = y_p \cot 13^\circ, \; y^+ > 50 \tag{2.22}$$

Based on observations, Piomelli (1989) also made a suggestion to consider coherent structures near-wall. The motion of high speed fluid toward or away from the wall, which takes place during sweep and ejection events, affects the wall shear stress. The impact of fast fluid pockets on walls causes the longitudinal and lateral vortex lines to stretch out, which leads to increased velocity fluctuations near the wall. On the other hand, the ejection of fast fluid masses induces the inverse effect, leading to a decrease in the wall shear stress. Therefore, the wall model should include these events and can be written in the form

$$\tau_{12,w} = \langle \tau_w \rangle - c u_* \tilde{v}(x + \Delta_s, y_p, z) \tag{2.23}$$

$$\tau_{32,w} = \frac{\langle \tau_w \rangle}{\langle \tilde{u}(x, y_p, z) \rangle} \tilde{w}(x + \Delta_s, y_p, z) \tag{2.24}$$

The term c is a dimensionless constant of order 1. Moreover, one should notice that all wall models mentioned above require the iterative process to obtain the friction velocity and average wall shear stress. However, there is another method which was proposed by Werner and Wengle (1989). They introduced a wall model based on the instantaneous velocity profile given by

$$u^+ = y^+, \ y^+ \le 11.8 \tag{2.25}$$

$$u^+ = A(y^+)^B, \ y^+ > 11.8 \tag{2.26}$$

The constant A is 8.3 and B is 1/7. Here, the log-law profile in equation (2.3) is replaced by the approximate power law (1/7) profile. The model assumed that the instantaneous tangential velocity components at the first near-wall nodes are parallel to the wall and are in phase with the wall shear stress. The values of the tangential velocity can be related to the wall shear stress by integrating the velocity profiles, which are given in the equations above, over the height of wall cells. As a result, this model can provide the analytical wall shear stress, and the iterative process is not required. In order to understand this model in more detail, it is derived as follows.

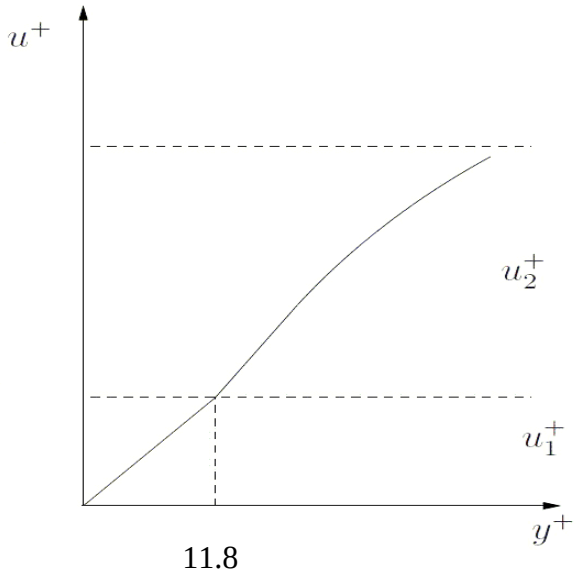

Figure 2.7 The Werner-Wengel (WW) velocity profiles.

Figure 2.7 shows the Werner-Wengle velocity profiles which are given as

Linear profile: $u^+ = y^+ \quad for \ y^+ \le y_m^+$

Power law: $u^+ = A(y^+)^B \quad for\ y^+ > y_m^+ \quad with\ A = 8.3\ and\ B = 1/7$

By definition,

$$y^+ = \frac{u_* y}{\nu} \tag{2.27}$$

$$u^+ = \frac{U}{u_*} \tag{2.28}$$

where U is the magnitude of gas velocity at the first grid point parallel to the wall , y is the distance from the wall. The intersection point ($y = y_m$ *and* $U=U_m$) of the two laws provides

$$y^+ = y_m^+ = A^{\frac{1}{(1-B)}} = 11.81 \tag{2.29}$$

By assuming that the first grid point is located at the centroid of the wall cells, the distance y from the wall to the centroid is equal to half of the height of wall cells ($\Delta y = 2y$).

For the linear law-of-the-wall region ($\Delta y^+ \le y_m^+$ *and* $U \le U_m$) , we have

$$\frac{U}{u_*} = \frac{y u_*}{\nu} = \frac{\Delta y u_*}{2\nu}$$

$$u_*^2 = \frac{U\nu}{y}$$

Hence

$$\tau_w = \rho u_*^2 = \frac{2\rho\nu U}{\Delta y}\ ,\ U \le U_m \tag{2.30}$$

Then

By integrating the velocity profile over the height of wall cells, we obtain

$$u^+ = \frac{1}{\Delta y^+}\int_0^{\Delta y^+} y^+ dy = \frac{1}{\Delta y^+}\frac{y^{+^2}}{2}\Bigg|_0^{\Delta y^+}$$

Therefore, the maximum velocity for linear law is given as

$$U_m = \left(\frac{\nu}{2\Delta y}\right) A^{\frac{2}{(1-B)}} \tag{2.31}$$

For the power law region $(\Delta y^+ > y_m^+ \ and \ U > U_m)$, we get

$$u^+ = \frac{1}{\Delta y^+}\left(\int_0^{y_m^+} u_1^+ dy + \int_{y_m^+}^{\Delta y^+} u_2^+ dy\right)$$

$$u^+ \Delta y^+ = \left(\int_0^{y_m^+} y^+ dy + \int_{y_m^+}^{\Delta y^+} A(y^+)^B dy\right)$$

$$= \left(\frac{y_m^{+2}}{2}\right) + \left(\frac{A}{1+B}\right)\left[\left(\Delta y^+\right)^{(1+B)} - \left(y_m^+\right)^{(1+B)}\right]$$

Finally, we obtain

$$U\left(\frac{1+B}{A}\right)\left(\frac{\Delta y}{\nu}\right) = \frac{1}{2} A^{\frac{2}{(1-B)}}\left(\frac{1+B}{A}\right) + \left(\frac{\Delta y}{\nu}\right)^{(1+B)} u_*^{(1+B)} - A^{\left(\frac{1+B}{1-B}\right)}$$

$$u_*^{(1+B)} = \left(\frac{1+B}{A}\right)\left(\frac{\nu}{\Delta y}\right)^B U + \left(\frac{1-B}{2}\right)\left(\frac{\nu}{\Delta y}\right)^{(1+B)} A^{\frac{(1+B)}{(1-B)}}$$

Therefore, the formulation of wall shear stress is given as

$$\tau_w = \rho u_*^2 = \rho\left[\left(\frac{1-B}{2}\right) A^{\left(\frac{1+B}{1-B}\right)}\left(\frac{\nu}{\Delta y}\right)^{(1+B)} + \left(\frac{1+B}{A}\right)\left(\frac{\nu}{\Delta y}\right)^B U\right]^{\frac{2}{(1+B)}} \ , \ U > \left(\frac{\nu}{2\Delta y}\right) A^{\frac{2}{(1-B)}}$$

The closed form of the streamwise shear stress is given by

$$\tau_w = \frac{2\rho\nu U}{\Delta y} \ , \ U \le \frac{\nu}{2\Delta y} A^{\frac{2}{1-B}} \tag{2.32}$$

$$\tau_w = \rho\left\{\frac{1-B}{2} A^{\frac{1+B}{1-B}}\left(\frac{\nu}{\Delta y}\right)^{1+B} + \frac{1+B}{A}\left(\frac{\nu}{\Delta y}\right)^{B} U\right\}^{\frac{2}{1+B}}, U > \frac{\nu}{2\Delta y} A^{\frac{2}{1-B}} \tag{2.33}$$

where ν is molecular viscosity and Δy is the height of the first cells near the walls.

In summary, most of models which are described above, such as Schumann (1975), Grotzbach (1987), and Piomelli (1989), calculate the mean wall shear stress using the iterative solution. However, by Werner and Wengle (1989) velocity profile approximation, the wall shear stress can be explicitly calculated.

2.4.2 Simplified boundary layer equations model

This method employs the turbulent boundary layer assumptions. To obtain the local wall shear stress, Hoffmann and Benocci (1995) analytically integrated the governing equations of the turbulent boundary layers which include eddy viscosity. They proposed a numerical solution of the local wall shear stress in the form

$$\tau_{12,w} = (\nu + \nu_t)\frac{\partial \overline{u}}{\partial y}\bigg|_0^Y - \overline{u}_Y \overline{v}_Y + \frac{d}{dx}\int_0^Y \overline{u}^2 dy - Y\frac{dP_{ext}}{dx} - \frac{d}{dt}\int_0^Y \overline{u} dy \tag{2.34}$$

$$\tau_{32,w} = \frac{\langle \tau_w \rangle}{\langle \tilde{u}(x, Y, z) \rangle} \tilde{w}(x, Y, z) \tag{2.35}$$

$$\overline{v}_Y = -\frac{d}{dx}\int_0^Y \overline{u}\,dy \tag{2.36}$$

As can be seen in equation (2.34), the pressure and unsteady terms are included in the model. The term $\frac{dP_{ext}}{dx}$ is equivalent to the external pressure gradient and v is kinematic viscosity. The term v_t is turbulent eddy viscosity, which is related with the turbulence models from the core flow. The test results with a channel flow agree with experimental data.

Moreover, Wang (1999) used a similar approach to calculate the flow over the trailing edge of an airfoil. The calculations are accurate in the zero or favorable pressure gradient regions of the flow, but the flow in the adverse pressure gradient region is not predicted accurately.

2.4.3 Zonal approaches

This approach used different grids in each computational domain, which is known as the two layer model (TLM). A secondary grid is located within the first cell near walls which is called the inner layer. Balaras & Benocci (1994) and Balaras et al. (1996) introduced this concept of two layer models in the literature. A different set of equations were solved at the inner and the outer layers. The Navier-Stokes equations were solved in the core flows while RANS equations were performed in near-wall models. The boundary layer equations used in the model can be rewritten in form

$$\frac{\partial \widetilde{u}_i}{\partial t} + \frac{\partial\left(\widetilde{u}_i \widetilde{u}_n\right)}{\partial x_n} = -\frac{\partial \overline{p}}{\partial x_i} + \frac{\partial}{\partial x_n}\left[\left(\nu + \nu_t\right)\frac{\partial \widetilde{u}_i}{\partial x_n}\right] \tag{2.37}$$

The index “i” are 1 and 3 and the index “n” is normal direction. The pressure term $\bar{p}$, which is assumed to be independent of the distance from walls, is computed from the LES outer flow equations. As expected, the integration of the above boundary layer equations leads to the wall shear stress components, which are used as boundary conditions for the outer flow calculation. Also, the normal velocity components are obtained from continuity equations

$$\tilde{u}_n = -\int_0^{x_n} \left(\frac{\partial \tilde{u}_1}{\partial x_1} + \frac{\partial \tilde{u}_3}{\partial x_3} \right) dx_n \tag{2.38}$$

Balaras & Benocci (1994) and Balaras et al. (1996) also proposed the artificial eddy turbulent viscosity based on the magnitude of the resolved strain rate tensor along with a damping function to assure the correct behavior of viscosity ν_t near walls. The eddy viscosity can be expressed as

$$\nu_t = (\kappa y)^2 D(y) \left| \tilde{S} \right| \tag{2.39}$$

The damping function is

$$D(y) = 1 - \exp\left[-\left(\frac{y^+}{25} \right)^3 \right] \tag{2.40}$$

The term y is the distance to the wall and κ is the Von Karman constant. An interesting implication is that the computational costs for this model are not significantly higher than those of equilibrium stress models, because only two one-dimensional problems are solved without Poisson equation.

2.4.4 Hybrid RANS/LES

Alternatively, one approach for the wall shear stress model is based on the idea of merging LES with RANS to model the near wall regions. The same grid is employed within the inner and outer layers, but only the turbulence model is switched. This is a different concept when comparing with the previous zonal approach. The equations reduce to unsteady RANS equations in the near-wall regions, while the governing equations take on the form of LES equation away from the wall. This model was introduced by Spalart et al. (1997) and was named Detached Eddy Simulation (DES).

In particular, this model employs a one-equation turbulence model to determine the eddy viscosity coefficients. The model itself switches back and forth from RANS to LES by changing the local length scale, which leads to a variation of eddy viscosity in the flow field. As a result, this model does not depend on zones. However, there are some issues for wall models that employ the hybrid RANS/LES scheme. Because there are different scales between the LES and RANS approaches, a mean velocity mismatch is created at the interface regions (Piomelli, 2002). This is known as logarithmic laws mismatch, which also was supported by the work of Davidson and Peng (2003).

2.4.5 Conclusion of LES wall shear stress models

In summary, the equilibrium stress model is the least computationally expensive model, while the cost of hybrid RANS/LES method is highest because the wall normal direction must be solved, such as in the model of Spalart et al. (1997). The disadvantage of the hybrid RANS/LES method is the logarithmic layer mismatch of mean velocity at inner/outer interface. Also, this method is not a pure LES simulation, because it is performed by different turbulence models (RANS and LES) within the same computational domain of interest. The equilibrium model can

predict reasonable results in attached flows and mild pressure gradients (Piomelli, 2002). Moreover, by logarithmic law modification, this equilibrium model can easily include the wall surface roughness. Zonal models have had some success in flows in which the outer layer drives the inner one. At present, it is still not clear which methods are the best for LES wall models.

However, these successful LES results are reported for only simple channel flows (Deardorff, 1970; Balaras et al., 1996; Piomelli, 1999). This may not work well with engines since the flow fields in engines are highly transient, non-stationary, and turbulent (Celik, 2001). Also, the geometry in engines is complex, so the application of these models to engine flows may be problematic. Therefore, one must be careful when they are applied with engine cases.

2.5 Existing LES wall shear stress and wall heat transfer models

In KIVA engine codes, one possible option for LES simulations is that the standard RANS based wall shear stress model is applied at wall boundary conditions. The local wall shear stresses are calculated from known filtered velocity near walls. The LES equilibrium laws may be approximated to apply in engines if the computational grids in the boundary layers are larger than the boundary layer thickness (Celik et al., 2001). The fluctuating component of velocity may be removed by the filtering process. Hence, the assumption of equilibrium laws may be reasonable (Celik et al., 2001).

Moreover, for wall heat flux predictions, the first attempt for wall heat transfer modeling in LES is the VDHT model of Han et al. (1997), which includes the variation of gas density and turbulent Prandtl number across the thermal boundary layers. The information of filtered temperature near walls is employed in these wall heat transfer formulations. Also, a sub-grid scale turbulent kinetic energy near walls is used to calculate friction velocity. The heat flux

results are calculated from this model. More details of these formulations are discussed in the next section.

However, it is found that the standard wall shear stress model in the KIVA engine code is derived from existing RANS law of the wall models. These models are based on time averaging, which is not present in LES. The values of filtered velocity gradients near walls may not produce a good scale with local wall shear stresses results, which are estimated from standard wall shear stress model in the KIVA engine code. Therefore, the standard wall shear stress model in the KIVA engine code is improved when the LES technique is used. Similar to the VDHT model of Han et al. (1997), this model needs to be modified when used for LES simulations, because its formulation relies on a RANS-based wall model. The discussion above shows that there is some room for improvement in the wall shear stress model and wall heat transfer model when using with LES for engine CFD calculations.

2.6 Review of turbulent flow and heat transfer in a square duct

In the present work, it is a minimum requirement to validate a new wall model with a square duct before it is moved to engine complex flow cases. Since there is some limit of available experimental data of wall shear stress and wall heat transfer in engines which have been published in literature, one option to test new wall models is that the model constant from new models is calibrated from existing square duct results.

The forced turbulent heat convection in a straight square duct is one of the fundamental problems in thermal science and fluid mechanics. The behavior of wall variables in a turbulent square duct and boundary layer flows is of considerable interest in applications involving drag and heat transfer. Several fundamental studies of turbulent flow in square and rectangular ducts

exist in the literature. Direct numerical simulations (DNS) have been carried out for a square duct by Gavrilakis (1992) and Huser and Biringen (1993), with Reynolds numbers of 4,410 and 10,000, respectively. Large eddy simulations of square and rectangular ducts have been reported by Madabhuhi et al. (1991) at a Reynolds number of 5,800, and by Su et al. (1994) at a Reynolds number up to 49,000.

Nikuradse (1930) was the first pioneer to test in a straight duct and observe the mean secondary flow of rectangular cross section, which cannot be found in circular straight ducts. Although the magnitude of secondary flows are only about 2-3 percent of the streamwise mean velocity, this motion makes a reduction in volumetric flow rate and causes the axial velocity field to be distorted. The secondary flows are perpendicular to the main flow directions and are produced in the cross sectional plane, which is directed from the center of the duct to the corners. Madabhushi et al. (1991) proposed that these secondary flows come from the anisotropy of the Reynolds stress. These flows usually carry momentum from the center area to wall regions along the corner bisectors. As a result, they dominate the local wall shear stress along the duct periphery. The secondary motion produces an increase in the wall shear stress towards the corners. Figure 2.8 (a) shows the mean secondary velocity vectors whereas the contours of mean streamwise velocity at a cross-sectional plane are illustrated in Figure 2.8 (b). All quantities are averaged over the four quadrants. Many experimental studies have been conducted to investigate the flow characteristics in a square duct (Brundrett et al., 1964 & Melling et al.,1976 & Gessner et al., 1979).

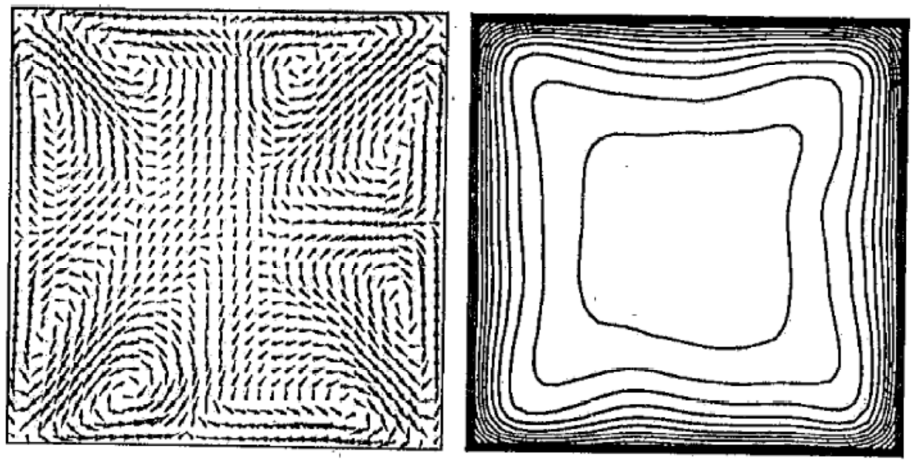

Figure 2.8 Numerical results of square duct flows with Re =42,000. (a) Left: mean secondary velocity vectors, (b) right: contours of mean streamwise velocity at a cross-sectional plane (Balaras et al., 1996)

A large amount of experimental data is available in the literature for fully developed turbulent heat transfer in a square duct. Similar to momentum transfer, the thermal energy is also transported by secondary flow. Novotny (1964) showed the results of Nusselt number for turbulent air flows in a square duct with two isolated and two uniform heat flux walls. Brundrett et al. (1964) reported the distributions of the mean temperature profiles in a square duct and revealed that the influence of the secondary flow appear in the local wall heat flux distributions. In numerical simulations, Launder et al. (1973) calculated the mean temperature distributions in the duct with the assumption that the turbulent Prandtl number is constant over the duct cross section. The same results were also shown by Nakayama et al. (1986) and Myong (1991). The works of Emery et al. (1980) performed the mean temperature distribution in a square duct and compared their numerical results with experiment. Fujita et al. (1988) made the numerical simulation for turbulent flow and heat transfer in a square duct with two roughened facing walls.

2.7 Wall treatment in the KIVA engine code

The numerical implementation of the turbulent boundary layer equations in KIVA code is discussed here. More details can be found in the literature (Amsden et al., 1989).

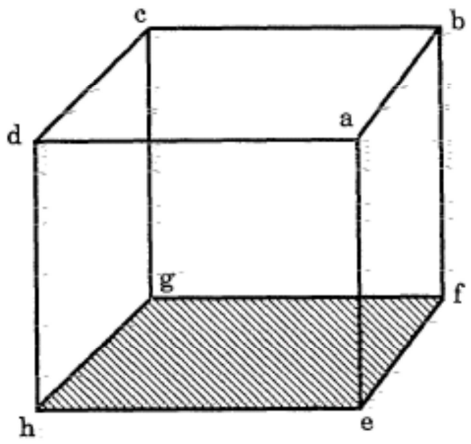

Figure 2.9 The schematic of KIVA wall cells (Amsden et al., 1989)

Consider a wall cell adjacent to the wall as shown in Figure 2.9. Nodes e, f, g, and h lie on the wall, while nodes a, b, c, and d are in the fluid. First, to calculate the wall shear stress, the tangential velocity $\underline{u}$ is calculated by

$$\left|\underline{u}\right| = \left| \frac{1}{4} * \left(\underline{u}_a + \underline{u}_b + \underline{u}_c + \underline{u}_d \right) \right| \tag{2.41}$$

Equation (2.41) assumes the normal velocity at point a, b, c, and d is negligible. The tangential component may be replaced by the magnitude of the velocity. The magnitude of the normal velocity is calculated from the momentum equation. Also, the distance y from the wall is evaluated by

$$y = \left| \frac{1}{4} * \left[\left(\underline{x}_a - \underline{x}_e \right) + \left(\underline{x}_b - \underline{x}_f \right) + \left(\underline{x}_c - \underline{x}_g \right) + \left(\underline{x}_d - \underline{x}_h \right) \right] * \frac{A_a}{|A_a|} \right| \tag{2.42}$$

where A_a is the area vector of the face cell which lies on the wall. The standard wall shear stress in KIVA is calculated using the velocity wall function of law-of-the-wall conditions in Equations 2.7 and 2.8. The product $\tau_w A \Delta t$ contributes the total change in fluid momentum in each timestep due to wall friction associated with the wall cell. One-fourth of this change is allocated to each of the nodes e, f, g, and h. Moreover, for the thermal analysis, the heat flux results are calculated from wall heat transfer model. The term $q_w A \Delta t$ represents the energy loss to the wall, which is deducted from the internal energy of the cell. Also, the product $\tau_w u A \Delta t$ gives the kinetic energy dissipated by the wall friction, which is added to the internal energy of the cell.

2.8 Jet impingement on a flat plate

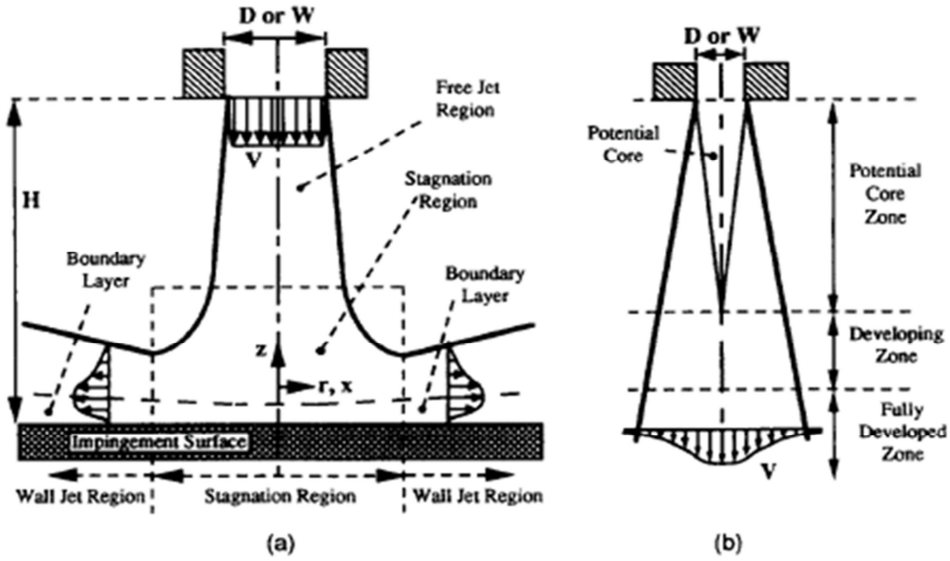

Figure 2.10 The schematic of impinging jets (a) Flow regions for an impinging free-surface jet; (b) flow zones of a free jet. (Viskanta, 1993)

The turbulent impinging jet is frequently used in engineering applications when high heat transfer rates which occur in the impingement region are required. The applications of these impinging jets are employed for heating and drying processes in glass, paper, and steel industries, and for cooling of turbine blades and electronic components. Most of those applications of interest are in turbulent regime with complex flow characteristics such as stagnation, recirculation, and adverse pressure gradient zones. Moreover, these many complex structures of impinging jets strongly effect on heat transfer rate. Therefore, the accurate flow field and heat transfer prediction of turbulent jets on the impingement plates is needed for those industrial applications.

There are a lot of numerical and experimental studies on the flow characteristics and heat transfer of jet impingement on wall surfaces in the literature. Both single jets and multiple jets were tested in many conditions including the effects of crossflow, jet orientation, and rotating surfaces. The present study is concerned with the case of a singular circular turbulent air jet at the ambient air temperature impinging on a flat stationary surface with a constant surface temperature. Therefore, only a single air jet is reviewed in this section.

2.8.1 Jet flow characteristics

The flow structure of a typical impinging jet is shown in Figure 2.10. Reynolds number of impinging jets which produced by an orifice or a nozzle can be defined as

$$\mathrm{Re} = \frac{U_b D_j}{\nu} \tag{2.43}$$

where the term U_b is bulk velocity of pipe flow, D_j is the diameter of pipe or jet diameter and ν is kinematic viscosity. A fully turbulent jet is considered when Reynolds number is greater than 3000. Figure 2.10a demonstrates the flow zones in an impinging jet which are commonly comprised of three main regions.

First, a free-jet area is the region which is unaffected from the impinged wall. This free-jet area can be subdivided into three regions including potential core regions, developing regions, and fully developed regions as shown in Figure 2.10b. After exiting from the nozzle towards the impinged walls, in a potential core, the jet velocity at the centerline does not change in the streamwise direction and is equal to its value at the nozzle exit. In a developing zone, the mixing between the existing jet and ambient air forms the shear layer which creates the entrainment of mass, momentum and energy at the jet boundary which leads to the decay of the axial velocity. The axial velocity profile is fully developed and similar in the developing regions. However, the incoming jets may or may not be fully developed when the jets hit the walls depending on the distance between the nozzle exit and impinged wall.

In the impinging zone, there is a rapid decrease in center velocity and axial momentum as corresponding static pressure rises when the jet reaches the wall. At the wall boundary, the stagnation point, where the mean velocity is zero is formed within the center of the impinging region. Also, the bulk flows of jet in the impingement regions are forced to change the direction and are turned into the outward radial direction with a strong angular acceleration. The boundary layer begins to grow from the point of impingement. The strong acceleration may keep the boundary layer laminar in the stagnation zone (Martin, 1977).

Away from the stagnation point, the flow develops along impingement surface in the form of the wall-jet. In the wall-jet regions, the flows are parallel to the impingement walls. As

the radial distance increases, the cross-sectional area of the flow in the wall jet region increases. Thus, the mean radial velocity decelerates in the flow direction while the jet spreads radially outward. The thickness of turbulent boundary layer increases. Commonly, the wall-jet is characterized by a strong shear with the turbulence level much higher than those of parallel flows. The friction coefficient is defined as

$$C_f = \frac{\tau_w}{\frac{1}{2}\rho U_b^2} \tag{2.44}$$

where the term τ_w is wall shear stress. Figure 2.11 shows the friction coefficient of a round impinging jet experiments with Reynolds number of 23,000 (Tummers, 2011). At the stagnation point, the value of friction coefficient is zero due to no mean velocity at that point.

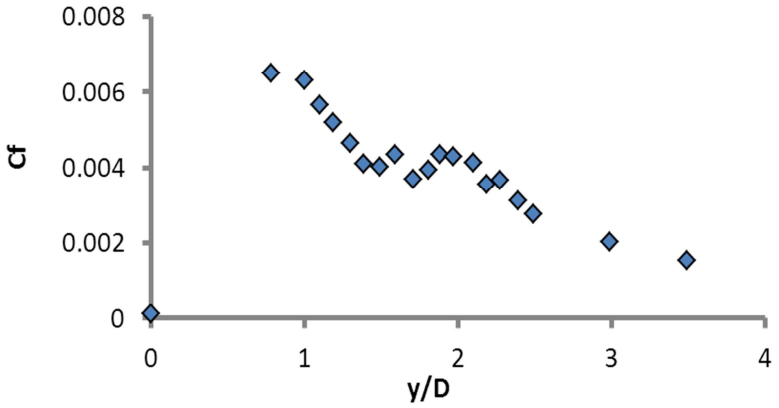

Figure 2.11 Friction coefficients versus radial position (Tummers, 2011)

2.8.2 Heat transfer characteristics

The direct impingement of turbulent jet onto an impinged wall promotes high local heat transfer rates. The strong aerodynamic and thermal interaction which exists between the incoming jets and the walls has an impact of the local heat transfer in the stagnation and wall-jet

regions. The local rate of wall-jet heat transfer is non-uniform and is not unique since it is dependent on many parameters such as Nusselt number (Nu), Reynolds number (Re), Prandtl number (Pr), the non-dimensional nozzle to plate spacing (H/D) and the displacement from the stagnation point (r/D) (Jambunathan et al., 1992). In general, the heat transfer distribution of wall-jet is given by the variation of the local Nusselt number with radial position and where the Nusselt number is defined as

$$Nu = \frac{hD}{k_f} \tag{2.45}$$

where the term D is the jet diameter, h is the heat transfer coefficient and k_f represents the thermal conductivity of fluid. In general, the thermal boundary conditions of wall-jet heat transfer can be divided into two categories i.e., a uniform wall heat flux and a constant wall temperature. The Nusselt number which is obtained from both thermal boundary conditions is the highest values when compared with a single-phase convection.

In turbulent jets, the statistically averaged Nusselt number (Nu) usually shows large values at the stagnation point. The value of Nu at the stagnation point cannot be fully associated with the level of turbulence. The main factor associated with large scale eddies are the broken ring vortices which impinge periodically on the wall surface (Hadziabdic et al., 2008). Also, the thickness of the boundary layer is very thin at the stagnation point. It leads to high stagnation point heat transfer because the heat transfer resistance is relatively low.

Moreover, after many different experimental techniques of jet impingement from the literature are explored, two definitions of the convective heat transfer coefficient are used and defined as

$$h = \frac{q_{conv}}{(T_w - T_{ad})} \tag{2.46}$$

$$h = \frac{q_{conv}}{(T_w - T_j)} \tag{2.47}$$

where the term T_{ad} is the adiabatic wall temperature and T_j is the jet temperature.

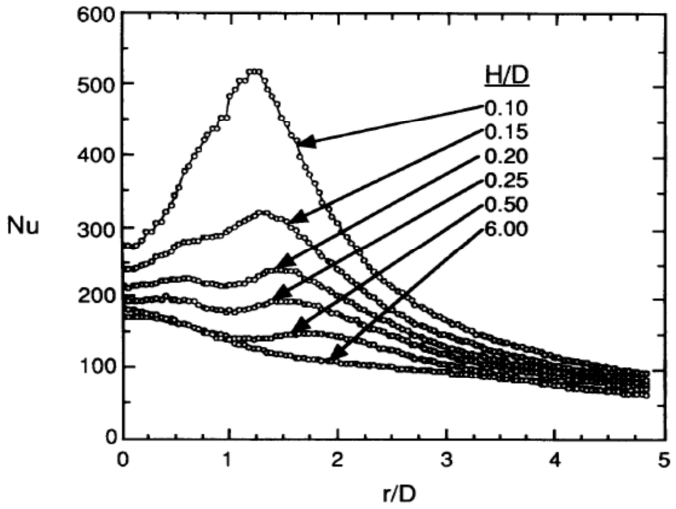

Figure 2.12 The radial variation the local Nusselt number (Lytle et al., 1991)

Equation 2.46 can be used when the thermal boundary condition of uniform heat fluxes are applied while Eq. (2.47) can be employed for either uniform wall heat flux or constant wall temperature thermal boundary condition. Figure 2.12 demonstrates the experimental data of the radial variation of local Nusselt number from air jet impingement with Reynolds number of 23,000 (Lytle et al., 1991). One thing can be seen from Figure 2.12, the shape of the radial heat transfer distribution is affected by the nozzle exit to plate spacing (H/D). Far away from a stagnation point, a rapid variation of heat transfer also can be observed. For the separation

H/D > 0.25, a local maximum heat transfer developed at the stagnation point (r/D=0). The variation of Nusselt number (Nu_{stag}) at the stagnation point has reported by works of Goldstein et al. (1986). The stagnation point heat transfer is relatively low and constant when the nozzle exit to plate distance (H/D) is located within the potential core length. The magnitude of stagnation point heat transfer increases with H/D for distance beyond the potential core length until it reaches a maximum at H/D = 8. Lee et al (1995) also found the maximum value of Nu_{stag} was at H/D = 6.

Colucci et al (1996), which mainly focused on the effect of Reynolds number, nozzle exit to plate spacing and nozzle geometry on local heat transfer coefficient, found the second peak value of Nusselt number in the heat transfer distribution at low spacing (H/D=0.25). The experiment was tested at low nozzle to plate spacing ($0.25 < H/D < 6.0$) and Reynolds number in the range of 10,000 to 50,000. Baughn et al. (1989) reported similar behavior of the second peak of Nusselt number distribution and concluded that the second maximum in the Nusselt number exists only the jets with ($H/D<6.0$).

The two peak maximum of heat transfer relates to the development of the boundary layer. In particular, the laminar boundary layer starts to develop from the stagnation point and eventually undergoes the transition to the turbulent boundary layer. This transition is believed to be responsible to the secondary peak in the Nusselt number distribution since the enhancement of mass transfer towards the wall. Another explanation for the second peak of Nusselt number was given by Jambunathan et al. (1992) who concluded that this second peak of heat transfer was due to rapid acceleration of jets in the deflection regions near the stagnation point. The acceleration jets promote higher local Nusselt numbers.

Cooper et al. (1993) studied a single turbulent jet impinging normal on a large plane surface with Reynolds number of 23,000 and 70,000. They used hot wire instrumentations to investigate the details of mean velocity and turbulence quantities. Inflow boundary condition and the fully developed of pipe flows were employed in the experiments. By the spacing (H/D) varying from 2.0 to 6.0, the heat transfer increases about 10%. From experimental data of Nishino et al. (1996), the turbulence statistics information of a single impinging jet at the stagnation point was reported.

Impinging jet studies using large eddy simulation (LES) are reviewed here. Voke et al. (1998) reported a computational study of the impingement plane jet with Re = 6,500. They studied a plane jet of water issuing from a plane channel focusing on temperature variations at the plate surface. The temperature two points correlations were shown in this research. Large eddy simulation of flow and heat transfer from an impinging rectangular slot jet was investigated by Cziesla et al. (2001). A dynamic subgrid-scale has been used for the small scales of turbulence. These works showed the flow structures of impinging jets and the distributions of mean velocities, velocity fluctuations and turbulent stresses were also reported.

A good agreement of predicted heat transfer results at the stagnation point was found when compared with experimental data. Hadziabdic et al. (2008) applied large eddy simulations techniques with a round normally impinging jet which exits from the long pipe with Re=20,000 and H/D =2.0. The flow field and heat transfer prediction were studied and verified with experimental data. More details of flow, vertical and turbulent structures were investigated.

2.8.3 Impinging jets in engines

The combustion process in direct injection compression ignition engines such as diesel engines has been studied for a long time. Impinging jet is one process which plays a role in the generation of localized regions with high levels of heat transfer. The high pressure level of liquid fuel is injected from nozzle exit into the combustion chamber during the power stroke. The fuel enters the environment with high momentum and travel towards the chamber wall. Small droplets are generated and vaporize when they mix with the high temperature compressed air. Since the air temperature and pressure are above the fuel's ignition point, the vapor self-ignites and the combustion process begins. The hot gases from combustion continue to move towards the combustion chamber wall. Impinging hot gas jets can generate very high levels of heat transfer coefficient in the impingement zone. This phenomenon also produces a localized high temperature spot on the combustion chamber walls which may reduce life cycles of mechanical engine structures.

Chapter 3 Wall model formulation

3.1 Introduction

To obtain better results for LES simulations, the specific goal of this study is to develop new wall models, such as a wall shear stress model and a wall heat transfer model. These models should rely on information from LES turbulent modeling in the core flows. Inaccurate predictions of the velocity wall function cause inaccurate predictions of thermal conditions near walls. Therefore, the accurate prediction of the velocity wall function is a prerequisite for an accurate prediction of wall heat transfer. This chapter shows the three wall model formulations which are tested in this research. First, a standard wall shear stress in the KIVA engine code is simulated with RANS techniques and the LES approach. Then, the improved Werner-Wengle wall model with LES is proposed. The results from all models are compared and discussed in this work.

3.2 LES governing equations in core flows (outer regions)

By applying a density-weighted LES spatial filtering operation on the continuity equations and the Navier-Stokes equations, the governing equations for the large (resolved) scales are obtained. The more detail can be found in appendix. Equation (3.1) is the LES filtered continuity equation.

$$\frac{\partial \bar{\rho}}{\partial t} + \frac{\partial \bar{\rho} \bar{u}_i}{\partial x_i} = 0 \tag{3.1}$$

The LES filtered momentum equation is given by

$$\frac{\partial \bar{\rho} \bar{u}_i}{\partial t} + \frac{\partial \bar{\rho} \bar{u}_i \bar{u}_j}{\partial x_j} = -\frac{\partial \bar{p}}{\partial x_i} + \frac{\partial}{\partial x_j}\left(\mu \frac{\partial \bar{u}_i}{\partial x_j}\right) - \frac{\partial \bar{\rho} \Gamma_{ij}}{\partial x_j} - \overline{F_i} \tag{3.2}$$

where the overbar indicates spatial filtering using the local CFD cell volume. The term F_i is the momentum sink due to the liquid spray drag in the resolved scale (Bharadwaj et al., 2009). The unclosed term Γ_{ij} is generally called the LES sub-grid stress tensor and needs to be modeled. Here, the dynamic structure model uses a non-viscosity relationship to model this unclosed sub-grid stress term $\Gamma_{ij.}$ This term is proportional to the sub-grid kinetic energy with the dynamically determined coefficient tensor L_{ij}.

$$\Gamma_{ij} = 2k_{sgs}\left(\frac{L_{ij}}{L_{kk}}\right) \tag{3.3}$$

The LES sub-grid kinetic energy is defined by

$$k_{sgs} = \frac{1}{2}\left(\overline{u_i u_i} - \overline{u}_i \overline{u}_i\right) \tag{3.4}$$

The coefficient is the normalized Leonard term which is obtained from the resolved gas phase velocity field as follows:

$$L_{ij} = \left(\overline{\overline{u_i u_j}} - \overline{\overline{u}_i \overline{u}_j}\right) \tag{3.5}$$

where the second overbar indicates a test filter operation with filter size equal to twice the base of filter size. Also, the LES sub-grid kinetics energy obtained from the transport equation (Pomraning et al., 2000) is given by

$$\frac{\partial \overline{\rho} k_{sgs}}{\partial t} + \frac{\partial \overline{\rho} \overline{u}_i k_{sgs}}{\partial x_i} = -\overline{\rho}\Gamma_{ij}\overline{S}_{ij} - \overline{\rho}\varepsilon_{sgs} + \frac{\partial}{\partial x_i}\left(\overline{\rho}\nu_{tk}\frac{\partial k_{sgs}}{\partial x_i}\right) \tag{3.6}$$

Here, the sub-grid dissipation rate ε_{sgs} and the sub-grid eddy viscosity term ν_{tk} are defined as (Ghosal et al., 1995 and Menon, 1996).

$$\nu_{tk} = c_k \overline{\Delta} k_{sgs}^{0.5} \tag{3.7}$$

$$\varepsilon_{sgs} = \frac{c_\varepsilon k_{sgs}^{1.5}}{\overline{\Delta}} \tag{3.8}$$

$$\overline{\Delta} = \left(vol\right)^{0.333} \tag{3.9}$$

where vol is cell volume, the term S_{ij} is the symmetric part of the deformation rate tensor, and the constants C_k and C_ε are set to 0.05 and 0.3, respectively. These LES formulations are implemented in the KIVA-3V-Release 2 code.

Moreover, the results from the traditional RANS turbulence technique are included and compared to the LES results. The more detail of the RANS governing equations in core flows can be found in the literature (Reitz, 1991). In order to provide accurate simulation results, the boundary conditions of those governing equations are needed. The wall models tested in this research are described in the next section.

3.3 Wall model formulations

This section shows the three wall model formulations which are tested in this work. First, a standard wall shear stress in the KIVA engine code is simulated with RANS techniques and the LES approach. Then, the improved Werner-Wengle wall model with LES is tested. The results from all models are compared and discussed in this research.

3.3.1 MODEL-I (RANS-LW)

In this model, RANS techniques (RANS-LW) are simulated with a standard wall shear stress model from the KIVA engine code which uses law-of-the-wall velocity conditions. These equations are summarized below (Amsden et al., 1989)

$$\tau_w = \rho\left(\frac{U}{u^+}\right)^2 \tag{3.10}$$

where τ_w is wall shear stress, ρ is gas density and U is the magnitude of gas velocity parallel to the wall and

$$u^+ = \left(\frac{yU}{\nu}\right)^{\frac{1}{2}} \quad , \frac{yU}{\nu} \le R_c \tag{3.11}$$

$$u^+ = \frac{1}{\kappa}\ln\left\{c_{lw}\left(\frac{yU}{\nu}\right)^{\frac{7}{8}}\right\} + B \quad , \frac{yU}{\nu} > R_c \tag{3.12}$$

where y is the distance from the wall and ν is molecular viscosity. The term $\frac{yU}{\nu}$ represents Reynolds number, which is based on the gas velocity relative to the wall. Also, the transition R_c is equivalent to 114 and the constant c_{lw} is equal to 0.15 (Amsden et al., 1989). These relations give κ = 0.4327 and B = 5.5. To obtain heat flux results in realistic engine calculations for thermal analysis, the classical wall heat transfer model of Han et al. (1997), which takes into account the variation of gas density and viscosity within the boundary layers (VDHT model), is employed, and the effect of sufficiently small non-dimensional wall normal distance y^+ is

included (Ra et al., 2006). More detailed assumptions used in the model derivation can be found in the reference. The corresponding formulation of wall heat flux is given as

$$q_W = \frac{\rho u_* c_p T \ln(\frac{T}{T_W})}{\left\{7.483 \arctan\ (0.0935 y^+)\right\}} \quad , \ y^+ \le 40 \tag{3.13}$$

$$q_W = \frac{\rho u_* c_p T \ln(\frac{T}{T_W})}{\left\{2.1 \ln(y^+) + 2.5\right\}} \quad , y^+ > 40 \tag{3.14}$$

Also

$$y^+ = \frac{u_* y}{\nu} \tag{3.15}$$

The friction velocity u_* is calculated from turbulent kinetic energy (tke) near walls as follows

$$u_* = (c_\mu^{0.25} tke_{nw}^{0.5}) \tag{3.16}$$

with the constant $C_\mu = 0.09$ (Han et al , 1997).

3.3.2 MODEL-II (LES-LW)

This LES models (LES-LW) are simulated with the standard wall shear stress model (law-of-the-wall velocity conditions) and the classical wall heat transfer model of Han et al. (1997). Eqs. (3.10-3.15) are also employed in the model. In the friction velocity calculation, since the turbulent kinetic energy does not exist in LES, this term is replaced by the near-wall sub-grid scale turbulent kinetic energy (ksg) (Banerjee et al., 2012).

$$u_* = (c_\mu^{0.25} k_{sgs\_nw}^{0.5}) \tag{3.17}$$

3.3.3 MODEL-III MODIFIED WERNER-WENGLE WALL SHEAR STRESS MODEL (IMPROVED LES-WW MODEL)

The original model introduced by Werner and Wengle (WW) is considered here (Werner et al., 1989). They have proposed a wall model for LES that is based on the linear law-of-the-wall and the power law profile of the form

$$u^+ = A(y^+)^B \tag{3.18}$$

where the constant A is equal to 8.3 and constant B is 1/7. This model assumes that instantaneous tangential velocity components at the first near-wall nodes are in phase with the wall shear stress. By integrating the velocity profile over the height of wall cells, the explicit form of wall shear stress formulations are obtained. A more detailed derivation can be found in the section 2.4.1. In particular, there are many previous LES wall shear stress models which have been proposed and tested in the literature. However, these models (Deardorff, 1970; Schumann, 1975; Grotzbach, 1987; Balaras et al., 1996) rely on the iteration process for friction velocity prediction and then the wall shear stresses are calculated. On the other hand, for the WW model, no iteration method is necessary because this model provides the wall shear stress explicitly. The model for calculating the wall shear stresses is given by Eqs. (2.32-2.33) and repeated here:

$$\tau_w = \frac{2\rho\nu U}{\Delta y} \;,\; U \le \frac{\nu}{2\Delta y} A^{\frac{2}{1-B}} \tag{3.19}$$

$$\tau_w = \rho\left\{\frac{1-B}{2} A^{\frac{1+B}{1-B}}\left(\frac{\nu}{\Delta y}\right)^{1+B} + \frac{1+B}{A}\left(\frac{\nu}{\Delta y}\right)^{B} U\right\}^{\frac{2}{1+B}}, U > \frac{\nu}{2\Delta y} A^{\frac{2}{1-B}} \tag{3.20}$$

where Δy is the height of the first cells near the walls. However, to provide better local wall shear stress results, the original WW model should be modified in the present work. The effect from small scale motions near walls should be included in the model. In particular, it employs the near-wall sub-grid scale turbulent kinetic energy, which relates to small scale motion. The near-wall sub-grid scale eddy viscosity is included in the outer fully turbulent region of the wall layer, which is characterized by the logarithmic layer, and is defined as

$$\nu_{tk\_nw} = c_{mw}(vol_{nw})^{0.33} k_{sgs\_nw}^{0.5} \tag{3.21}$$

where, vol_{nw} is the near-wall cell volume. The sub-grid scale kinetic energy is denoted by k_{sgs_nw} Therefore, Eq. (3.20) is modified as

$$\tau_w = \rho\left\{\frac{1-B}{2}A^{\frac{1+B}{1-B}}\left(\frac{\nu_{nw}}{\Delta y}\right)^{1+B} + \frac{1+B}{A}\left(\frac{\nu_{nw}}{\Delta y}\right)^{B} U\right\}^{\frac{2}{1+B}}, U > \frac{\nu}{2\Delta y}A^{\frac{2}{1-B}} \tag{3.22}$$

where
$$\nu_{nw} = \nu + \nu_{tk\_nw} \tag{3.23}$$

Also, the friction velocity can be defined as

$$u_* = \sqrt{\frac{\tau_W}{\rho}} \tag{3.24}$$

One thing to clarify here is that two different equations of predicted friction velocity are demonstrated in the research. Eq. (3.16) is introduced by the reference (Han et al., 1997) for RANS-LW model and Eq. (3.17) is employed by the reference (Banerjee et al., 2012) for LES-LW model, while the improved LES-WW model uses Eq. (3.24) to calculate friction velocity.

Moreover, to gain better heat flux results with LES simulations, the classical wall heat transfer (VDHT) model of Han et al. (1997) is modified to be coupled with the friction velocity from Eq. (3.24), which is calculated from the modified WW model. Also, the constant c_{hw} is inserted into this model to adjust scales from RANS wall model to LES scales. Finally, the formulation of the improved wall heat transfer is given as

$$q_W = \frac{\rho u_* c_p T \ln(\frac{T}{T_W})}{c_{hw}\left\{7.483\ \arctan(0.0935 y^+)\right\}},\ y^+ \le 40 \tag{3.25}$$

$$q_W = \frac{\rho u_* c_p T \ln(\frac{T}{T_W})}{c_{hw}\left\{2.1\ln(y^+) + 2.5\right\}},\ y^+ > 40 \tag{3.26}$$

The values of model constants C_{mw} and C_{hw} are chosen from validation studies on a square duct flow as shown in a later section.

3.4 Other sub-models

For the RANS-LW model, turbulence is modeled using the RNG k-ε turbulence model in KIVA-3V, while for the LES-LW and improved LES-WW turbulence models, the KIVA-3V code uses a non-viscosity dynamic structure model (DSM) which was developed by Pomraning et al., (2002), to model the unclosed sub-grid stress term in LES. Also, a detailed chemistry solver CHEMKIN (Kee et al., 1989) is employed for all tested models in this study for the combustion model. In particular, the CHEMKIN solver is integrated into the KIVA code to couple the chemistry and flow solutions. This CHEMKIN considers every cell a well stirred

reactor. The species concentrations and thermodynamic conditions are passed to the chemistry solver for each computational cell at each time step. A mixing-controlled direct chemistry (MCDC) model (Zhang et al., 2011) is also included for LES-LW and improved LES-WW models in the investigation.

For liquid spray break-up process, the KH-RT model is employed. Also, a skeletal reaction mechanism for n-heptane fuel, which has similar ignition characteristics with diesel fuel (Ra et al., 2003), is used to simulate diesel fuel chemistry. The mechanism includes 36 species and 76 reactions. However, the physical properties of the fuel in this work are represented with those of tetra-decane in the calculations (Ra et al., 2003).

Chapter 4 Validation test cases

4.1 Turbulent flow in a square duct

To validate all tested models, the flow in a square duct was chosen as a test case because the geometry is simple, and a large number of DNS results and experimental data are available for comparison. The square duct flow results of the RANS-LW, LES-LW, and improved LES-WW models are discussed. These results are compared with available experimental data, and the model constants c_{mw} and c_{hw} in the improved LES-WW model were calibrated based on the existing square duct results and were held fixed throughout the investigation.

4.1.1 Numerical setup

The numerical study of turbulent air (Pr = 0.71) flow and convective heat transfer in a square duct was investigated. The size of the square duct was equal to H*H*6H in the x, y, and z directions, respectively. The computational grid was uniform with 40*40*60 cells in three directions as shown in Figure 4.1. In order to avoid specified inflow and outflow boundary conditions, periodic boundary conditions were applied. In particular, the computational domain should be sufficient to capture the longest structure present in the flows when the periodic boundary conditions are used (Piomelli, 1999). The aspect ratio L/H was about 6.0, while L was the length of the duct. This length, which was suggested in the reference (Huijnen et al., 2005), is adequate to simulate turbulent flows. The boundary conditions at walls included new wall shear stress and wall heat transfer models. The initial velocity profiles were assumed to be $1/7^{th}$ power law. To generate turbulent motions, the initial condition for sub-grid scale turbulent kinetic energy was scaled with 10% of the mean velocity field. The constant wall temperature was chosen to be 350 K.

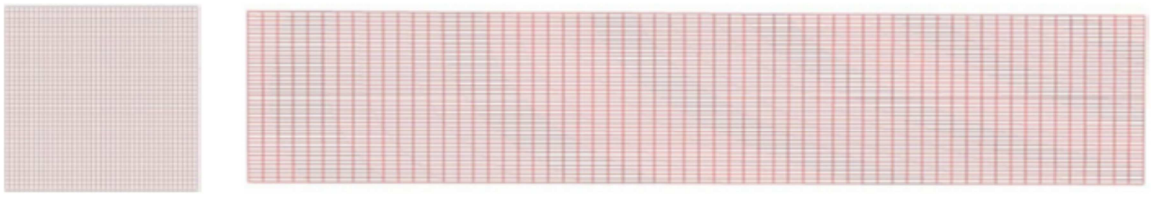

Figure 4.1 CFD mesh of a square duct

4.1.2 Results and discussion of square duct flows

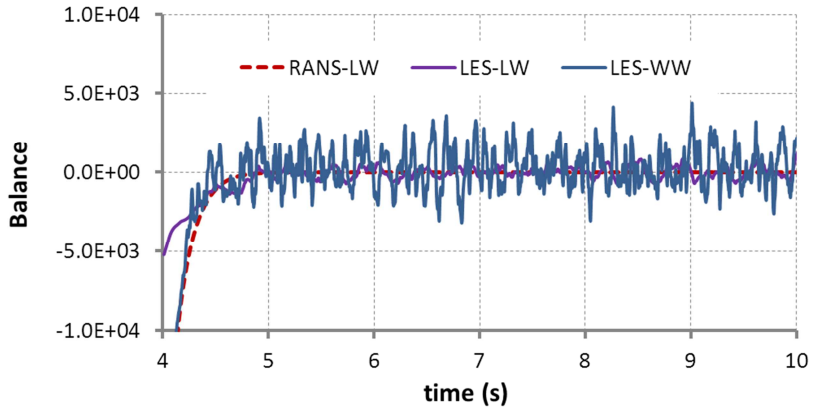

Figure 4.2 The balance term of a square duct flow

Non-zero constant forcing terms, which were the mean part of the pressure gradient, were used to maintain constant mass flow rate during flow simulations (Huijnen et al., 2005). The statistics for obtaining the average velocity and temperature fields and the turbulent intensities were not collected until the turbulence flow field had become stationary. In particular, the stationary flow field was identified by the balance between the average shear stress at the walls and the mean streamwise pressure gradient (Madabhushi et al., 1991). The balance term of the square duct flow simulations is presented in Figure 4.2. Here, the balance term is the difference between the forcing term and the average shear stress at the walls. It is clear that the turbulent

flow field was stationary by about t=5s (1s after restart). The statistical data were obtained by averaging the flow field both in time and in the streamwise (homogeneous) direction from t=5 to 10s. In near-wall flows, a good indicator of the wall shear stress model and the wall heat transfer model is the prediction of the friction factor and Nusselt number when compared with the correlations. The corresponding friction factor and Nusselt number for the square duct flow are defined as

$$f = \frac{8\tau_w}{\rho U_b^2} \tag{4.1}$$

And

$$Nu = \frac{hD_h}{k} = \frac{q_w D_h}{A(T_m - T_w)k} \tag{4.2}$$

where U_b is the bulk velocity over the square cross section, D_h is the hydraulic diameter, k is the gas thermal conductivity, and h is the convection heat transfer coefficient. The term T_m is the mean temperature over the square cross section and T_w is the wall temperature. Also, the friction factor correlation from Petukhov (1970) is defined as

$$f_{corr} = (0.790 \ln \mathrm{Re}_D - 1.64)^{-2.0} \tag{4.3}$$

while the Nusselt number correlation for fully developed turbulent flow in tubes comes from Gnielinski (1976) and is given as

$$Nu_{fd} = \frac{\left(\frac{f}{8}\right)(\mathrm{Re}_D - 1000)\,\mathrm{Pr}}{1.0 + 12.7\left(\frac{f}{8}\right)^{0.5}(\mathrm{Pr}^{0.67} - 1.0)} \tag{4.4}$$

Several computations have been performed for the square duct, with different values of the first near-wall grid points being used in each case. First, in order to calibrate the model

constant c_{mw} in the wall shear stress model, the results from the adiabatic condition (no heat transfer effect) are investigated. Figures 4.3 and 4.4 show the ratios of the predicted friction factors and Nusselt numbers to their respective correlations as a function of y^+ of the first near-wall grid points. Here, because the influence of the wall in the KIVA engine code is considered only at the first wall-adjacent cell, the distance y^+ in the wall shear stress and wall heat transfer formulations is the distance from the first grid nodes to the walls.

Figure 4.3 shows the trend of the predicted friction factor as predicted by the improved LES-WW model with adiabatic condition. The model constant c_{mw} in Eq. (3.21) was varied in a range from 0.002 to 0.05.

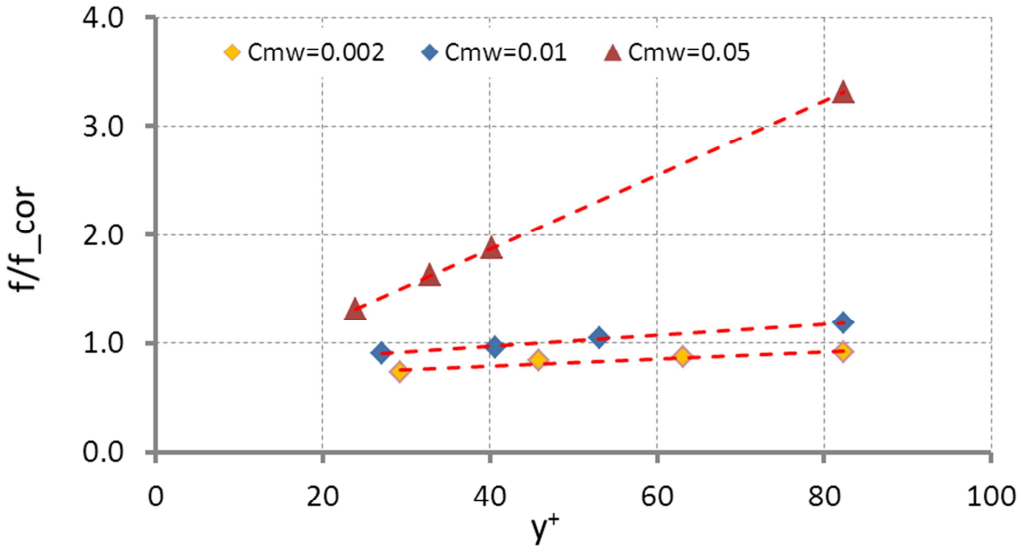

Figure 4.3 Ratio of the friction factor predicted by the improved LES-WW model to the correlation as a function of y+ at the first near-wall grid points

For each value of c_{mw}, the non-zero constant forcing terms were used to maintain constant mass flow rate and the stationary values of predicted friction factor and the values of y^+ at the first grid points were calculated. As can be seen in Figure 4.3, the friction factor was over-

predicted when the model constant c_{mw} was equal to 0.05 and the results from c_{mw} = 0.01 agree very well with the correlations for a wide range of y^+. Thus, the model constant c_{mw} in Eq. (3.21) was chosen to be 0.01.

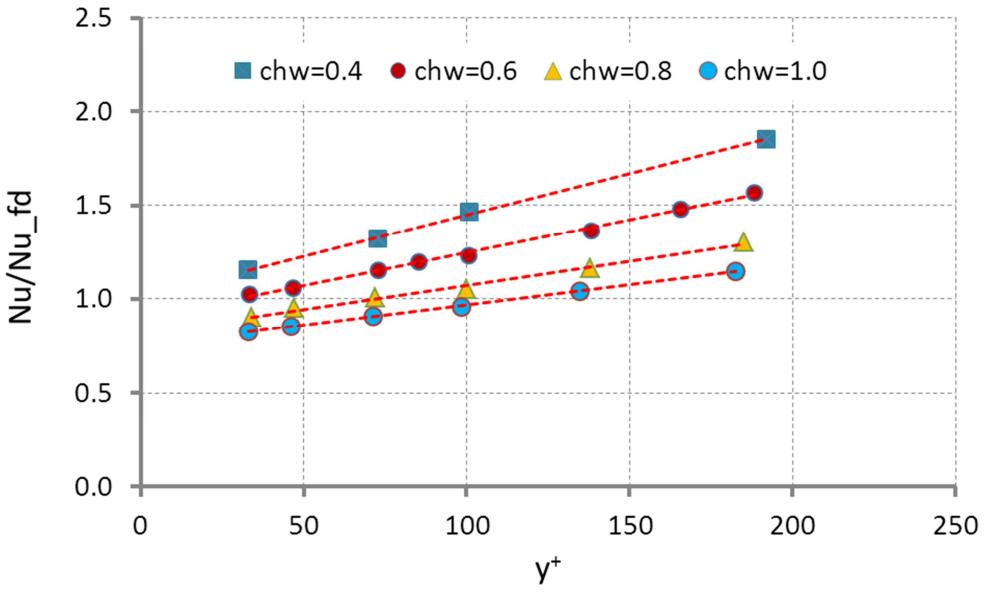

Figure 4.4 Ratio of the Nusselt number predicted by the improved LES-WW model to the correlation as a function of y+ at the first near-wall grid points with c_{mw} = 0.01

Figure 4.4 shows the ratio of the Nusselt number as predicted by the improved LES-WW model to the correlation as a function of y^+ at the first near-wall grid points with a constant wall temperature. In Figure 4.4, the model constant c_{hw} in Eqs (3.25) and (3.26) was varied in a range from 0.4 to 1.0, while the model constant c_{mw} was kept constant. For each value of $c_{hw,}$ the forcing terms were also employed to maintain constant mass flow rate, and the stationary values of predicted Nusselt number and the values of y^+ at the first grid points were calculated. The predicted Nusselt number agrees well with the correlations in the wide range of y^+ when the model constant c_{hw} is equal to 0.8.

Therefore, in this present work, the model constants c_{mw} and c_{hw} in the improved LES-WW model were set to 0.01 and 0.8, respectively throughout the study.

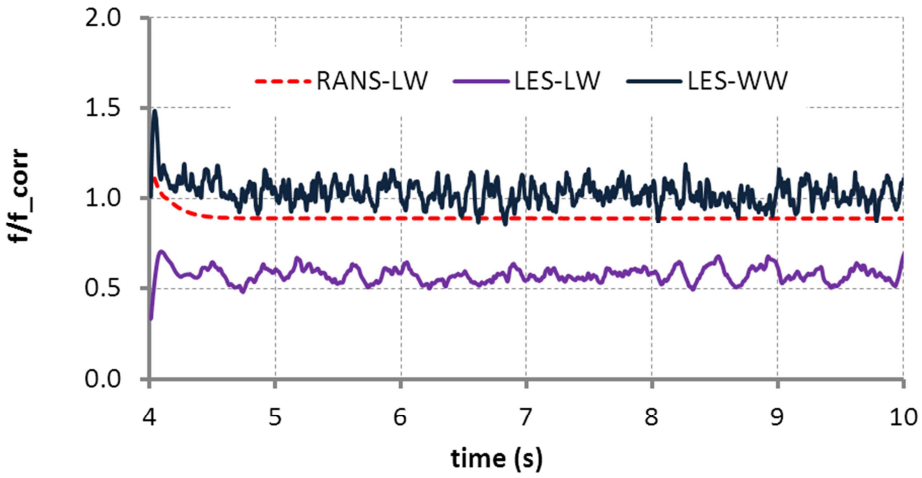

Figure 4.5 Ratio of mean friction factor predicted by the RANS-LW, LES-LW and improved LES-WW models to correlations over wall areas of a square duct at Re=50,000

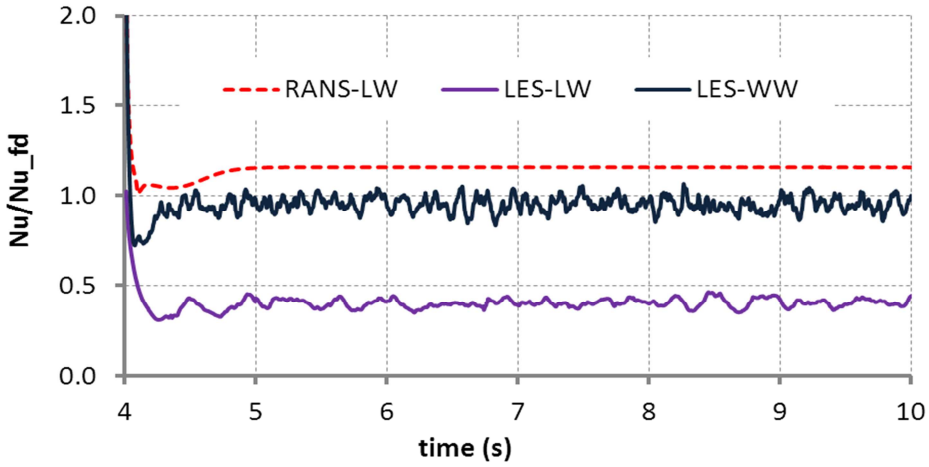

Figure 4.6 Ratio of mean Nusselt number predicted by the RANS-LW, LES-LW and improved LES-WW models to correlations over wall areas of a square duct at Re=50,000

Figures 4.5 and 4.6 show the mean friction factor and Nusselt number predicted by the RANS-LW, LES-LW and improved LES-WW models after model calibration. These results

were averaged over four wall areas of a square duct with a Reynolds number of 50,000, which was based on the bulk velocity and duct height (H). It is clear that only the results from the RANS-LW and improved LES-WW models match very well with the correlations, while the friction factor (wall shear stress prediction) and Nusselt number are under-predicted for the LES-LW model. The friction factor from the LES-LW model was about 50% less than those from the RANS-LW and LES-WW models, and the Nusselt number was about 60% less. A possible cause for this difference is that the length scales are different between the LES turbulence techniques that are used to simulate the bulk flow motions and law-of-the-wall velocity conditions in Eq. (3.10). This leads to under-prediction of the velocity scale (i.e., friction velocity) near walls.

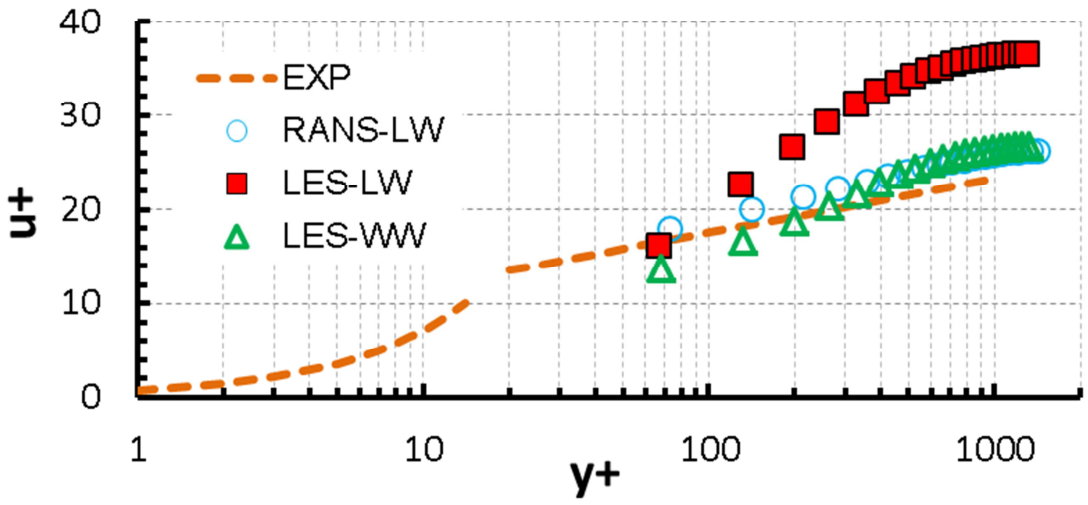

Figure 4.7 Mean velocity profiles in wall layer as predicted by the RANS-LW, LES-LW, and improved LES-WW models at Re = 50,000

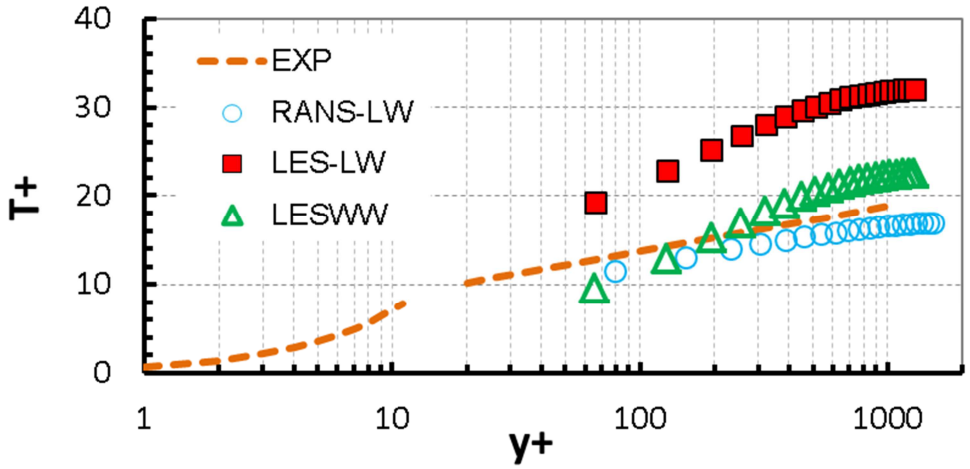

Figure 4.8 Mean temperature profiles in wall layer as predicted by the RANS-LW,LES-LW, and improved LES-WW models for constant wall temperature at Re = 50,000

The non-dimensional mean streamwise velocity along the wall bisector predicted by the RANS-LW, LES-LW, and improved LES-WW models is shown in Figure 4.7. This mean velocity is normalized by the local friction velocity averaged over four walls and is compared to experimental data (Wei et al., 1989). Equation (3.24) is used to calculate the friction velocity. The location of the first grid point is y^+ = 70. In Figure 4.7, good agreeement with the experimental data is seen for the RANS-LW model, while the LES-LW calculation shows large over-prediction. The improved LES-WW model under-predicts u^+ relative to experimental data for small y^+ and agrees fairly well with experimental data when $y^+ > 100$. Also, Figure 4.8 shows the mean temperature profiles along the wall bisector normalized by local friction temperature averaged over four walls and plotted in wall coordinates. The mean temperature differences and friction temperature are given as

$$T^+ = \frac{T - T_w}{T_*} \tag{4.5}$$

$$T_* = \frac{q_w}{\rho c_p u_*} \tag{4.6}$$

where T_w is the wall temperature and q_w is the wall heat flux. Similar to the mean velocity profiles, good agreeement is seen between the experimental data and the RANS-LW model, while the LES-LW calculation shows large over-prediction, as seen in Figure 4.8. Also, the values of mean temperature T^+ as predicted by the improved LES-WW model are largely under-predicted near the walls. A fairly good agreement with experimental data (Kay, 1994) is found when using the value of $y^+ > 100$.

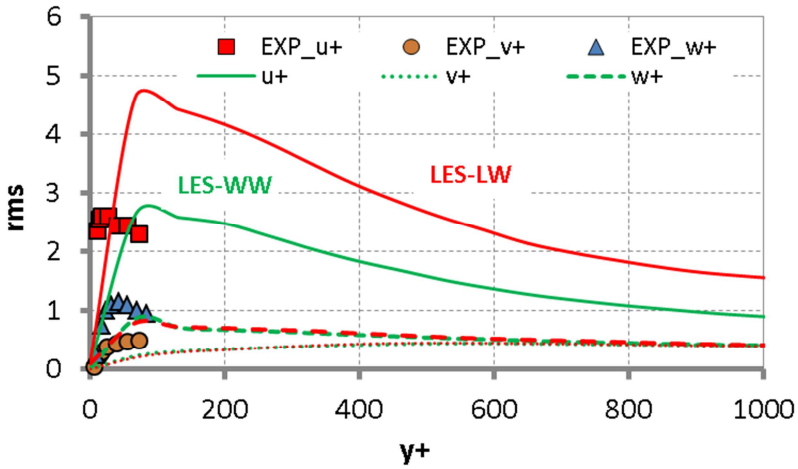

Figure 4.9 Turbulence intensities in the wall layer as predicted by the LES-LW (red) and improved LES-WW (green) models at Re = 50,000

Figure 4.9 shows the turbulence intensity values of u^+_{rms}, v^+_{rms}, and w^+_{rms} as computed by the LES-LW and improved LES-WW models. These rms values were normalized by the local friction velocity averaged over four walls. The present computations as predicted by the improved LES-WW model agree well with experimental data (Balint et al., 1991) for u^+_{rms}, while the LES-LW calculation shows mostly over-prediction. Also, the computed normal and spanwise

directions (v^{+}_{rms} and w^{+}_{rms}) are under-predicted in the wall vicinity. This error may come from a common problem with LES calculations in which only the resolved or filtered part (large scales) are plotted. Another reason for the discrepancy between the computed and experimental values of v^{+}_{rms} and w^{+}_{rms} is that the computed values indicate only the fluctuating component of the LES resolved value, while the experimental data deal with the fluctuations of instantaneous values. Here, because the resolved velocity (large scale) does not exist in the RANS-LW model, only information from the LES-LW and improved LES-WW model are plotted in Figure 4.9.

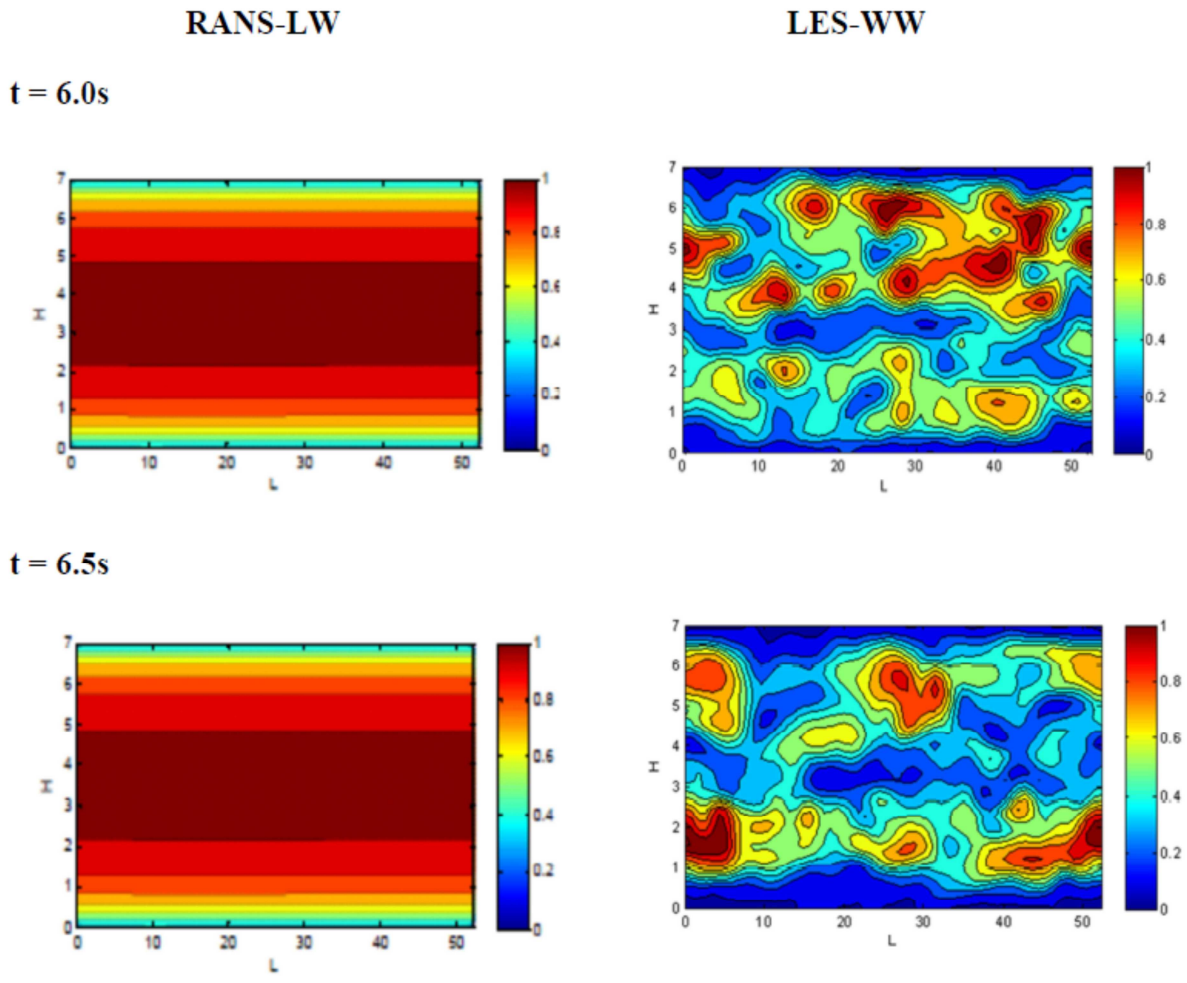

Figure 4.10 Comparisons of contour plots of locally normalized wall heat fluxes as predicted by the RANS-LW and improved LES-WW models at t=6s and t=6.5s

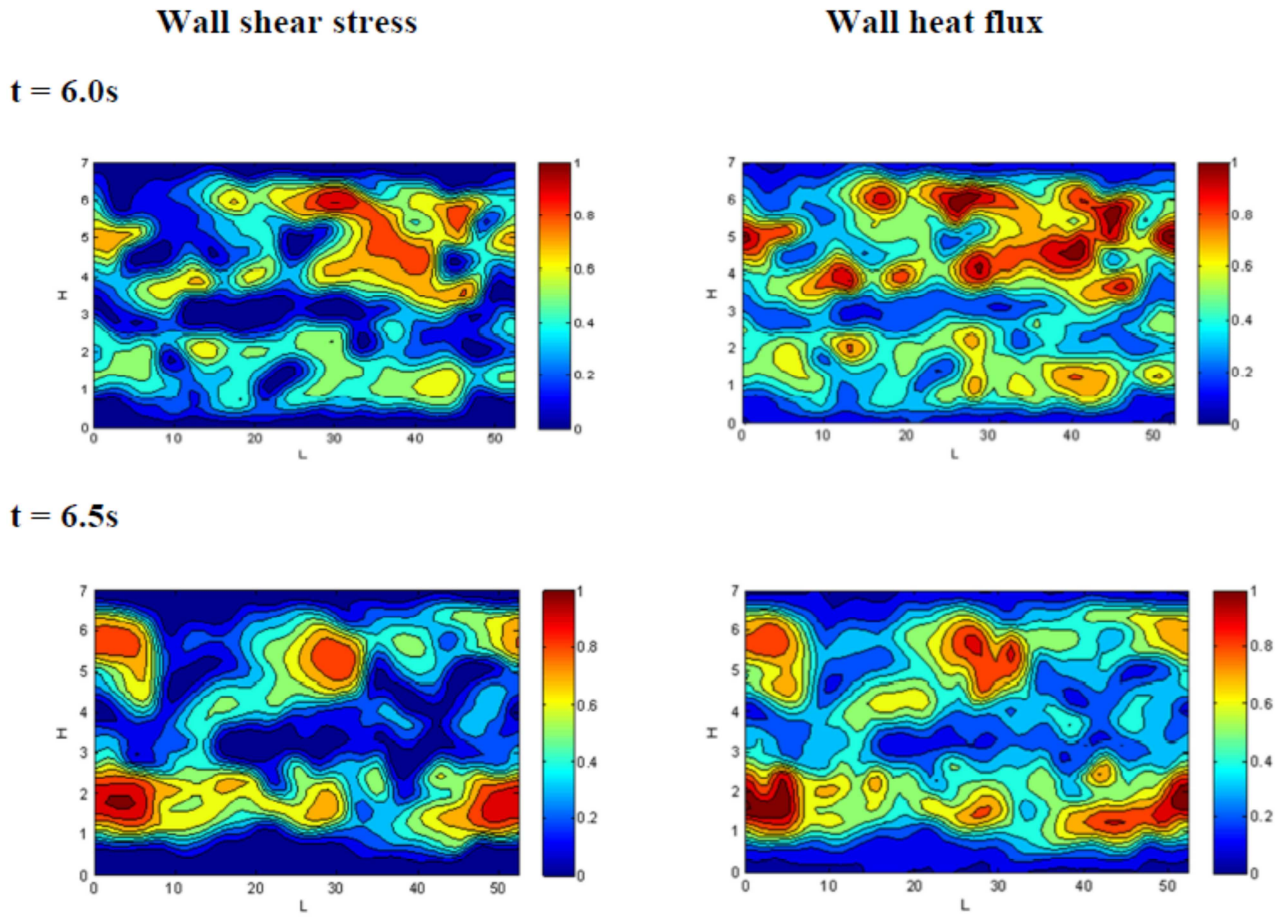

Figure 4.11 Comparisons of contour plots of locally normalized wall shear stresses and wall heat fluxes as predicted by the improved LES-WW model at t=6.0s and t=6.5s

Figure 4.10 shows comparisons of contour plots of locally normalized wall heat fluxes as predicted by the RANS-LW and the improved LES-WW models at t=6.0s and t=6.5s Also, comparisons of contour plot of locally normalized wall shear stresses and wall heat fluxes as predicted by the improved LES-WW model can be seen in Figure 4.11. The contour plots of the local wall shear stress from one wall are normalized by the maximum wall shear stress values while the local wall heat flux distributions from one wall are normalized by the maximum heat flux values.

As can be seen in Figures 4.10, the wall shear stress and heat flux results from the improved LES-WW model can provide more detailed local information of wall shear stresses and heat fluxes near walls, and the improvement of LES wall models can be observed. Similar flow structure between wall shear stress and wall heat flux can be captured as shown in Figure 4.11.

In summary, from all results of the square duct flows, the improved LES-WW model can provide a better estimation of the wall shear stress and wall heat transfer, which are represented by the friction factor and Nusselt number calculations, when compared with the LES-LW model. Also, all results from the improved LES-WW model agree well with experimental data in square duct flows and provide reasonable wall information with a high degree of accuracy.

Therefore, the LES-WW model is an improvement for LES wall models in channel flow applications. Next, the improved LES-WW model was tested with impinging jet flows applications.

4.2 Jet impingement on a flat plate

Impinging jet flows are widely employed in engineering applications due to their high heat transfer performance. In diesel engines, impinging hot gas jets to a combustion chamber generate very high heat transfer coefficients in the impingement zone. The magnitude of heat transfer prediction near the stagnation point is important, and accurate heat flux distributions are needed. These results may help to understand the predicted heat flux results in areas where the hot gas jets impacts on the piston surfaces. The study conducted in this section will test the RANS-LW, LES-LW, and improved LES-WW models with impinging air flow normal to a flat plate. The results from wall shear stress models are included. Recent experiments on circular jets

impinging on a flat plate (Baughn et al., 1989 and Tummers et al., 2011) are selected for model validation.

4.2.1 Test case description

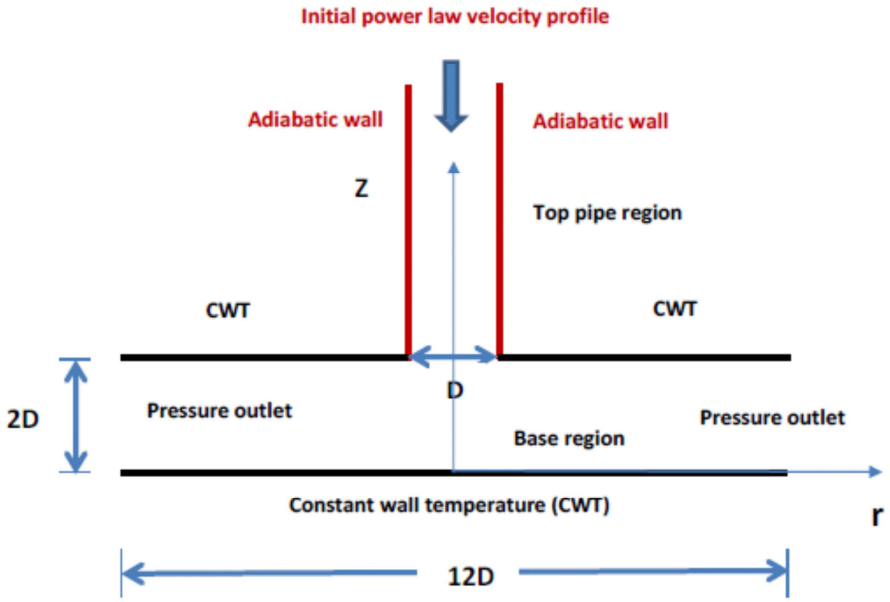

Figure 4.12 Configuration and computational domain for the impinging jets on a flat plate

The computational domain for impinging jets was divided into the two regions shown in Figure 4.12. First, in the top pipe region, the initial velocity profiles at the inlet were assumed by the $1/7^{th}$ power law. To generate turbulent motions, the initial condition for sub-grid scale turbulent kinetic energy was scaled with 10% of the jet bulk velocity in the pipe. The length of the pipe is 26D, which can provide a fully developed flow at the exit, and the adiabatic wall was applied at the pipe surfaces.

In the base region, the distance between the pipe exit and the wall surfaces is H=2D and the turbulent jet impinges normally on the surface with size of 12D, as sketched in Figure 4.12. The inlet and initial condition of air in the pipe and the base region was set to 350 K. In order to

be consistent with thermal boundary conditions of a square duct flow and all following engine test cases, constant wall temperature boundary conditions (CWT) were used on the top wall and the bottom, or impingement, wall, while the outlet pressure boundary conditions were applied at the ambient exits. The constant wall temperature was chosen to be 280 K, which matched with experimental data. The boundary conditions of the sub-grid scale turbulent kinetic energy were the Neumann boundary conditions.

Cylindrical coordinate were used for the computational domain of the impinging jet. The original point (r=0) was located at the center line. The velocity components in the axial (z), radial (r) and azimuthal (θ) directions are denoted by W, U and V.

The new wall shear stress and wall heat transfer models were included for all walls in the computational domains. Because the research focuses on the impingement wall, the non-dimensional heat transfer coefficient, i.e., Nusselt number and the skin friction coefficient on the impingement surface were calculated and compared with existing experimental data. Also, the flow fields on the impingement wall were investigated.

4.2.2 Numerical setup

The numerical study of impinging jets was tested with two different computational grids i.e., grid JA and grid JB as shown in Figure 4.13. In the top pipe with a diameter 2.0 cm, the computational grids JA and JB were 10*10 cells in the cross section plane and 100 cells in the axial direction. Only the resolution within the base region was changed between grid JA and grid JB, as the resolution here affects the heat flux results on the impingement wall (bottom wall). The base has a diameter of 24 cm and height of 4 cm. Grid JA comprised of 42,000 cells with a mesh of 30*30*20 cells while grid JB consisted of 71,000 cells with a mesh of 36*36*30 cells.

The grid spacing in the normal direction of impingement wall is $\Delta z^+ = 120$ for grid JA and $\Delta z^+ = 60$ for grid JB.

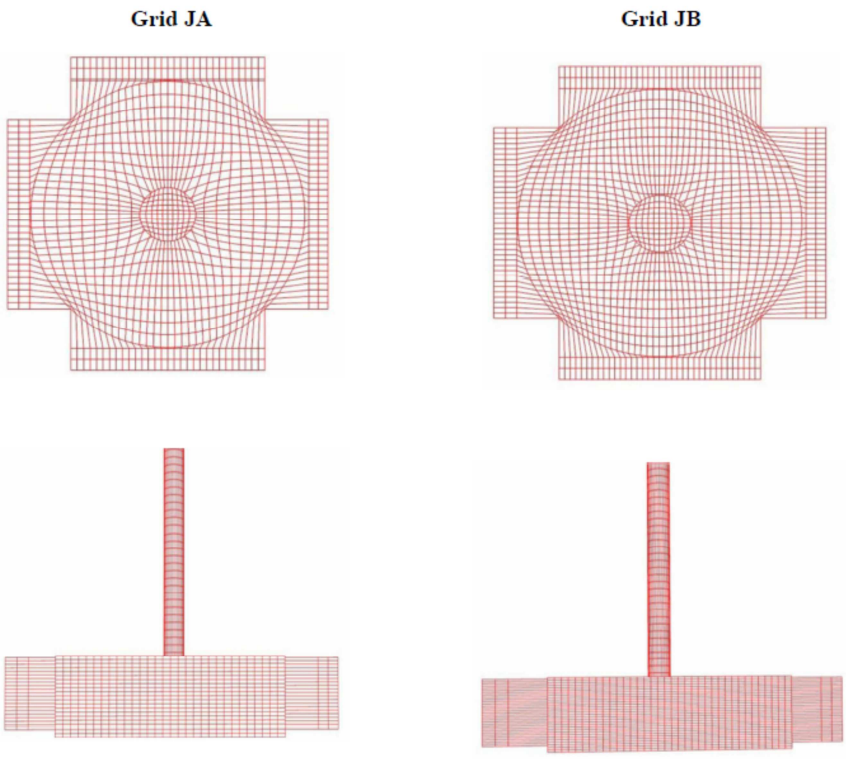

Figure 4.13 CFD meshes (grid JA and grid JB) of the impinging jet on a flat plate

4.2.3 Results and discussion of jet impingement

Figure 4.14 shows large-eddy simulation results with the improved LES-WW wall model of impinging jets flowing within a long pipe at a constant Reynolds number (Re) of 21,000, corresponding to a jet bulk velocity (W_b) of about 2,000 cm/s. The round jet issuing from a fully developed pipe flow as shown in Figure 4.15 enters the base region and impinges on the target wall surfaces. The shapes of normalized axial velocity profiles no longer change with location in the pipe as shown in Figure 4.15.

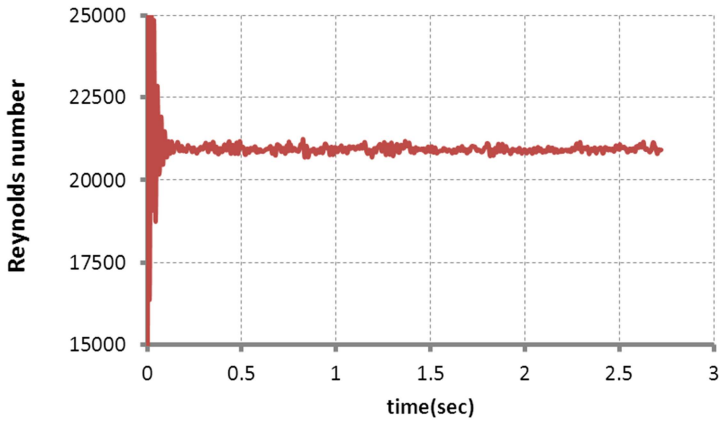

Figure 4.14 Reynolds number versus time of the flow in the top pipe

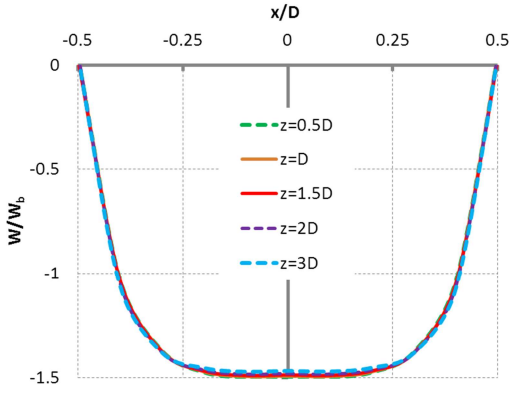

Figure 4.15 Time average of normalized axial mean velocity at different distances measured from pipe exit

4.2.4 Mean flow properties and turbulence statistics

The axial and radial mean velocity components and root mean square (r.m.s) of their fluctuations at the stagnation point (r/D =0) and r/D=0.5 as predicted by the improved LES-WW model are shown in Figures 4.16 and 4.17, respectively. These axial mean velocity and r.m.s values are normalized by the jet bulk velocity, W_b. The experiment data are selected from works of Geers et al., (2004) to compare with calculated values. The mean axial velocity, W, and the mean radial velocity, U, at r/D=0 (centerline) are shown in Figure 4.16a. On the centerline, the

axial mean velocity remains nearly constant from the pipe exit (Z/D=2.0) up to Z/D=0.4, while, below the position Z/D=0.4, the flow decelerates while the jet flows approach to the wall. As can be seen in Figure 4.16b, at the position r/D =0.5, the strong flow deflection due to the impingement wall makes the mean radial velocity (U/W_b) start to increase and reaches the maximum value near the wall whereas the mean axial velocity (W/W_b) approaches to zero.

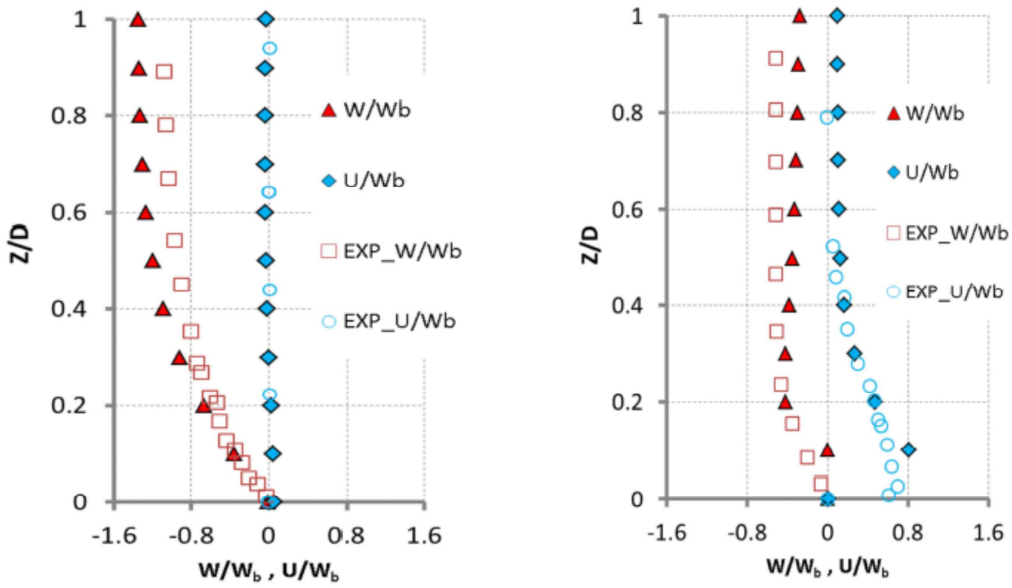

Figure 4.16 Comparisons of measured and computed mean axial and radial velocity profiles as predicted by the improved LES-WW model at (a) a stagnation point (r/D=0) and (b) r/D =0.5.

For the r.m.s. values as shown in Figure 4.17a and 4.17b, the mean axial and radial velocity fluctuations decrease down to zero due to the wall-blocking effect (Hadziabdic et al., 2008). However, the r.m.s value of the radial velocity increases again in the near-wall region owing to the near-wall shear. At the centerline (r/D=0), the r.m.s values of the axial and radial velocity fluctuation are over-predicted in the region Z/D < 0.3 while the results agree fairly well when Z/D > 0.3. At r/D = 0.5, the velocity fluctuations are higher than those of values at the centerline. The mean velocity components at the point r/D = 0.5 agree fairly well with the

selected experiment data until Z/D < 0.4. The discrepancies between the r.m.s values of the velocity fluctuations predicted by the improved LES-WW model and experiment data can be observed in Figure 4.17b in the region Z/D > 0.4.

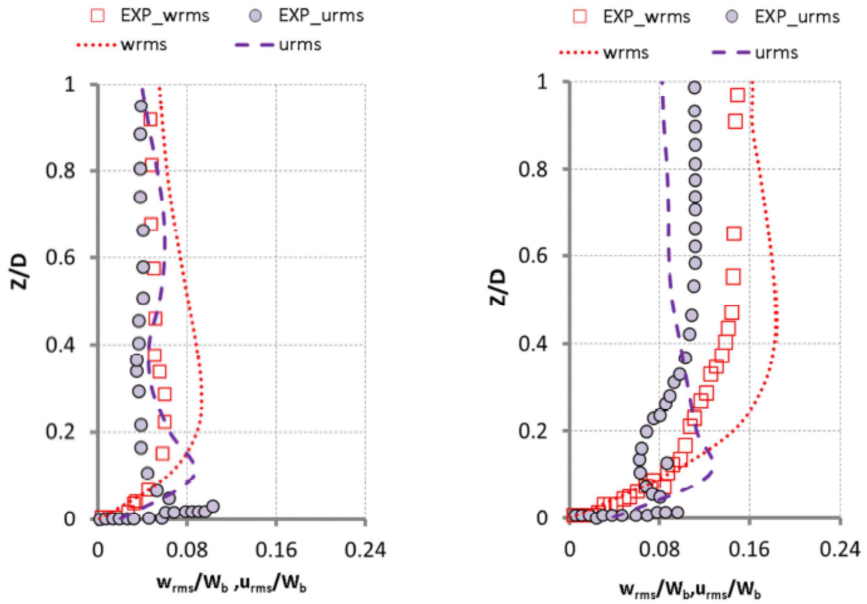

(a) (b)

Figure 4.17 Comparisons of measured and computed root mean square (r.m.s) of axial and radial velocities as predicted by the improved LES-WW model at (a) a stagnation point (r/D=0) and (b) r/D =0.5.

Figure 4.18 shows the contour plots of instantaneous values of wall heat flux on the impingement wall predicted by the RANS-LW, LES-LW and improved LES-WW models at t=1.8s, 2.0s, 2.2s, respectively. The magnitude of plotted heat fluxes are varied from 1,000 to 8,000 W/m^2. The contour of heat fluxes is non-uniform and the heat flux results from improved LES-WW model can provide more flow structure and more local information on the impingement wall. Figure 4.19 compares the contour plots of instantaneous values of wall shear stress and wall heat flux on the impingement wall predicted by the improved LES-WW model.

As can be seen in Figure 4.19, similar flow structure between wall shear stress and wall heat flux can be captured.

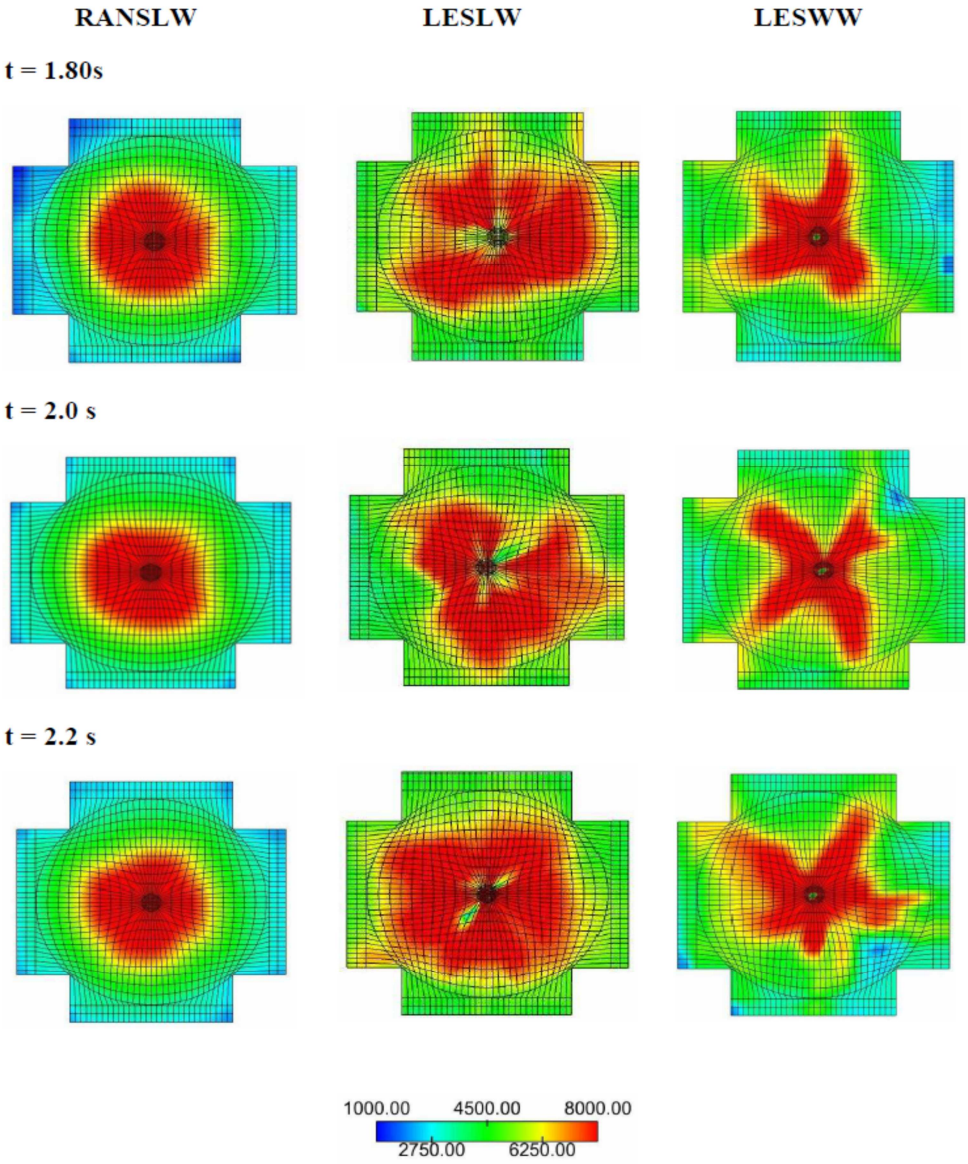

Figure 4.18 Contour plots of wall heat flux on the impingement wall as predicted by the RANS-LW, LES-LW and improved LES-WW models varied from 1,000 to 8,000 W/m^2

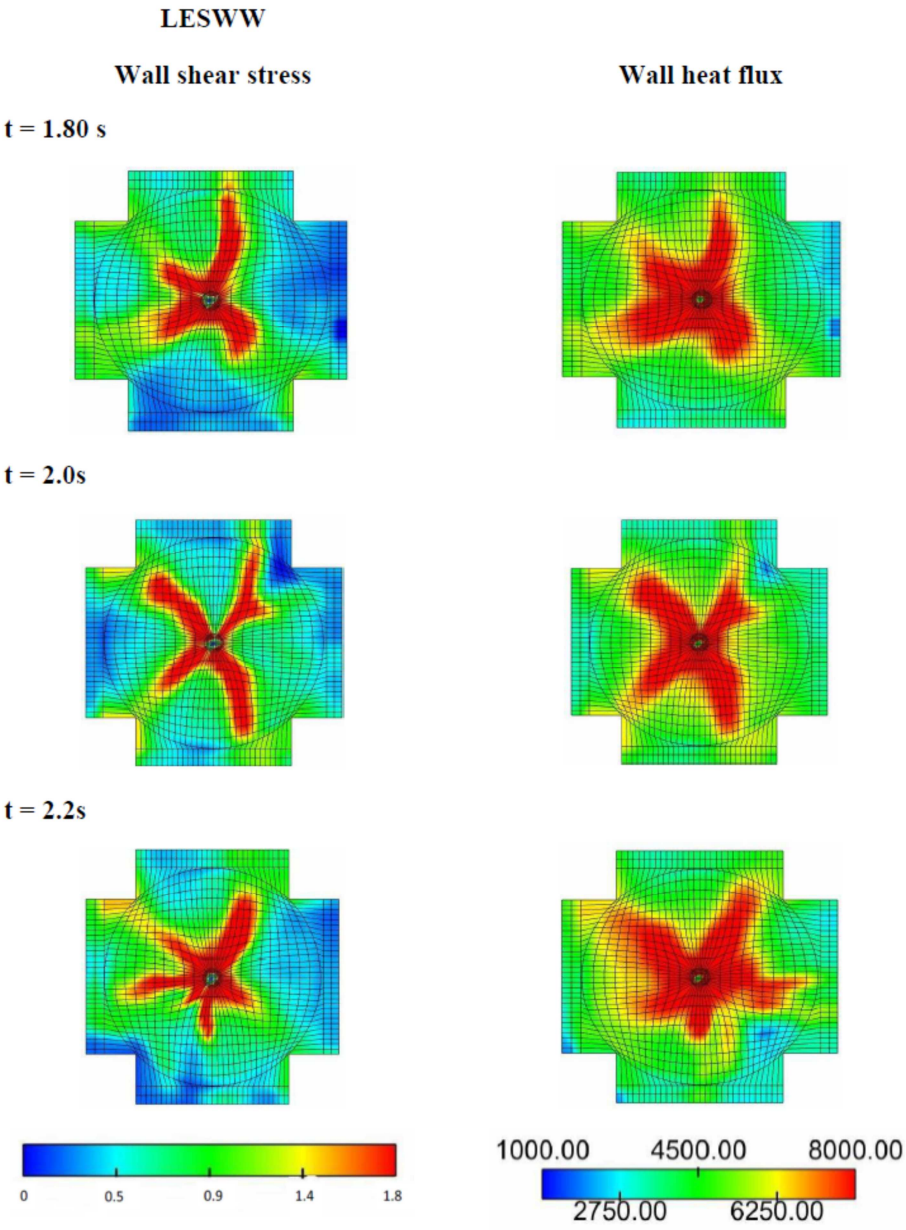

Figure 4.19 Contour plots of wall shear stress varied from 0 to 1.8 N/m^2 and wall heat flux on impingement wall varied from 1,000 to 8,000 W/m^2 as predicted by the improved LES-WW model

During the post-processing step in this present work, the predicted skin friction coefficient and Nusselt number are stored in each wall surface of the impingement wall. The plots of the time averaged values of these surface properties with the centroid of those surfaces are shown in Figures 4.20 and 4.21.

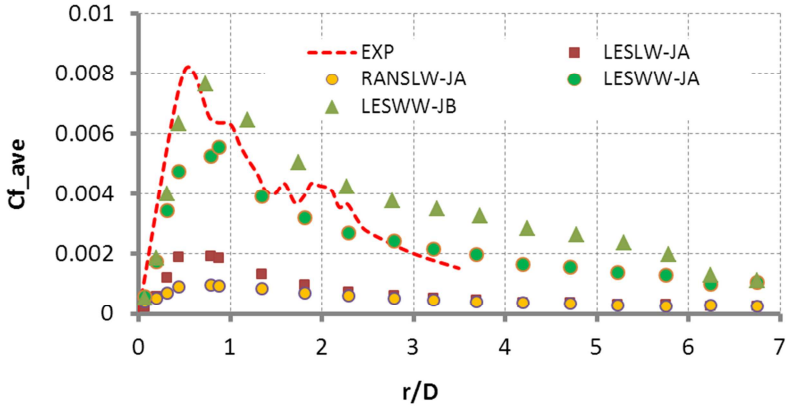

Figure 4.20 Time-averaged skin friction coefficients as predicted by the RANS-LW, LES-LW and improved LES-WW models with Re = 21,000 and H/D = 2.0

For the velocity field, the radial variation of the time-averaged skin friction coefficients as predicted by all test models is illustrated in Figure 4.20. The skin friction coefficient can be defined as

$$C_f = \frac{\tau_w}{\frac{1}{2}\rho W_b^2} \tag{4.32}$$

whrere τ_w is wall shear stress which can be calculated from models in Eqs (3.10) , (3.19) and (3.20). The term W_b is a jet bulk velocity in the pipe. The experimental data of Tummers et al., (2011) are selected to compare with the skin friction coefficient as predicted from the RANS-LW, LES-LW and improved LES-WW models. In Figure 4.20, starting from zero at the centerline, the largest local skin friction coefficient appears near r/D = 0.5. After this point, the local skin friction coefficient decreases rapidly. The skin friction coefficient predicted by the improved LES-WW model agrees well with experimental data, while the results from the RANS-LW and LES-LW models are significantly under-predicted. It can be concluded that the wall

shear stress from Eqs (3.10) which is predicted by the RANS-LW and LES-LW models may not work well with impinging jet applications.

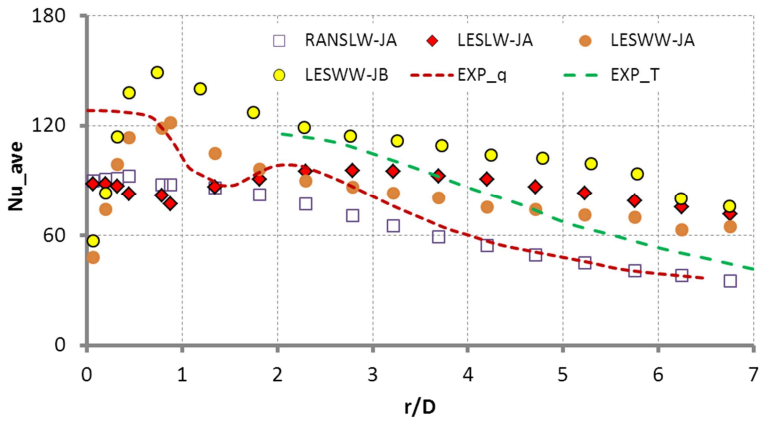

Figure 4.21 Time-averaged Nusselt number as predicted by the RANS-LW, LES-LW and improved LES-WW models with Re = 21,000 and H/D = 2.0

For the thermal field, the distribution of time-averaged Nusselt number as predicted by all test models is shown in Figure 4.21. The Nusselt number is defined as

$$Nu = \frac{hD_h}{k} = \frac{q_w D_h}{(T_{jet} - T_w)k} \tag{4.9}$$

whrere q_w is the convective heat transfer from hot gas to wall calculated from models in Eqs (3.13-3.14) and (3.25-3.26). The term T_{jet} is gas temperature of wall cells and T_w is wall temperature. The physical properties are evaluated at the film temperature which is defined as

$$T_f = \frac{1}{2}(T_{jet} + T_w) \tag{4.10}$$

The Nusselt number prediction in this present work is compared with experimental measurements (green color) of Sagot et al. (2008). They measured heat transfer between gas and wall at a uniform wall temperature with Reynolds number of 23,000 and a nozzle to plate distance (H/D) of 2.0. These data are available when r/D > 2.0. Moreover, the classical

measurement data (red color) of Baughn et al. (1989) which were conducted at a uniform heat flux with Reynolds number of 23,000 are included to provide comparisons near the stagnation point. From figure 4.21, it is clear that the values of Nusselt number from the measurement are largest at the stagnation point and decrease monotonically in the wall jet region (r/D > 2.0). In Figure 4.21, the Nusselt number predictions from the RANS-LW and improved LES-WW models agree fairly well with the experimental data of Sagot et al. (2008), while the LES-LW model shows over-prediction when r/D > 2.0.

Also, the discrepancies of predicted Nusselt number can be found in Figure 4.21. The improved LES-WW model under-predicts the Nusselt number near the stagnation point. Because the convective heat transfer calculation of the improved LES-WW model is strongly dependent on the values of wall shear stress, the decrease of predicted Nusselt number may come from the decrease of predicted wall shear stress when r/D < 2.0. However, the Nusselt number distribution as predicted by the improved LES-WW model has a similar trend with experimental data from the literature when H/D < 2.0 as shown in Figure 2.12. In other words, inconsistencies between the experimental conditions and the numerical studies may occur in the present work.

In summary, from all results of the impinging jets, the improved LES-WW model can provide a better estimation of the wall shear stress, which is represented by the time-averaged skin friction coefficients, when compared with the RANS-LW and LES-LW models. Also, for wall heat transfer prediction, the Nusselt numbers predicted by the RANS-LW and improved LES-WW models agree fairly well with experimental data when r/D > 2.0, while the LES-LW over-predicts. Therefore, the improved LES-WW model is an improvement for LES wall models in impinging jets. Next, the RANS-LW, LES-LW, and improved LES-WW models were simulated in diesel combustion.

Chapter 5 Diesel combustion simulations

5.1 Introduction

The present research develops wall heat transfer models to use for heavy duty truck engines. Thus, all test wall models are simulated in diesel combustion. The heat flux results from 11 points on the piston surface as predicted from the RANS-LW, LES-LW and improved LES-WW models are compared with experimental data obtained by surface thermocouples. A few sets of experimental data from previous works of Hendricks (2011) are selected to represent a wide variety of diesel combustion. The baseline engine condition (Run41) is discussed and more engine condition simulations are performed. To examine the predicted heat fluxes from all tested wall models more fully, the magnitude and phasing of peak heat fluxes prediction, and the trends and the spatial effects of those results are compared with experimental data. A parametric study of diesel combustion operating variables is also investigated.

5.2 Overview of diesel combustion

In a diesel engine, only air is initially introduced into the cylinder while liquid fuel is injected into the combustion chamber with high velocity starting close to the end of the compression stroke near the position of top dead center (TDC). The liquid droplets interact with the surrounding air in the cylinder, creating a transfer of momentum and thermal energy. The liquid droplets break up and vaporize, and the vaporized fuel mixes with the surrounding air, forming a combustible mixture. The combustion process initially begins with slow chemical reactions due to the relatively low mixture temperature and the lack of radical species. With the increase of mixture temperature and the accumulation of the radical species, the chemical reactions increase rapidly, and ignition starts. The time difference between the start of injection

(SOI) and the time of ignition is called ignition delay. A premixed mixture is accumulated during the ignition delay and is fuel rich. It reacts rapidly in a few crank angle degrees when it is ignited. The fast consumption of the premixed mixture is usually called the premixed burn and shown by a spike on the heat release curve.

After the premixed burn, a turbulent diffusion flame forms at the jet periphery where the mixture is close to the stoichiometric conditions. Combustion during this stage is usually called the diffusion burn or mixing controlled combustion. It occurs over a wide span on the heat release curve.

5.3 Validation setup: Engine Geometry

The measurement data (Hendricks, 2011) from a single cylinder oil test engine (SCOTE) by Caterpillar (CAT) with 2.44L displacement was used to validate computational results in this study. At maximum speed, the SCOTE is rated at 62 kW. A summary of the main geometrical data is listed in Table 5.1.

Table 5.1 Caterpillar SCOTE specification (Hendricks, 2011)

Displaced volume	2.44L
Bore*Stroke	13.72*16.51 cm
Number of nozzles	6, equally spaced
Connecting rod length	26.16 cm
Geometric compression	16.1:1
Number of valves	4
IVC/EVO	-143/130
Squish height	0.197 cm
Piston bowl design	Mexican hat

5.4 Piston heat flux measurements

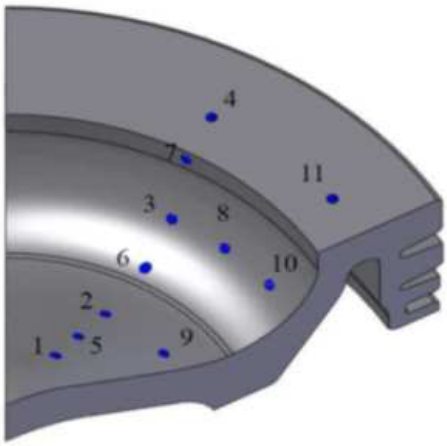

Figure 5.1 Thermocouple locations on the piston surfaces (adapted from Hendricks, 2011)

The heat flux measurements of the conventional diesel combustion were used for model validation. By using a wireless telemetry system and 11 fast-response thermocouples which were attached to the piston surface, instantaneous surface temperatures were measured (Hendricks, 2011). Then high resolution heat flux results were obtained after using heat transfer analysis. The thermocouple locations on the piston surfaces are shown in Figure 5.1. On the primary axis, the first cutting plane (TC#1-TC#7) passes through a spray axis and the second cutting plane (TC#9-TC#11) is located in the middle between two adjacent spray planes. However, in the measurement reports of this engine, TC#4 failed while running the test. Therefore, only 10 thermocouple locations on the piston surfaces were chosen to monitor wall heat flux results.

5.5 In-cylinder computational grids

To save computational time, sector symmetry was assumed and periodic boundary conditions were applied for each injector hole. A 60˚ sector mesh was used to represent one-sixth of the engine combustion chamber. The first study conducted in this work was to understand the impact of grid resolution. The following section steps through comparisons of the simulation results to the experimental data in the baseline engine condition (Run 41) summarized in Table 5.3. Only the resolutions of radial direction in the bowl geometry were refined, as the resolution in this area strongly affects heat flux predictions.

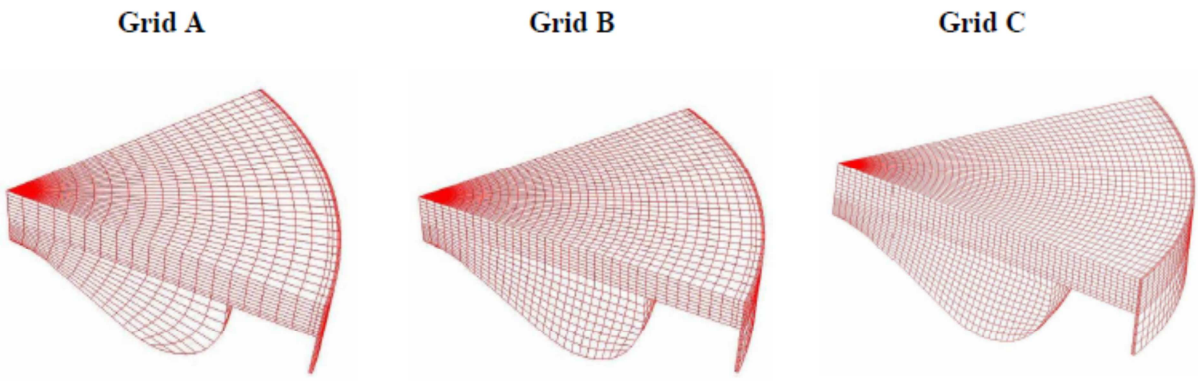

Figure 5.2 Three computational grids used for sector mesh simulations

To resolve sufficient flow structure, LES usually requires a finer mesh resolution than RANS. However, the finer mesh requires a larger computational expense as summarized in Table 5.2. Due to the advantage of the dynamic structure model (DSM), the mesh resolution can be reduced to the extent of RANS resolution. Many previous reports also shows that DSM model used in this framework can capture the main flow characteristics in LES simulations (Shethaji et. al, 2005; Jhavar et. al., 2006; Hu et. al, 2007)

Table 5.2 Summary of computational grids used for sector mesh simulations

	grid A	grid B	grid C
Cells at BDC	42,000	70,000	91,000
Azimuthal resolution	2˚	2˚	2˚
Radial direction in the bowl region	3.5 mm	1.75 mm	1.36 mm
Axial direction	4.0 mm	4.0 mm	4.0 mm
Running CPU time (IVC→EVO)	6 days	12 days	17 days

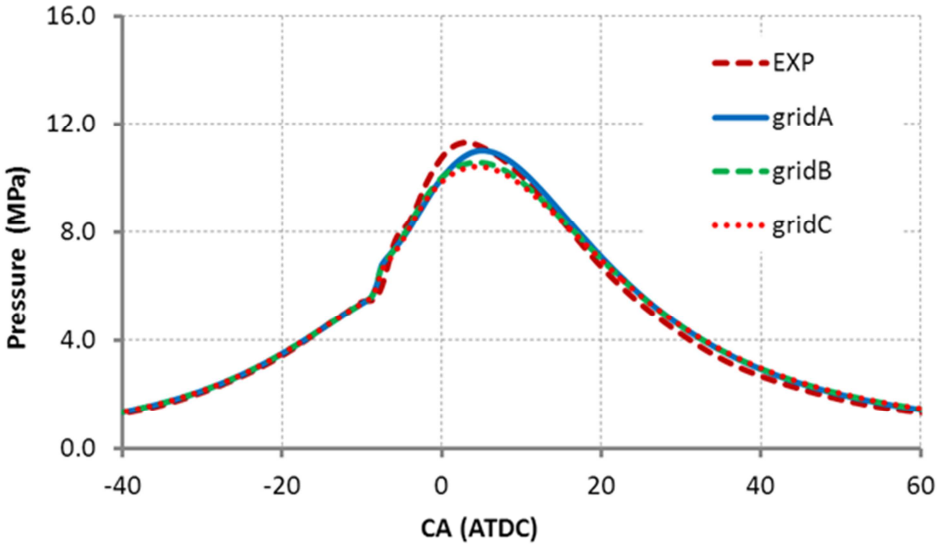

Figure 5.3 Comparison of cylinder pressure prediction from three computational grids used for sector mesh simulations as predicted by the improved LES-WW model run in the baseline conditions (Run41)

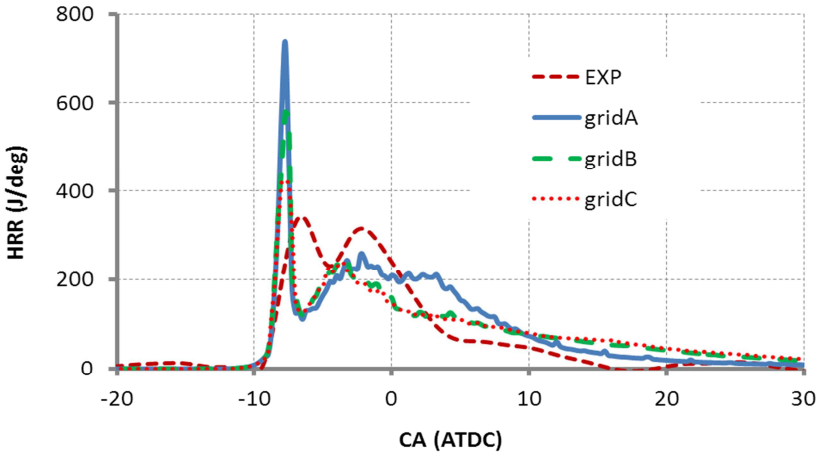

Figure 5.4 Comparison of predicted chemical heat release from three computational grids used for sector mesh simulations as predicted by the improved LES-WW model run in the baseline conditions (Run41)

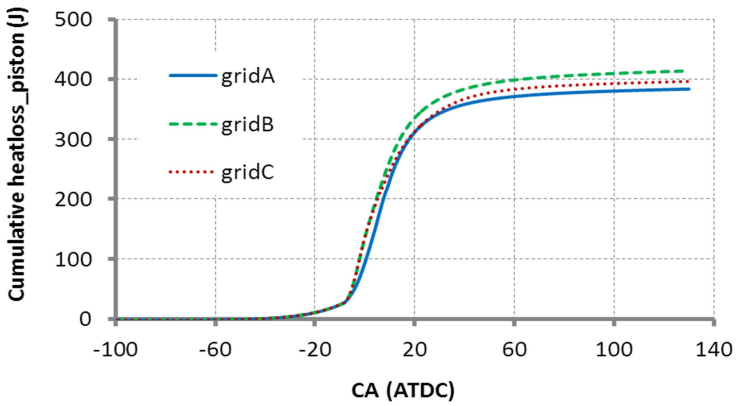

Figure 5.5 Comparison of predicted cumulative heat loss from the piston surface from three computational grids used for sector mesh simulations as predicted by the improved LES-WW model run in the baseline conditions (Run41)

Figures 5.3 through 5.5 show the comparison of predicted cylinder pressure, chemical heat release and cumulative heat loss on the piston surface for three different computational grids based on operating conditions summarized in Table 5.3. It can be seen that there is no significant change in results of grid A, grid B and grid C with the predicted pressure trace, chemical heat

release and cumulative heat loss on the piston surface. Therefore, to save computational time, grid A was chosen to simulate all diesel engine conditions in this present work.

5.6 Initial conditions & boundary conditions

In this study, the computational domain consisted of one section of the modeled engine cylinder which was used for simulations between inlet valve close (IVC) and exhaust valve open (EVO). Therefore, the model computes only the closed volume part of the engine cycle. The simulations were started at the intake valve closure (IVC) with uniform in-cylinder mixture distribution assumptions. The swirl was initialized based on the wheel flow velocity profile and the sub-grid kinetic energy was initialized at IVC by scaling with the mean piston speed. The boundary conditions of the sub-grid scale turbulent kinetic energy were the Neumann boundary conditions. The boundary conditions at walls included new wall shear stress and wall heat transfer models. Also, the pressure and temperature at IVC were given based on the experimental data. The wall temperature on piston surfaces was assumed to be constant throughout the study and was based on averaged measurement data.

5.7 Baseline engine results (Run 41)

For model validation, the engine test case at Run41 was selected as a baseline case in the present study due to the availability of a contour plot of experimentally measured heat fluxes on the piston surface. These plots are compared with those of predicted heat fluxes by the RANS-LW, LES-LW, and the improved LES-WW models. Table 5.3 summarizes the engine condition for the baseline case (Run41) which was obtained from literature (Hendricks, 2011).

Table 5.3 Caterpillar SCOTE engine conditions for the baseline case (Run 41)

Engine speed (rpm)	1300
IMEP gross (bar)	7.93
Swirl ratio	0.7
Fuel flow rate (g/min)	59.0
SOI ($^{\circ}$ATDC)	-13.52
DI duration (CA$^{\circ}$)	12.12
EGR rate (%)	0
Equivalence ratio	0.39
Intake pressure (bar)	1.533
Intake temperature (K)	312.65
IVC pressure (bar)	1.637
IVC temperature (K)	387.32
Avg. constant wall temperature on piston surface (K)	500.0

In order to understand the predicted results from three test wall models, the important sub-models used in the simulations are reviewed here. Table 5.4 compares the turbulence model, combustion model, spray model and wall models used by the RANS-LW, LES-LW and improved LES-WW models during the simulations.

Table 5.4 Summary of important sub-models used in the simulations

	RANSLW	LESLW	LESWW
Turbulence model	RANS (Reitz,1991)	LES (Rutland,2011)	LES (Rutland,2011)
Combustion model	CHEMKIN (Kee et al., 1989)	CHEMKIN+MCDC (Zhang et al. ,2011)	CHEMKIN+MCDC (Zhang et al.,2011)
Spray model	KH-RT model (Beale et al.,1999)	KH-RT model (Beale et al.,1999)	KH-RT model (Beale et al.,1999)
Wall shear stress model	Law-of-the-wall (LW) Eqs. (3.10-3.12)	Law-of-the-wall (LW) Eqs. (3.10-3.12)	Improved WW model Eqs. (3.19-3.24)
Wall heat transfer model	Variable density heat transfer model (VDHT) Eqs. (3.13-3.14)	Variable density heat transfer model (VDHT) Eqs. (3.13-3.14)	Adjusted scale VDHT Eqs. (3.25-3.26)

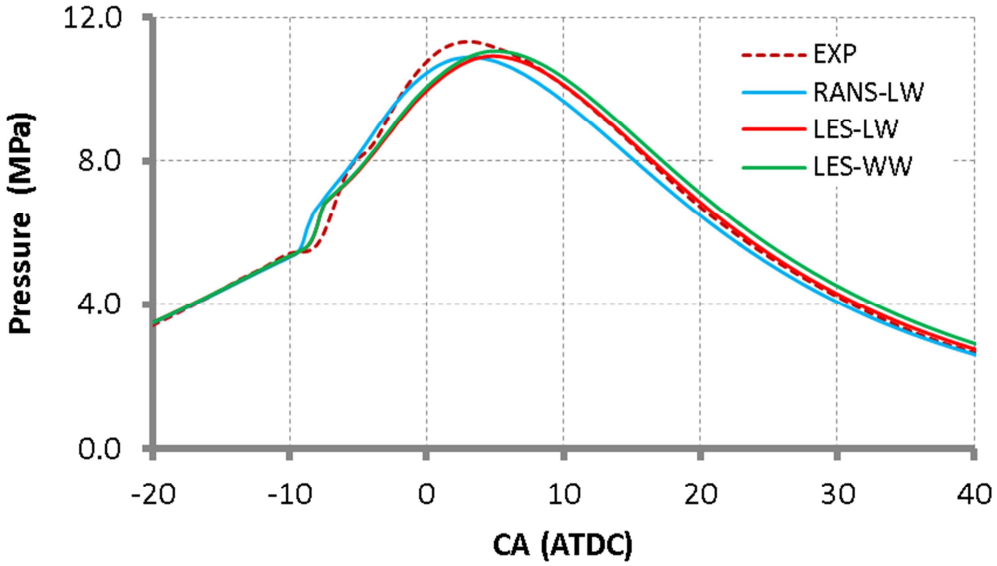

Figure 5.6 Comparisons of computed and measured cylinder pressure for Run 41, with the start of injection at 13.52 degrees before TDC

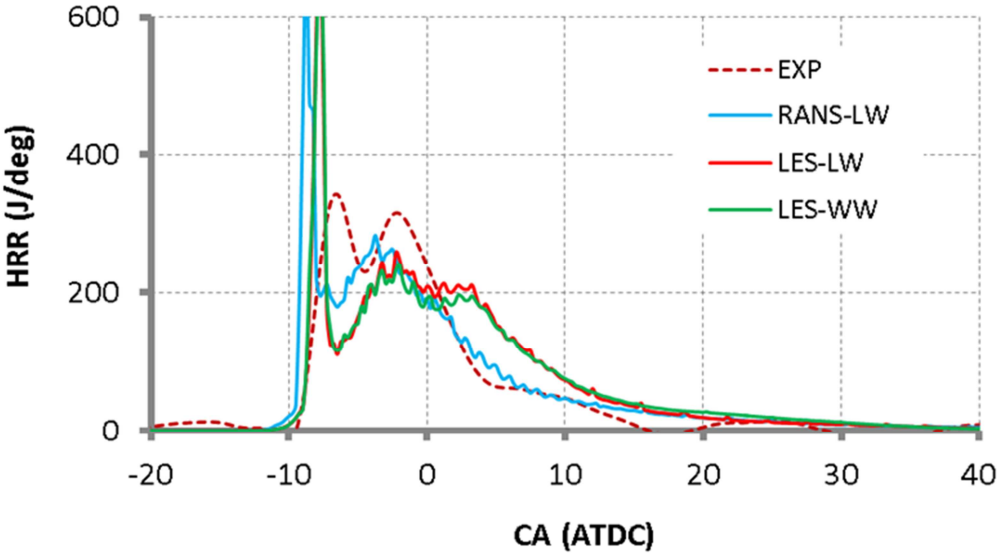

Figure 5.7 Comparisons of computed and measured chemical heat release rate for Run 41, with the start of injection at 13.52 degrees before TDC

Comparisons between measured and computed in-cylinder pressure and heat release rate as predicted by the RANS-LW, LES-LW, and improved LES-WW models are shown with experimental data in Figures 5.6 and 5.7. Figure 5.8 also shows the comparisons of computed in-cylinder bulk temperature as predicted by the RANS-LW, LES-LW, and improved LES-WW models. Good agreement with the experimental pressure trace can be seen for all three models in Figure 5.6. With the CHEMKIN detailed chemistry model, the RANS-LW model calculations shows slightly earlier ignition and results in less burning during the expansion stroke with underestimation of in-cylinder pressure and bulk temperature level.

In Figure 5.7, the heat release rate curve and the location of the cool flame and main heat release as predicted by all three models are shown. As can be seen, the heat release rate calculations from the LES-LW and improved LES-WW models have a lower peak heat release and longer combustion duration due to mixing controlled direct chemistry (CHEMKIN+MCDC). The LES-LW and improved LES-WW models do not differ significantly in heat release rate. Because the heat release rate comes from the chemical heat released during combustion, heat loss through the walls do not directly affect the combustion calculation. However, it can be seen from Figure 5.8 that the in-cylinder bulk temperature in the LES-LW model is slightly lower than in the improved LES-WW model. Because the total amount of chemical energy release (area under the curve) in the LES-LW and improved LES-WW wall models are almost the same, these differences may come from different wall heat transfer rates, which is confirmed in Figure 5.9. The LES-LW model has 38 percent higher cumulative heat loss than the improved LES-WW model.

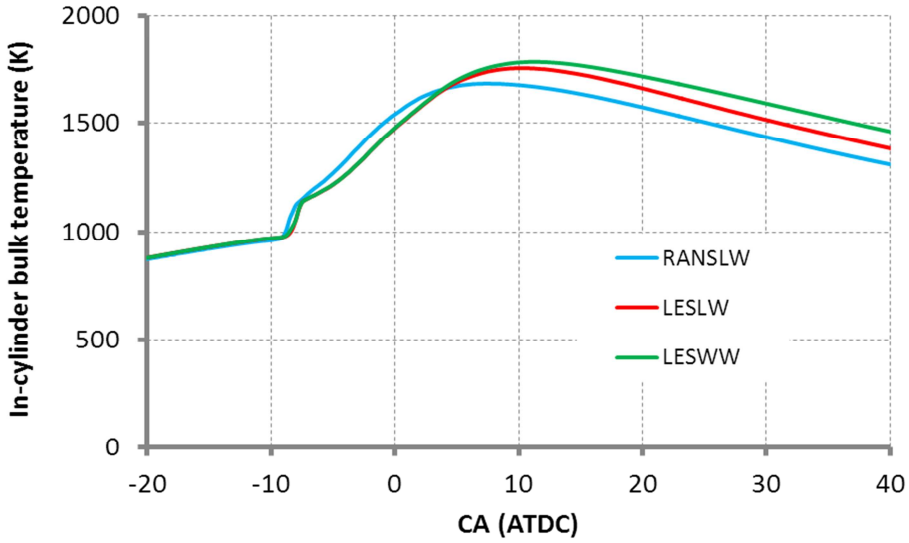

Figure 5.8 Comparisons of computed in-cylinder bulk temperature as predicted by the RANS-LW, LES-LW, and improved LES-WW model for Run41, with the start of injection at 13.52 degrees before TDC

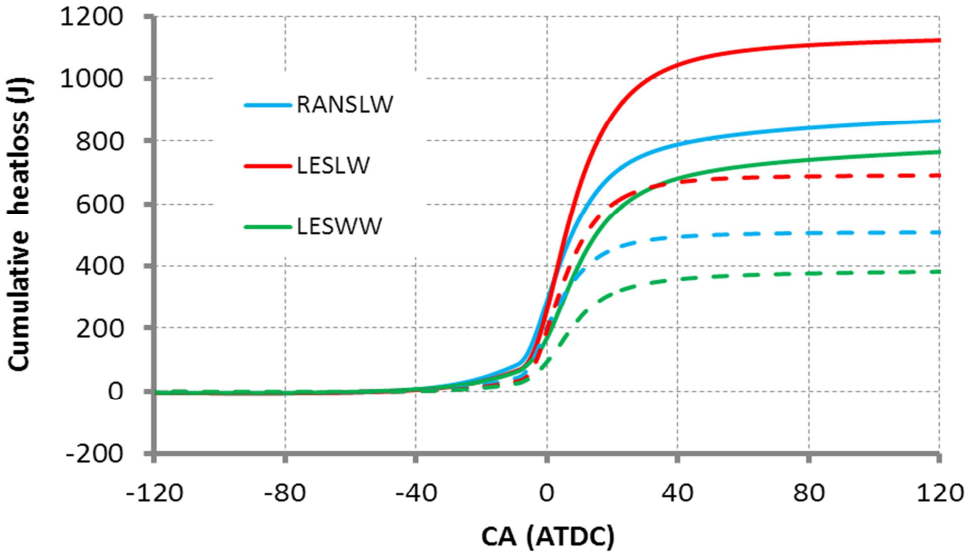

Figure 5.9 Comparisons of computed cumulative heat loss (J) as predicted by the RANS-LW, LES-LW and improved LES-WW model for Run41, with the start of injection at 13.52 degrees before TDC (dotted line=only piston surfaces)

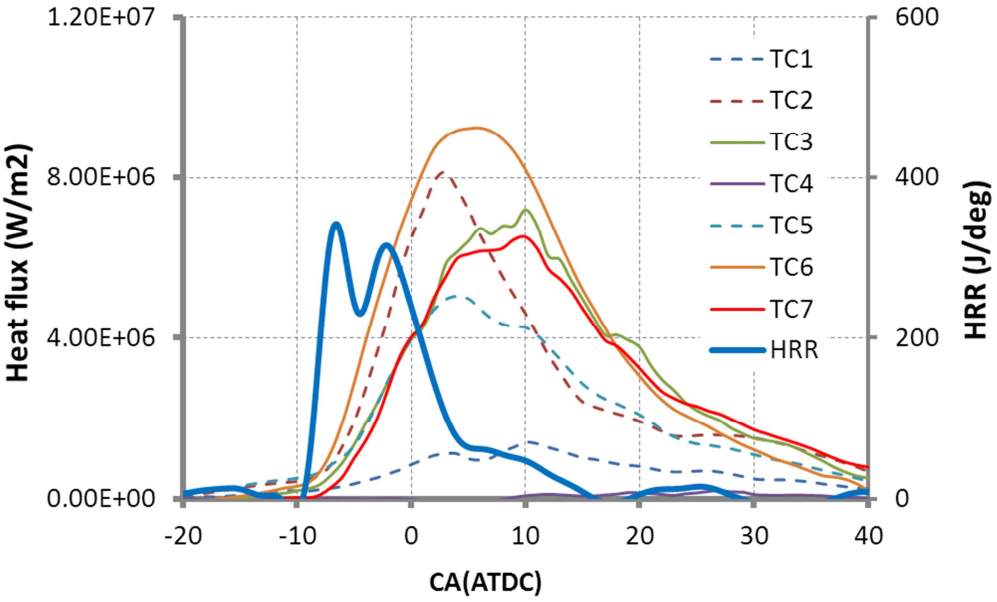

Figure 5.10 Experimental heat flux measurements showing the spatial effects along the primary spray axis for Run41

Next, comparisons of the local heat flux at the thermocouple locations will be made using the three models and the experimental data of Hendricks (2011). Figure 5.10 illustrates experimental heat flux measurements showing the spatial effects along the primary spray axis. The heat release rate is given for reference. The thermocouple location TC#5 is the first to detect the heat flux. The heat flux progresses radially outward on the primary spray plane and phasing delay can be seen. The next thermocouples to capture the combustion process are TC#2, TC#6, TC#3, and TC#7. The thermocouple location TC#1 shows the lowest predicted heat flux because the diesel spray actually targets beyond this point.

In Figures 5.11-5.14, similar global wall heat flux results were predicted from all three wall models during the early compression stroke. The magnitude of the heat flux results is very

small before the combustion occurs. However, the heat flux prediction from all tested models becomes quite different during the combustion event.

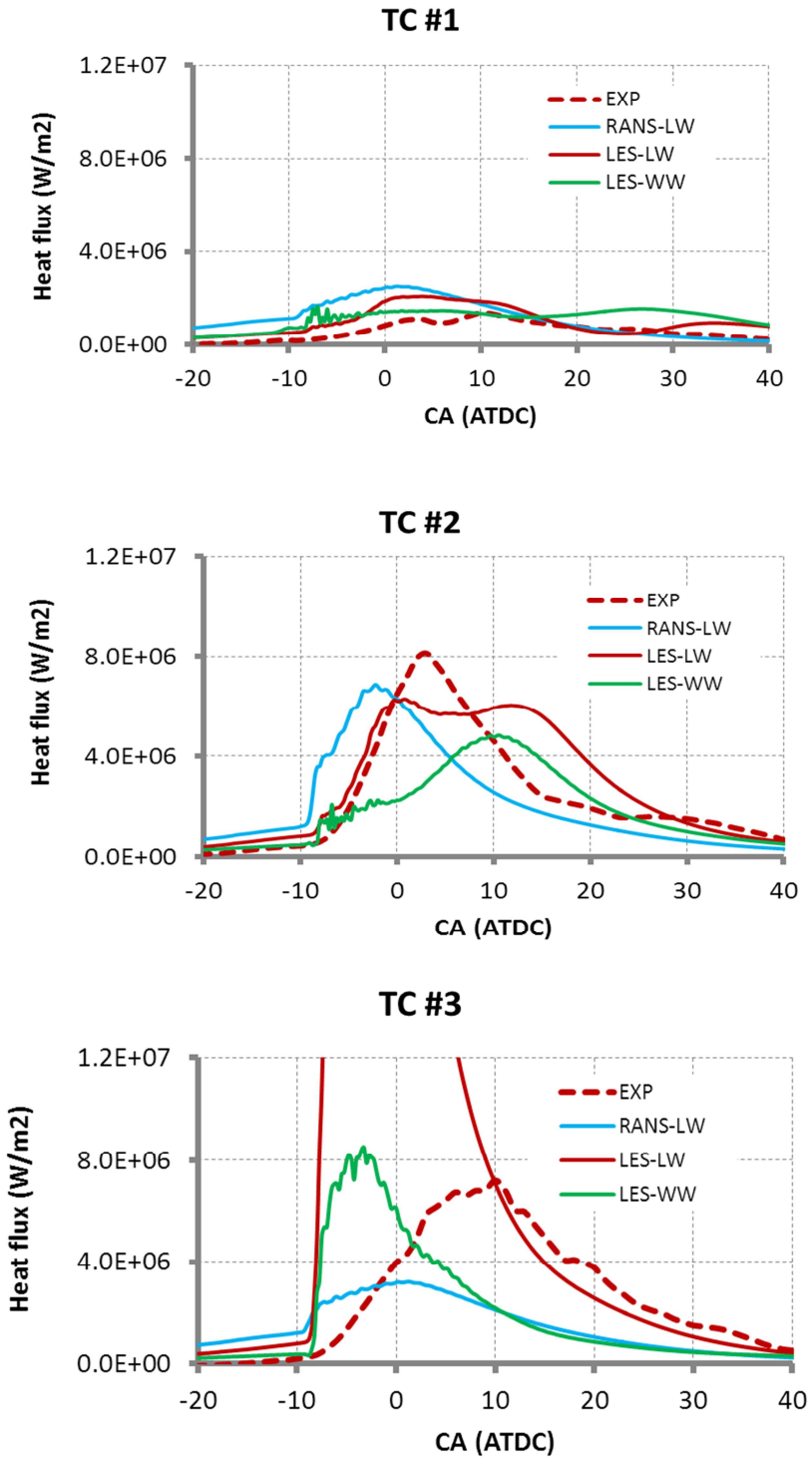

Figure 5.11 Comparisons of heat flux on piston surface at TC#1-TC#3 (spray axis) for Run41

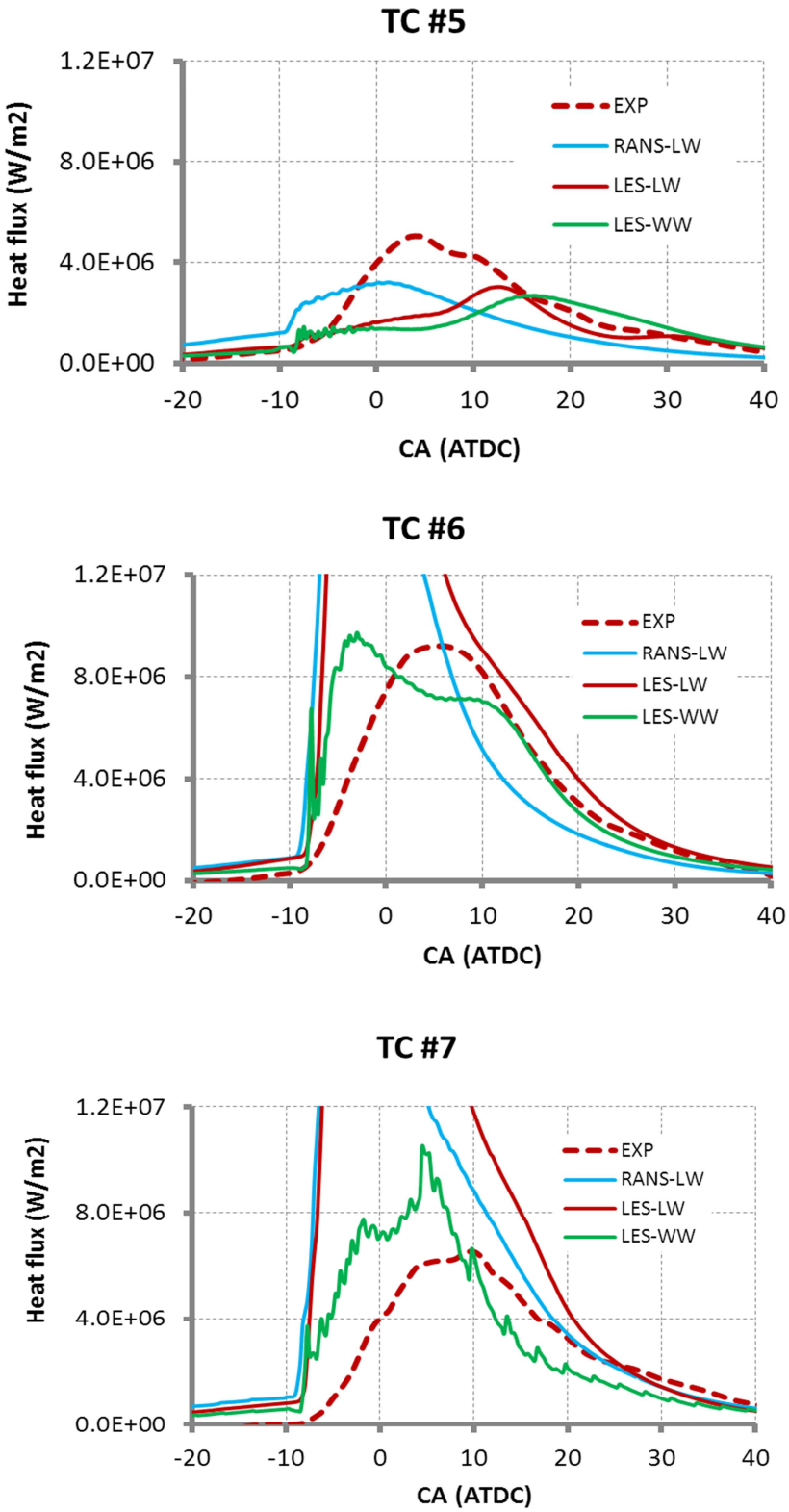

Figure 5.12 Comparisons of heat flux on piston surface at TC#5-TC#7 (spray axis) for Run41

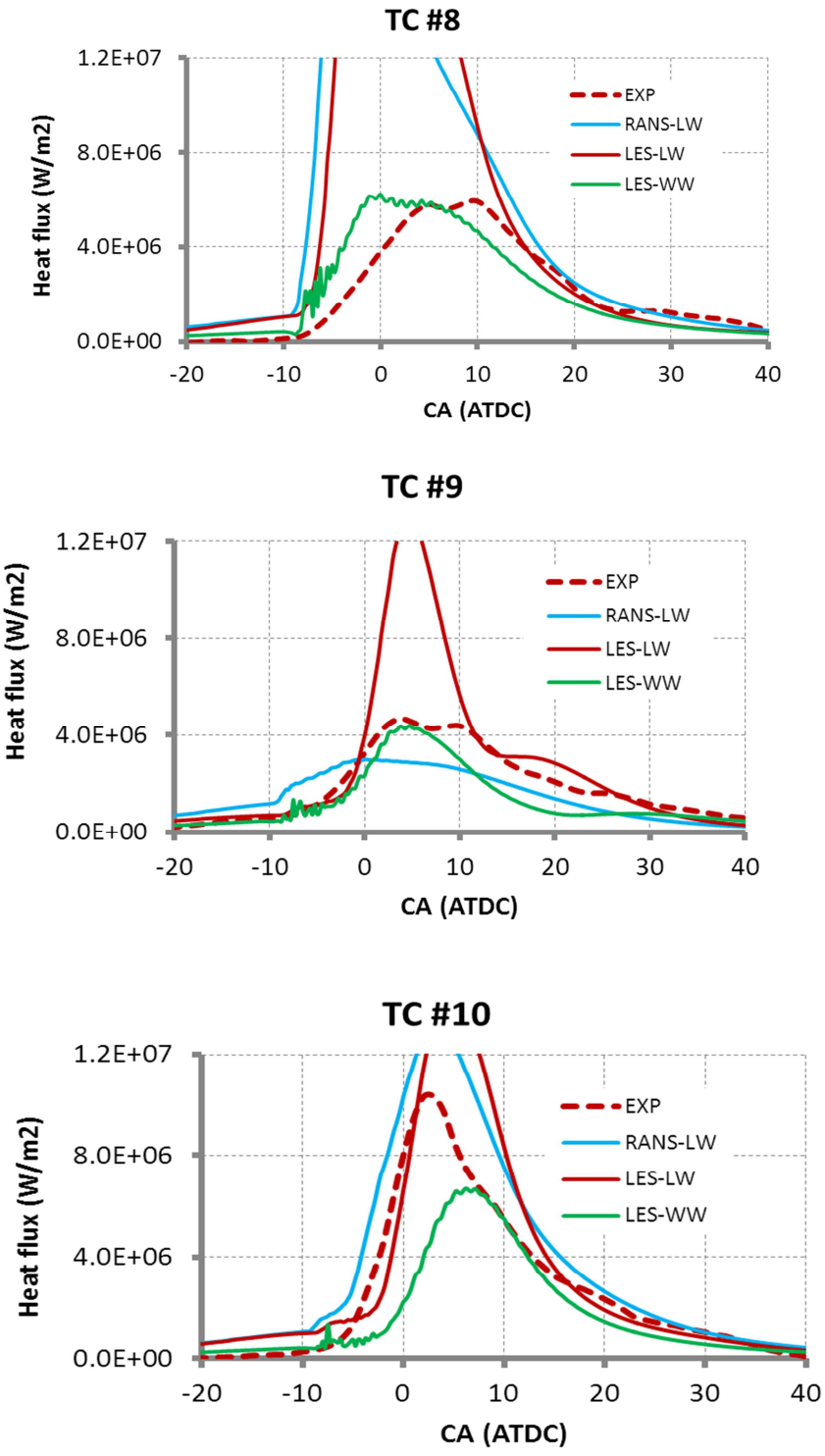

Figure 5.13 Comparisons of heat flux on piston surface at TC#8-TC#10 (mid-way between two adjacent sprays) for Run 41

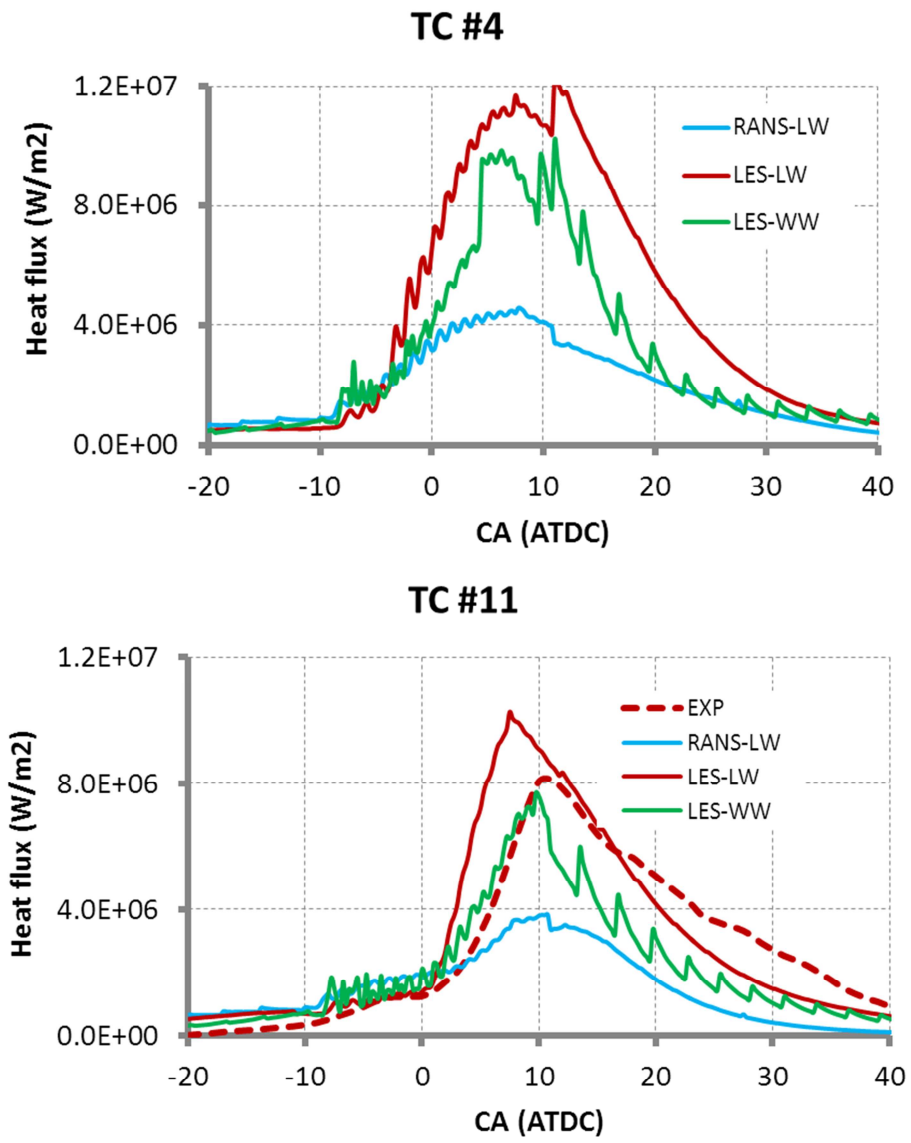

Figure 5.14 Comparisons of heat flux on the piston surface in squish areas TC#4 and TC#11 for Run41

In Figures 5.11 and 5.12, comparisons of measured and computed heat fluxes on the primary spray axis as predicted by the RANS-LW, LES-LW, improved LES-WW models show that the heat flux due to combustion was first detected by TC#6 and TC#3. Because the mid-point between two adjacent spray planes is off from the primary axis, a phasing difference

occurs. The location TC#9 was the next to detect the heat flux, followed by TC#10 and TC#11 in the squish region. At the locations of TC#1, #2 and #5 near the piston dome, the magnitude of heat flux was lower when compared with other locations. The same order of magnitude of heat flux can be found between the measurement and the prediction. This suggests that the flame front may not reach the center of the piston (Kleemann et al., 2003).

In Figure 5.14, the thermocouple locations #4 and #11 are located within the squish region on the piston surface. They usually show a very high heat flux under most conventional diesel combustion conditions because of the high relative gas velocities present. In the measurement report, TC#4 failed while running the test and no experimental data is available for TC#4 to compare against the models.

One observation is that the shift in phasing of the heat flux peak between the predicted heat flux and measurement data can be seen on the thermocouple locations #3, #6 and #7, which are located on the spray axis in Figures 5.11 and 5.12. The premixed combustion initiation process occurs on the periphery of the fuel spray, and this corresponds with the physical location of thermocouples #3, #6 and #7. These thermocouples can detect the higher values of chemical heat release which came from the premixed combustion event, which can be seen from the chemical heat release shape in Figure 5.7. Moreover, it is clear that the heat flux results on the first spray plane from the RANS-LW and LES-LW models are over-predicted at TC#5-8, while the LES-WW model heat flux results agree fairly well with the experimental data. The reason is that the formulation of heat flux in the RANS-LW and LES-LW models relies on the friction velocity. In RANS-LW, the constant C_μ in Eq. (3.16) may be tuned to obtain a good scale between the friction velocity and turbulent kinetic energy. For the LES-LW model, the scale between friction velocity and a sub-grid turbulent kinetic energy from the above equations may

not be appropriate. The constant $C_\mu = 0.09$ in Eq. (3.17), which was derived from RANS techniques, does not exist in LES governing equation. The friction velocity from Eq. (3.24) may be used to provide better heat flux results for wall-model-based LES (LES-WW).

In Figure 5.15, the contour plots of the heat fluxes on the piston surface at the baseline engine conditions are illustrated. For the contour plot comparison, plots of the heat flux distribution on the piston surfaces were generated from experimental data (Hendricks, 2011), and symmetry of the heat flux results about the spray axis (center line) were assumed, as seen in Figure 5.15. This technique does not allow for the influence of swirl to be captured by these plots. The color plots of measured heat flux results on the piston surface were generated using Delaunay triangulation to map the recorded discrete heat flux triplet data onto an evenly spaced polar grid. The piston surface was projected onto a flat 2-D plane using total arc length between thermocouples to set radial distance spacing. The contour grid was filled by interpolating between the discrete thermocouple locations using natural neighbor interpolation (Hendricks, 2011).

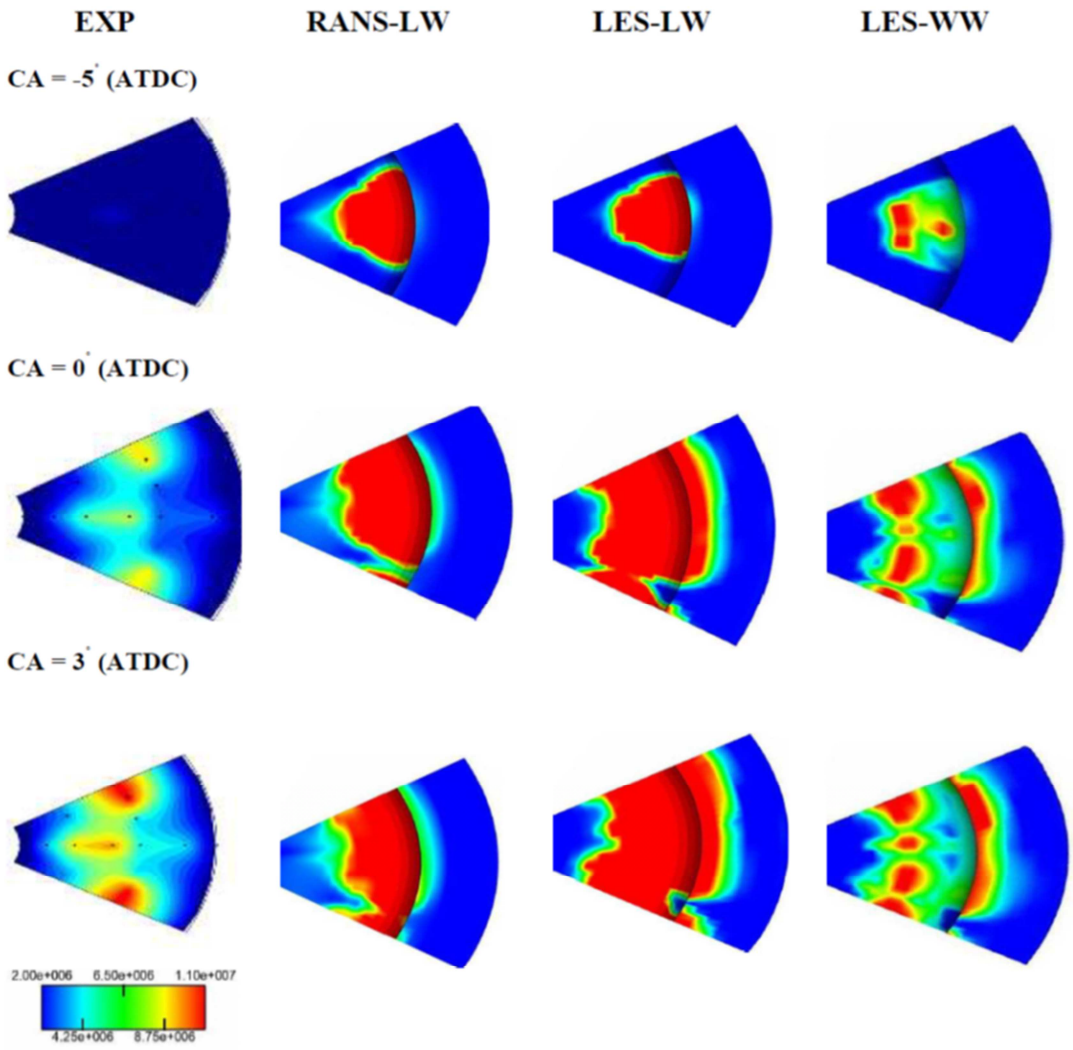

Figure 5.15 Comparisons of measured and computed heat flux distributions on the piston surface as predicted by the RANS-LW, LES-LW, and improved LES-WW models for the period -5° (ATDC) to +3° (ATDC). The scale of plotted heat fluxes varies from $2*10^6$ to $1.1*10^7$ W/m^2

The general picture of the combustion sequence and heat flux pattern development are summarized as follows. At CA = -5° ATDC, thermocouple #6 starts registering the effects of the spray and its possible impingement. From TDC to +3° after TDC, higher heat fluxes progress radially outward on the piston surfaces. After +3°, larger heat fluxes can be seen in the squish

region. Moreover, the results from all tested models are compared. It can be seen that the contour plot of heat fluxes from the improved LES-WW model agrees fairly well with the experimental data. The non-uniform distribution of surface heat fluxes can be captured accurately by the LES-WW model, and a significant improvement is shown in Figure 5.15 when compared with the RANS-LW and LES-LW models.

Here, in order to more fully understand the heat flux calculation of the RANS-LW, LES-LW, and improved LES-WW models, the computed numerator and denominator in Eqs. (3.13-3.14) and (3.25-3.26) are compared. Also, the instantaneous local values at the wall cell of each term within those equations are explored. The large error of computed heat flux at thermocouple TC#6 as predicted by the RANS-LW and LES-LW models can be seen when compared with experimental data and this location is used for investigation.

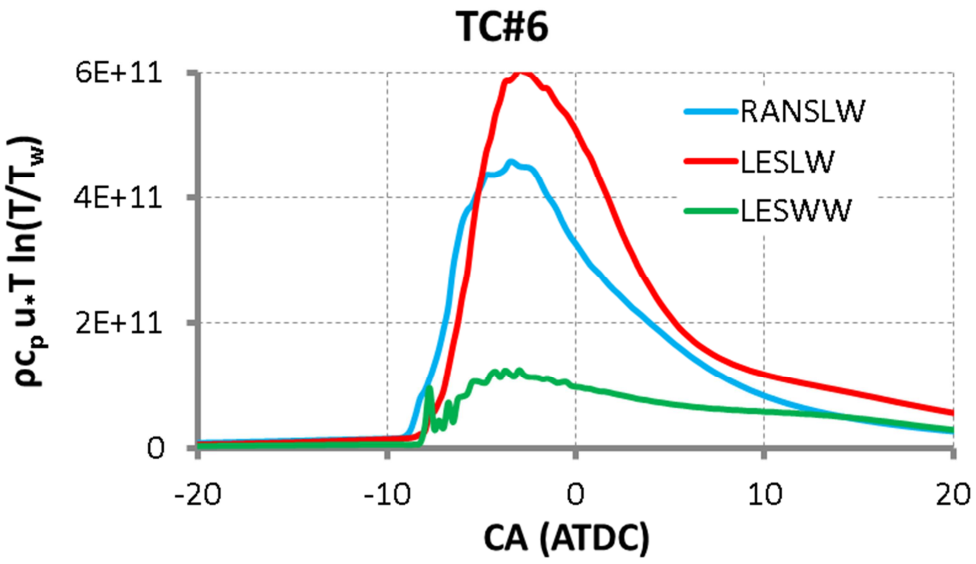

Figure 5.16 Comparisons of the computed numerator as predicted by the RANS-LW, LES-LW, and improved LES-WW models at the wall cell for thermocouple location TC#6

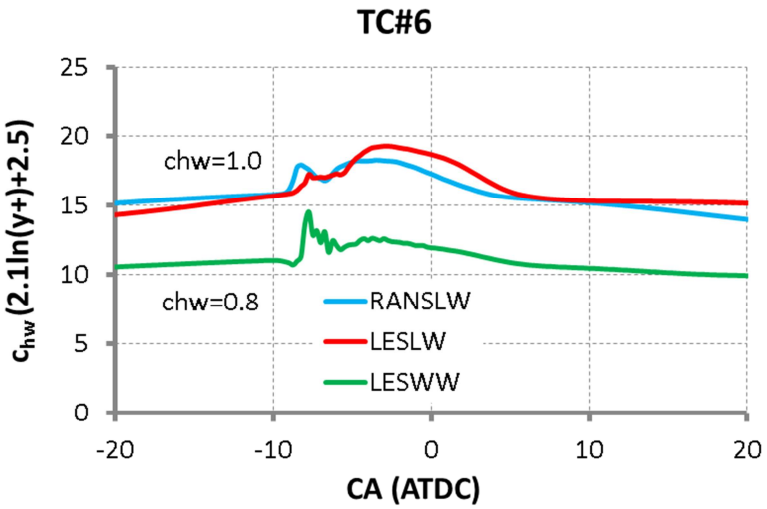

Figure 5.17 Comparisons of the computed denominator as predicted by the RANS-LW, LES-LW, and improved LES-WW models at the wall cell for thermocouple location TC#6

The comparisons of the computed numerator and denominator of heat flux calculations as predicted by the RANS-LW, LES-LW and improved LES-WW models at wall cell for thermocouple location TC#6 are shown in Figures 5.16 and 5.17. With the denominator calculation, the model constant c_{hw} equals to 1.0 for the RANS-LW and LES-LW models, while it is 0.8 for the improved LES-WW model. It is clear that there is insignificant differences in the computed denominator for heat flux calculation among all tested wall models. The dissimilar computed numerators as shown in Figure 5.16 make the heat flux prediction from the tested wall models totally different. Therefore, the magnitude of predicted heat flux in each wall model is strongly dependent on its numerator. The numerator is also related with gas density (ρ), specific heat (c_p), friction velocity (u_*), and gas temperature (T) at the wall cells while the wall temperature (T_w) was assumed to be constant.

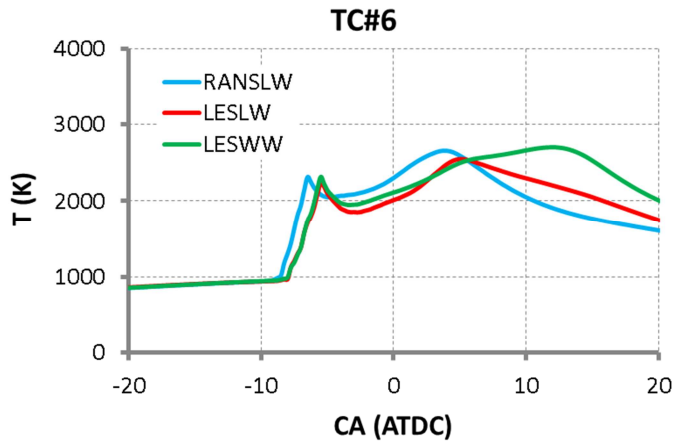

Figure 5.18 Comparisons of computed gas temperature at the wall cell for thermocouple location TC#6

The comparisons of computed gas temperature at the wall cell for thermocouple location TC#6 are shown in Figure 5.18. The same order of magnitude for gas temperature as predicted by the RANS-LW, LES-LW, and improved LES-WW models can be observed. That means the gas density and specific heat which depend on those gas temperatures may also provide insignificantly different values. Figure 5.19 also shows the discrepancies of calculated friction velocity u_* from the RANS-LW, LES-LW, and improved LES-WW models.

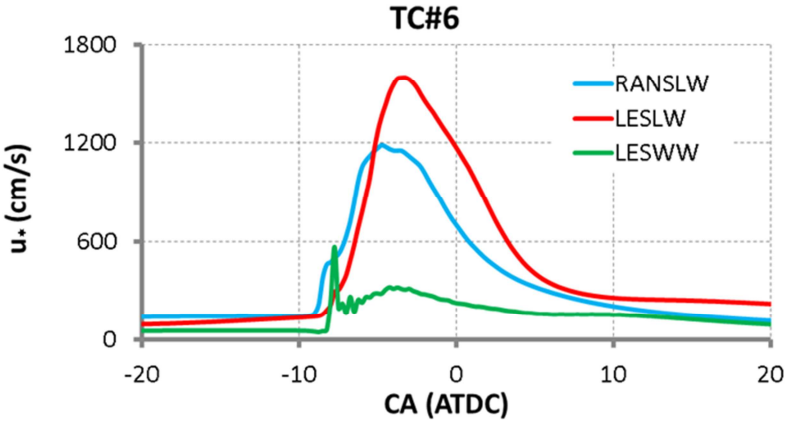

Figure 5.19 Comparisons of computed friction velocity of the wall cell at the location of thermocouple TC#6 for Run41

Therefore, the heat flux prediction in Equations (3.13-3.14) and (3.25-3.26) is strongly dependent on the choice of the friction velocity term. The RANS-LW and LES-LW use Equations (3.16) and (3.17) which employs turbulent kinetic energy (tke) and sub-grid scale turbulent kinetic energy near walls (ksg) to calculate the friction velocity, while Equation (3.24), which is scaled with the computed wall shear stress (τ_w), is employed for the improved LES-WW model. Because the location of thermocouple TC#6 was located at the bowl wall on the primary spray axis, the higher values of turbulent kinetic energy and sub-grid scale turbulent kinetic energy may affect the friction velocity prediction. The over-prediction of friction velocity by the RANS-LW and LES-LW models on the thermocouple TC#6 is responsible for the largely different heat flux results when compared with experimental data.

Figure 5.20 illustrates the comparisons of computed wall shear stress and wall heat flux distribution on the piston surface as predicted by the improved LES-WW model at CA = -5° ATDC, 0° ATDC , and +3° ATDC. The predicted wall shear stress and wall heat transfer from the improved LES-WW model provide more local information on the piston surface and the locally maximum and minimum values can be observed in Figure 5.16. Because the predicted friction velocity from Equation (3.24), which used information from wall shear stress, was employed in the heat flux calculation, the contour plots of wall shear stress and wall heat flux predictions are observed to be similar. Therefore, the heat flux calculations in the improved LES-WW model are strongly dependent on the predicted wall shear stress. The contour plots of wall shear stress and wall heat flux on the piston surface provide more local information, which is consistent with the concepts of LES techniques.

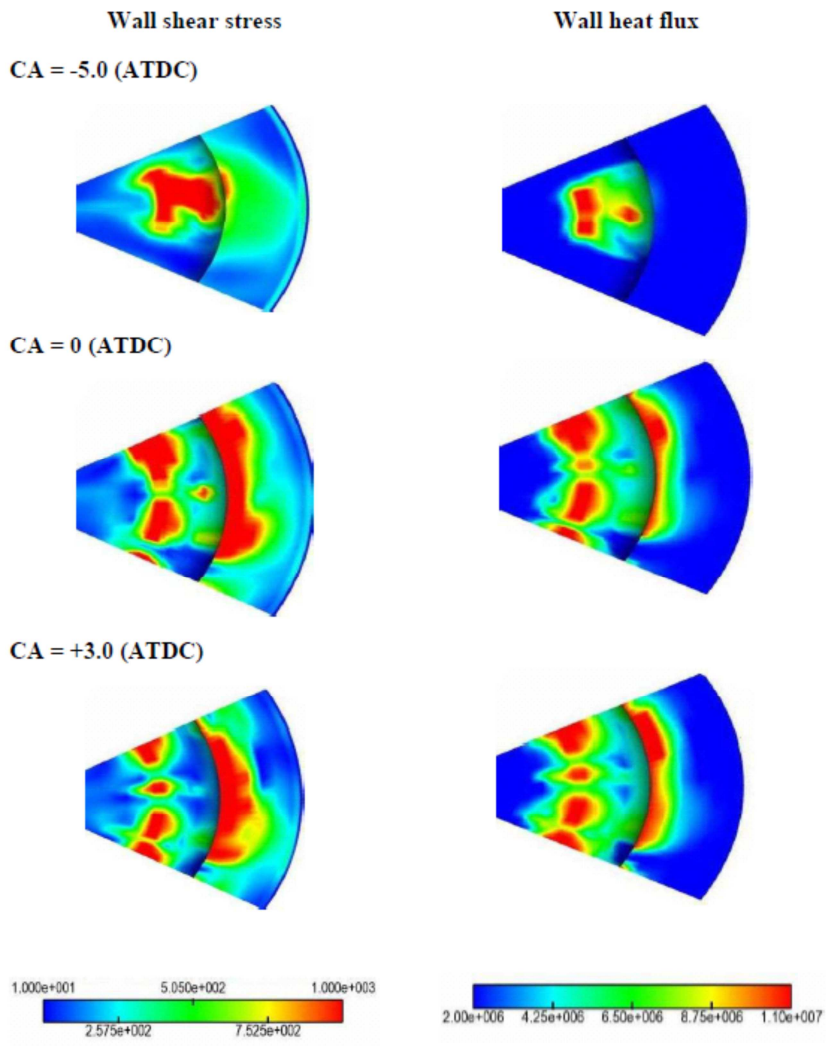

Figure 5.20 Comparisons of computed wall shear stress and wall heat flux distribution on the piston surface as predicted by the improved LESWW models for period -5° (ATDC) to +3° (ATDC). The scale of wall heat fluxes varies from $2*10^6$ to $1.1*10^7$ W/m^2 and 1 to 100 N/m^2 for wall shear stress

5.8 Test engine conditions

Different operating conditions on a single cylinder engine are presented in this section. The experimental results of pressure trace, chemical heat release rate, and surface heat flux are compared with the simulation results. Testing was done at fifteen operating conditions, which are presented in Table 5.5 and Table 5.6.

Table 5.5 Summary of selected diesel engine conditions

	DOF 62	Run 52	Run 51	Run 69	Run 63	DOF 38	DOF 50
RPM	1300	1300	1300	900	1750	1300	1300
Load(bar)	9.75	12.44	15.49	14.89	15.10	8.75	9.07
P_inj (MPa)	150	150	150	150	150	60	90
Fuel flow rate (g/cycle)	0.12	0.15	0.19	0.18	0.18	0.12	0.12
SOI (°ATDC)	-3.25	-9.42	-11.72	-6.01	-16.59	-1.75	-2.70
Swirl ratio	0.70	0.70	0.70	0.70	0.70	0.70	0.70
DI duration (CA°)	15.16	18.13	21.90	15.72	27.64	22.22	18.69
EGR rate (%)	0	0	0	0	0	0	0
Equivalence ratio	0.601	0.609	0.598	0.610	0.600	0.600	0.61
Intake pressure (bar)	1.311	1.535	1.916	1.973	1.858	1.308	1.286
IVC pressure (bar)	1.460	1.654	2.070	2.135	2.060	1.466	1.488
IVC temperature (K)	398	369	364	392	376	388	383
Piston surface temperature	504	535	559	544	584	489	495

Table 5.6 Summary of selected diesel engine conditions (continue)

	Run 40	Run 39	Run 42	Run 43	Run 44	Run 33	Run 36	Run 38
RPM	1300	1300	1300	1300	1300	1300	1300	1300
Load(bar)	7.98	7.97	7.92	7.85	7.37	9.34	9.29	9.08
P_inj (MPa)	150	150	150	150	150	150	150	150
Fuel flow rate (g/cycle)	0.091	0.091	0.091	0.091	0.09	0.104	0.106	0.105
SOI (°ATDC)	-11.01	-8.46	-6.0	-3.51	-0.91	-7.20	-7.40	-7.40
Swirl ratio	0.70	0.70	0.70	0.70	0.70	0.70	0.70	0.70
DI duration (CA°)	11.89	12.20	12.21	12.22	12.20	13.52	13.73	13.66
EGR rate (%)	0	0	0	0	0	0	0	0
Equivalence ratio	0.388	0.388	0.388	0.384	0.386	0.342	0.417	0.467
Intake pressure (bar)	1.531	1.531	1.540	1.548	1.553	1.926	1.703	1.530
IVC pressure (bar)	1.639	1.636	1.647	1.655	1.657	2.115	1.861	1.633
IVC temperature (K)	374	386	388	389	389	319	315	398
Piston surface temperature	491	484	478	473	469	490	494	495

These test cases were chosen to examine the effect of different loads (DOF62, Run52, and Run51), engine speeds (Run69, Run51, and Run63), injection pressures (DOF62, DOF38, and DOF50), start of injection (Run39, Run40, Run42, Run43, and Run44), and equivalence ratio (Run33, Run36, and Run38). All test cases were used for validating the proposed wall heat model. The main objective in this section is to compare the predicted heat flux results as predicted by the RANS-LW, LES-LW, and the improved LES-WW models with experimental data. However, only the comparisons of computed and measured cylinder pressure and the comparisons of computed and measured chemical heat release rate are shown. The computed and measured heat flux can be found in appendix. It is apparent that the majority of the predicted heat flux results from each thermocouple location (TC#1-TC#11) follow similar trends when compared with experimental data. Those trends and the error analysis from those heat flux results are summarized in a later next section.

5.8.1 DOF62

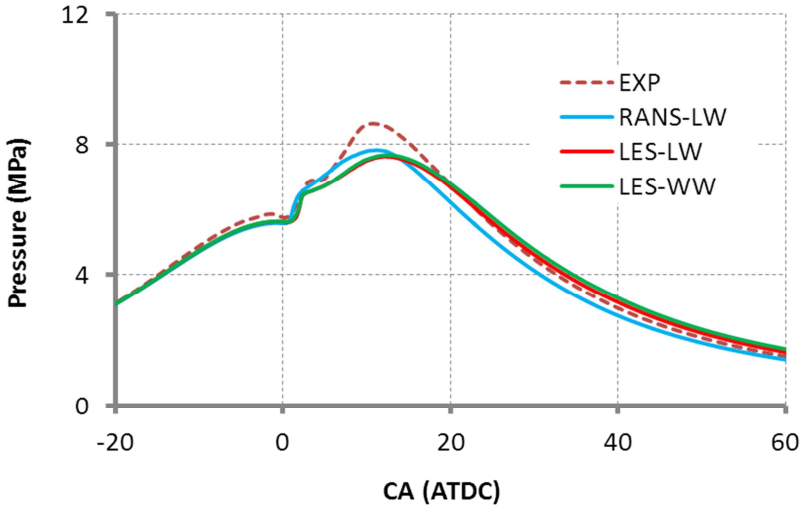

Figure 5.21 Comparisons of computed and measured cylinder pressure for DOF62, with the start of injection at 3.25 degrees before TDC.

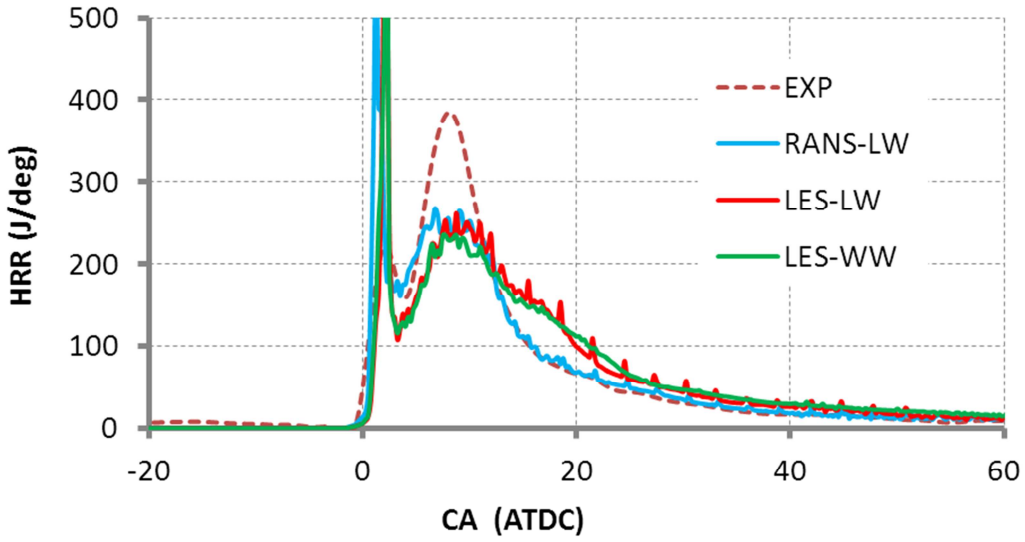

Figure 5.22 Comparisons of computed and measured chemical heat release rate for DOF62, with the start of injection at 3.25 degrees before TDC.

Comparisons between measured and computed in-cylinder pressure and heat release rates as predicted by RANS-LW, LES-LW, and the improved LES-WW models are shown in Figures 5.21 and 5.22 from case DOF62, with an SOI of 3.25 degrees before TDC. A slight difference in motor pressure trace from all three test models can be observed in Figure 5.21, while a good agreement in phasing of ignition can be seen in Figure 5.22. The locations of predicted cool flame and main heat release rate agree fairly well with experimental data. Similar trends of chemical heat release rate relative to the baseline case (Run41) in Figure 5.7 are captured here for the RANS-LW model. With the CHEMKIN detailed chemistry model, the RANS-LW model results in less burning during the expansion stroke, with underestimation of in-cylinder pressure.

5.8.2 Run52

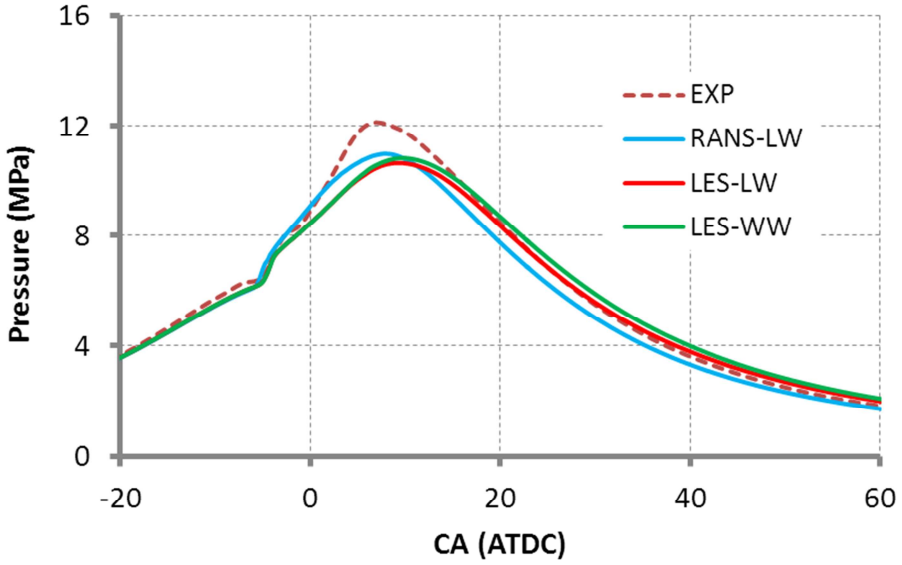

Figure 5.23 Comparisons of computed and measured cylinder pressure for Run52, with the start of injection at 9.42 degrees before TDC.

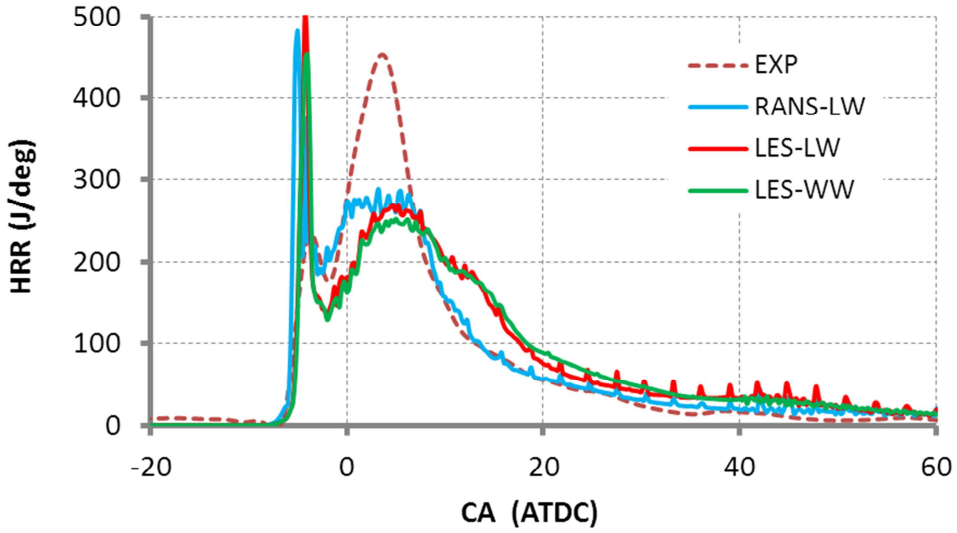

Figure 5.24 Comparisons of computed and measured chemical heat release rate for Run52, with the start of injection at 9.42 degrees before TDC.

The comparisons between measured and computed in-cylinder pressure and heat release rates as predicted by RANS-LW, LES-LW, and the improved LES-WW models are illustrated in Figures 5.23 and 5.24 from Run52 with an SOI of 9.42 degrees before TDC. A slight difference in the pressure trace from all three test models can be observed in Figure 5.23, while a good agreement in phasing of ignition can be seen in Figure 5.24. Similar trends of chemical heat release rate relative to the baseline case (Run41) in Figure 5.7 are captured here for the RANS-LW model. The RANS-LW model results in less burning during the expansion stroke, with underestimation of in-cylinder pressure.

5.8.3 Run51

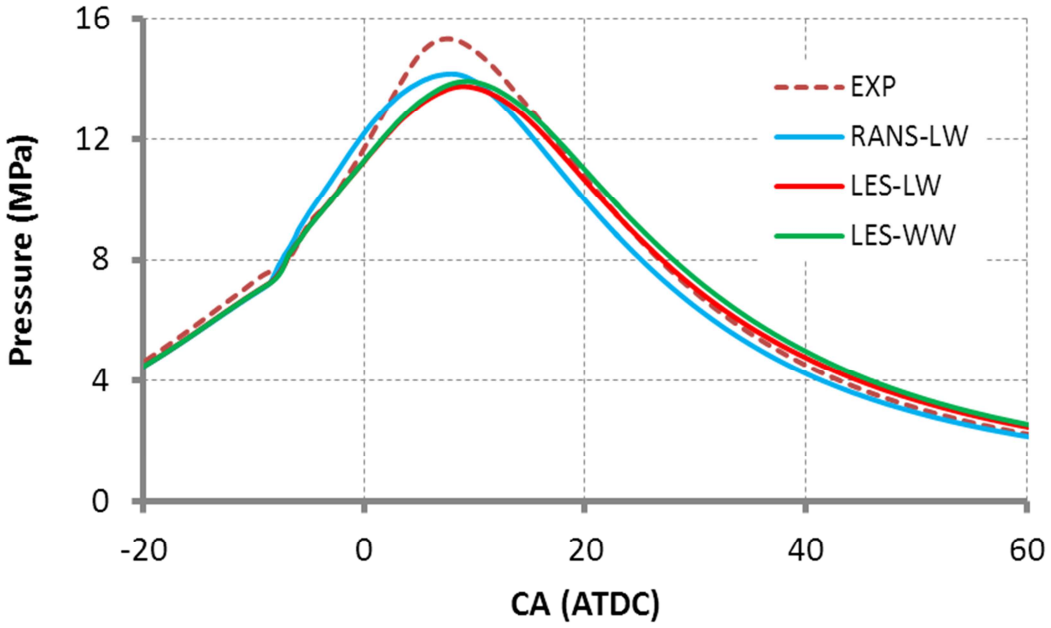

Figure 5.25 Comparisons of computed and measured cylinder pressure for Run51, with the start of injection at 11.72 degrees before TDC.

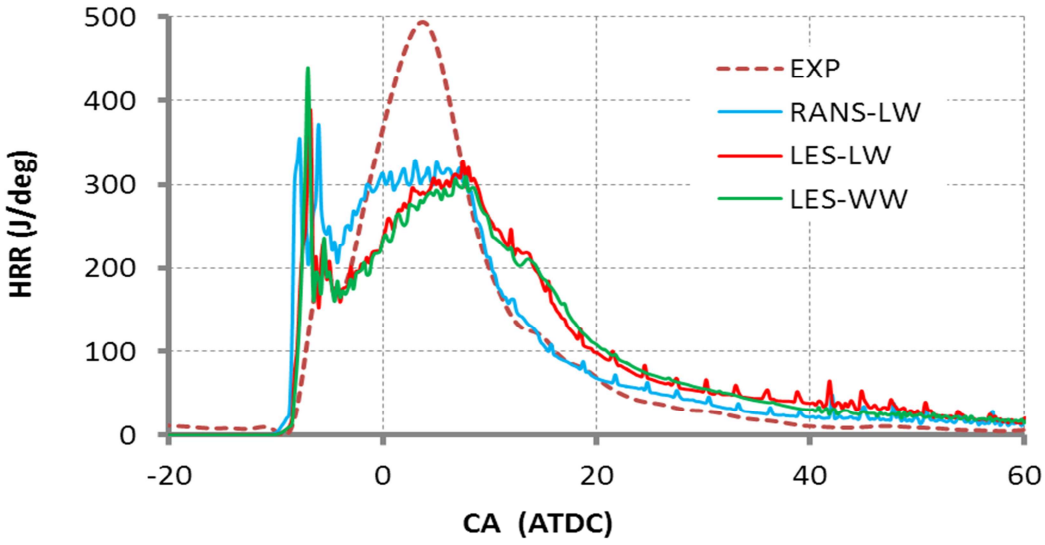

Figure 5.26 Comparisons of computed and measured chemical heat release rate for Run51, with the start of injection at11.72 degrees before TDC.

The comparisons between measured and computed in-cylinder pressure and heat release rates as predicted by the RANS-LW, LES-LW, and improved LES-WW models are illustrated in Figures 5.25 and 5.26 from Run51, with an SOI of 11.72 degrees before TDC. A slight difference in the pressure trace from all three test models can be observed in Figure 5.25, while a good agreement in phasing of ignition can be seen in Figure 5.26. The RANS-LW model is observed to over-predict the pressure trace.

5.8.4 Run69

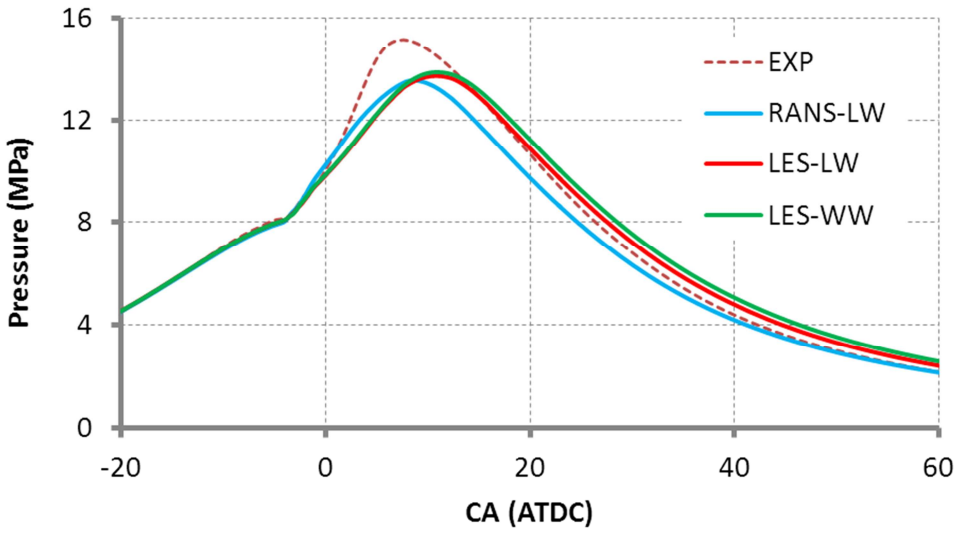

Figure 5.27 Comparisons of computed and measured cylinder pressure for Run69, with the start of injection at 6.01 degrees before TDC.

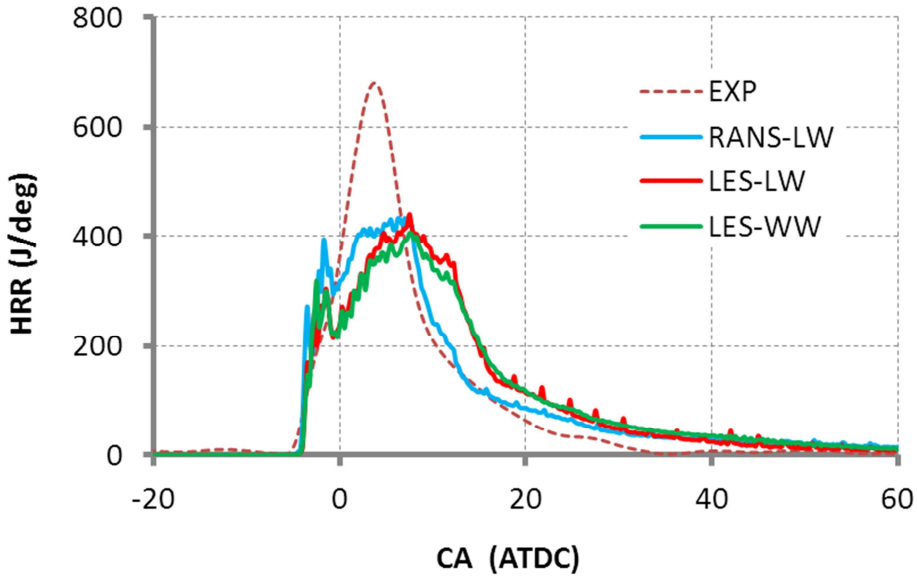

Figure 5.28 Comparisons of computed and measured chemical heat release rate for Run69, with the start of injection at 6.01 degrees before TDC.

The comparisons between measured and computed in-cylinder pressure and heat release rates as predicted by the RANS-LW, LES-LW, and improved LES-WW models are illustrated in Figures 5.27 and 5.28 for Run69, with an SOI of 6.01 degrees before TDC. A good agreeement in pressure trace and phasing of ignition as predicted by the RANS-LW, LES-LW, and improved LES-WW models can be seen in Figures 5.27 and 5.28. Similar trends of chemical heat release rate relative to the baseline case (Run41) in Figure 5.7 are captured here for the RANS-LW model.

5.8.5 Run63

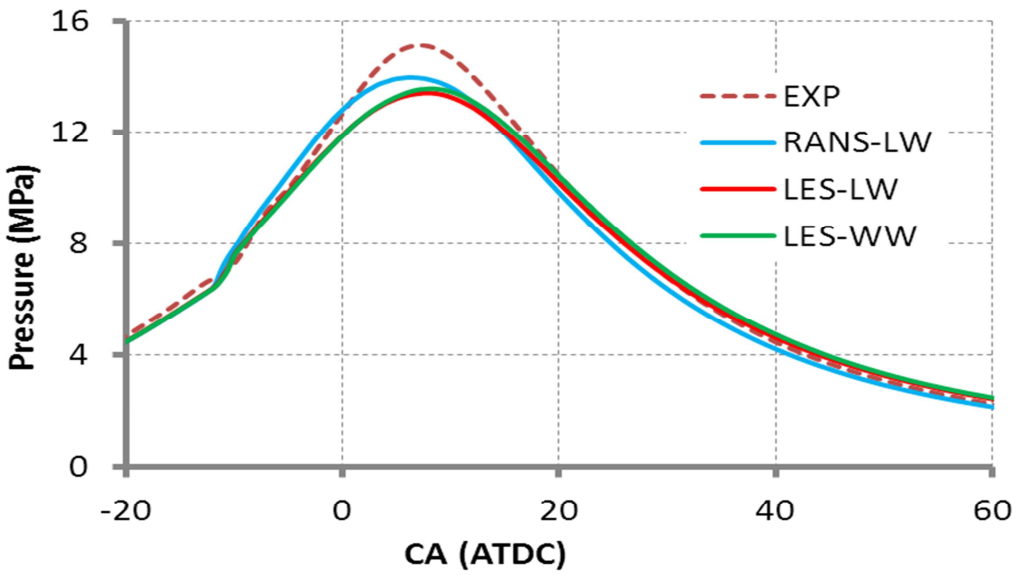

Figure 5.29 Comparisons of computed and measured cylinder pressure for Run63, with the start of injection at 16.59 degrees before TDC.

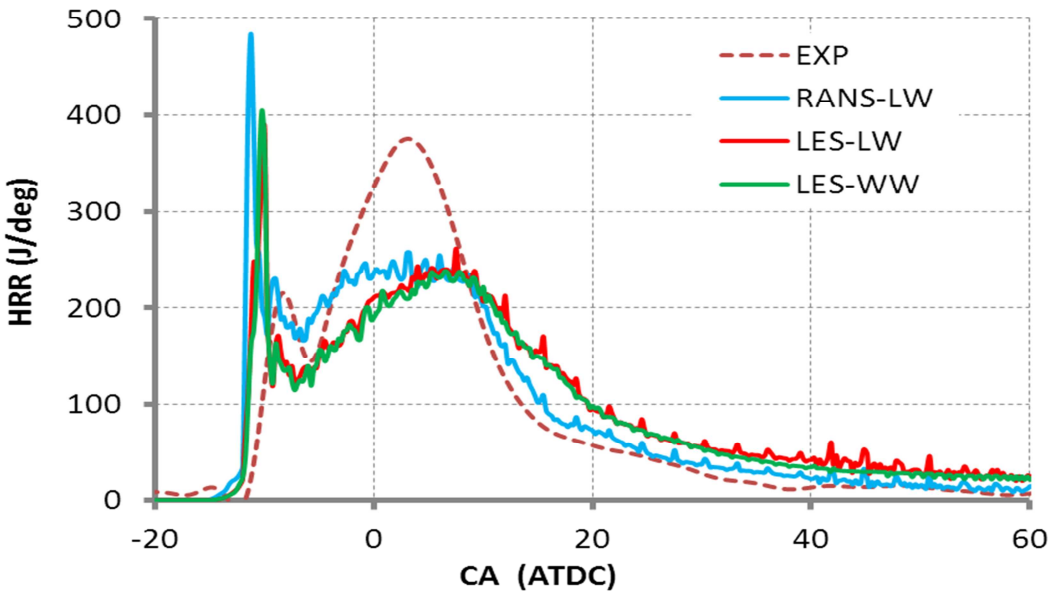

Figure 5.30 Comparisons of computed and measured chemical heat release rate for Run63, with the start of injection at 16.59 degrees before TDC.

The comparisons between the measured and computed in-cylinder pressure and heat release rates as predicted by the RANS-LW, LES-LW, and the improved LES-WW models are shown in Figures 5.29 and 5.30 for Run63, with an SOI of 16.59 degrees before TDC. A slight difference in the pressure trace from all three test models can be observed in Figure 5.29, while a slightly over-prediction in phasing of ignition can be seen in Figure 5.30. Similar trends of chemical heat release rate relative to the baseline case (Run41) in Figure 5.7 are captured here for the RANS-LW model.

5.8.6 DOF38

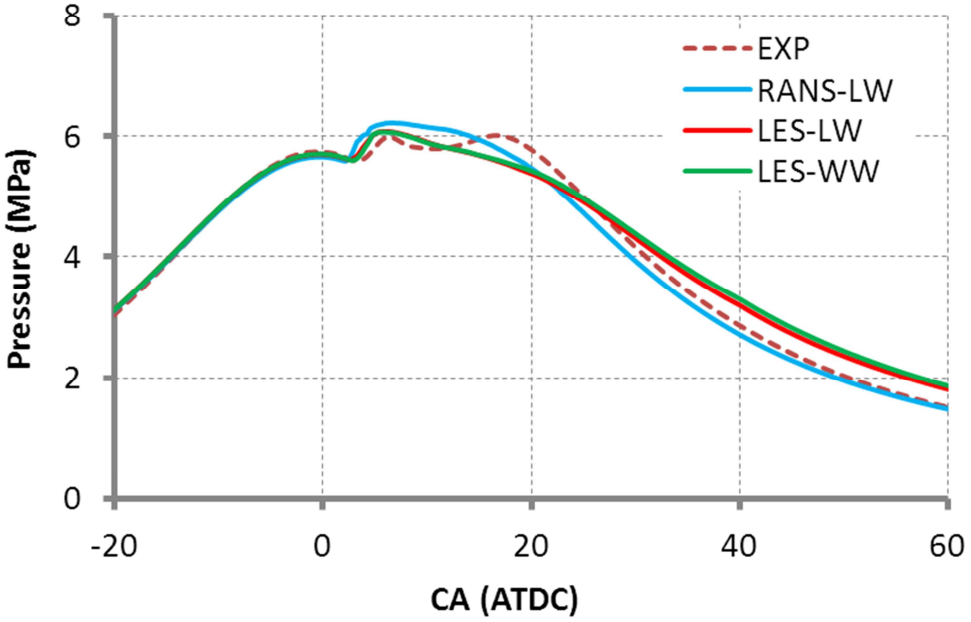

Figure 5.31 Comparisons of computed and measured cylinder pressure for DOF38, with the start of injection at 1.75 degrees before TDC.

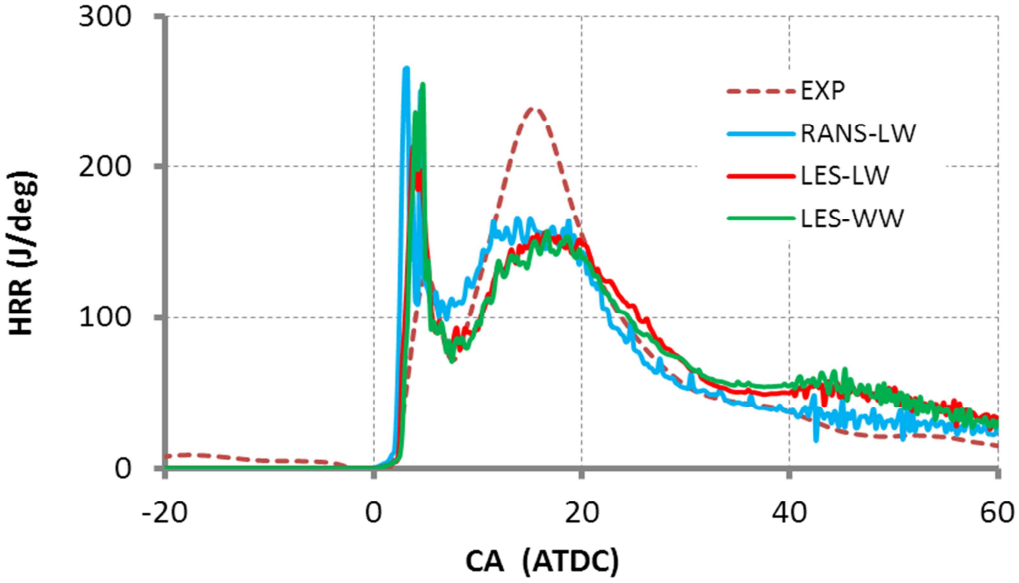

Figure 5.32 Comparisons of computed and measured chemical heat release rate for DOF38, with the start of injection at 1.75 degrees before TDC.

The comparisons between the measured and computed in-cylinder pressure and heat release rates as predicted by the RANS-LW, LES-LW, and the improved LES-WW models are shown in Figures 5.31 and 5.32 for DOF38, with an SOI of 1.75 degrees before TDC. A good agreement in the pressure trace from all three test models can be observed in Figure 5.31, while a slight over-prediction in phasing of ignition can be seen in Figure 5.32. However, the pressure trace as predicted by the RANS-LW model agrees fairly well with the experimental results.

5.8.7 DOF50

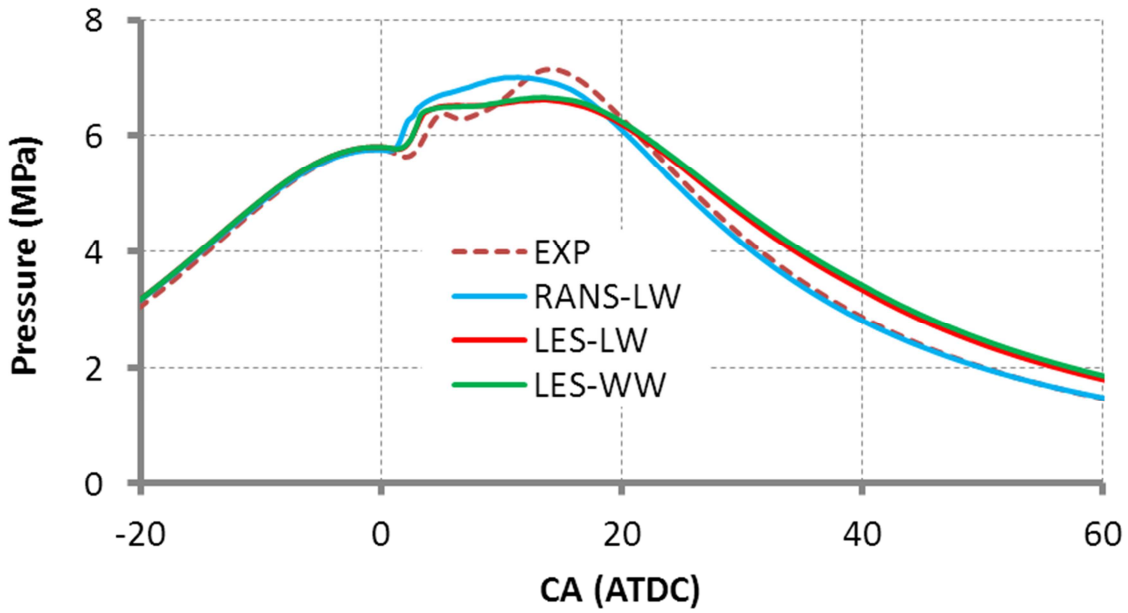

Figure 5.33 Comparisons of computed and measured cylinder pressure for DOF50, with the start of injection at 2.70 degrees before TDC.

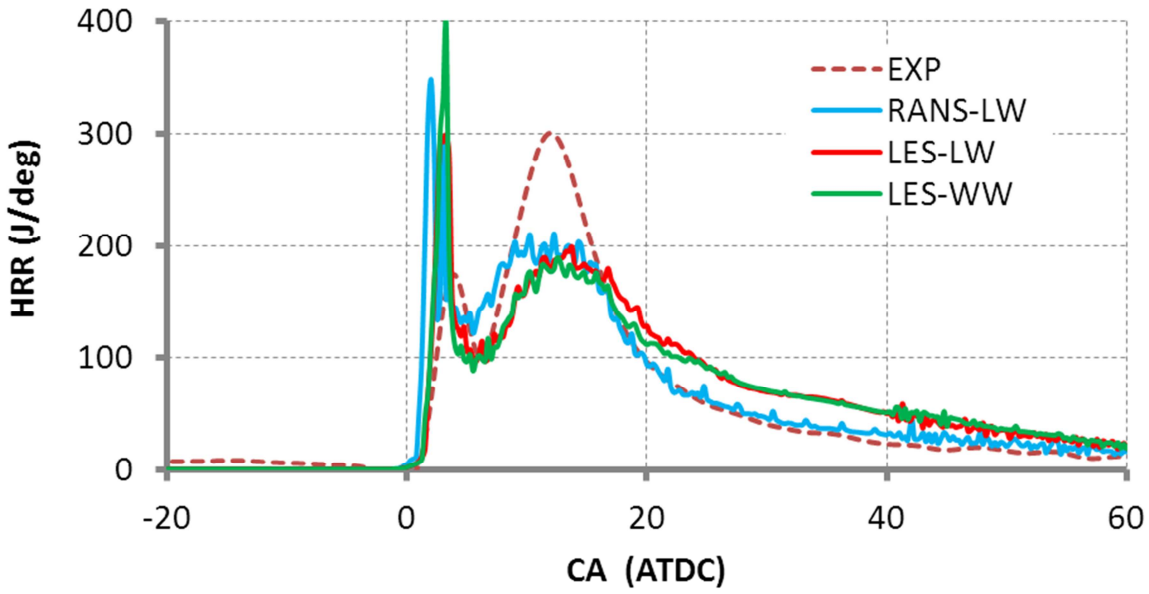

Figure 5.34 Comparisons of computed and measured chemical heat release rate for DOF50, with the start of injection at 2.70 degrees before TDC.

Figure 5.33 shows the comparisons of computed and measured cylinder pressure, while the comparisons of computed and measured chemical heat release rate are shown in Figure 5.34. The start of injection was advanced to 2.70 degrees before TDC. Good agreeement is seen in the pressure trace as predicted by the RANS-LW, LES-LW, and improved LES-WW models, while the RANS-LW calculation shows slightly earlier ignition timing.

5.8.8 Run40

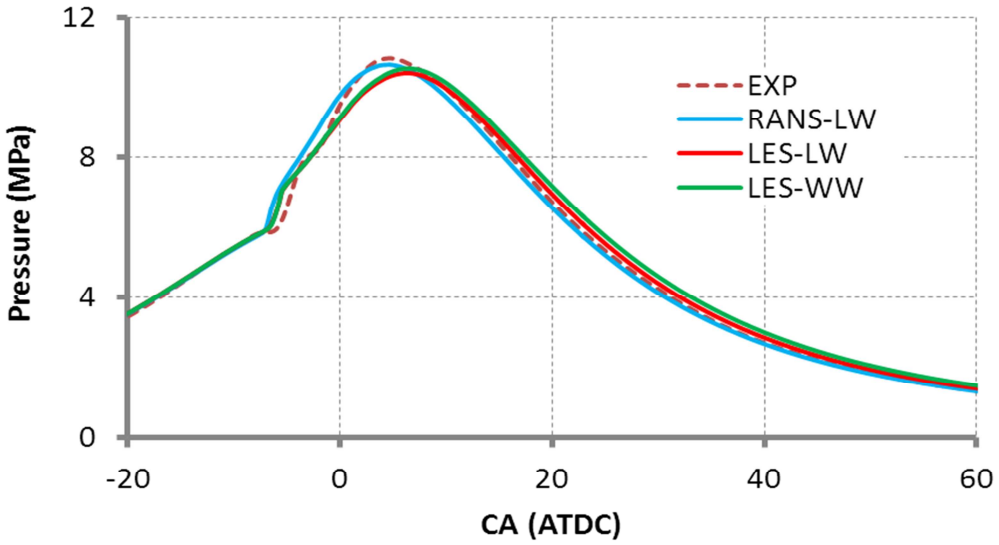

Figure 5.35 Comparisons of computed and measured cylinder pressure for Run40, with the start of injection at 11.01 degrees before TDC.

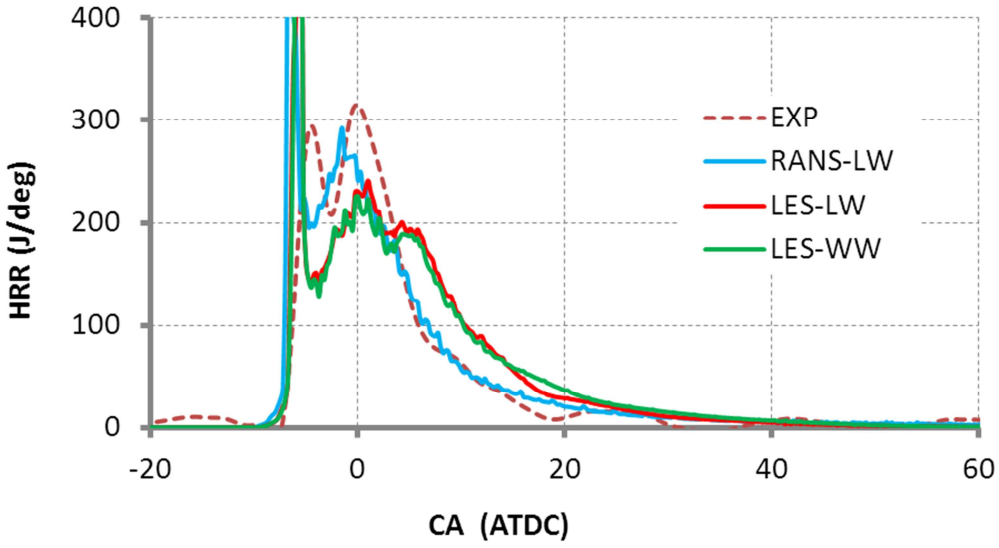

Figure 5.36 Comparisons of computed and measured chemical heat release rate for Run40, with the start of injection at 11.01 degrees before TDC.

The comparisons between measured and computed in-cylinder pressure and heat release rates as predicted by the RANS-LW, LES-LW, and the improved LES-WW models are illustrated in Figures 5.35 and 5.36 for Run40, with an SOI of 11.01 degrees before TDC. A good agreeement in the pressure trace and phasing of ignition as predicted by the RANS-LW, LES-LW, and improved LES-WW models can be seen in Figures 5.35 and 5.36. Similar trends of chemical heat release rate relative to the baseline case (Run41) in Figure 5.7 are captured here for the RANS-LW model.

5.8.9 Run39

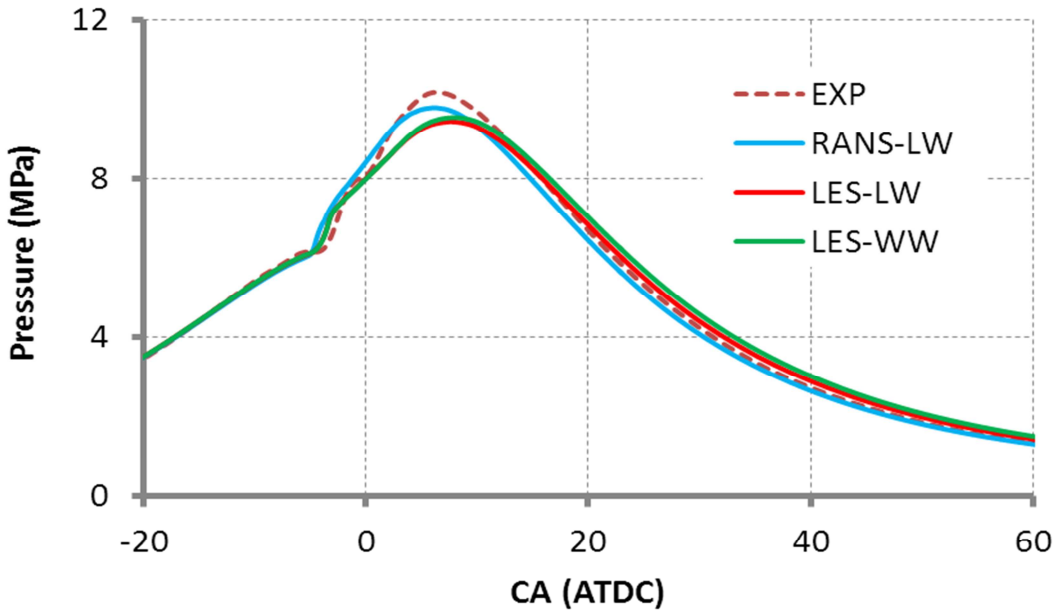

Figure 5.37 Comparisons of computed and measured cylinder pressure for Run39, with the start of injection at 8.46 degrees before TDC.

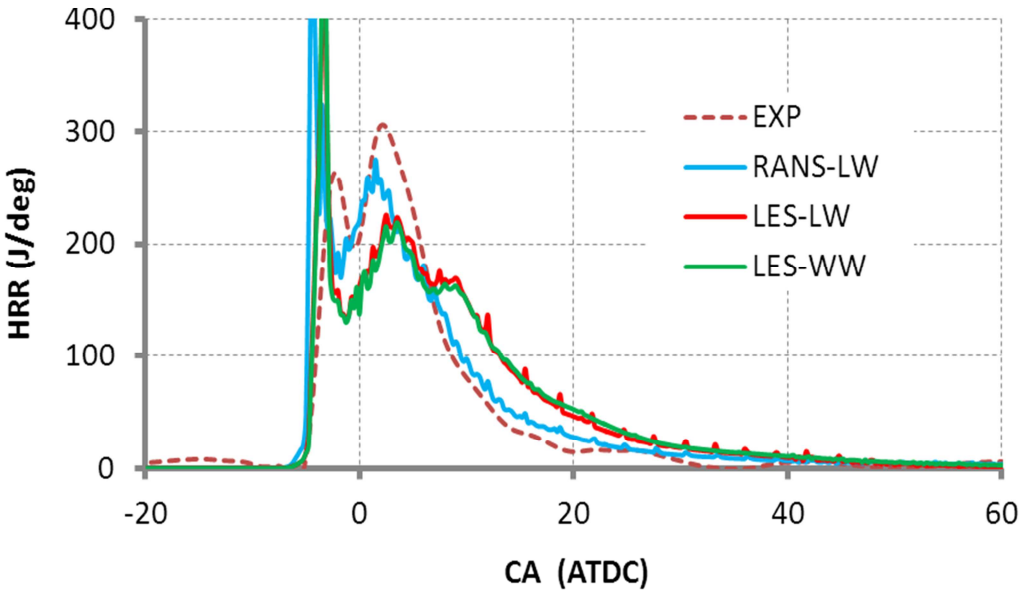

Figure 5.38 Comparisons of computed and measured chemical heat release rate for Run39, with the start of injection at 8.46 degrees before TDC.

The comparisons between the measured and computed in-cylinder pressure and heat release rates as predicted by the RANS-LW, LES-LW, and the improved LES-WW models are illustrated in Figures 5.37 and 5.38 for Run39, with an SOI of 8.46 degrees before TDC. A good agreeement in the pressure trace and phasing of ignition as predicted by the RANS-LW, LES-LW, and improved LES-WW models can be seen in Figures 5.37 and 5.38. Similar trends of chemical heat release rate relative to the baseline case (Run41) in Figure 5.7 are captured here for the RANS-LW model.

5.8.10 Run42

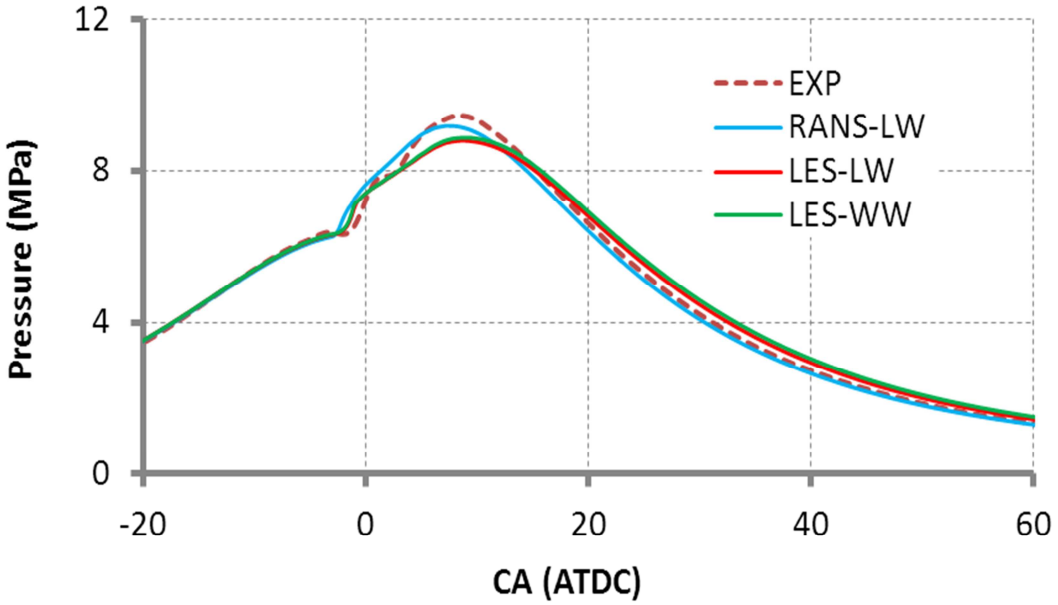

Figure 5.39 Comparisons of computed and measured cylinder pressure for Run42, with the start of injection at 6.0 degrees before TDC.

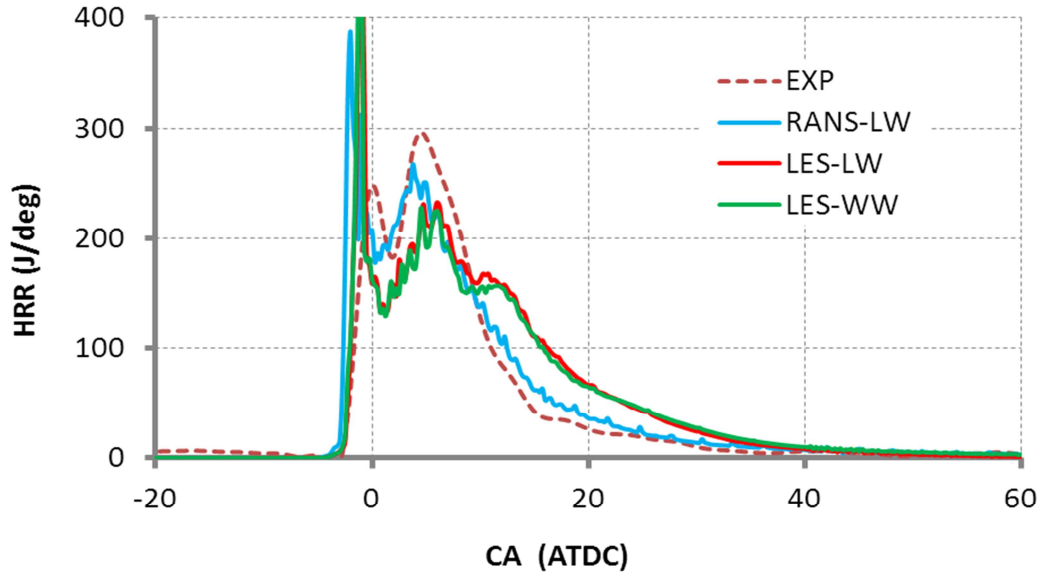

Figure 5.40 Comparisons of computed and measured chemical heat release rate for Run42, with the start of injection was 6.0 degrees before TDC.

The comparisons between the measured and computed in-cylinder pressure and heat release rates as predicted by the RANS-LW, LES-LW, and the improved LES-WW models are illustrated in Figures 5.39 and 5.40 for Run42, with an SOI of 6.0 degrees before TDC. A good agreeement in the pressure trace and phasing of ignition as predicted by the RANS-LW, LES-LW, and improved LES-WW models can be seen in Figures 5.39 and 5.40. Similar trends of chemical heat release rate relative to the baseline case (Run41) in Figure 5.7 are captured here for the RANS-LW model.

5.8.11 Run43

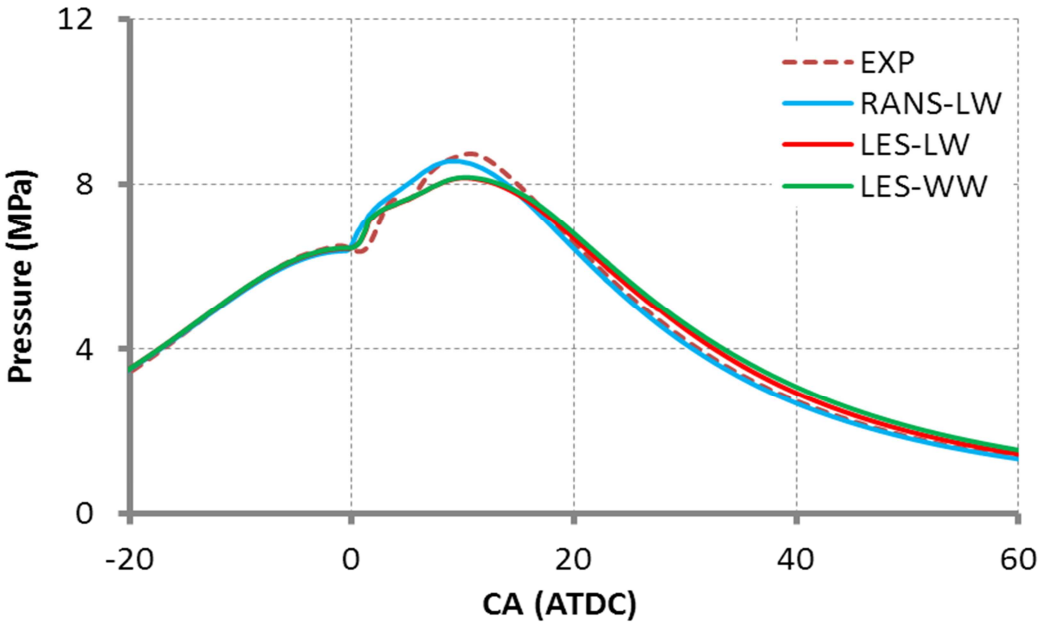

Figure 5.41 Comparisons of computed and measured cylinder pressure for Run43, with the start of injection at 3.51 degrees before TDC.

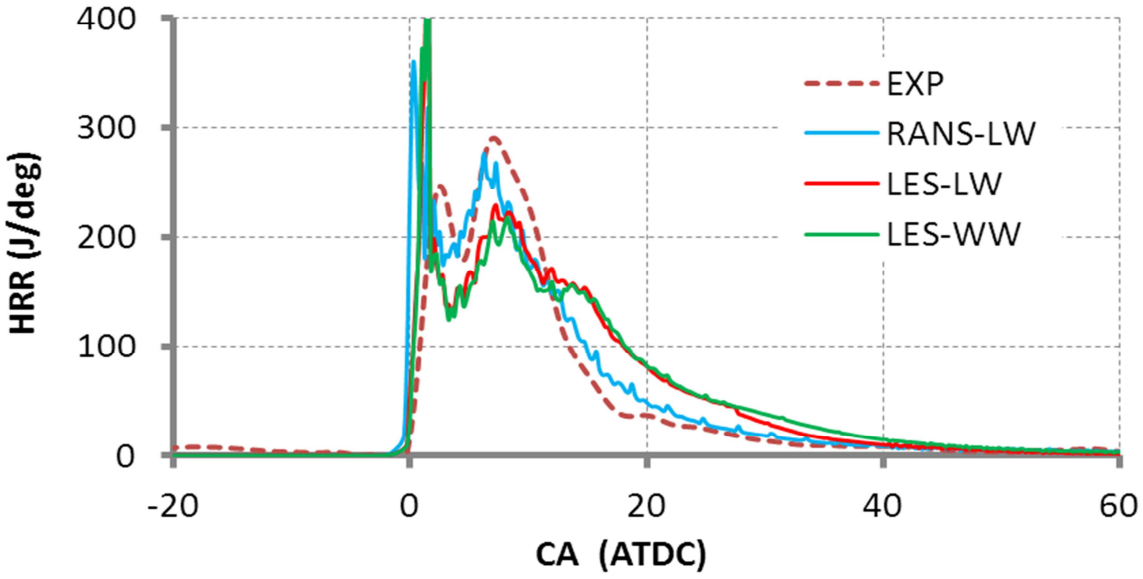

Figure 5.42 Comparisons of computed and measured chemical heat release rate for Run43, with the start of injection at 3.51 degrees before TDC.

The comparisons between the measured and computed in-cylinder pressure and heat release rates as predicted by the RANS-LW, LES-LW, and the improved LES-WW models are illustrated in Figures 5.41 and 5.42 for Run43, with an SOI of 3.51 degrees before TDC. A good agreeement in the pressure trace and phasing of ignition as predicted by the RANS-LW, LES-LW, and improved LES-WW models can be seen in Figures 5.41 and 5.42. Similar trends of chemical heat release rate relative to the baseline case (Run41) in Figure 5.7 are captured here for the RANS-LW model.

5.8.12 Run44

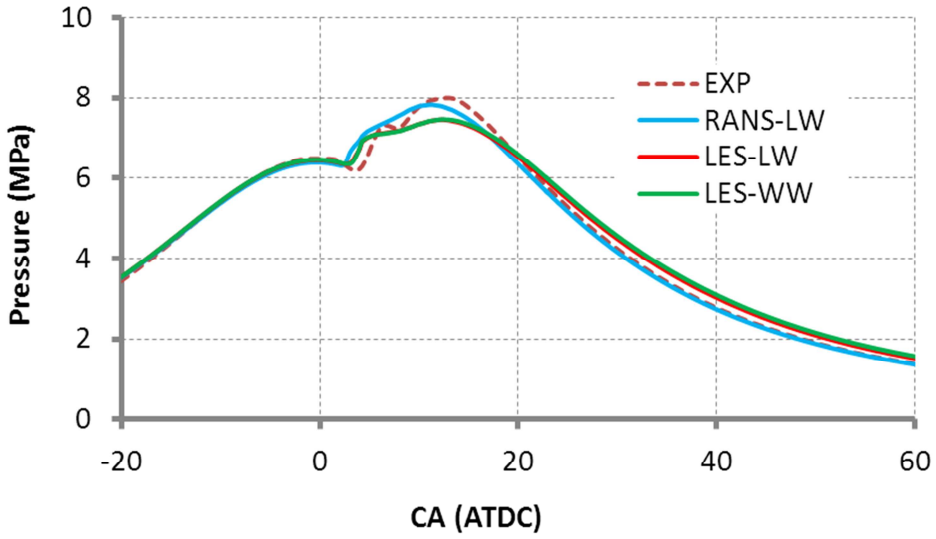

Figure 5.43 Comparisons of computed and measured cylinder pressure for Run44, with the start of injection at 0.91 degrees before TDC.

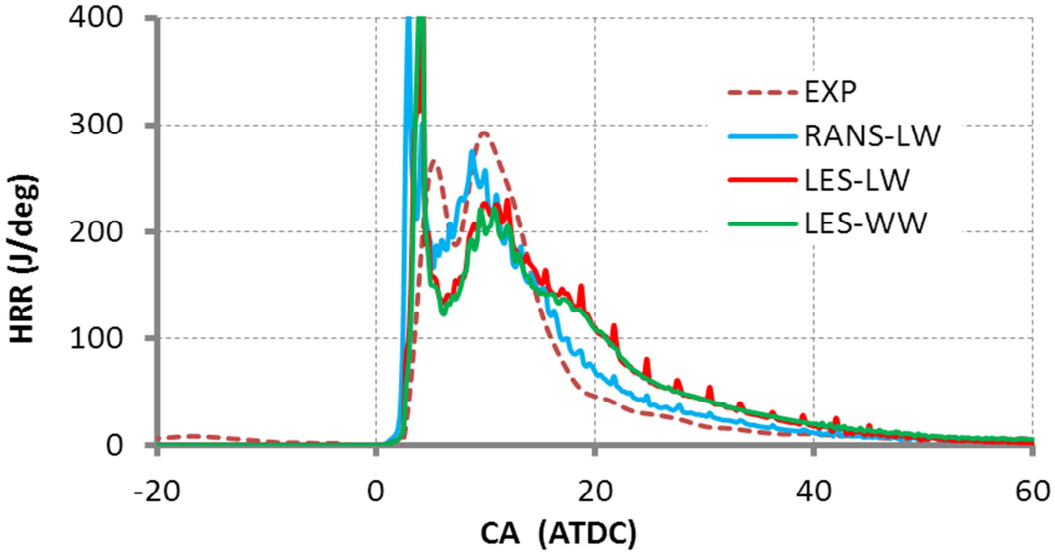

Figure 5.44 Comparisons of computed and measured chemical heat release rate for Run44, with the start of injection at 0.91 degrees before TDC.

The comparisons between the measured and computed in-cylinder pressure and heat release rates as predicted by the RANS-LW, LES-LW, and the improved LES-WW models are illustrated in Figures 5.43 and 5.44 for Run44, with an SOI of 0.91 degrees before TDC. A good agreeement in the pressure trace and phasing of ignition as predicted by the RANS-LW, LES-LW, and improved LES-WW models can be seen in Figures 5.43 and 5.44. Similar trends of chemical heat release rate relative to the baseline case (Run41) in Figure 5.7 are captured here for the RANS-LW model.

5.8.13 Run33

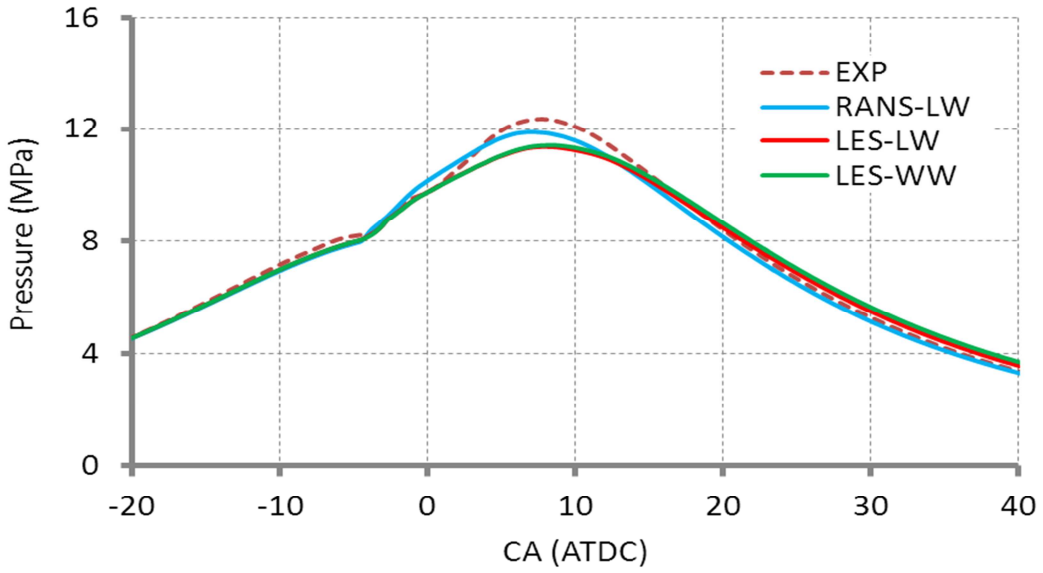

Figure 5.45 Comparisons of computed and measured cylinder pressure for Run33, with the start of injection at 7.20 degrees before TDC.

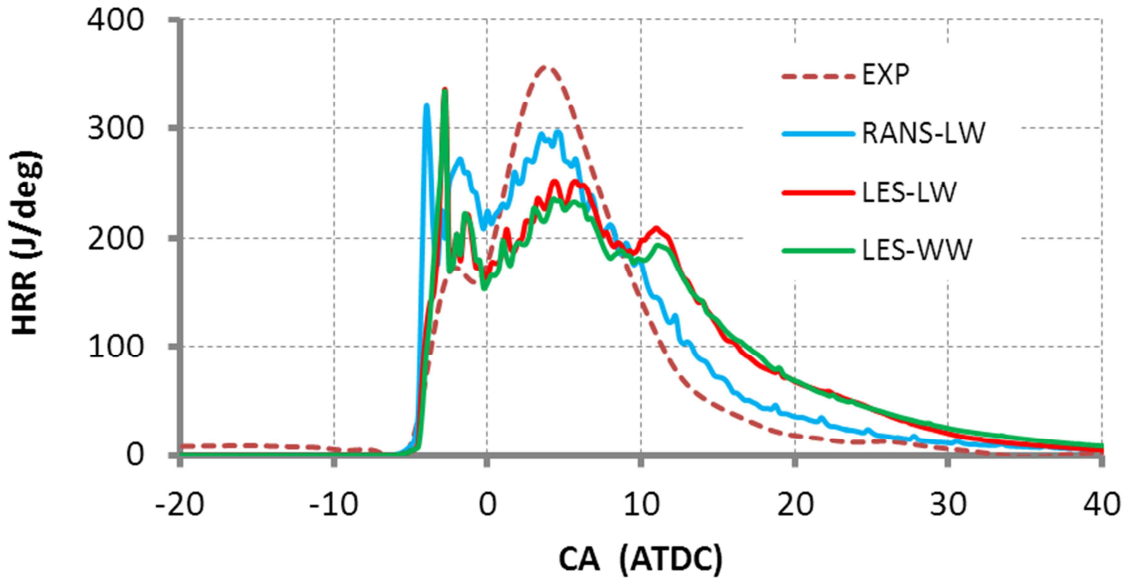

Figure 5.46 Comparisons of computed and measured chemical heat release rate for Run33, with the start of injection at 7.20 degrees before TDC.

The comparisons between the measured and computed in-cylinder pressure and heat release rates as predicted by the RANS-LW, LES-LW, and the improved LES-WW models are shown in Figures 5.45 and 5.46 for Run33, with an SOI of 7.20 degrees before TDC. A slight difference in the pressure trace from all three test models can be observed in Figure 5.45, while a good agreement in phasing of ignition can be seen in Figure 5.46. Similar trends of chemical heat release rate relative to the baseline case (Run41) in Figure 5.7 are captured here for the RANS-LW model.

5.8.14 Run36

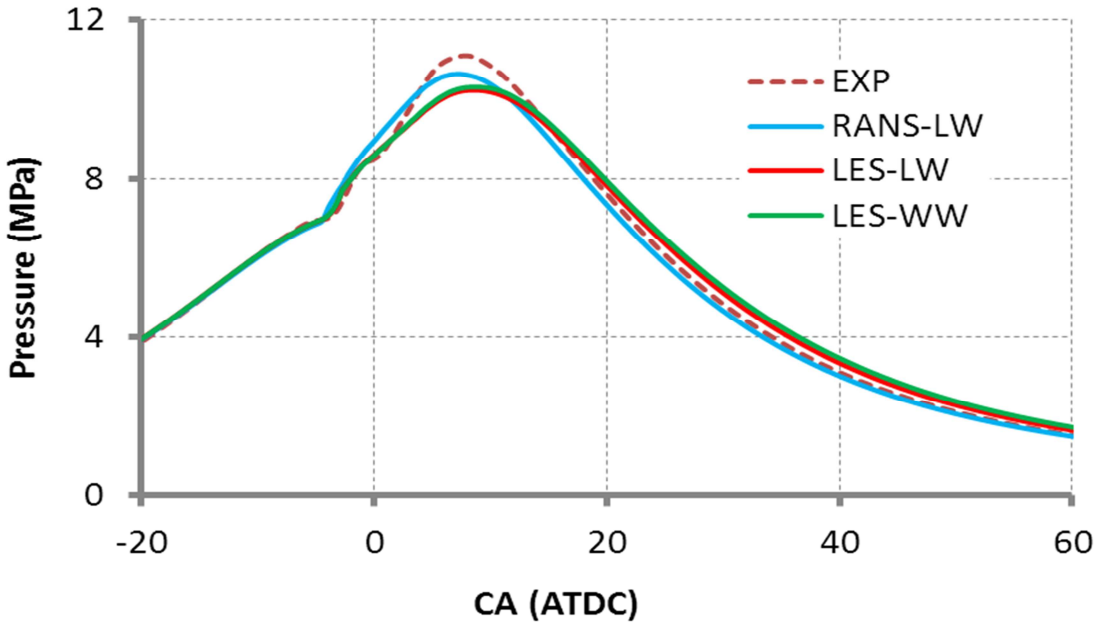

Figure 5.47 Comparisons of computed and measured cylinder pressure for Run36, with the start of injection at 7.40 degrees before TDC.

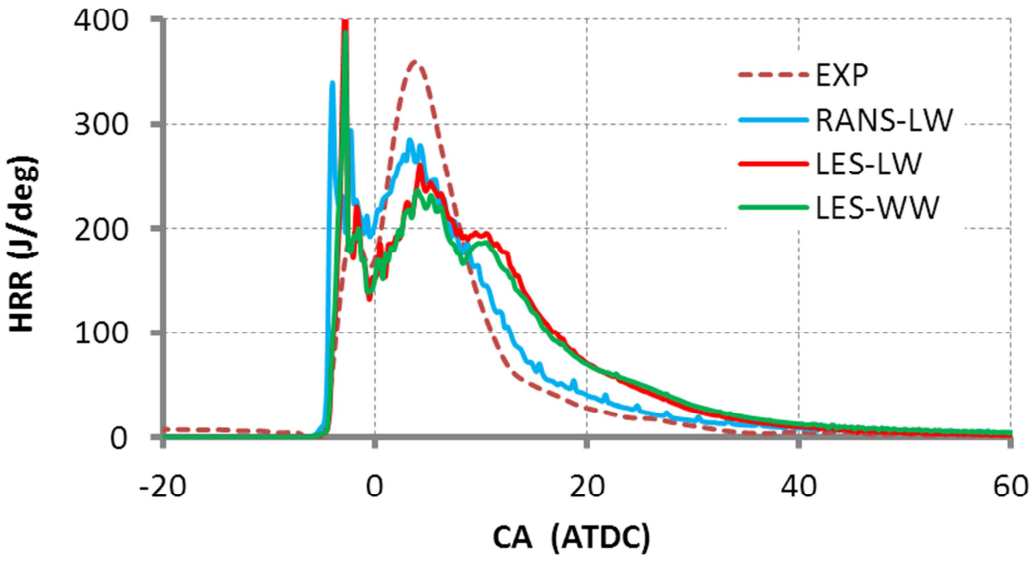

Figure 5.48 Comparisons of computed and measured chemical heat release rate for Run36, with the start of injection at 7.40 degrees before TDC.

The comparisons between the measured and computed in-cylinder pressure and heat release rates as predicted by the RANS-LW, LES-LW, and the improved LES-WW models are illustrated in Figures 5.47 and 5.48 for Run36, with an SOI of 7.40 degrees before TDC. A good agreeement in the pressure trace and phasing of ignition as predicted by the RANS-LW, LES-LW, and improved LES-WW models can be seen in Figures 5.47 and 5.48. Similar trends of chemical heat release rate relative to the baseline case (Run41) in Figure 5.7 are captured here for the RANS-LW model.

5.8.15 Run38

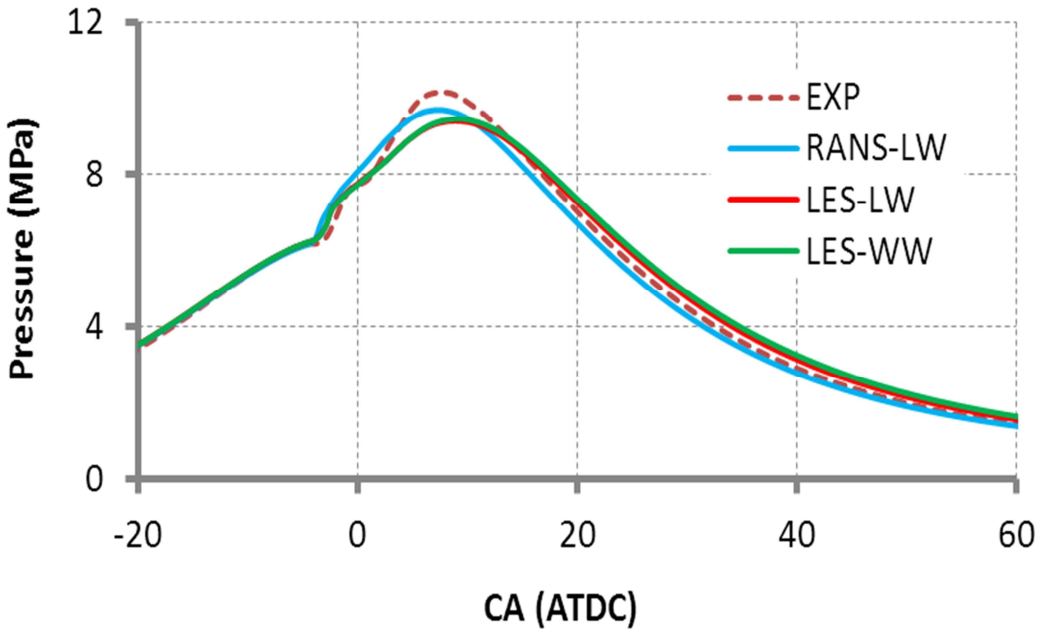

Figure 5.49 Comparisons of computed and measured cylinder pressure for Run38, with the start of injection at 7.40 degrees before TDC.

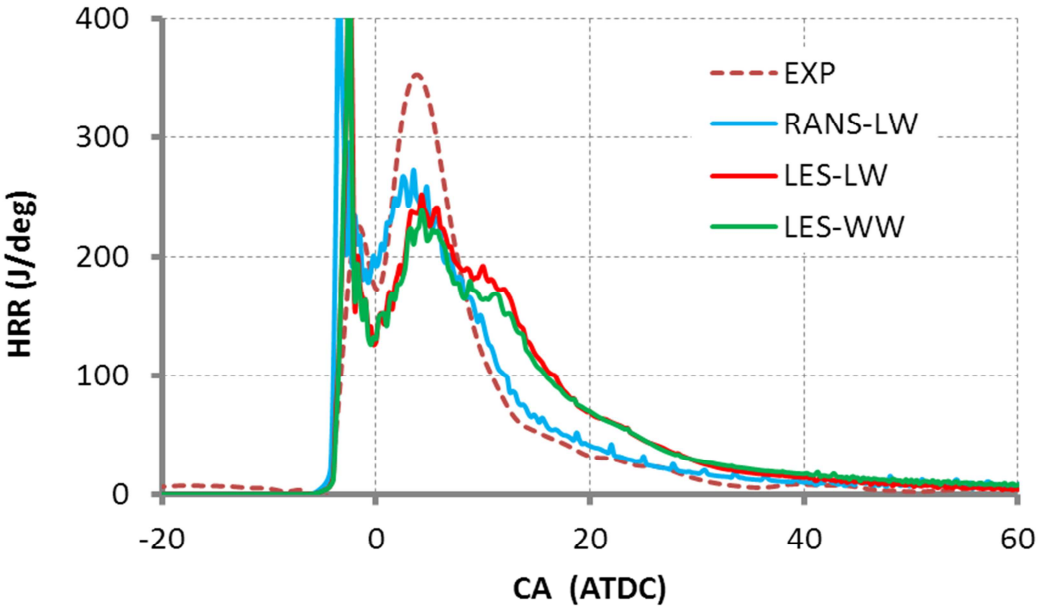

Figure 5.50 Comparisons of computed and measured chemical heat release rate for Run38, the start of injection at 7.40 degrees before TDC.

Figure 5.49 shows the comparisons of computed and measured cylinder pressure, while the comparisons of computed and measured chemical heat release rate are shown in Figure 5.50. For Run38, the start-of-injection timing was advanced to 7.40 before TDC. A good agreeement in the pressure trace and phasing of ignition as predicted by the RANS-LW, LES-LW, and improved LES-WW models can be seen in Figures 5.49 and 5.50. Similar trends of chemical heat release rate relative to the baseline case (Run41) in Figure 5.7 are captured here for the RANS-LW model.

5.9 Conclusion from comparisons of predicted heat fluxes and measurement data

In this section, because the overall trend for all cases is similar so data from Run41 (the baseline case) are chosen as representative. During the post-processing step in the present work, the predicted heat fluxes are stored in each wall surface within the computational domain, i.e., a 60° sector. The interpolation of those scalar heat flux quantities into the nearest nodes, which matched with the thermocouple locations reported in the literature, was employed.

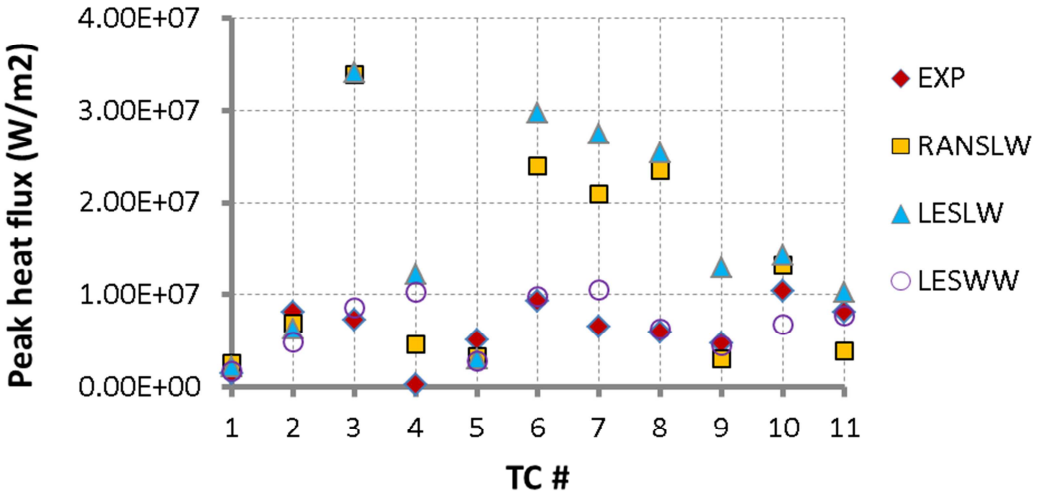

Figure 5.51 Peak heat flux in W/m^2 for each thermocouple location for Run41 as predicted by the improved LES-WW model.

Table 5.7 Summary of percent difference between the maximum computed heat fluxes as predicted by all tested models and experimental data for Run41

Diff (%)	TC #1	TC #2	TC #3	TC #4	TC #5	TC #6	TC #7	TC #8	TC #9	TC #10	TC #11
RANSLW	81	-15	371	0	-36	159	220	295	-36	28	-53
LESLW	51	-23	374	0	-40	222	322	328	176	37	26
LESWW	19	-40	18	0	-47	6	61	5	-6	-35	-5

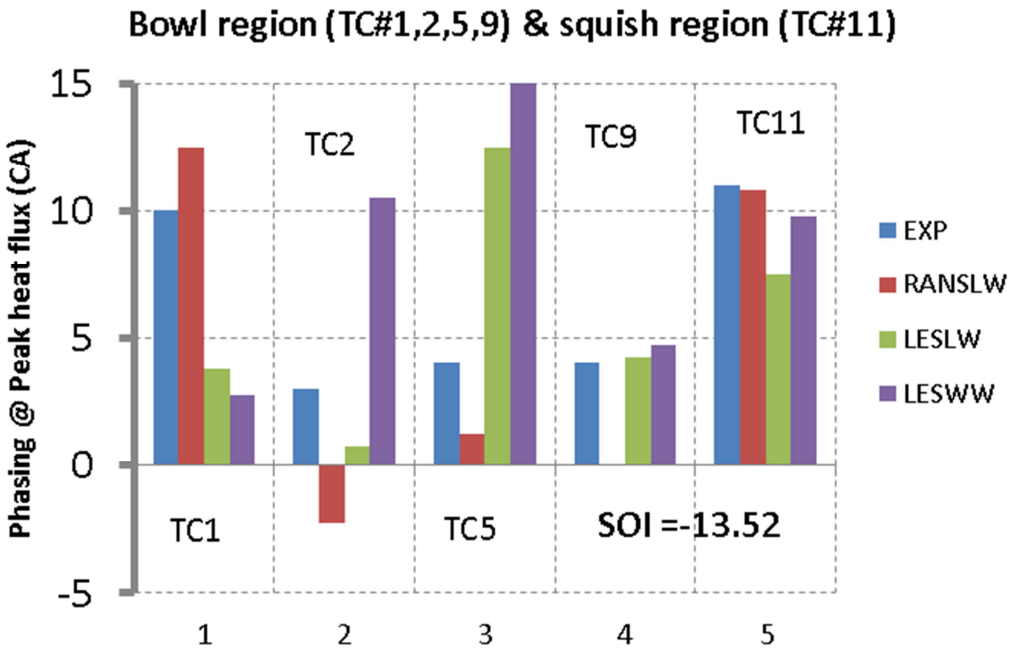

Figure 5.52 Comparisons of phasing at the maximum values of predicted heat flux at thermocouples located in bowl and squish regions for Run41

Figure 5.51 shows the magnitude of peak heat flux at each thermocouple location as predicted by each model and the experimental data for Run41, and the discrepancies of those results in percent can be seen in Table 5.7. One observation from Table 5.7 is that an extreme difference with experimental data occurred for the RANS-LW and LES-LW models at TC#3, TC#6, and TC#7, which were located on the primary spray axis. Also, the phasing at the maximum predicted heat flux compared with experimental data for all thermocouples is shown in Figures 5.52 and 5.53. A significant advance in the phasing at the maximum heat flux as predicted by all tested wall models can be seen at TC#3 and TC#6 in Figure 5.53.

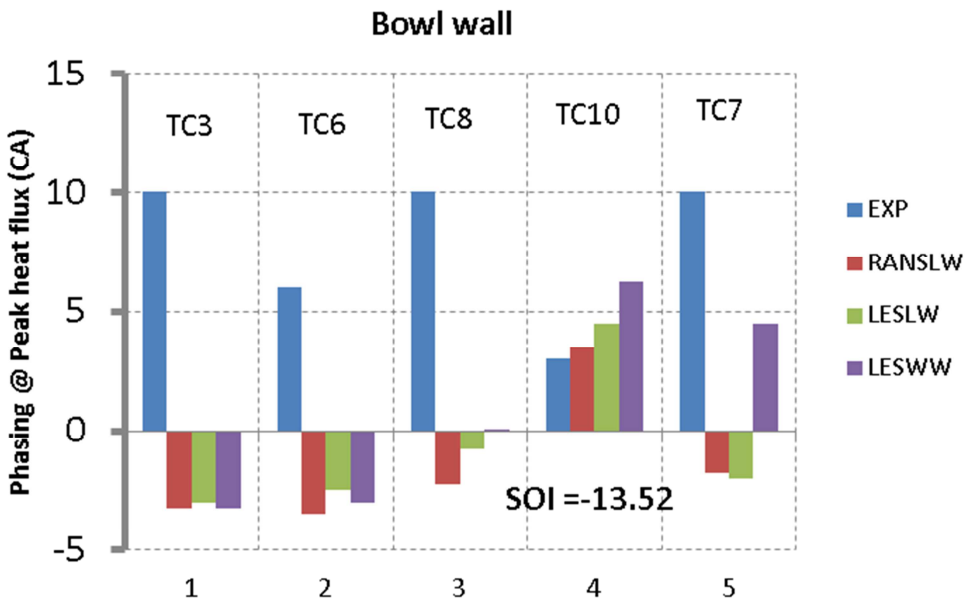

Figure 5.53 Comparisons of phasing at the maximum values of predicted heat flux and measurement data at thermocouples located on bowl walls for Run41

Based on predicted heat flux results from all engine test cases, which were listed in Table 5.5 and 5.6, the global trends of predicted heat flux results can be concluded as follows:

1) During the early compression stoke, the magnitude of heat flux is very small before the combustion occurs for all test cases.
2) The thermocouples TC#3 and TC#6, which were located on the primary spray axis at the bowl walls, always detect the heat flux rise first.
3) The magnitude of the peak heat flux at TC#3 and TC#6 as predicted by the improved LES-WW model agrees fairly well with experimental data, while the results from the RANS-LW and LES-LW are over-predicted. Also, the phasing of the maximum heat fluxes of those thermocouples is significantly advanced when compared with experimental data.

4) Similar to the trend for TC#6, the improved LES-WW model agrees fairly well with experimental data, while the results from the RANS-LW and LES-LW are over-predicted at thermocouple TC#7 and TC#8.
5) The magnitude of heat flux results as predicted by all models at thermocouple TC#1, which was located near the piston dome, are always the same order of magnitude as the experimental data.
6) For thermocouples TC#2, TC#5, and TC#10, the results of the improved LES-WW are always under-predicted, while fairly good agreement with the experimental data can be seen from the RANS-LW and LES-LW models.
7) A slight difference is observed between the predicted and experimental phasing at the maximum heat flux for TC#1, TC#10, and TC#11.
8) The magnitude of computed heat fluxes as predicted by the improved LES-WW model is in the range of typical measured values in diesel combustion, while most heat flux results from LES-LW are over-predicted.

5.10 Parametric study of diesel combustion operating variables

One objective of the present study is to explore the trend of heat flux results as predicted by the improved LES-WW model, which was simulated under conventional diesel combustion conditions. An engine speed sweep, SOI sweep, injection pressure sweep, equivalence ratio sweep, and engine load sweep are investigated in this section.

5.10.1 Engine speed (RPM) sweep

Table 5.8 Summary of selected test conditions for RPM sweep

	Run69	Run51	Run63
RPM	900	1300	1750
Pinj (MPa)	150	150	150
Load (bar)	14.89	15.49	15.11
Fuel (g/cycle)	0.1814	0.18659	0.18067
SOI	-6.01	-11.72	-16.59
ϕ	0.609817	0.598409	0.599361

For the engine speed sweep, cases with high load and rich equivalence ratio, Run69, Run51, and Run63, which were listed in Table 5.5 and 5.6, were chosen for simulations. Three engine speeds were investigated, i.e., 900, 1300 and 1750 RPM, while engine loads and equivalence ratios were held constant. In general, increases in engine speed result in an increase in heat flux for a given equivalence ratio and load. Figure 5.54 shows an example of speed scaling at the location of thermocouple TC#2, which was located in the bowl region. As can be seen in Figure 5.54, the magnitude of peak heat flux is higher at TC#2 when engine speed increases. Figure 5.55 shows experimental measurements of peak flux during engine speed sweep, while the peak heat flux predicted by the improved LES-WW model for each thermocouple location as a function of engine speed is shown in Figure 5.56. In theory, the speed scaling trend should hold over the entire range of data. The breakdown in the speed scaling relationship can be observed in Figures 5.55 and 5.56. The use of only eleven local data points (TC#1-TC#11) may not be enough to justify the speed scaling concept, and more sampling data should be investigated. Another observation is that this failure in speed scaling may come from the spray jets and their interaction with the moving piston (Hendricks, 2011).

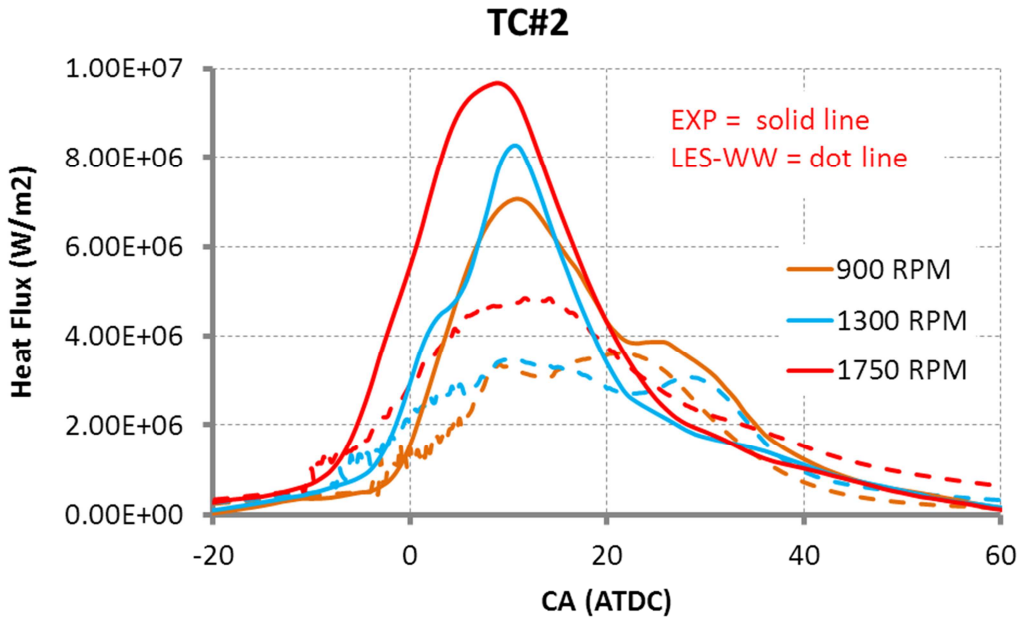

Figure 5.54 Comparisons of measured heat flux and computed heat flux as predicted by the improved LES-WW model during engine speed sweep at TC#2.

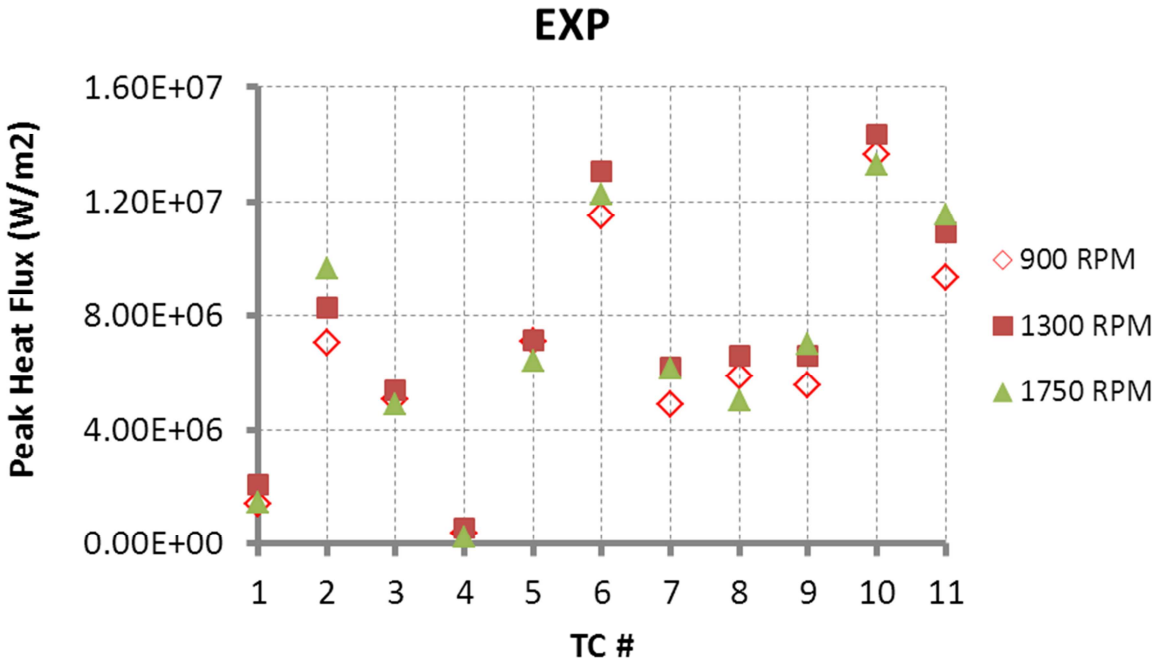

Figure 5.55 Experimental measurements of peak heat flux in W/m^2 at each thermocouple location for different engine speeds.

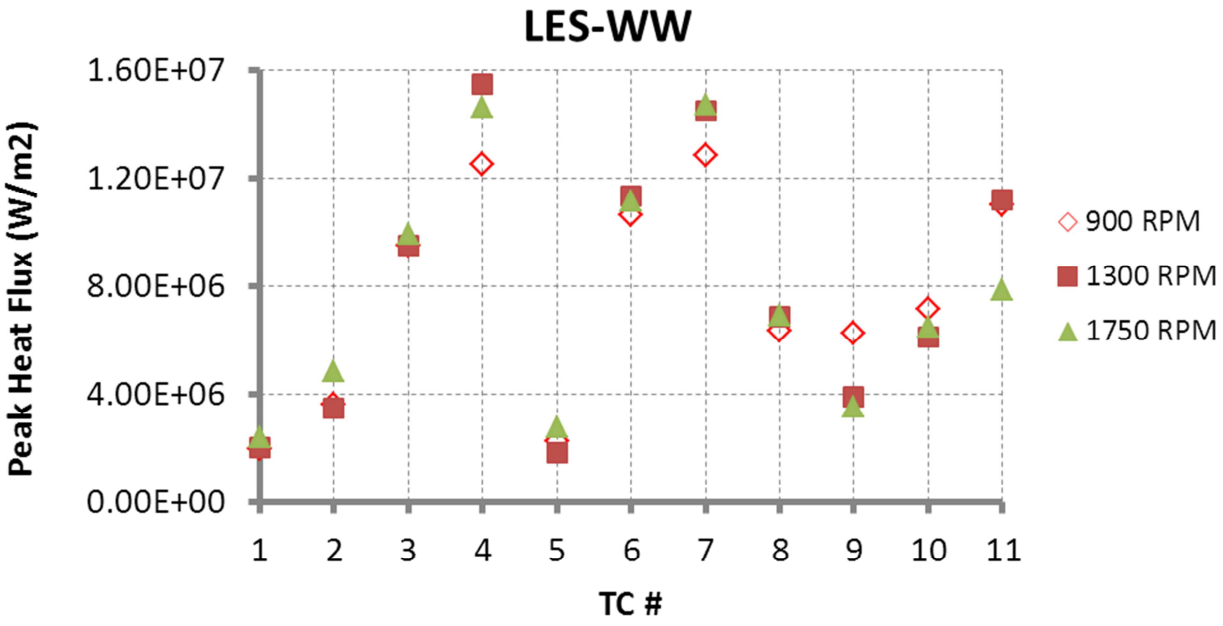

Figure 5.56 Peak heat flux in W/m^2 at each thermocouple location for different engine speeds as predicted by the improved LES-WW model.

5.10.2 SOI sweep

The baseline case (Run41), Run40, Run39, Run42, Run43 and Run 44 were selected for the SOI timing sweep investigation. Those conditions were summarized in Table 5.9. The engine load, engine speed, injection pressure and equivalence ratio were kept constant for this sweep. A range of SOI timing begins from partially premixed combustion (-13.52 ATDC) to more-mixing controlled combustion (-0.91 ATDC) regime. Experimental data of chemical heat release during SOI sweep as shown in Figure 5.57 for reference. In Figure 5.58, the computed chemical heat release rate as predicted by the improved LES-WW model during SOI sweep is illustrated. Also, Figures 5.59 and 5.60 show heat flux variation from experimental data and computed by the improved LES-WW model during the SOI timing sweep at the thermocouple location TC#6.

Similar trends of heat flux variation relative to the experimental data are captured here for the improved LES-WW model.

Table 5.9 Summary of selected test conditions for an SOI sweep

	Run41	Run40	Run39	Run42	Run43	Run44
RPM	1300	1300	1300	1300	1300	1300
Pinj(MPa)	150	150	150	150	150	150
Load(bar)	7.93	7.98	7.97	7.92	7.85	7.77
Fuel(g/cycle)	0.090	0.091	0.091	0.091	0.091	0.091
SOI	-13.52	-11.01	-8.40	-6.0	-3.51	-0.91
ϕ	0.390	0.388	0.388	0.388	0.384	0.386

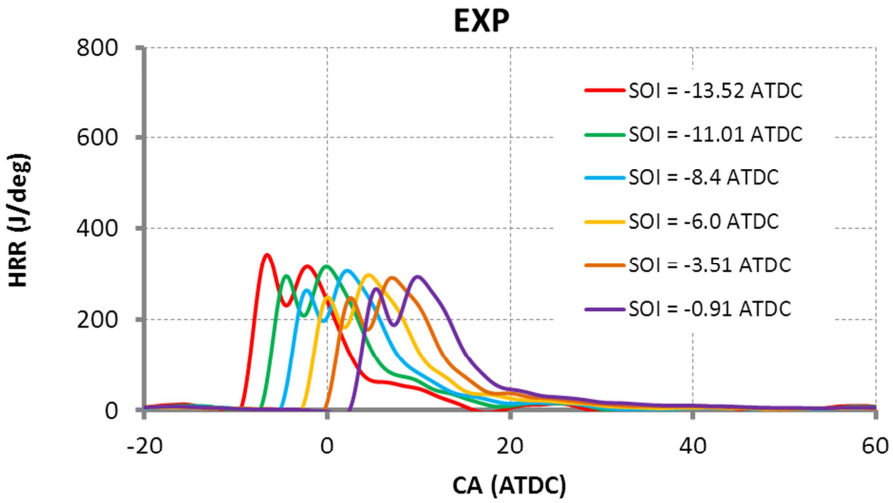

Figure 5.57 Experimental data of chemical heat release during SOI sweep

In Figure 5.58, the spike of computed chemical heat release rate decreases as the magnitude and duration of mixing controlled chemical heat release rate are the same when SOI timing is moved closer to the top dead center. The influence of premixed combustion decreases and finishes at SOI =-0.91° ATDC. In particular, the first spike of heat flux in Figure 5.60 completely disappears. For the mixing controlled combustion regime, the maximum peak heat

flux occurs at SOI = -8.4° ATDC, as seen in Figure 5.60. After that point, the peak heat flux begins to decrease. The combustion begins after the piston is already beyond the top dead center, so the hot gas is expanded and the bulk gas temperature is lower. This leads to the decrease in peak heat flux.

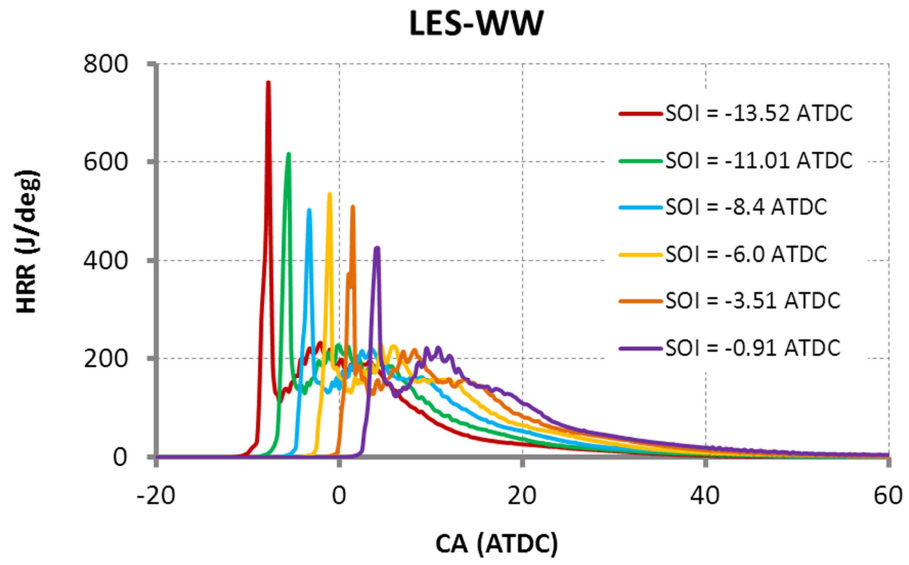

Figure 5.58 The computed chemical heat release during SOI sweep as predicted by the improved LES-WW model

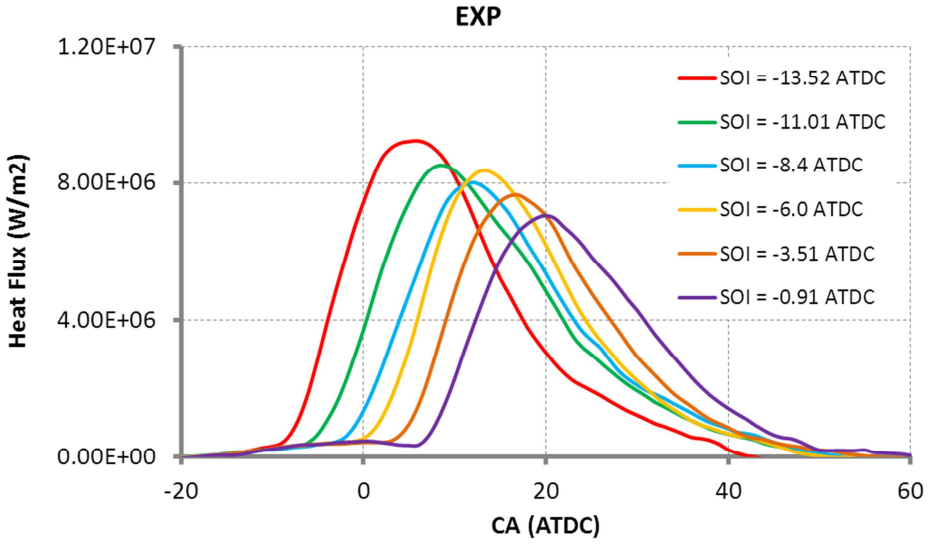

Figure 5.59 Experimental data of heat flux variation for an SOI timing sweep at the thermocouple location TC#6

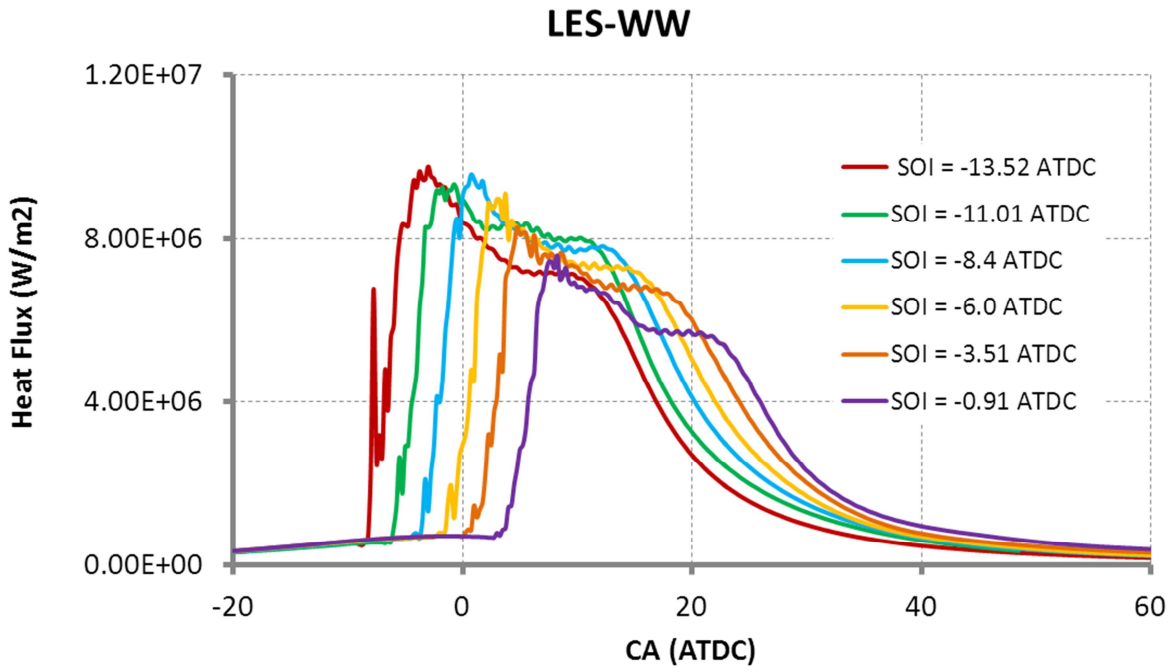

Figure 5.60 Heat flux variation for an SOI timing sweep at the thermocouple location TC#6 as predicted by the improved LES-WW model

5.10.3 Injection pressure sweep

The common rail injection pressure was swept at values of 60, 90, and 150 MPa. The test conditions of DOF38, DOF50, and DOF62 were selected for these simulations as shown in Table 5.10. The load and equivalence ratio were kept constant at about 9 bar and 0.60, respectively. Figure 5.61 shows experimental data of chemical heat release during the injection pressure sweep. Also, the computed chemical heat release as predicted by the improved LES-WW model during the injection pressure sweep is illustrated in Figure 5.62. Higher chemical heat release rate and shorter combustion duration with increasing injection pressure can be observed in Figures 5.61 and 5.62 for both premixed combustion and mixing-controlled combustion regimes.

Table 5.10 Summary of selected test conditions for the injection pressure sweep

	DOF38	DOF50	DOF62
RPM	1300	1300	1300
Pinj(MPa)	60	90	150
Load(bar)	8.75	9.07	9.75
Fuel(g/cycle)	0.12	0.12	0.12
SOI	-1.75	-2.70	-3.25
ϕ	0.60	0.61	0.60

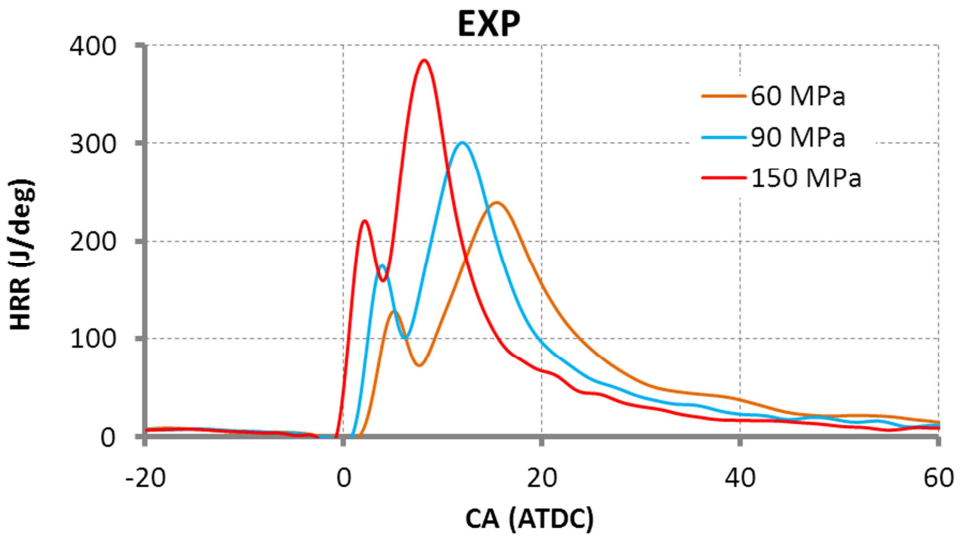

Figure 5.61 Experimental data of chemical heat release during the injection pressure sweep

With higher injection pressure, the same amount of liquid fuel is injected into a combustion chamber within a shorter period of time. As expected, the injection momentum increases. The level of turbulence is increased, resulting in higher heat flux results. Figure 5.63 shows an example of the injection pressure sweep as predicted by the improved LES-WW model at the location of thermocouples TC#9, which were located in the bowl region. Experimental heat flux measurement at TC#9 is included for the reference.

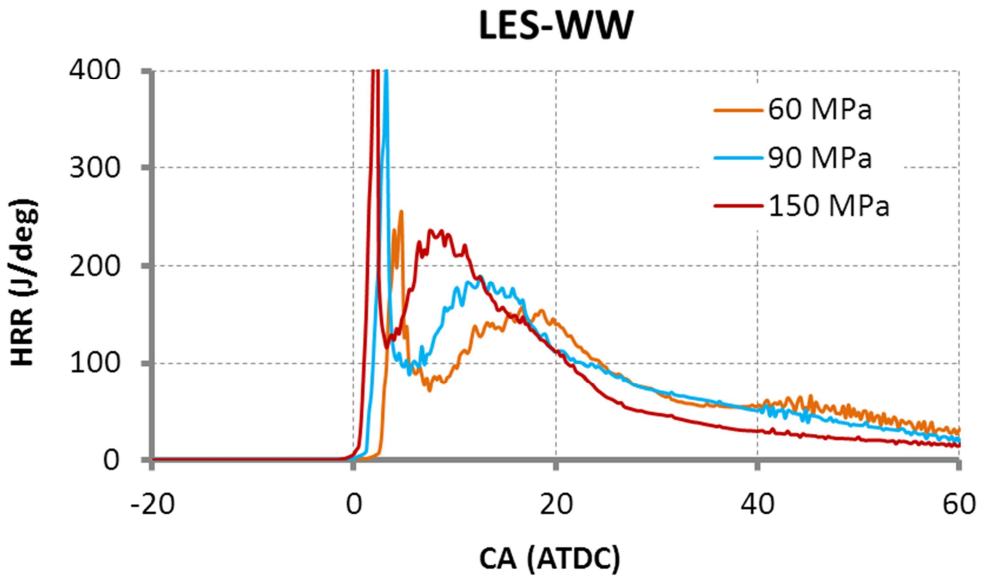

Figure 5.62 The computed chemical heat release as predicted by the improved LES-WW model during the injection pressure sweep

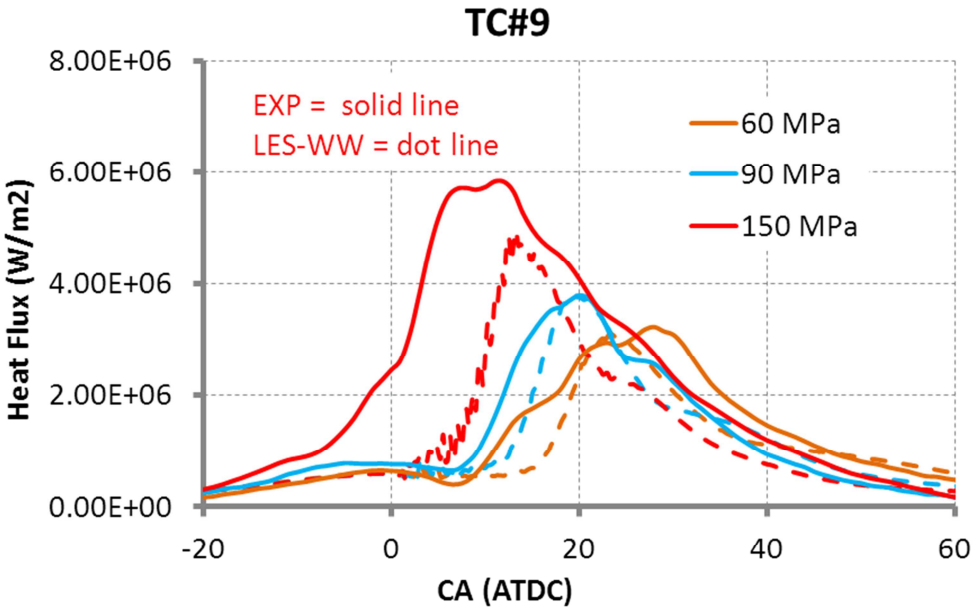

Figure 5.63 Comparisons of measured heat flux and computed heat flux as predicted by the improved LES-WW model during the injection pressure sweep at TC#9.

5.10.4 Equivalence ratio (φ) sweep

Table 5.11 Summary of selected test conditions for the equivalence ratio sweep

	Run33	Run36	Run38
RPM	1300	1300	1300
Pinj(MPa)	150	150	150
Load(bar)	9.34	9.29	9.08
Fuel(g/cycle)	0.1038	0.10593	0.10525
SOI	-7.20	-7.4	-7.4
ϕ	0.342	0.417	0.467
CA_{50}	4.52	4.73	4.92

For the equivalence ratio sweep, the intake air pressure was varied while the fueling rate, engine load, and 50% combustion timing point (CA_{50}) were kept constant as shown in Table 5.11. Experimental cases Run33, Run36, and Run38, which were listed in Table 5.6, were chosen for simulations. Three equivalence ratios were investigated, i.e., 0.342, 0.417 and 0.467. In general, the higher equivalence ratio increases the fuel enrichment.

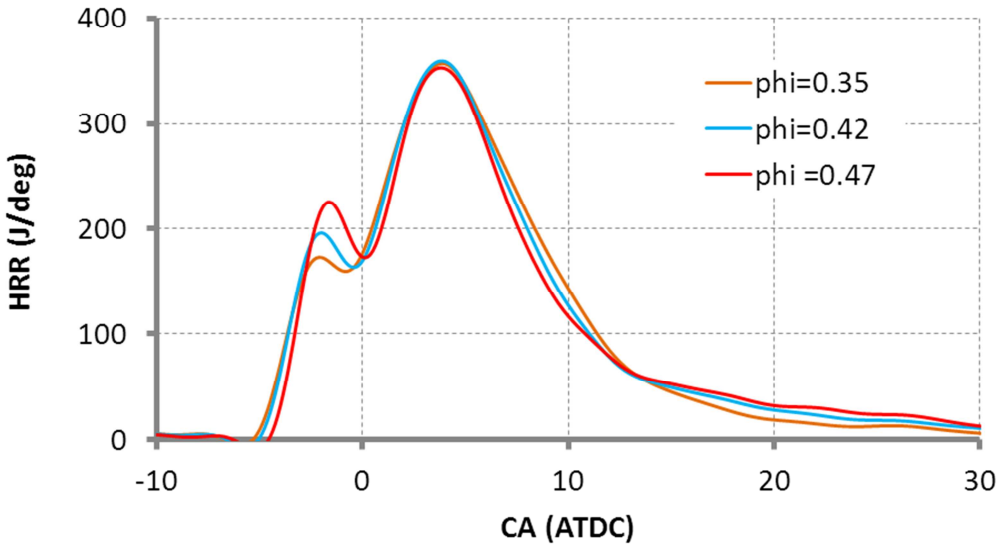

Figure 5.64 Experimental data of chemical heat release during the equivalence ratio sweep (line labels indicate the global equivalence ratio)

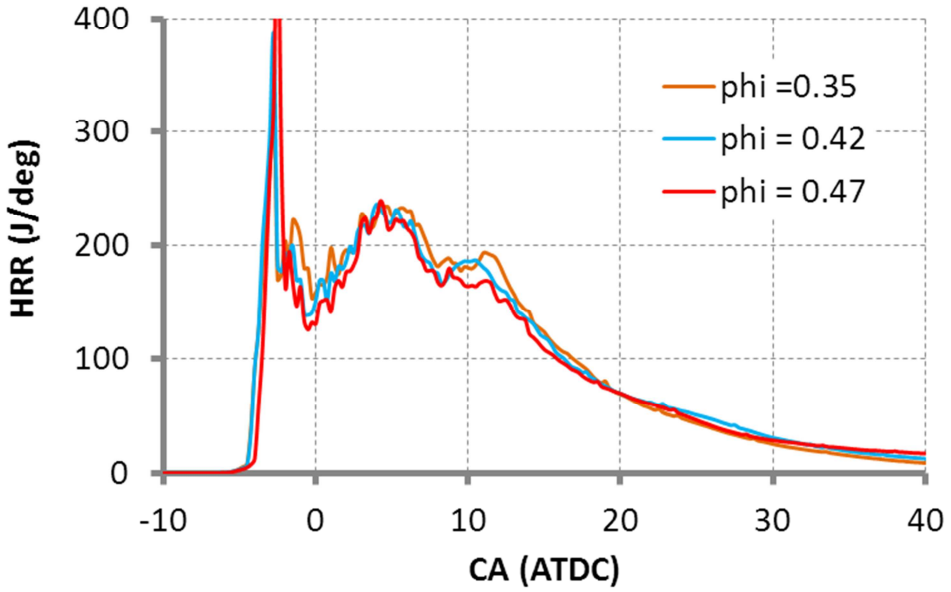

Figure 5.65 The computed chemical heat release as predicted by the improved LES-WW model during equivalence ratio sweep (line labels indicate the global equivalence ratio)

Since the diesel combustion always operates at lean fuel/air ratio with an equivalence ratio less than 1, increasing the equivalence ratio results in higher bulk temperature and heat transfer rate. Figure 5.64 illustrates experimental data of chemical heat release during the equivalence ratio sweep. Figure 5.65 shows the computed chemical heat release rate as predicted by the improved LES-WW model. It is observed that the heat release rate increases in the premixed combustion regime with equivalence ratio, while the magnitude and combustion duration of heat release rate in the mixing-controlled phase are the same. Figure 5.66 shows the equivalence ratio sweep at the location of thermocouples TC#9, which was located in the bowl region. Experimental heat flux measurement at TC#9 is included for the reference. Higher heat flux due to more fuel enrichment as predicted by the improved LES-WW model can be seen in Figure 5.66.

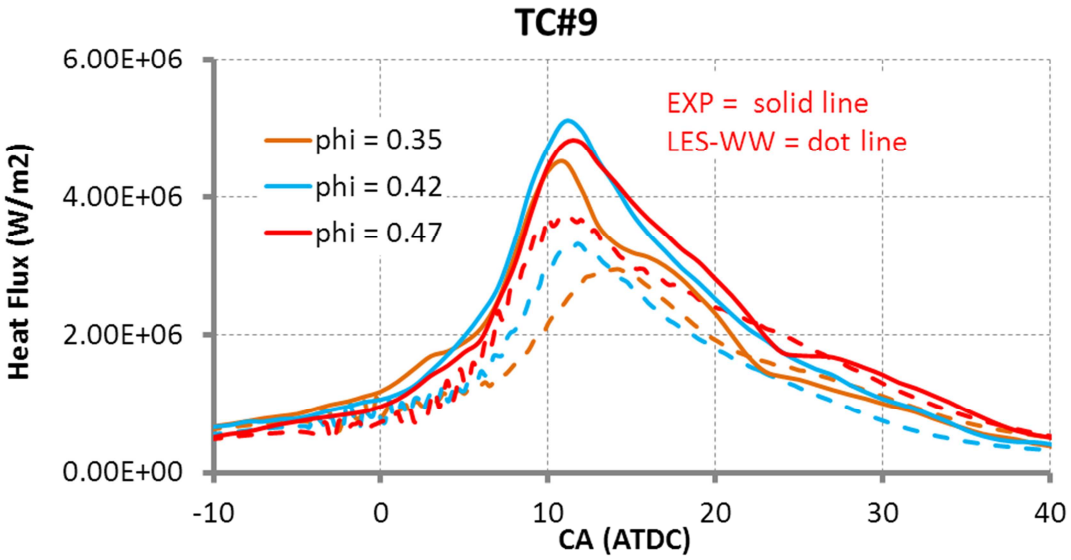

Figure 5.66 Comparisons of measured heat flux and computed heat flux as predicted by the improved LES-WW model at the thermocouple location TC#9 during the equivalence ratio sweep (line labels indicate the global equivalence ratio)

5.10.5 Engine load sweep

Nine different operating conditions listed in Table 5.12 were chosen to represent a wide variety of diesel combustion conditions. The equivalence ratio was chosen to be 0.6, and three engine speeds were investigated, i.e., 900, 1,300, and 1,750 RPM. In the engine load sweep, more fuel is injected into the combustion chamber and more induced air is also needed to maintain the equivalence ratio. Figures 5.67-5.72 show the chemical heat release from experimental data and computed by the improved LES-WW model at 900, 1,300, and 1750 RPM, respectively. Experimental data of chemical heat release rate is included for the reference. It is apparent that the magnitude and combustion duration within the premixed combustion is varied, but the heat release in the mixing-controlled regime increases with engine load. As a global trend, increased engine load generally results in an increase in heat flux for a given equivalence ratio and engine speed.

Table 5.12 Summary of selected test conditions for the engine load sweep

	DOF61	Run69	DOF64
RPM	900	900	900
Pinj(MPa)	150	150	150
Load(bar)	9.68	14.89	16.40
Fuel(g/cycle)	0.12	0.1814	0.20
SOI	-3.25	-6.01	-1.25
ϕ	0.605	0.610	0.594
	DOF62	Run52	Run51
RPM	1300	1300	1300
Pinj(MPa)	150	150	150
Load(bar)	9.75	12.44	15.49
Fuel(g/cycle)	0.12	0.1494	0.1866
SOI	-3.25	-9.42	-11.72
ϕ	0.601	0.609	0.598
	DOF27	Run62	Run63
RPM	1750	1750	1750
Pinj(MPa)	150	150	150
Load(bar)	10.11	12.51	15.1
Fuel(g/cycle)	0.12	0.1509	0.18067
SOI	-12.0	-15.1	-16.59
ϕ	0.603	0.60	0.60

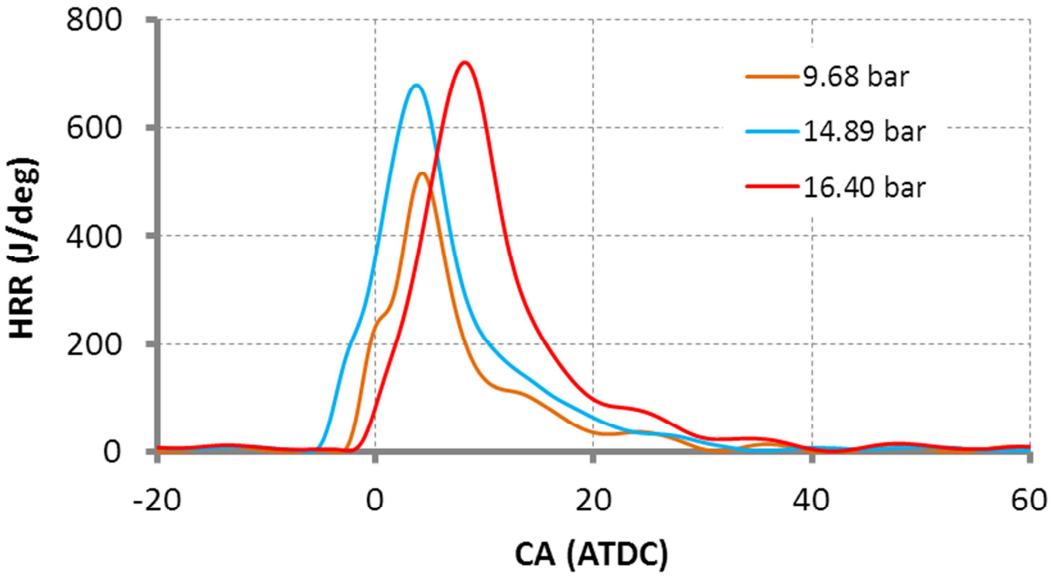

Figure 5.67 Experimental data of chemical heat release during the engine load sweep at 900 RPM

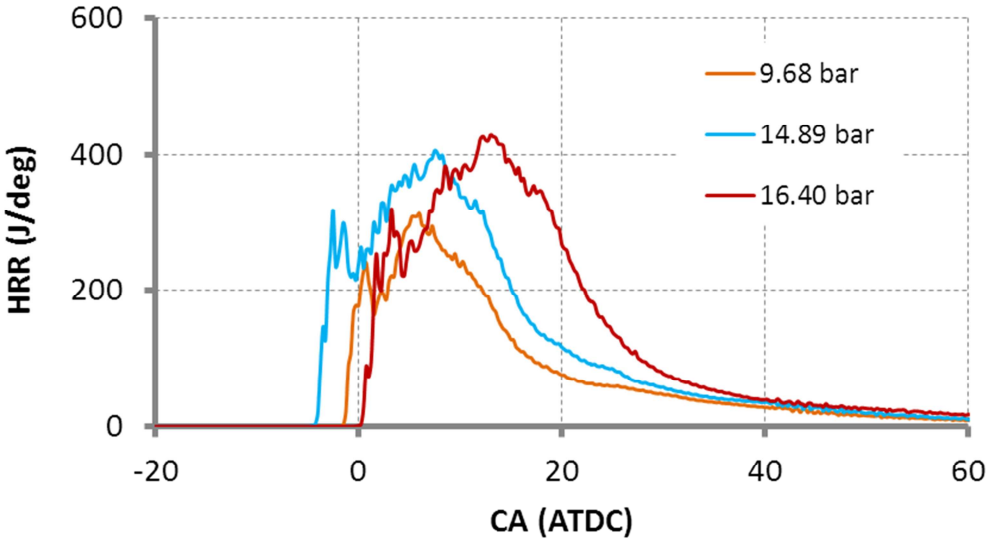

Figure 5.68 The computed chemical heat release as predicted by the improved LES-WW model during the engine load sweep at 900 RPM

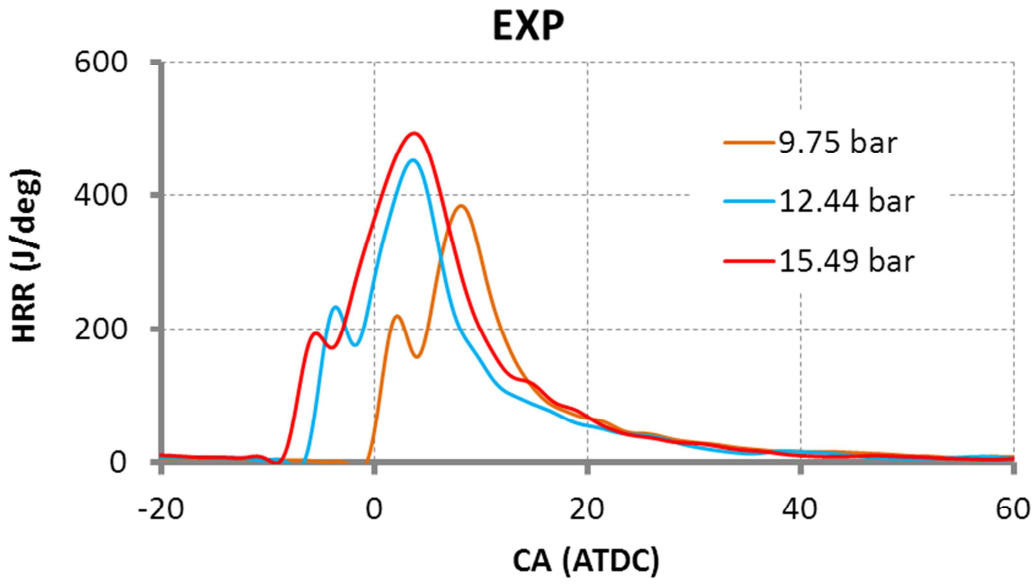

Figure 5.69 Experimental data of chemical heat release during the engine load sweep at 1,300 RPM

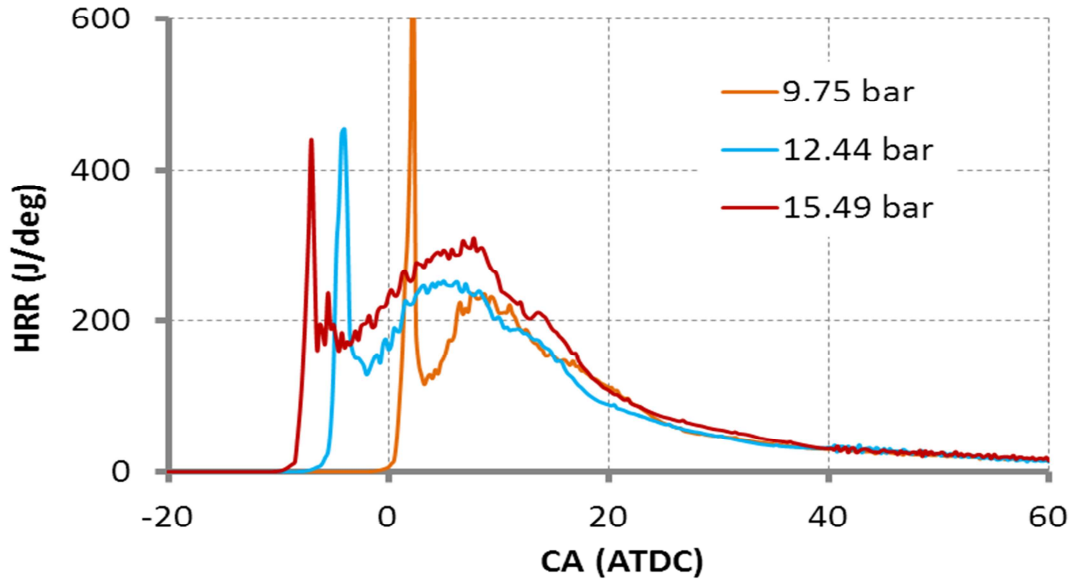

Figure 5.70 The computed chemical heat release as predicted by the improved LES-WW model during the engine load sweep at 1,300 RPM

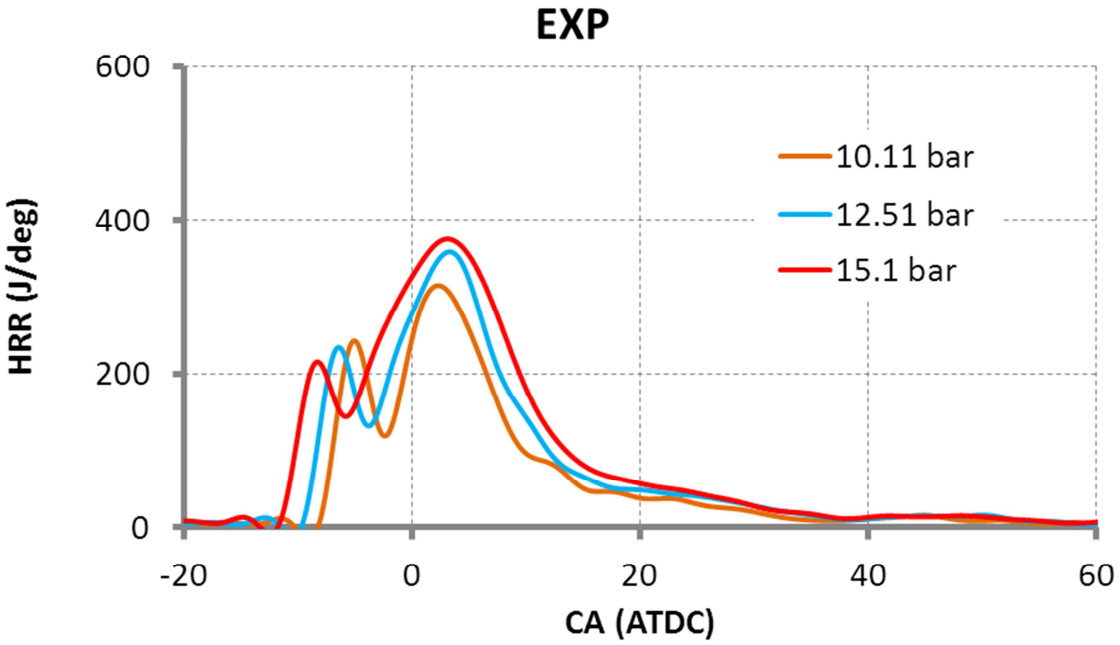

Figure 5.71 Experimental data of chemical heat release during the engine load sweep at 1,750 RPM

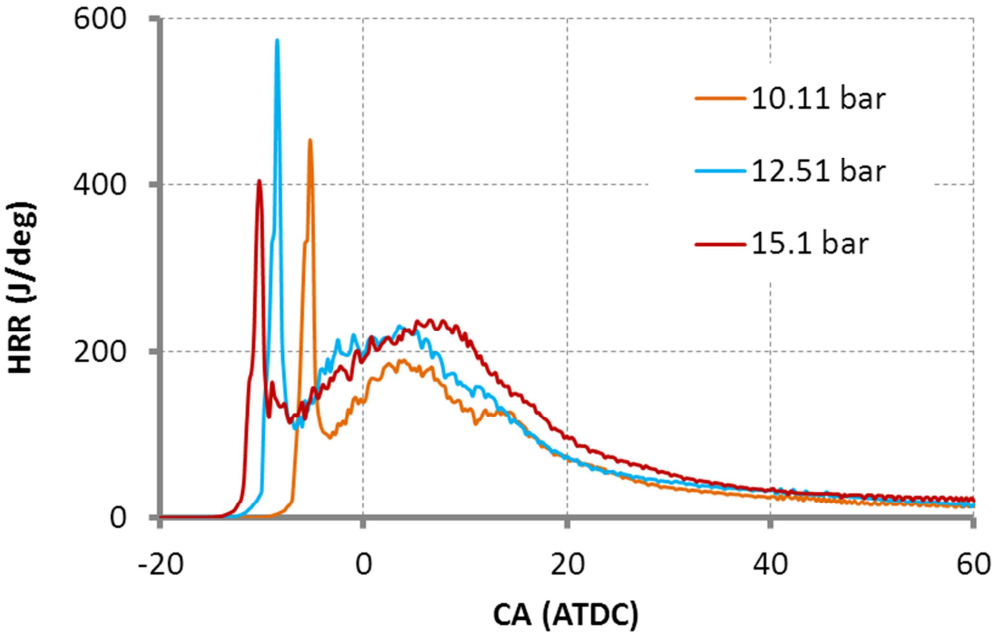

Figure 5.72 The computed chemical heat release as predicted by the improved LES-WW model during the engine load sweep at 1,750 RPM

Figures 5.74 and 5.75 show examples of load scaling as predicted by the improved LES-WW model at the location of thermocouple TC#6, which was located in the bowl wall. However, the breakdown of load scaling occurs at lower speed can be seen in Figure 5.73. In other words, at higher speed, the load scaling trends holds up well due to the increase in the rate of mixing controlled combustion, which is where the majority of heat release takes place. Experimental heat flux measurements at TC#6 are included for the reference.

In summary, because only a few data points of local heat flux results on the piston surface are available here, these results may be not enough to capture the global trends. The spray jet and piston movement may also affect to those heat fluxes. However, the heat flux results as predicted by the improved LES-WW model are able to capture the expected trends as shown in this section.

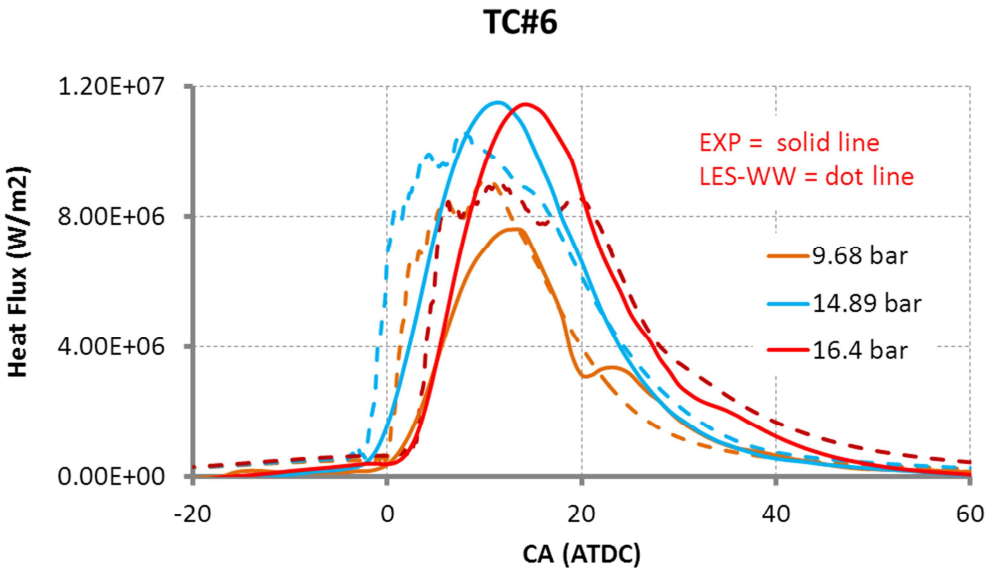

Figure 5.73 Comparisons of measured heat flux and computed heat flux as predicted by the improved LES-WW model at the thermocouple location TC#6 during the engine load sweep at 900 RPM

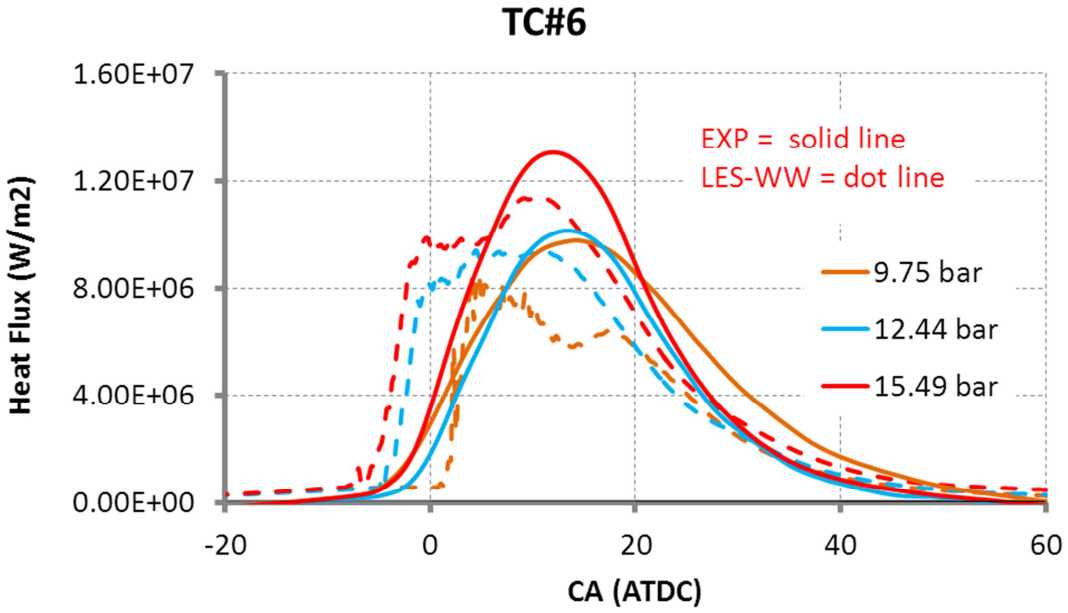

Figure 5.74 Comparisons of measured heat flux and computed heat flux as predicted by the improved LES-WW model at the thermocouple location TC#6 during the engine load sweep at 1,300 RPM

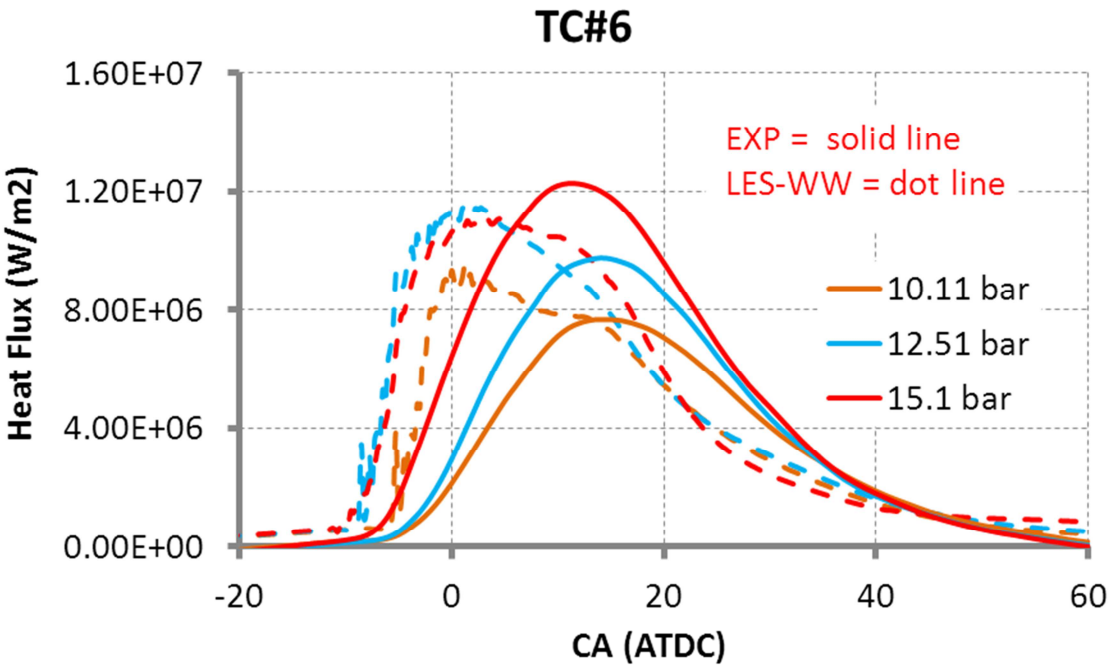

Figure 5.75 Comparisons of measured heat flux and computed heat flux as predicted by the improved LES-WW model at the thermocouple location TC#6 during the engine load sweep at 1,750 RPM

Chapter 6 Conclusions and future work

6.1 Conclusions

In the present work, improved wall shear stress and wall heat transfer models for LES simulation techniques were developed from the wall shear stress model by Werner-Wengle (1989) and wall heat transfer model by Han et al. (1997). These models were modified to better predict the shear stress and heat fluxes near walls in LES applications. The available experimental data from square duct flows were used to validate and determine the model constants of the improved LES-WW model. The friction factor and Nusselt number predictions were in good agreement with experimental results, and the resulting time- and spatially-averaged velocity and temperature wall functions from the new wall models matched well with the law-of-the-wall experimental data. In order to study the effect of hot air impinging on walls, jet impingement on a flat plate was also tested with the new wall models. The effect of the time-averaged friction coefficient and Nusselt number on the impingement was investigated.

Moreover, the model was validated using experimental data from a Caterpillar engine operated with conventional diesel combustion. Sixteen diesel engine conditions including the baseline case were simulated. In each case, the computational pressure and heat release were predicted well when compared with the experimental measurements. There was successful matching between the predicted and measured wall heat fluxes at ten points on the piston surface. Compared with the previous RANS-based wall models, the improved LES-WW model provided more accurate predictions and better agreement with experimental data.

These studies have given us much more confidence in the possibilities for further research on the improved engine wall models for large eddy simulation (LES).

6.2 Future work

In square duct flows, there is still much which needs to be explored. First, the direct numerical solution (DNS) data from square duct flows are required for the further validations. In particular, the details of the wall shear stress model could be evaluated using DNS results. The scatter plot of wall shear stress computed from DNS data and those from the RANS-LW, LES-LW, and improved LES-WW wall models should be investigated (DNS vs. RANS-LW, DNS vs. LES-LW, and DNS vs. improved LES-WW). The PDF of relative error from all tests could be compared.

Moreover, simulation runs should be performed with mesh refinement in order to check grid independence of the square duct flow results. The model of sub-grid scale eddy viscosity and the near-wall sub-grid scale turbulent kinetic energy should be studied in more detail. Also, the distribution of viscous shear stress, turbulent shear stress, and the total shear stress in square duct flows could be examined. The studies of two-point correlation coefficient and power spectra could also be included.

In order to obtain more confidence with the impinging jet, many tests should be conducted. The Reynolds number and the non-dimensional jet exit to surface ratio (H/D) should be varied while wall temperature will be kept constant. To validate, more available experimental data in the literature with constant wall temperature could be employed. The time-averaged Nusselt number and friction coefficient should be computed and compared with those experimental data. The proposed wall heat transfer model for LES in the present work may be modified in order to improve the predicted heat flux results near the stagnation point.

For the engine test cases, more engine conditions from different engines, i.e., a GM diesel engine should be simulated to obtain confidence in the heat flux results predicted by the

improved LES-WW model. For the combustion model, a spike over-prediction within the premixed combustion regime on the heat release curve should be studied in more detail. This spike may produce higher heat flux results on thermocouples TC#3 and TC#6, which were located on a primary spray plane. Because the predicted heat flux results are strongly dependent on the combustion model, a classic shell CTC combustion model is another option to check these higher spike effects.

Moreover, to save computational time, more efforts are required in parallel computation. A few subroutines in the KIVA engine code should be modified to be able to run parallel computations, and the computation time is expected to be reduced.

In addition, future efforts are expected to use GT-power in combination with the LES simulations. Accurate initial conditions of pressure and temperature for simulations will be needed, and GT-power may help in this regard.

References

Alexopoulos, C. C. (1964), “Temperature and Velocity Distributions and Heat Transfer for Turbulent Air Flow in a Square Duct”, M.A. Sc. Thesis, Dept. of mechanical Engineering , Univ. of Toronto, Toronto, Ontario, Canada

Alkidas, AC., (1980), “Heat transfer characteristics of a spark-ignition engine”, Trans ASME J. Heat Transfer, 102(2), pp.189-193

Amsden A. A., O'rourke P. J., et al. (1989), “KIVA II: A Computer Program for Chemically Reactive Flows with Sprays”, Los Alamos National Laboratory.

Angelberger, C., Poinsot, T., et al. (1997), "Improving Near-Wall Combustion and Wall Heat Transfer Modeling in SI Engine Computations", SAE Technical Paper 972881

Annand, W. J. D., (1963), “Heat Transfer in the Cylinders of Reciprocating Internal Combustion Engines”, Proceedings of the Institution of Mechanical Engineers, vol. 177, no.36, pp. 973-996

Balaras, E. and Benocci, C., (1994), “Subgrid-sclae models in finite difference simulations of complex wall bounded flows”, In: Applications of Direct and Large eddy simulation. AGARD CP551, pp. 2.1-2.5.

Balaras, E., Benocci,C., et al. (1996), “Two-layer approximate boundary conditions for large-eddy simulations”, AIAA Journal, 34, pp. 1111

Balint, J. L., Wallace, J. M., et al. (1991), “The velocity and vorticity vector fields of a turbulent boundary layer. Part2. Statistical properties”, J. Fluid Mech., 228, pp. 53-86

Banerjee, S., Liang, T., et al. (2010), “Validation of an LES Multi Mode Combustion Model for Diesel Combustion”, SAE Technical Paper 2010-01-0361

Banerjee, S. and Rutland, C. J., (2012), “Numerical Investigation of High Powered Diesel Mode Transition Using Large Eddy Simulations”, SAE Technical Paper 2012-01-0693

Baughn, J. and Shimizu, S., (1989), “Heat transfer measurements from a surface with uniform heat flux and an impinging jet”, ASME J. Heat Transfer, 111, pp. 1096-1098

Beale, J. C. and Reitz, R. D., (1999), “Modeling spray atomization with the Kelvin-Helmholtz/Rayleigh-Taylor hybrid model”, Atomization and Sprays, 9, pp.623-650

Bharadwaj, N., Rutland, C. J., et al. (2009), “Large eddy simulation modeling of spray-induced turbulence effects”, Int. J Engine Res., 10(2), pp. 97-119

Borman G., Nishiwaki K., (1987), “Internal-Combustion Engine Heat Transfer”, Progress in Energy and Combustion Science, Vol. 13. pp. 1-46

Bradshaw, P. and Huang, G. P. (1995), “The law of the Wall in Turbulent Flow”, Proc. R. Soc. London , Ser. A, 451, pp. 165-188

Breuer, M. , Jaffrezic, B., et al. (2008), “Hybrid LES-RANS technique based on a one-equation near-wall model”, Theor. Comput. Fluid. Dyn. , 22, pp. 157-187

Brundrett, E. and Baines, W. D. (1964), “The production and diffusion of vorticity in duct flow”, J. Fluid Mech., 19, pp. 375-394

Celik, I. B. and I. Yavuz, et al. (2001), “Large eddy simulations of in-cylinder turbulence for internal combustion engines: a review”, Int. J Engine Res. 2(2): pp. 119-148

Chang, J., Guralp, O., et al. (2004), “New Heat Transfer Correlation for an HCCI Engine Derived from Measurements of Instantaneous Surface Heat Flux”, SAE Technical Paper 2004-01-2996

Chapman, D.R. (1979), “Computational aerodynamics development and outlook”, AIAA Journal, 17, pp. 1293

Chieng, C. C. and Launder, B. E. (1980), “On the calculation of turbulent heat transport downstream from an abrupt pipe expansion”, Numer. Heat Transf., 3, pp. 189-207

Chumakov, S. G. and Rutland, C. J. (2004), “Dynamic structure models for Scalar Flux and Dissipation in Large-Eddy Simulation Model”, AIAA Journal, 42(6), pp. 1132-1139

Chumakov, S. G. and Rutland, C. J. (2005), “Dynamic structure subgrid-scale models for large eddy simulation”, Int. J. Numer. Meth. Fluids, 47, pp. 911-923

Colucci, D. and Viskanta, R. (1996), “Effect of nozzle geometry on local convective heat transfer to confined impinging air jet”, Expl Thermal Fluid Sci., 13, pp. 71-80

Cooper, D., Jackson, D., et al. (1993), “Impinging jet studies for turbulence model assessment-I Flow-field experiments”, Int. J. Heat and Mass Transfer, 36, pp. 2675-2684

Cziesla, T., Chattopadhyay, H., et al., (2001), “Large-eddy simulation of flow and heat transfer in an impinging slot jet”, Int. J. Heat and Fluid Flow, 22(5), pp. 500-508

Dao, K., Uyehara OA, et al. (1973), “Heat transfer rates at gas-wall interfaces in motored piston engine”, SAE Technical Paper 730632

Davidson, L. and Peng, S.H. (2003), “Hybrid LES-RANS modeling: a one-equation sgs model combined with a k-ω model for predicting recirculating flows”, Int. J. Numer. Meth. Fluids, 43, pp. 1003-1018

Deardorff, J. W., (1970), “A numerical study of three-dimensional turbulent channel flow at large Reynolds numbers”, J. Fluid Mech., 41, pp. 453

Eichelberg, G. (1939), “Some New Investigations on Old Combustion Engine Problems”, Engineering, vol. 148, pp.463-466 and 547-550

Emery, A. F., Neighbors, P. K., et al. (1980), “The numerical prediction of developing turbulent flow and heat transfer in a square duct”, J. Heat transfer, 102, pp. 51-57

Fujita,H. ,Yokosawa, H., et al. (1988), “Fully Developed Turbulent Flow and Heat Transfer in a Square Duct with Two Roughened Facing Walls”, Chemical Engineering Communications, 74, pp. 95-110

Gavrilakis, S., (1992), “Numerical simulation of low-Reynolds-number turbulent flow through a straight square duct”, J. Fluid Mech., 244, pp. 101-129

Geers, L., Hanjalic, K., et al. (2004), “Experimental investigation of impinging jet arrays”, Exps. Fluids, 36, pp. 946-958

Germano , M., Piomelli, U., et al. (1991), “A dynamic subgrid-scale eddy viscosity model”, Phys. Fluids A, 3(7), pp. 1760-1765

Gessner, F. B., Po, J. K., et al. (1979), “Measurement of developing turbulent flow in a square duct”, In Turbulent Shear Flows I, Springer, pp.119

Ghosal, S. and Moin, P. (1995), “The basic equations of the large eddy simulation of turbulent flows in complex geometry”, J. Comput. Phys., 118, pp. 24

Ghosal,S., Lund, T., et al. (1995), “A Dynamic Localization Model for Large-eddy Simulation of Turbulent Flows”, J. Fluid Mech., 286, pp.229-255

Gnielinski, V., (1976), Int. Chem. Eng., 16, 359

Goldstein, R. J., Behbahani, A. I., et al., (1986), “Streamwise Distribution of the Recovery Factor and the Local Heat Transfer Coefficient to an Imping Circular Air Jet”, Int. J. Heat and Mass Transfer, 21(8), pp. 1227-1235

Grotzbach, G. (1987), “Direct Numerical and Large Eddy Simulation of Turbulent Channel Flows”, in N. P. Cheremisinoff (ed.), Encyclopedia of Fluid Mechanics, Vol. 6, Gulf, pp. 1337-1391

Hadziabdic, M. and Hanjalic, K., (2008), “Vortical structure and heat transfer in a round impinging jet”, J. Fluid Mech., 596, pp. 221-260

Han, Z., Uludogan, A., et al. (1996), "Mechanism of Soot and NOx Emission Reduction Using Multiple-injection in a Diesel Engine", SAE Technical Paper 960633

Han Z., and Reitz R. D., (1997), “A temperature wall function formulation for variable-density turbulent flows with application to engine convective heat transfer modeling”, Int. J. Heat and Mass transfer, 40(3), pp. 613-625

Haworth, D.C., (1999), “Large-Eddy Simulation of In-Cylinder Flows”, Oil and Gas Science and Technology Rev., 54, No. 2, pp. 175-185

Hendricks, T., (2011), Ph.D. Thesis, Mech. Engr. Dept., UW-Madison

Heywood J.B. (1988), Internal Combustion Engine Automotive Technology Series. McGraw-Hill Book Company, New York.

Hoffman, G., Benocci, C., (1995), “Approximate wall-boundary conditions for large eddy simulations”, In: Benzi, R. (Ed.), Advances in Turbulence V. Kluwer Academic Publishers, pp.222-228

Hohenberg, G. F., (1979), “Advanced Approaches for Heat Transfer Calculations”, SAE Technical Paper 960633

Hu, B., Jhavar R., et al. (2007), “Combustion Modeling of Diesel Combustion with Partially-Premixed Conditions”, SAE Technical Paper 2007-01-0163

Huber, K., Woschni, G., et al. (1990), “Investigations on Heat Transfer in Internal combustion Engines under Low Load and Motoring Conditions”, SAE Technical paper 905018

Huh, K., Chang, I., and Martin, J., (1990), "A Comparison of Boundary Layer Treatments for Heat Transfer in IC Engines", SAE Technical Paper 900252

Huijnen, V. , Somers, L. M. T., et al. (2005), “Validation of the LES approach in Kiva-3V on a square duct geometry”, Int. Numer. Meth. Engng, pp. 1-12

Huser, A., and Biringen, S., (1993), “Direct numerical simulation of turbulent flow in a square duct”, J. Fluid Mech., 257, pp. 65-95

Isshiki, N. and Nishiwaki, N. (1970), “Study on Laminar Heat Transfer of Inside gas with Cyclic Pressure Change on an Inner Wall of a Cylinder Head”, Proceedings of the 4th International Heat Transfer Conference, FC3.5, pp. 1-10

Jambunathan, K., Lai, E., et al. (1992), “A Review of Heat Transfer Data for Single Circular Jet Impingement”, Int. J. Heat Fluid Flow, 13, pp. 106-115

Jhavar, R. and Rutland, C. J. (2006), “Using Large Eddy Simulations to study Mixing effects in Early Injection Diesel Engine Combustion”, SAE Technical Paper 2006-01-0871

Jennings, M.J. and Morel, T., (1990), “An improved near wall heat transfer model for Multi-Dimensional Engine Flow Calculations”, SAE Technical Paper 900251

Kays, W.M., (1994), “Turbulent Prantl Number-Where Are We?”, ASME J. Heat Transfer, Vol. 116, p. 284

Kee, R.J., Rupley, F.M., et al. (1989), “CHEMKIN-II: A FORTRAN Chemical Kinetics Package for the Analysis of Gas-Phase Chemical Kinetics”, Sandia Report, SAND 89-8009.

Kleemann, A. and Gosman, A., (2003), “Heat Transfer Sensitivity Study for an Advanced Diesel Engine”, SAE Technical Paper 2003-01-0561

Kojima, T. and Nishiwaki K., (1994), “Numerical analysis of heat transfer in heat insulated diesel engines”, Jpn SAE Rev, 15, pp.133-140

Krieger, R.B., and Borman, G. L., (1966), “The computation of Apparent Heat Release for Internal Combustion Engines”, ASME, Pap 66-WA/DGP-4

Launder, B. E. and Spalding D. B. (1974), “The numerical computation of turbulent flows”, Comput. Meth. Appl. Mech. Engng, 3, pp. 269

Launder, B. E. and Ying, W. M. (1973), “Prediction of flow and heat transfer in ducts of square cross-section”, Proc. Inst. Mech. Engrs. , 187, pp. 455-461

Lee, D. H., Chung, Y. S., et al. , (1995), “Heat transfer from a Flat Plate to a Fully Developed Axisymmetric Impinging Jet”, J. Heat Transfer, 117, pp. 772-776

Lytle, D. and Webb, B.W. (1991), “Secondary heat transfer maxima for air jet impingement at low nozzle-to-plate spacing”, In Experimental Heat Transfer, Fluid Mechanics and Thermodynamics (ed. J. F. Keffer, R. K. Shah & E. N. Ganic), Elsevier.

Madabhushi, R. K. and Vanka, S. P. (1991), “Large eddy simulation of turbulence-driven secondary flow in a square duct”, Phys. Fluids A, 3(11), pp. 2734-2745

Martin, H. (1977), “Heat and Mass Transfer Between Impinging Gas Jets and Solid Surfaces”, Adv. Heat Transfer, 13, pp. 1-60

Melling, A. and Whitelaw, J. H. (1976), “Turbulent flow in a rectangular duct”, J. Fluid Mech. Vol. 78, pp. 289-315

Menon, S., Yeung, P. K., et al. (1996), “Effect of subgrid models on the computed interscale energy transfer in isotropic turbulence”, Computers and Fluids, 25(2), pp. 165-180

Moin, P., Squires, K, et al. (1991), “A dynamic subgrid-scale model for compressible turbulence and scalar transport”, Phys. Fluids A, 11(3), pp. 2746-2757

Myong, H. K. (1991), “Numerical investigation of fully developed turbulent fluid flow and heat transfer in a square duct”, Int. J. Heat and Fluid Flow, 12(4), pp. 344-352

Nijeweme, DJO, Kok JBW, et al. (2001), “Unsteady in-cylinder heat transfer in a spark engine: experiments and modeling”, Proc Inst Mech Eng, Part D, J. Automob Eng, 215, pp. 747-760

Nikuradse, J. (1930), “Turbulence Stromung in nicht kreisformigen Rohren”, Ing. Arch. ,1, pp. 306-332

Nishino, K., Samada, M., et al., (1996), “Turbulence statistics in the stagnation region of an axisymmetric impinging jet flow”, Intl J. Heat Fluid Flow, 17, pp. 93-201

Novotny, J. L., Mccomas, S. T., et al. (1964), “Heat Transfer for Turbulent Flow in Rectangular Ducts With Two Heated and Two Unheated Walls”, AIChE J., 10, pp. 466-470

Nusselt, W. (1923), “Der Warmeubergang in der Verbrennungskraftmaschine (the Heat Transfer in the Internal Combustion Engine)”, V. D. I.Forschungsheft, 264

Overbye VD, Bennethum JE, et al. (1967), “Unsteady heat transfer in engines”, SAE Technical Paper 670931

Pallares, J., and Davidson, L., (2000), “Large-eddy simulations of turbulent flow in a rotating square duct”, Phys Fluids, 12, pp. 2878-2894

Park, H., Assanis, D., and Jung, D., (2009), "Development of an In-Cylinder Heat Transfer Model with Compressibility Effects on Turbulent Prandtl Number, Eddy Viscosity Ratio and Kinematic Viscosity Variation", SAE Technical Paper 2009-01-0702

Petuknov, B.S., in T. F. Irvine, et al. (1970) ,Eds., Advances in Heat Transfer, Vol. 6,Academic Press, New York

Piomelli, U., (1999), “Large-eddy simulation: achievements and challenges”, Progress Aero. Sci., 35, pp. 335

Piomelli, U. and Balaras, E. (2002), “Wall-layer models for large-eddy simulations”, Annual Review of Fluid Mechanics, 34, pp. 349-374

Piomelli, U., Balaras, E., et al. (2003), “The inner-outer layer interface in large-eddy simulations with wall-layer models”, Int. J. Heat and Fluid Flow, 24, pp. 538-550

Piomelli, U., Cabot W.H, et al. (1991), “Subgrid-scale backscatter in turbulent and transitional flows”, Phys. Fluid A: Fluid Dynamics, 3(7), pp. 1766

Piomelli, U., Ferziger, J., et al. (1989), “New Approximate Boundary Conditions for Large Eddy Simulations of Wall-Bounded Flows”, Physics of Fluids, Vol.1, No.6, pp. 1061-1068

Pomraning, E., (2000), “Development of Large Eddy Simulation Turbulence Models”, PhD Dissertation, University of Wisconsin-Madison

Pomraning, E., and Rutland, C.J. (2002), “A Dynamic One-Equation Non-Viscosity LES Model”, AIAA Journal, 44, pp. 689-701

Poulos, S. G., and Heywood, J. B., (1983), “The effect of chamber geometry on spark-ignited engine combustion”, SAE Technical Paper 830334

Ra, Y., Reitz, R., et al. (2006), “Effects of Piston Crevice Flows and Lubricant Oil Vaporization on Diesel Engine Deposits”, SAE Technical Paper 2006-01-1149

Rakopoulos, C. D., Kosmadakis, G. M., et al. (2010), “Critical evaluation of current heat transfer models used in CFD in-cylinder engine simulations and establishment of a comprehensive wall-function formulation”, Applied Energy, 87, pp. 1612-1630

Reitz, R., (1991), "Assessment of Wall Heat Transfer Models for Premixed-Charge Engine Combustion Computations", SAE Technical Paper 910267

Rutland, C. J., (2011), “Large-eddy simulations for internal combustion engines-a review”, Int. J Engine Res, 12(5), pp. 421-451

Sagot, B., Antonini, G. , et al. (2008), “Jet impingement heat transfer on a flat plate at a constant wall temperature”, Int. J. Thermal. Sci., 47, pp. 1610-1619

Schmidt, R. C., Kerstein, A. R., et al. (2003), “Near-wall LES closure based on one-dimensional turbulence modeling”, J. Comp. Phys., 186, pp. 317-355

Schumann, U., (1975), “Subgrid-scale models for finite difference simulations of turbulent flows in plane channels and annuli”, J. Comp. Phys., 18, pp. 376-404

Smagorinski, J., (1963), “General circulation experiments with primitive equations, I-the basic experiment”, Monthly Weather Rev., 91, pp.99-164

Spalart, P., Jou, W.-H., et al. (1997), “Comments of the feasibility of LES for wing and on the hybrid RANS/LES approach”, In: Advances in DNS/LES, 1st AFOSR Int. Conf. on DNS/LES. Greden Press.

Su, M.D. and Friedrich, R. (1994), “Investigation of fully developed turbulent flow in a straight duct with large eddy simulation”, ASME J. Fluid Eng., 116(4), pp. 677-684

Tummers, M. J., Jacobse J., et al., (2011), “Turbulent flow in the near field of a round impinging jet”, Int. J. Heat and Mass transfer , 54, pp. 4939-4948

Viskanta, R. (1993), “Heat transfer to impinging isothermal gas and flame jets”, Experimental Thermal Fluid Science, 6, pp. 111-134

Voke, P. R. and Gao, S. (1998), “Numerical study of heat transfer from an impinging jet”, Intl J. Heat and Mass Transfer, 41, pp. 671-680

Wang, M. (1999), “LES with wall models for trailing edge aeroacoustics”, Annual Research Briefs, Center for Turbulence Research, Stanford Univ., Stanford, CA, pp. 355-364

Wei, T., and Willmarth, W.W., (1989), “Reynolds-number effects on the structure of a turbulent channel flow”, J. Fluid Mech., 204, pp. 57-95

Werner, H. and Wengle, H., (1989), “Large eddy simulation of flow over a square rib in a channel”, In Proceedings of 7th Symposium on Turbulent Shear Flows, Stanford University, California, 21-23 August 1989, pp. 10.21-10.26

White, F. M. (2003), Fluid Mechanics, 5th Edition, McGraw-Hill, Inc., New York, NY.

Woschni, G. (1967), “A Universally Applicable Equation for the instantaneous Heat Transfer Coefficient in the Internal Combustion Engine”, SAE Technical Paper 670931

Yang, J. and Martin J. K. (1989), “Approximate Solution One-Dimensional Energy Equation for Transient, Compressible, Low Mach Number Turbulent Boundary Layers Flows”, J. Heat Transfer, Vol.111, pp. 619-624

Yang, J., Pierce, P., Martin, J., et al., (1988), “Heat Transfer Predictions and Experiments in a Motored Engine”, SAE Technical Paper 881314

Zhang, Y., and Rutland, C.J., (2011), “A mixing controlled direct chemistry (MCDC) model for diesel engine combustion modeling using large eddy simulation”, Combust Theor Model, 16(3), pp. 571-588

Appendix A-Simulation background

Many methods for simulating highly turbulent flows have been developed. Most of them can be characterized into three groups: Direct Numerical Simulation (DNS), Reynolds-Averaged Navier-Stokes equations (RANS), and Large Eddy Simulation (LES). First, all time scales and space scales in the flow field are resolved by the DNS method. The three-dimensional time-dependent Navier-Stokes equations are solved numerically without using turbulence models. This approach is very accurate and is appropriate for fundamental research. Due to the huge computational expense, this method can simulate only low Reynolds number with simple geometry applications. Alternately, for the traditional RANS simulations, only mean flow equations are resolved numerically by using a time-averaging process, while all large and small scales of turbulence are modeled. This averaging process tends to remove information regarding the local turbulent flow structure. Therefore, the RANS method may not be appropriate when it is employed in flows with strong local changes, such as flow inside the combustion chamber of internal combustion engines.

LES is one of the more sophisticated methods to simulate complex turbulent flows. The main concept is to solve spatially averaged motions of fluids, which is different from the RANS techniques. In LES, the large scale (grid size) motions which contain most of the kinetic energy of the flow are solved directly. Only small sub-grid scale motions (scale smaller than the grid size), which are believed to be more isotropic and universal in characteristics, are modeled. Because most of the energy of turbulence scales is solved in LES, the resolution is sufficient to capture more energetic large-scale fluctuations in the flow field than those of RANS simulation. In particular, more flow structures, eddies, and vortices are obtained from LES results (Rutland,

2011). Therefore, the turbulent simulation techniques based on LES may be more accurate when compared with RANS approach.

Appendix B-LES fundamentals

In LES, the flow field is separated into large-scale (resolved or filtered) and small scale (sub-grid) motion by filtering (spatially averaging) local flow variables. For any flow variable ϕ, the filtered value $\bar{\phi}$ can be written in terms of a convolution integral as

$$\bar{\phi}(\vec{x},t) = \int_V G(\vec{x}-\vec{y})\phi(\vec{x},t)d\vec{y} \tag{B.1}$$

The term $G(\vec{x}-\vec{y})$ is the filtering function, which is defined for the convolution operation on any flow variable ϕ and must satisfy the normalization condition as follows

$$\int_V G(\vec{x}-\vec{y})d\vec{y} = 1 \tag{B.2}$$

In other words, the filtering function $G(\vec{x}-\vec{y})$ is a kernel which is designed to damp out the fluctuations with a characteristic scale smaller than a filter width $\bar{\Delta}$. Commonly, the filter functions may be the box filter, which represents a weighted average in the physical space. It is defined as

$$G(\vec{x}) = \begin{cases} 1/\bar{\Delta} & if \ \left|\vec{x}\right| \le \bar{\Delta}/2 \\ 0 & otherwise \end{cases} \tag{B.3}$$

With this decomposition technique, a sub-grid part ϕ' of the local variable ϕ is introduced in the form

$$\phi' = \phi - \bar{\phi} \tag{B.4}$$

The resolved part relates to the large-scale flow motions and the sub-grid part relates to the small-scale flow motions. However, one important thing is that these LES decompositions of resolved and sub-grid scale should not be confused with the RANS decomposition of mean and fluctuating values.

Moreover, the LES method can be applied to any conservation equation (Moin et al., 1991). For reacting flows, the governing equations are conservation of mass, momentum, energy, and species, along with the ideal gas equation of state. In turbulent combustion, the density may vary significantly due to temperature change. This leads to an invalidation of the incompressible flow assumption which was used to derive the standard LES equations. Therefore, in order to account for density changes, a density weight filter operation (LES Favre average) is employed and indicated as follows

$$\tilde{\phi} = \frac{\overline{\rho\phi}}{\bar{\rho}} \tag{B.5}$$

Therefore, a Favre average flow variable is represented by $\tilde{\phi}$, while the sub-grid term is ϕ'' and is defined by

$$\phi'' = \phi - \tilde{\phi} \tag{B.6}$$

By applying the density-weighted LES spatial filtering operation on the Navier-Stokes equation and continuity equation, the governing equations for the large (resolved) scales are obtained. Equation (B.7) is the LES filtered continuity equation.

$$\frac{\partial \bar{\rho}}{\partial t} + \frac{\partial \bar{\rho}\tilde{u}_i}{\partial x_i} = 0 \tag{B.7}$$

The LES filtered momentum equation is given by

$$\frac{\partial \overline{\rho}\widetilde{u}_i}{\partial t}+\frac{\partial \overline{\rho}\widetilde{u}_i\widetilde{u}_j}{\partial x_j}=-\frac{\partial \overline{p}}{\partial x_i}+\frac{\partial}{\partial x_j}\left(\mu\frac{\partial \widetilde{u}_i}{\partial x_j}\right)-\frac{\partial \overline{\rho}\Gamma_{ij}}{\partial x_j} \tag{B.8}$$

These equations show the transport of the filtered velocity and contain additional terms that are located on the third term in the right hand side. This term represents the effect of the small scales (sub-grid) on the large scale flow motions (resolved scales). It is known as the sub-grid stress tensor (SGS) and is defined by

$$\Gamma_{ij}=\left(\overline{u_iu_j}-\bar{u}_i\bar{u}_j\right) \tag{B.9}$$

Because the sub-grid shear stress cannot be directly solved, as mentioned above, this term must be modeled to provide the approximate value of the actual sub-grid scale stress tensor. In general, the results of the LES method strongly depend on the filter width (filter length), which is a function of the local cell size of the computational grid. The filter length scale $\overline{\Delta}$ from the CFD grid is defined using the local CFD cell volume (Vol_{cell}) as follows

$$\overline{\Delta}=\left(vol\right)^{0.333} \tag{B.10}$$

The actual sub-grid stresses may also transfer energy from the sub-grid scale to the large scale in the backscatter phenomena (Piomelli et al., 1991). Therefore, those models may not effectively capture the real turbulence motion, and the backscatter effect should be taken into account. To overcome the backscatter limitation, the sub-grid kinetic energy (k_{sgs}) is introduced. A transport equation is also added to the dynamic model, as mentioned above, to ensure an energy budget between the resolved scale and SGS fluid motions (Menon et al., 1996). The SGS kinetic energy (k_{sgs}) is defined by

$$k_{sgs} = \frac{1}{2}\left(\overline{u_i u_i} - \overline{u}_i \overline{u}_i\right) \tag{B.11}$$

Also, the transport equation for $\left(k_{sgs}\right)$ is formulated from the momentum equation (Pomraning, 2000) and given by

$$\frac{\partial \overline{\rho}\, k_{sgs}}{\partial t} + \frac{\partial \overline{\rho}\, \widetilde{u}_i k_{sgs}}{\partial x_i} = -\overline{\rho}\, \Gamma_{ij} \widetilde{S}_{ij} - \overline{\rho} \varepsilon_{sgs} + \frac{\partial}{\partial x_i}\left(\mu_{tk} \frac{\partial k_{sgs}}{\partial x_i}\right) \tag{B.12}$$

The SGS dissipation rate (ε_{sgs}) and eddy viscosity term (μ_{tk}) are obtained from the scaling argument using k_{sgs} and the filter length scale $\overline{\Delta}$ (Ghosal et al., 1995 and Menon et al., 1996)

$$\varepsilon_{sgs} = \frac{c_\varepsilon k_{sgs}^{1.5}}{\overline{\Delta}} \tag{B.13}$$

$$\mu_{tk} = c_k \overline{\rho}\, \overline{\Delta}\, k_{sgs}^{0.5} \tag{B.14}$$

The constants C_k and C_ε are set to 0.05 and 0.3, respectively. A one-equation non-viscosity dynamic structure model (DSM) was developed by Pomraning et al. (2002). This model scales linearly with the ratio of the SGS kinetic energy over the trace of the Leonard stress term, while the tensor directions of SGS stress aligns with Leonard stress. It can be written in form

$$\Gamma_{ij} = 2k_{sgs}\left(\frac{L_{ij}}{L_{kk}}\right) \tag{B.15}$$

Moreover, a priori studies of LES with the dynamic structure model in fundamental flow configurations agrees well with DNS and experimental studies (Pomraning et al., 2002 and Chumagov et al., 2004). Also, several studies show that DSM can give excellent predictions of

engine in-cylinder flows (Jhavar et al., 2006; Hu et al., 2007; and Banerjee et al., 2010). Therefore, to obtain better results, the dynamic structure model is used in the research to model the sub-grid stress tensor. In addition to mass and LES momentum conservation equations, an LES energy equation and equation of state are required. A perfect gas behavior is assumed and the filtered ideal gas equation of state is (Moin et al., 1991)

$$\overline{p} = R\overline{\rho T} = R\overline{\rho}\widetilde{T} \tag{B.16}$$

One should notice that the decomposition techniques are not applied to the pressure and density field. Also, the energy equation can be filtered as

$$\frac{\partial\left(\overline{\rho}\,\widetilde{h}\right)}{\partial t} + \frac{\partial\left(\overline{\rho}\,\widetilde{u}_j\widetilde{h}\right)}{\partial x_j} = -\frac{\partial\overline{p}}{\partial t} - \frac{\partial\left(\overline{q}_j\right)}{\partial x_j} - \frac{\partial\left(q_j^{sgs}\right)}{\partial x_j} + \overline{\dot{Q}} \tag{B.17}$$

One should also notice that the mechanical energy contribution, i.e., pressure work and viscous dissipation, have been neglected in the energy equation, because only low Mach number flow is considered. The term filtered enthalpy $\widetilde{h}$ is equal to $c_p\widetilde{T}$ and the resolved heat flux is

$$\overline{q}_j = -k\left(\widetilde{T}\right)\frac{\partial\widetilde{T}}{\partial x_j} \tag{B.18}$$

This term $\overline{\dot{Q}}$ is the rate of heat input, c_p is the specific heat at constant pressure, and $k(\widetilde{T})$ is thermal conductivity, which is evaluated at the filter temperature, $\widetilde{T}$. Also, the SGS heat flux in the filtered energy equation is defined by

$$q_j^{sgs} = \overline{\rho}\left(\overline{u_j h} - \widetilde{u}_j\widetilde{h}\right) = \overline{\rho}c_p\left(\overline{u_j T} - \widetilde{u}_j\widetilde{T}\right) \tag{B.19}$$

Similar to the SGS stress, the SGS heat flux in the filtered energy equation is modeled. There are many previous SGS heat flux models in the literature (Chumakov et al., 2004), such as viscosity models, scale similarity models, and stretched-vortex models. An eddy viscosity model by Moin et al. (1991) is usually a convenient and efficient way to approximate the SGS heat flux. It can be expressed as

$$q_j^{sgs} = -\frac{\mu_{tk} c_p}{\mathrm{Pr}_{sgs}} \frac{\partial \tilde{T}}{\partial x_j} \tag{B.20}$$

The term Pr_{sgs} is the SGS turbulent Prantl number, which may be determined from a constant value assumption and the dynamic model calculation. In the same way, this term μ_{tk} is the SGS eddy viscosity, which may be calculated from universal coefficient models, scale similarity dynamic models, and one-equation models. The SGS heat flux in stationary and rotating square duct flow applications is approximated using the eddy viscosity model by Pallares et al. (2000).

Appendix C-Additional heat flux results

C.1 DOF62

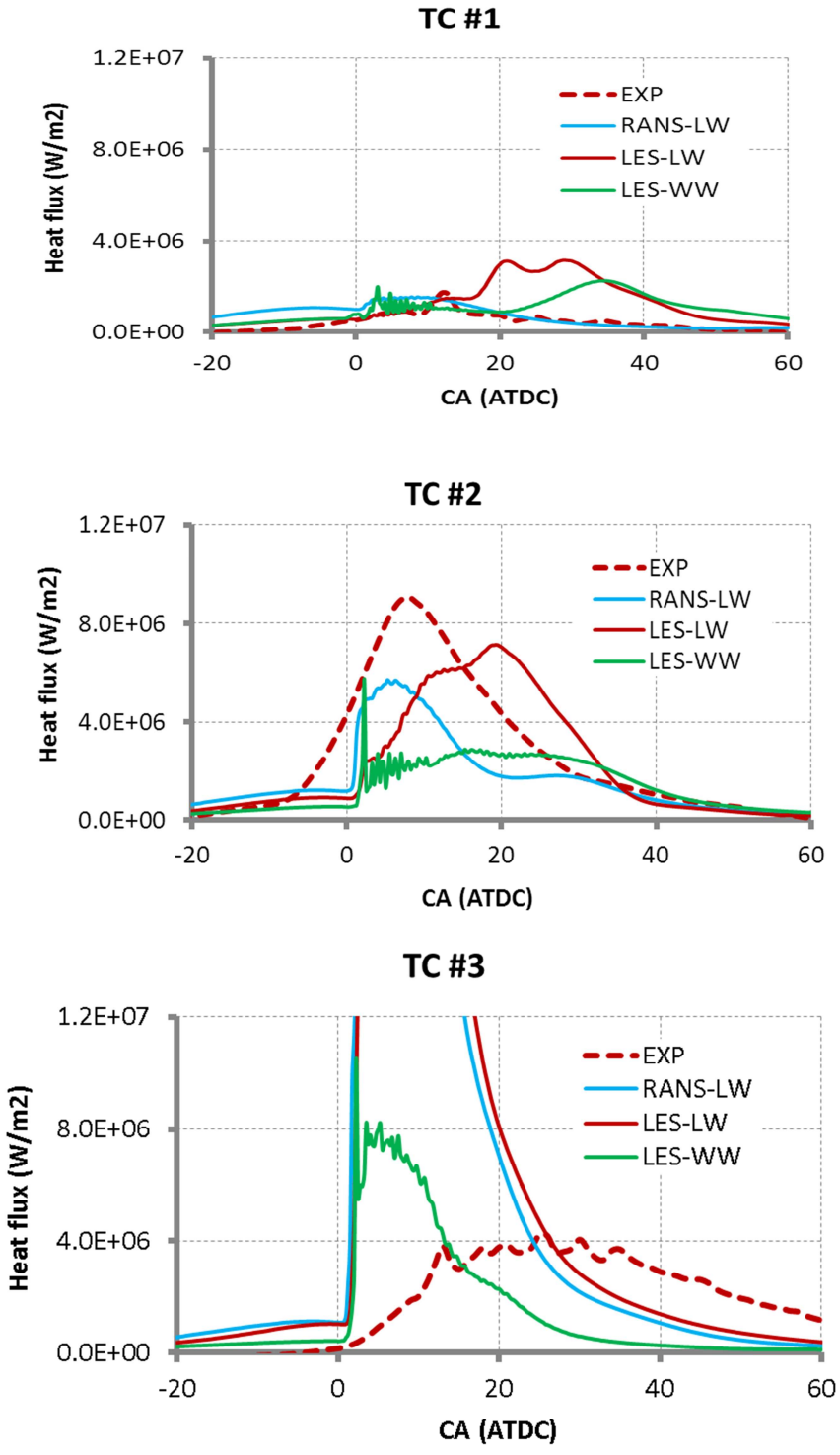

Figure C.1.1 Comparisons of heat flux on piston surface at TC#1-TC#3 (spray axis) for DOF62

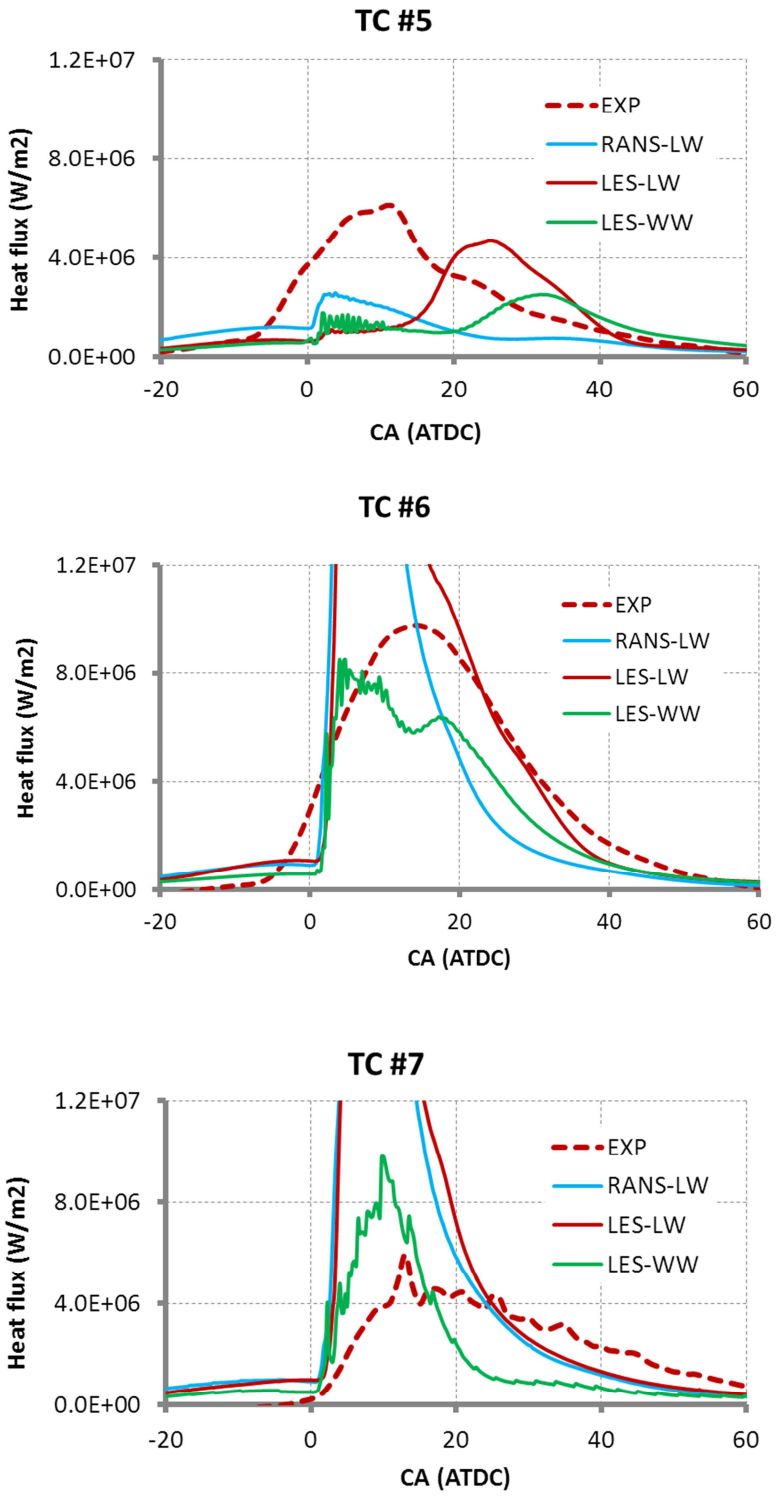

Figure C.1.2 Comparisons of heat flux on piston surface at TC#5-TC#7 (spray axis) for DOF62

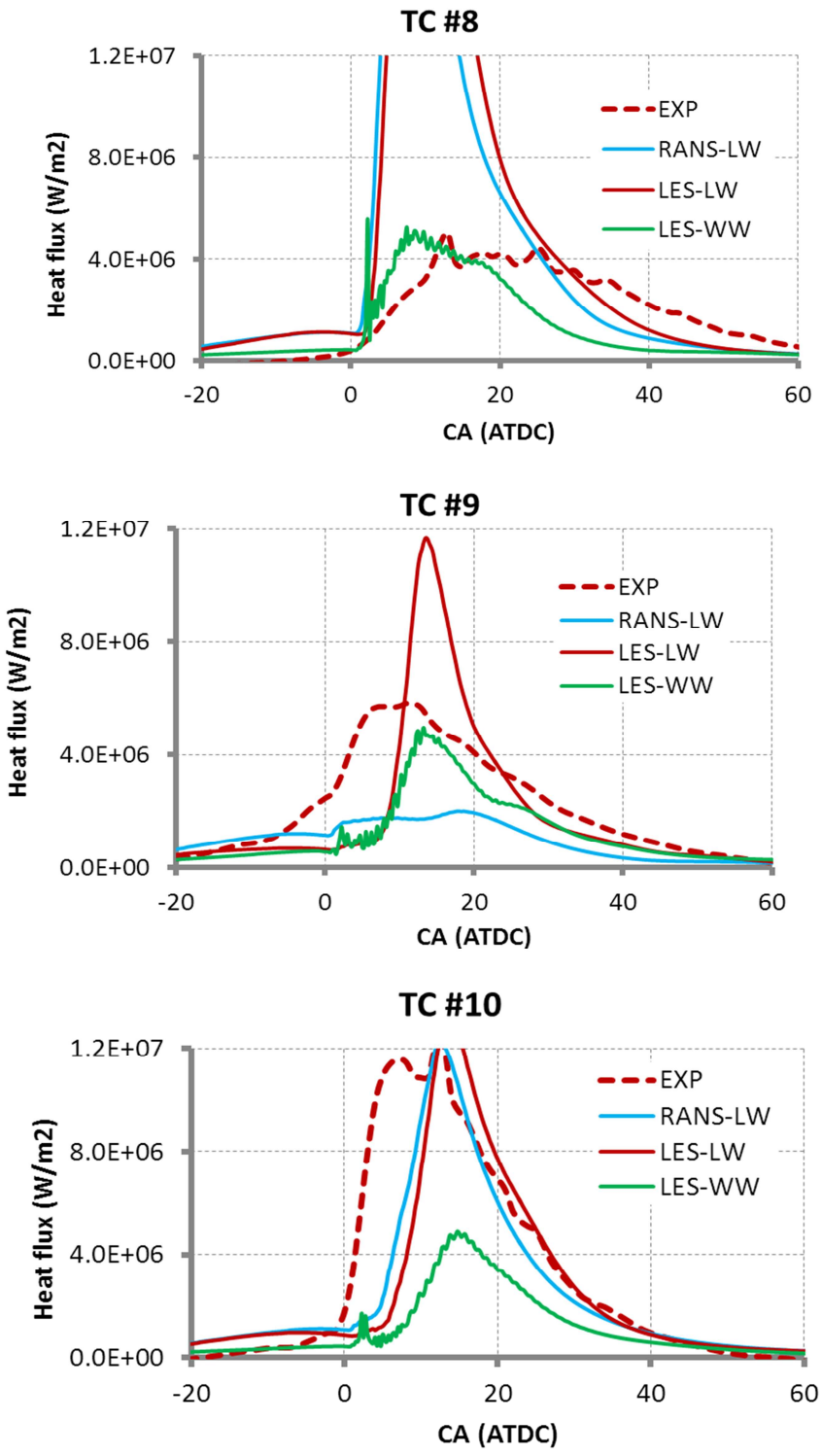

Figure C.1.3 Comparisons of heat flux on piston surface at TC#8-TC#10 (mid-way between two adjacent sprays) for DOF62

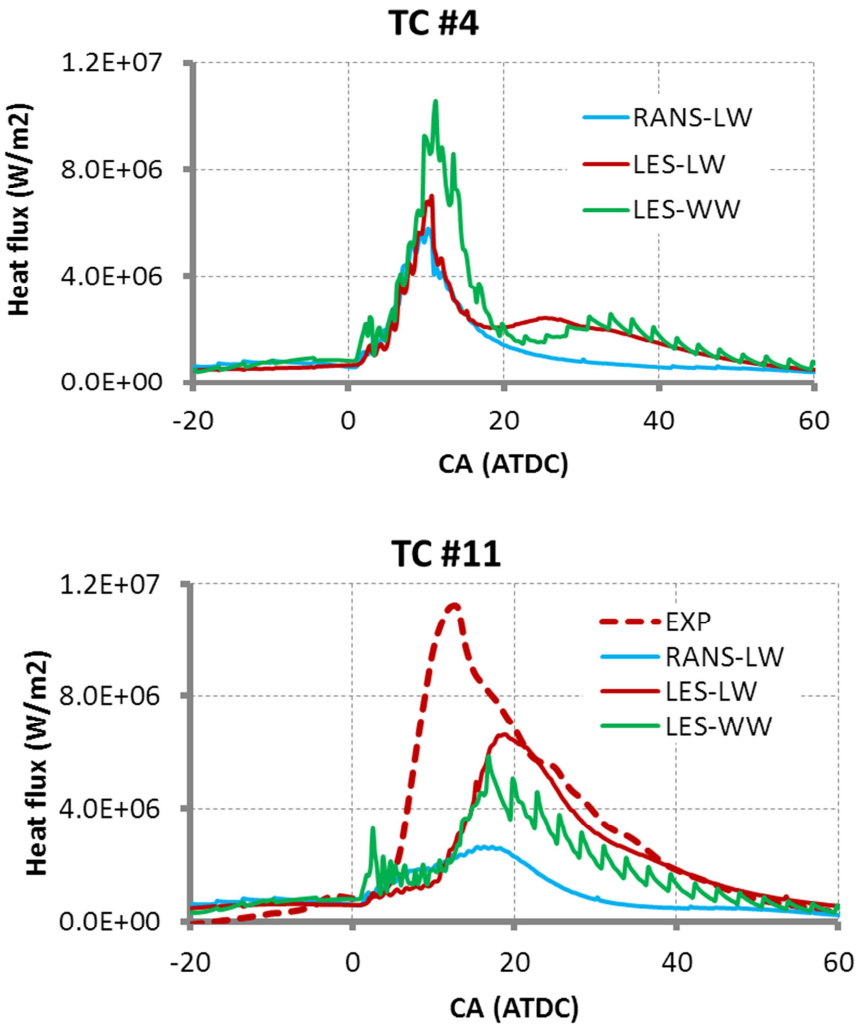

Figure C.1.4 Comparisons of heat flux on the piston surface in squish areas TC#4 and TC#11 for DOF62

C.2 Run52

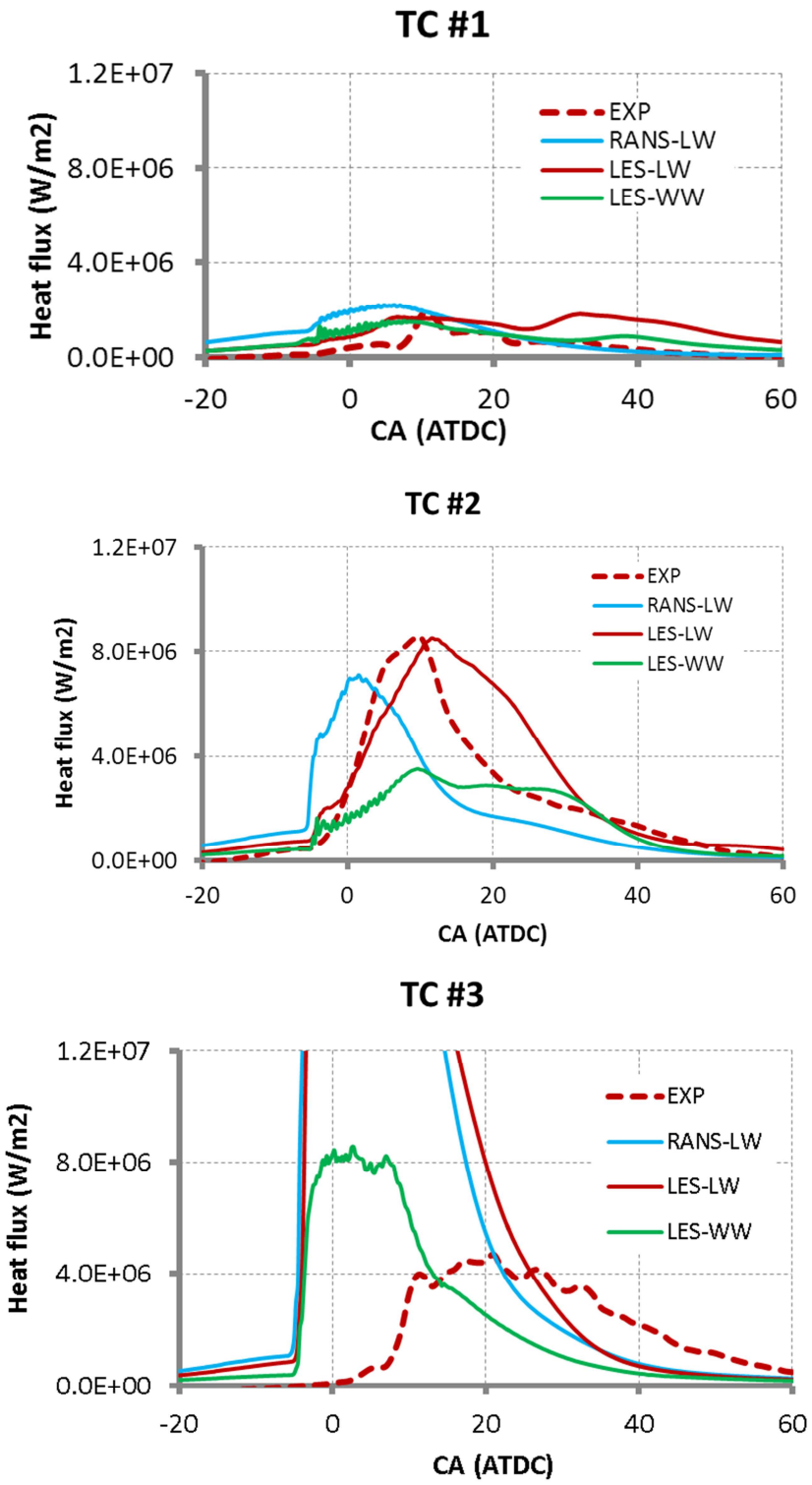

Figure C.2.1 Comparisons of heat flux on piston surface at TC#1-TC#3 (spray axis) for Run52

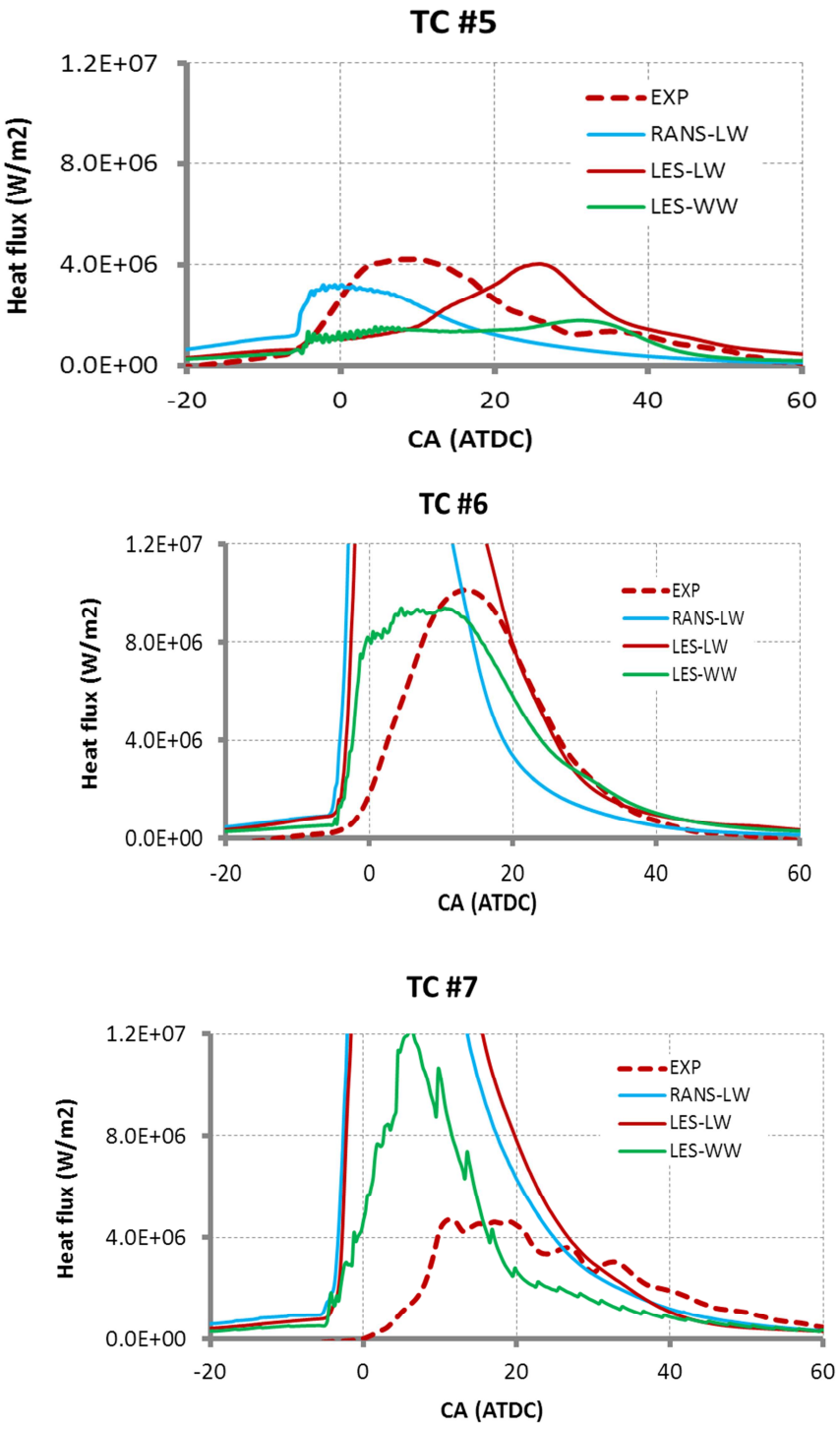

Figure C.2.2 Comparisons of heat flux on piston surface at TC#5-TC#7 (spray axis) for Run52

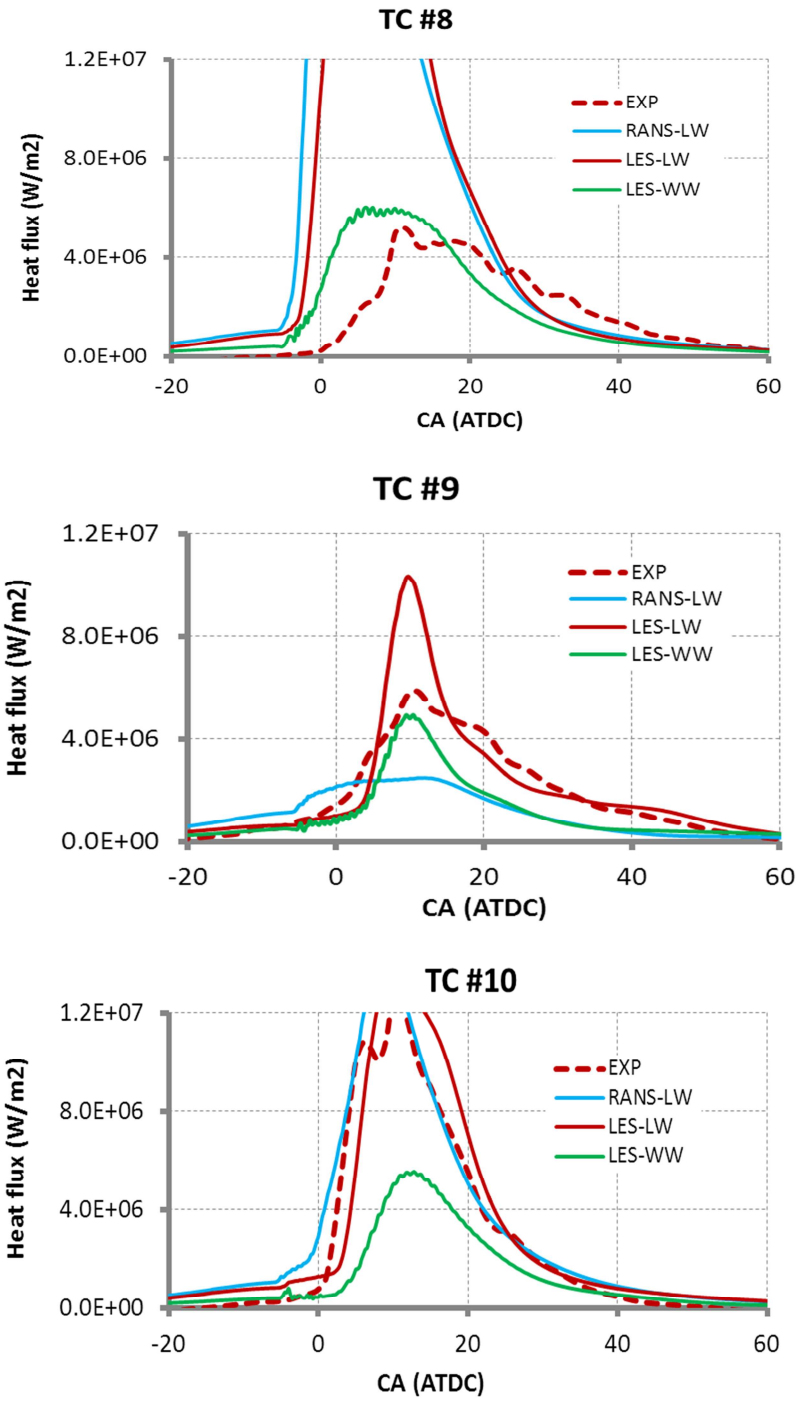

Figure C.2.3 Comparisons of heat flux on piston surface at TC#8-TC#10 (mid-way between two adjacent sprays) for Run52

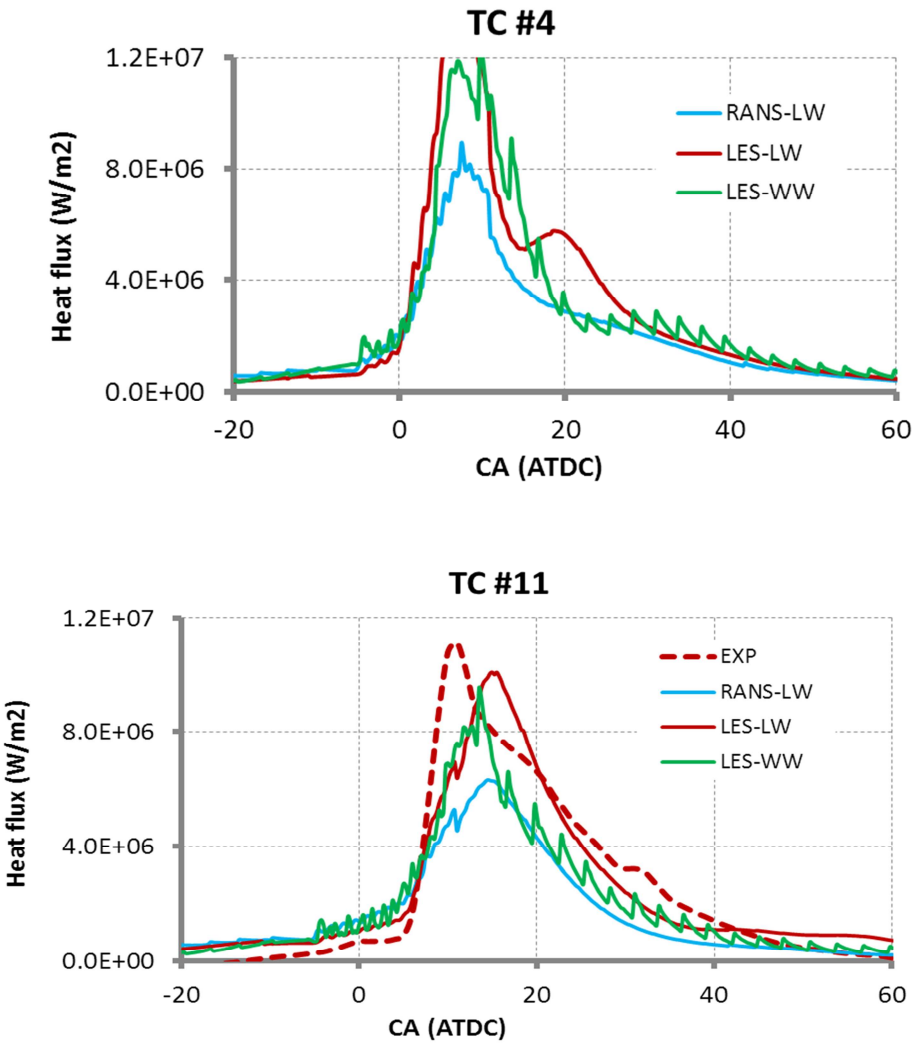

Figure C.2.4 Comparisons of heat flux on the piston surface in squish areas TC#4 and TC#11 for Run52

C.3 Run51

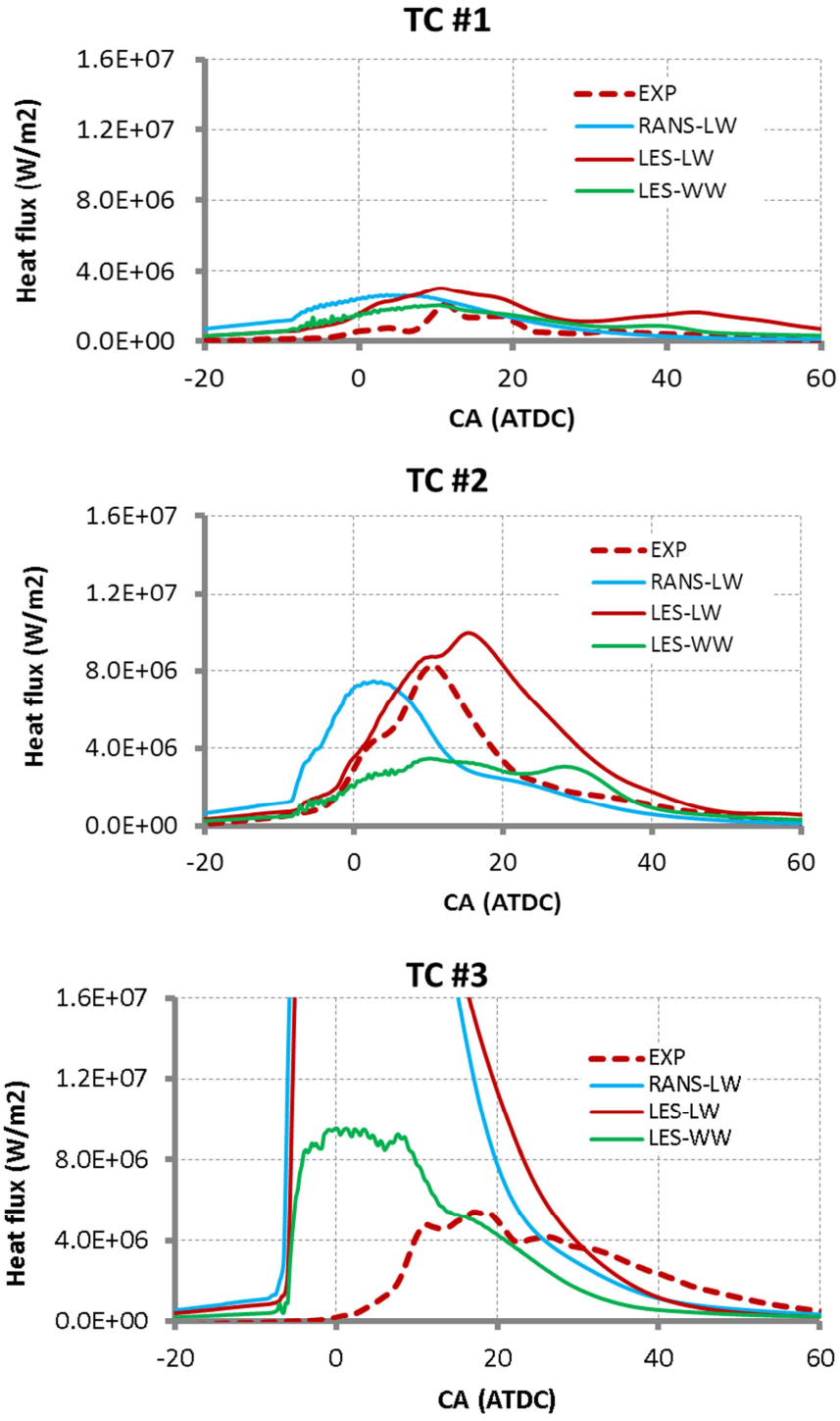

Figure C.3.1 Comparisons of heat flux on piston surface at TC#1-TC#3 (spray axis) for Run51

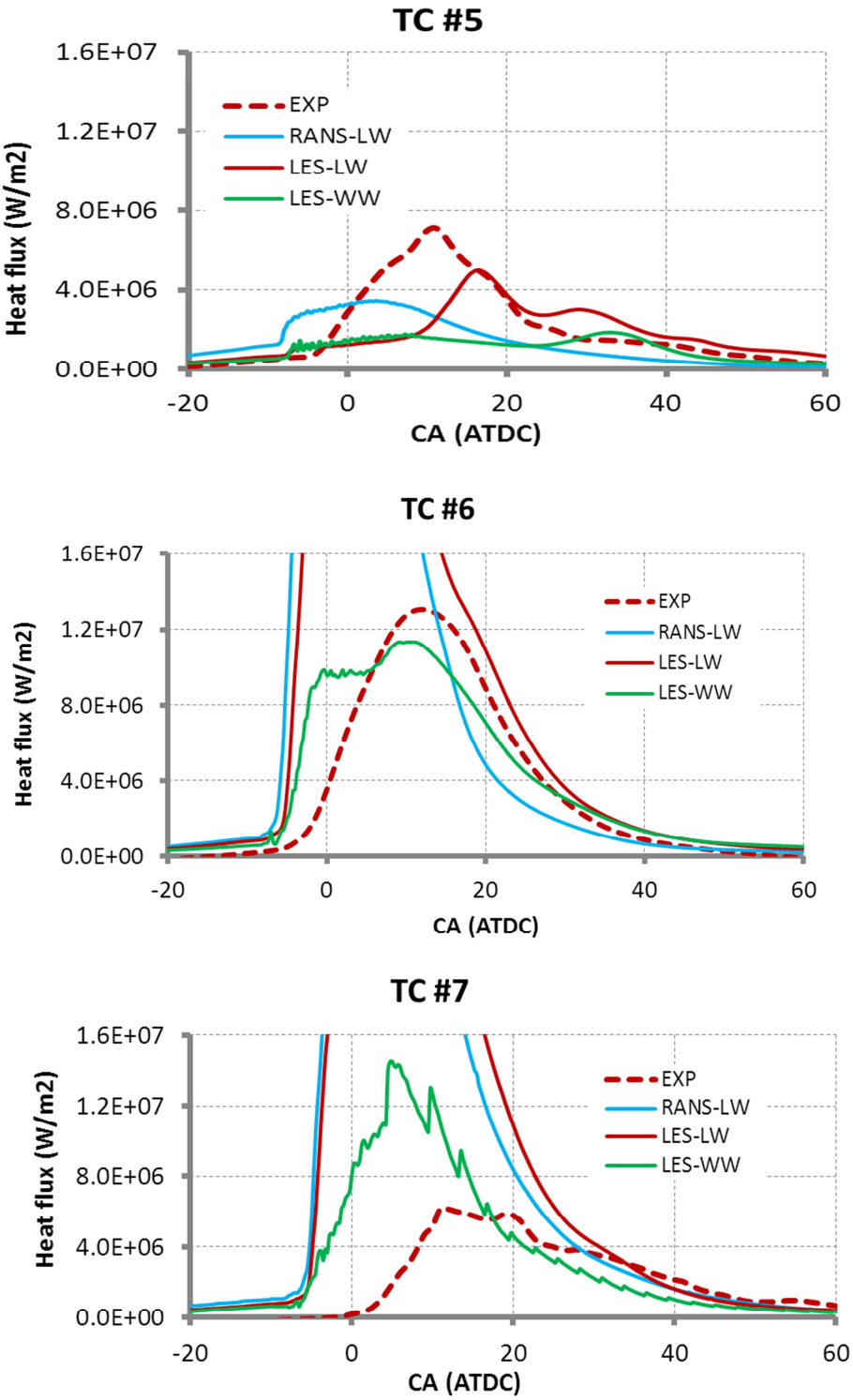

Figure C.3.2 Comparisons of heat flux on piston surface at TC#5-TC#7 (spray axis) for Run51

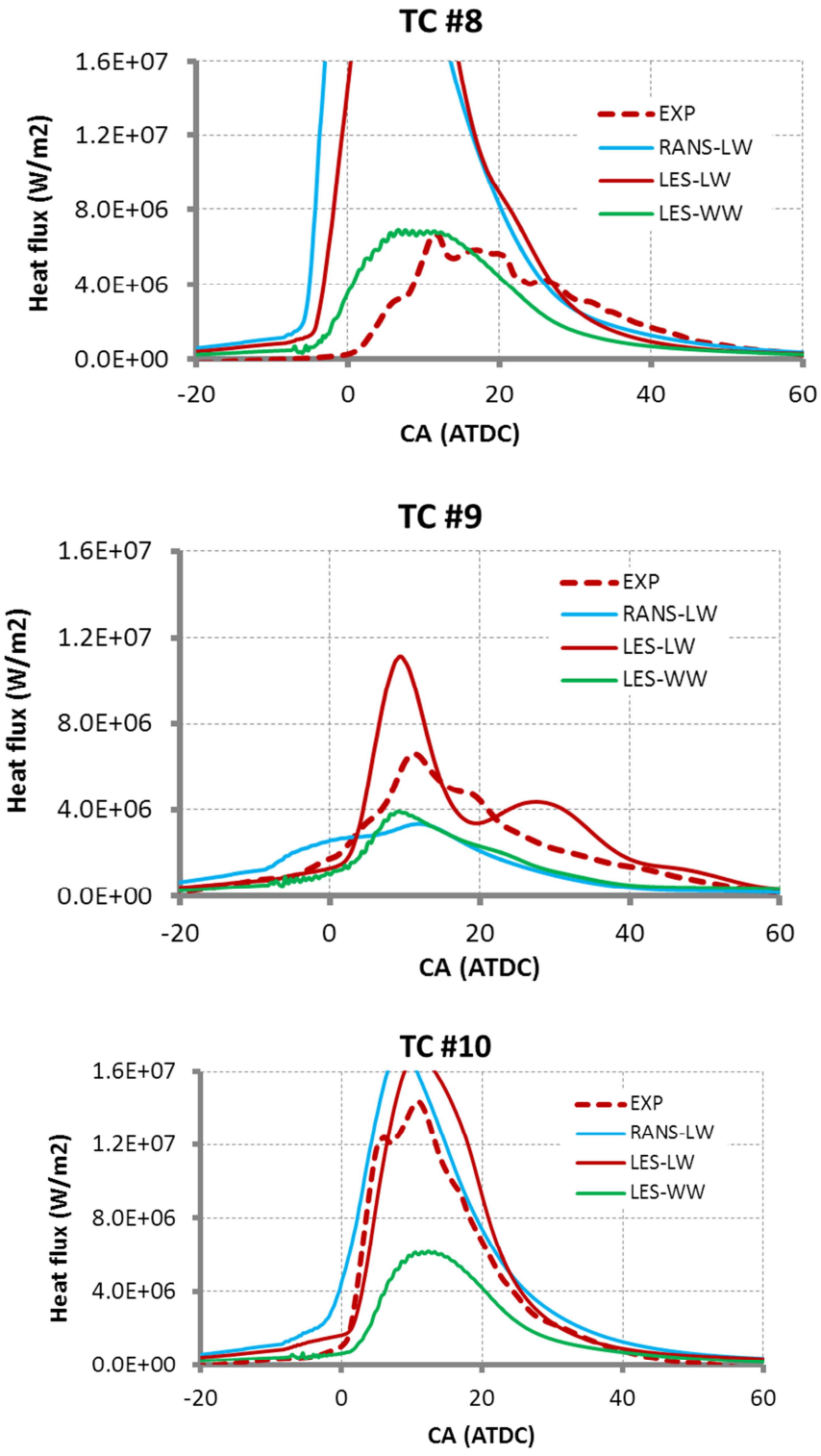

Figure C.3.3 Comparisons of heat flux on piston surface at TC#8-TC#10 (mid-way between two adjacent sprays) for Run51

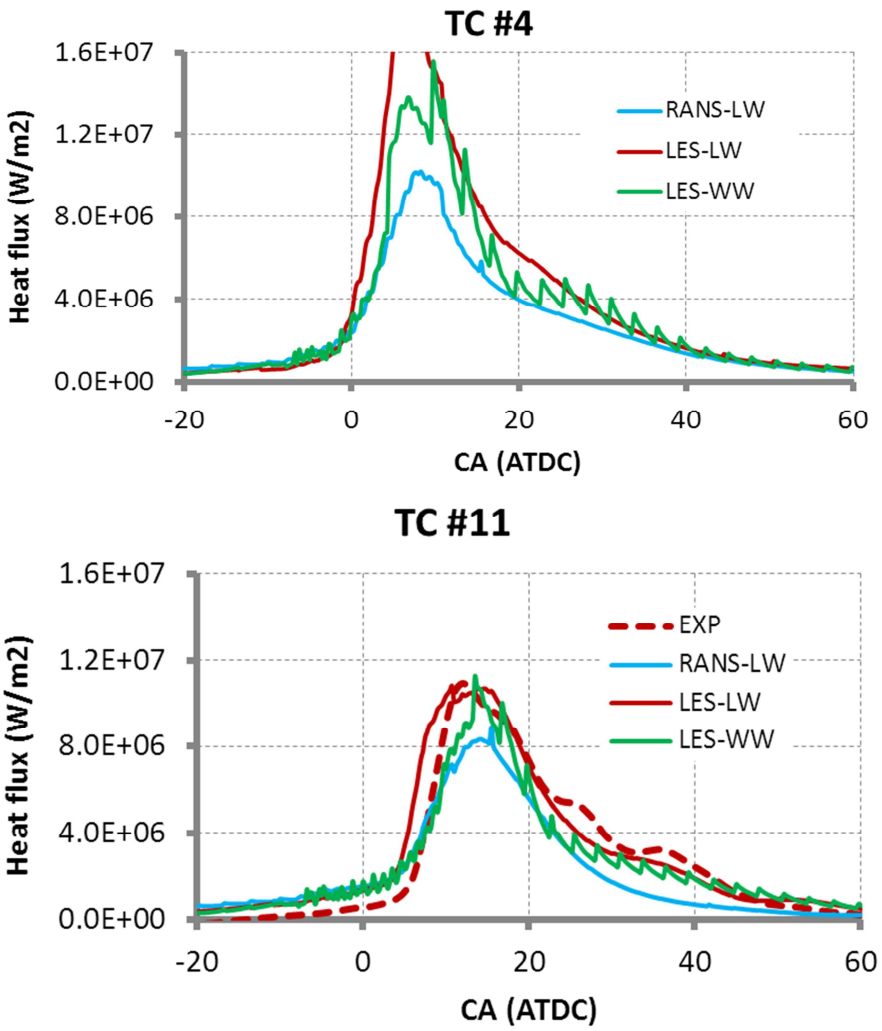

Figure C.3.4 Comparisons of heat flux on the piston surface in squish areas TC#4 and TC#11 for Run51

C.4 Run69

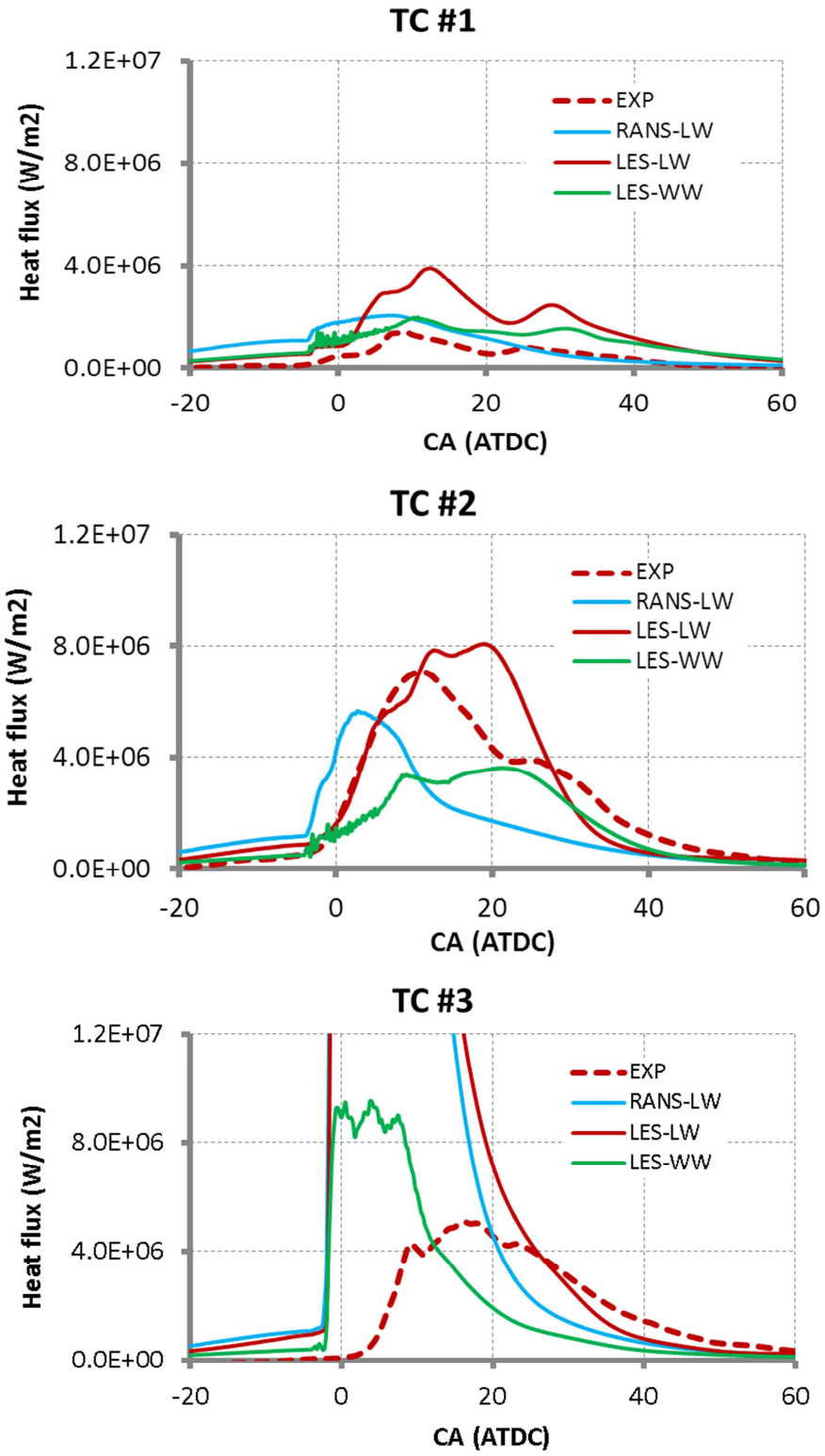

Figure C.4.1 Comparisons of heat flux on piston surface at TC#1-TC#3 (spray axis) for Run69

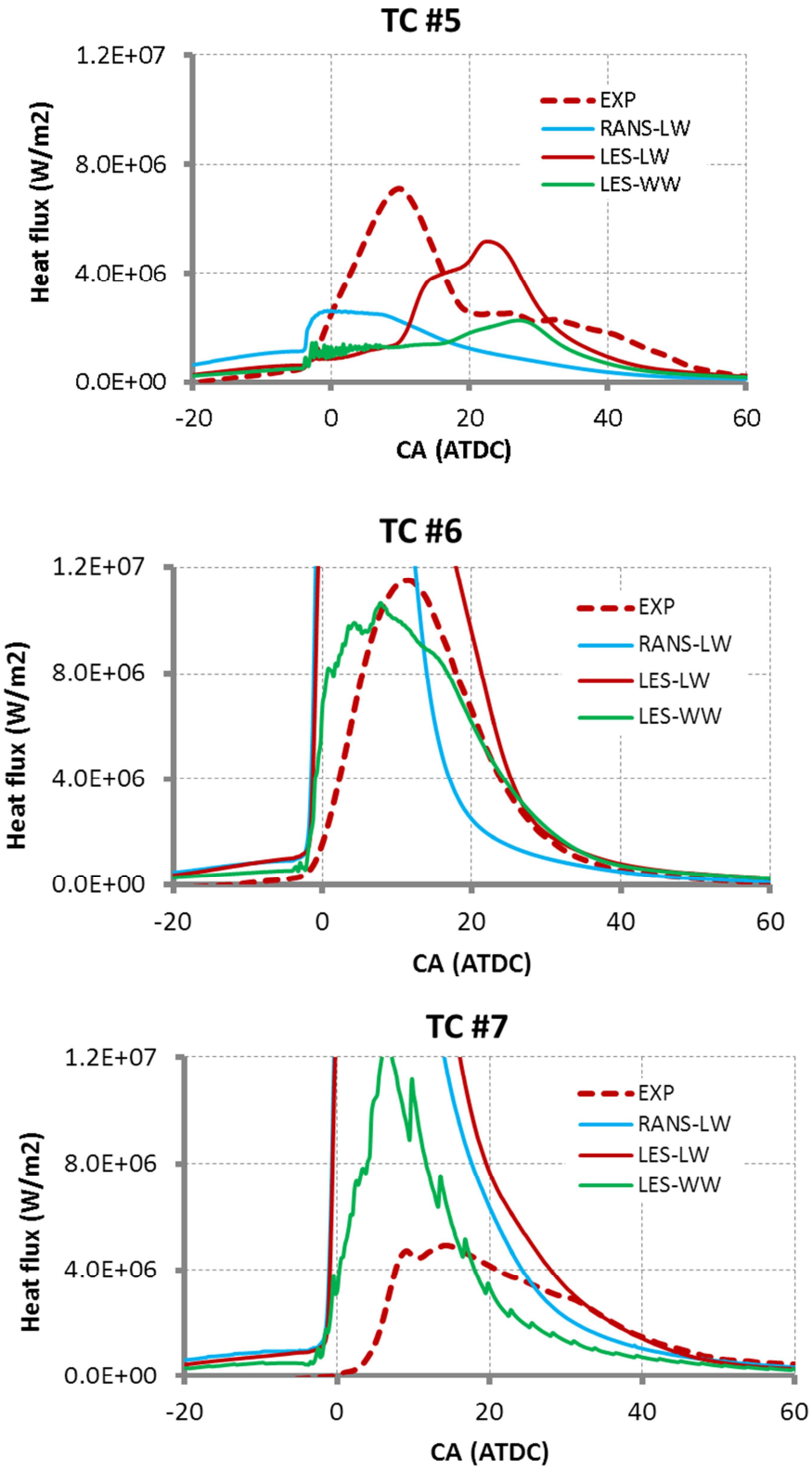

Figure C.4.2 Comparisons of heat flux on piston surface at TC#5-TC#7 (spray axis) for Run69

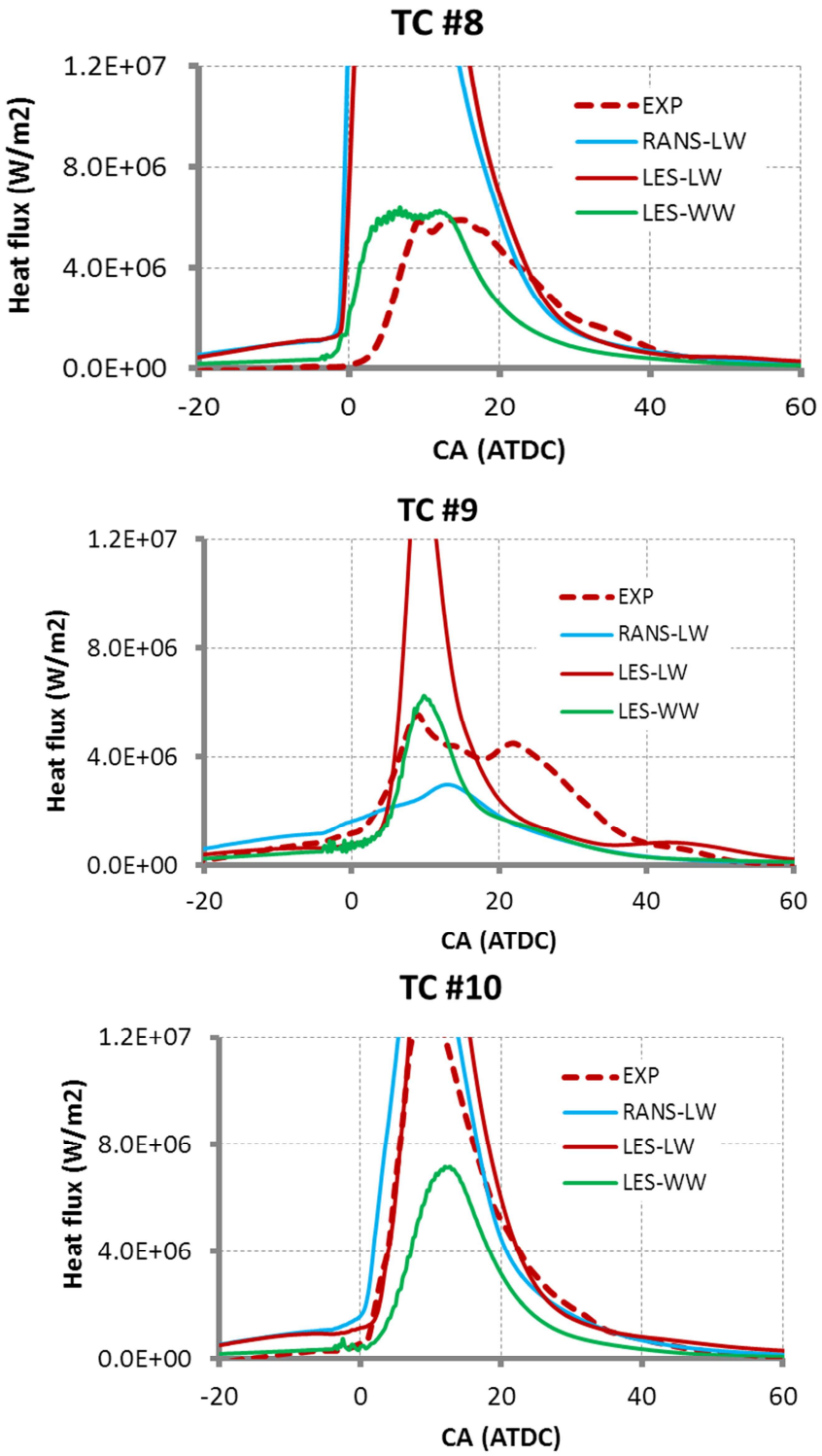

Figure C.4.3 Comparisons of heat flux on piston surface at TC#8-TC#10 (mid-way between two adjacent sprays) for Run69

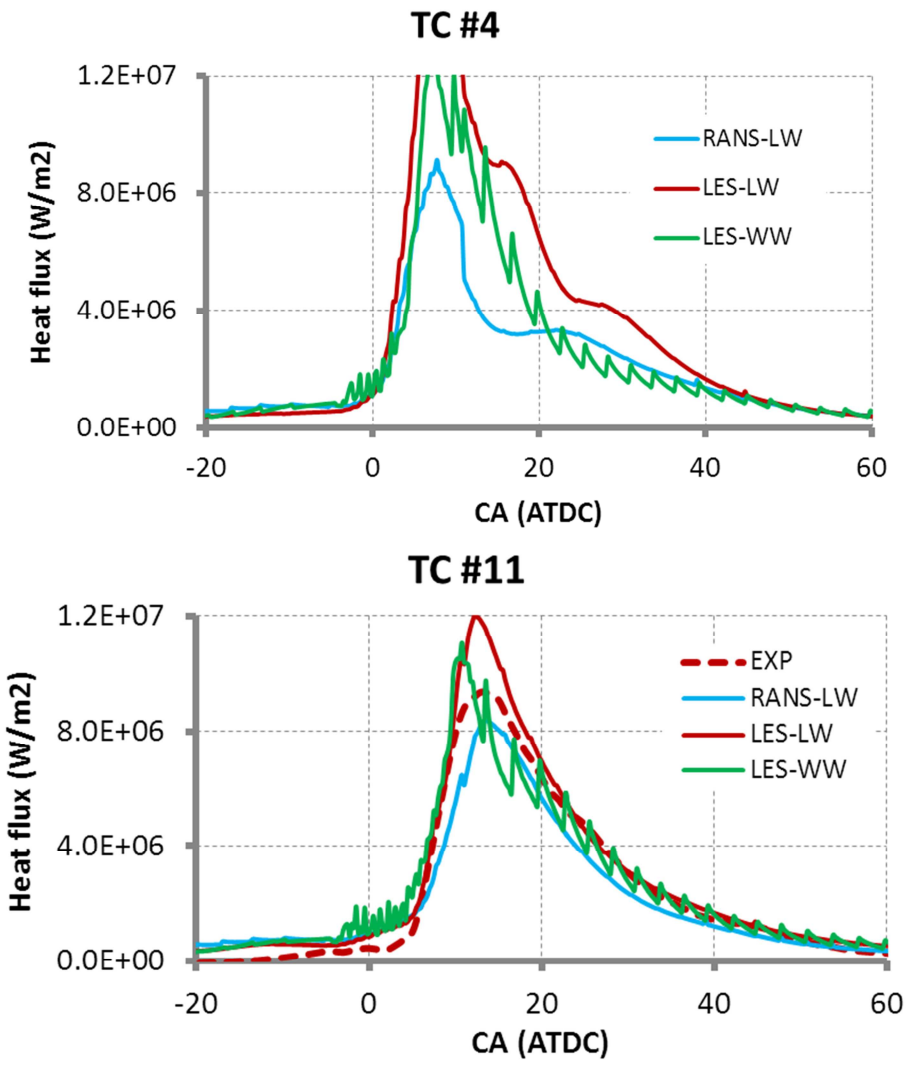

Figure C.4.4 Comparisons of heat flux on the piston surface in squish areas TC#4 and TC#11 for Run69

C.5 Run63

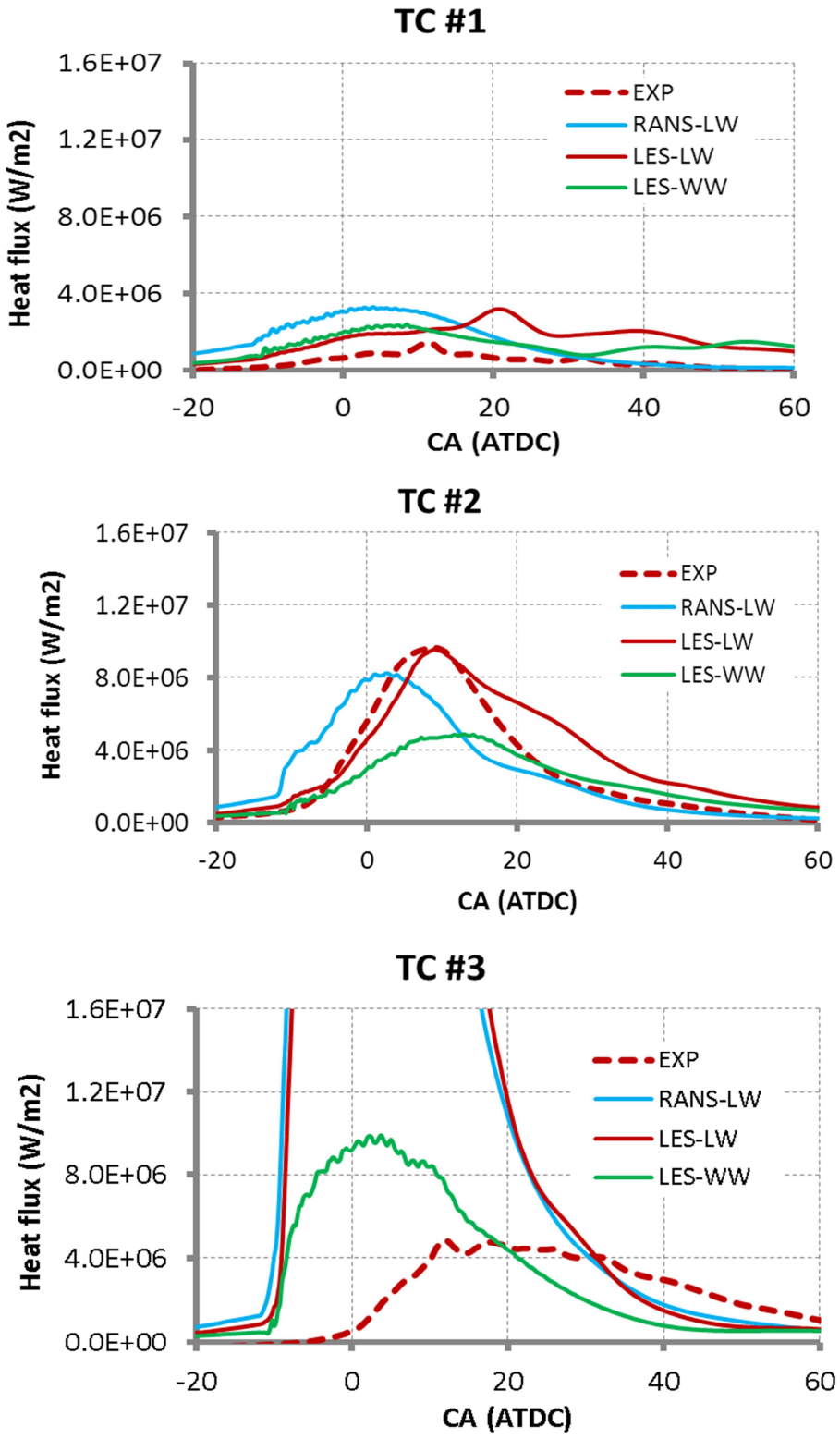

Figure C.5.1 Comparisons of heat flux on piston surface at TC#1-TC#3 (spray axis) for Run63

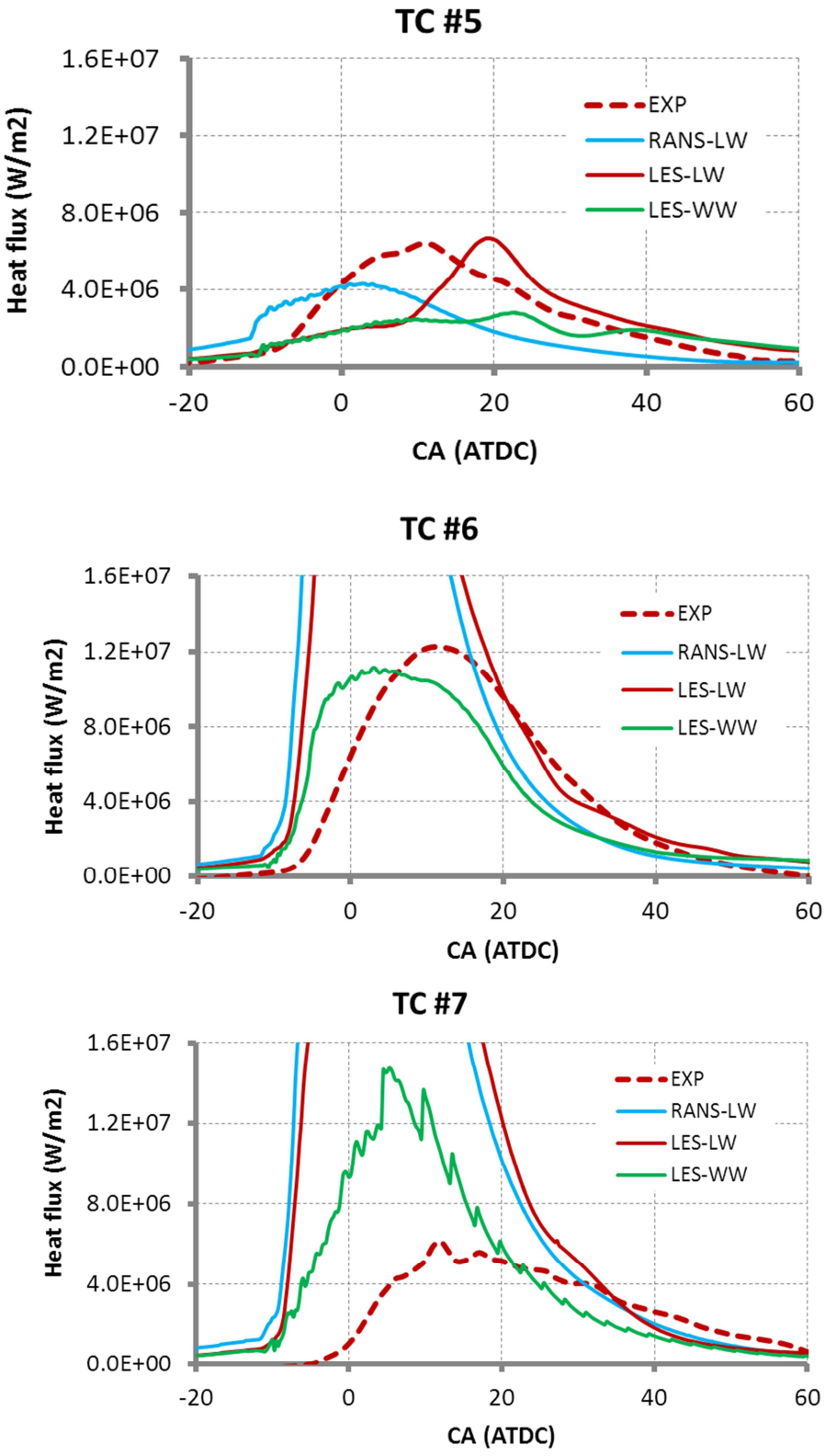

Figure C.5.2 Comparisons of heat flux on piston surface at TC#5-TC#7 (spray axis) for Run63

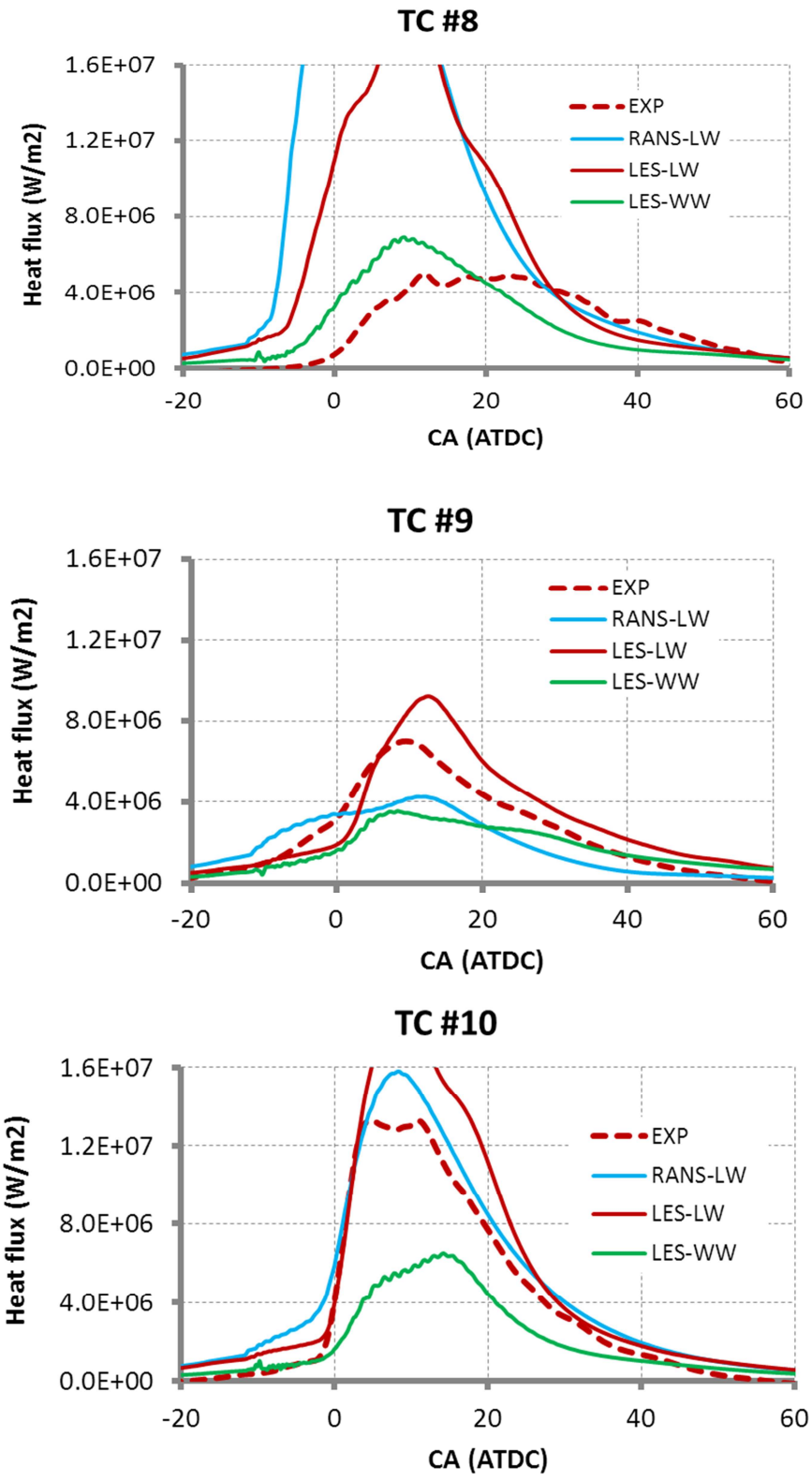

Figure C.5.3 Comparisons of heat flux on piston surface at TC#8-TC#10 (mid-way between two adjacent sprays) for Run63

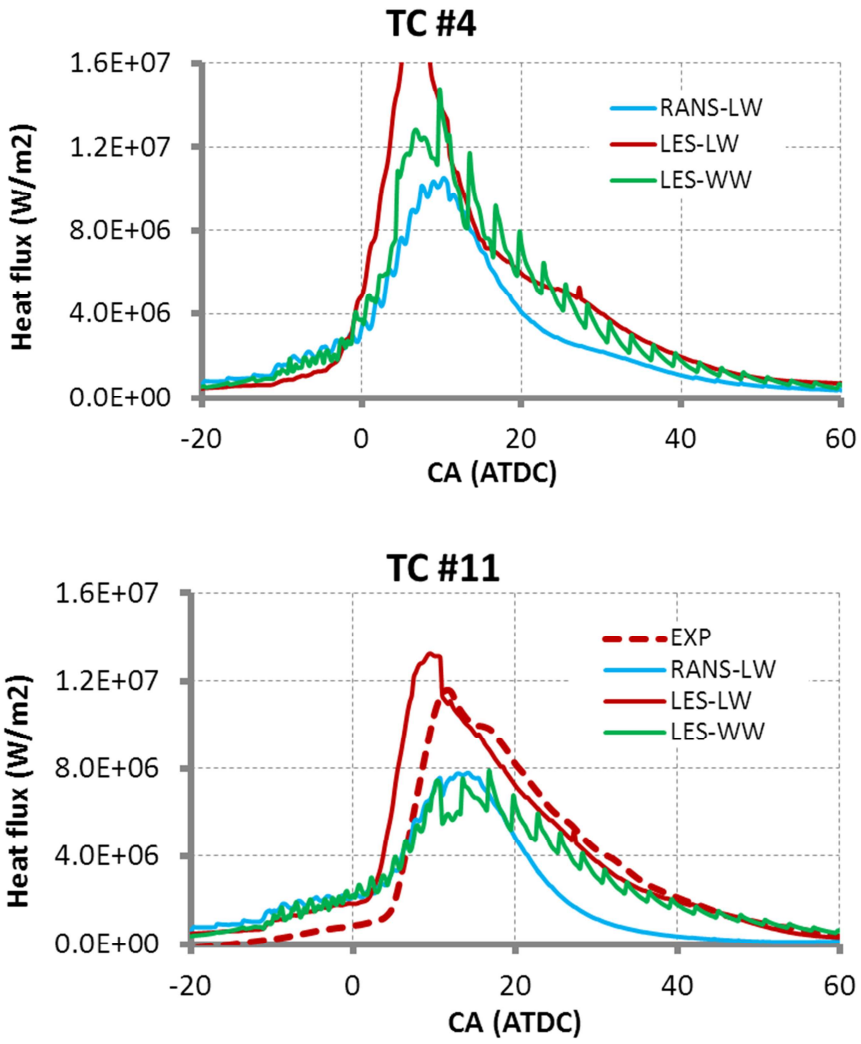

Figure C.5.4 Comparisons of heat flux on the piston surface in squish areas TC#4 and TC#11 for Run63

C.6 DOF38

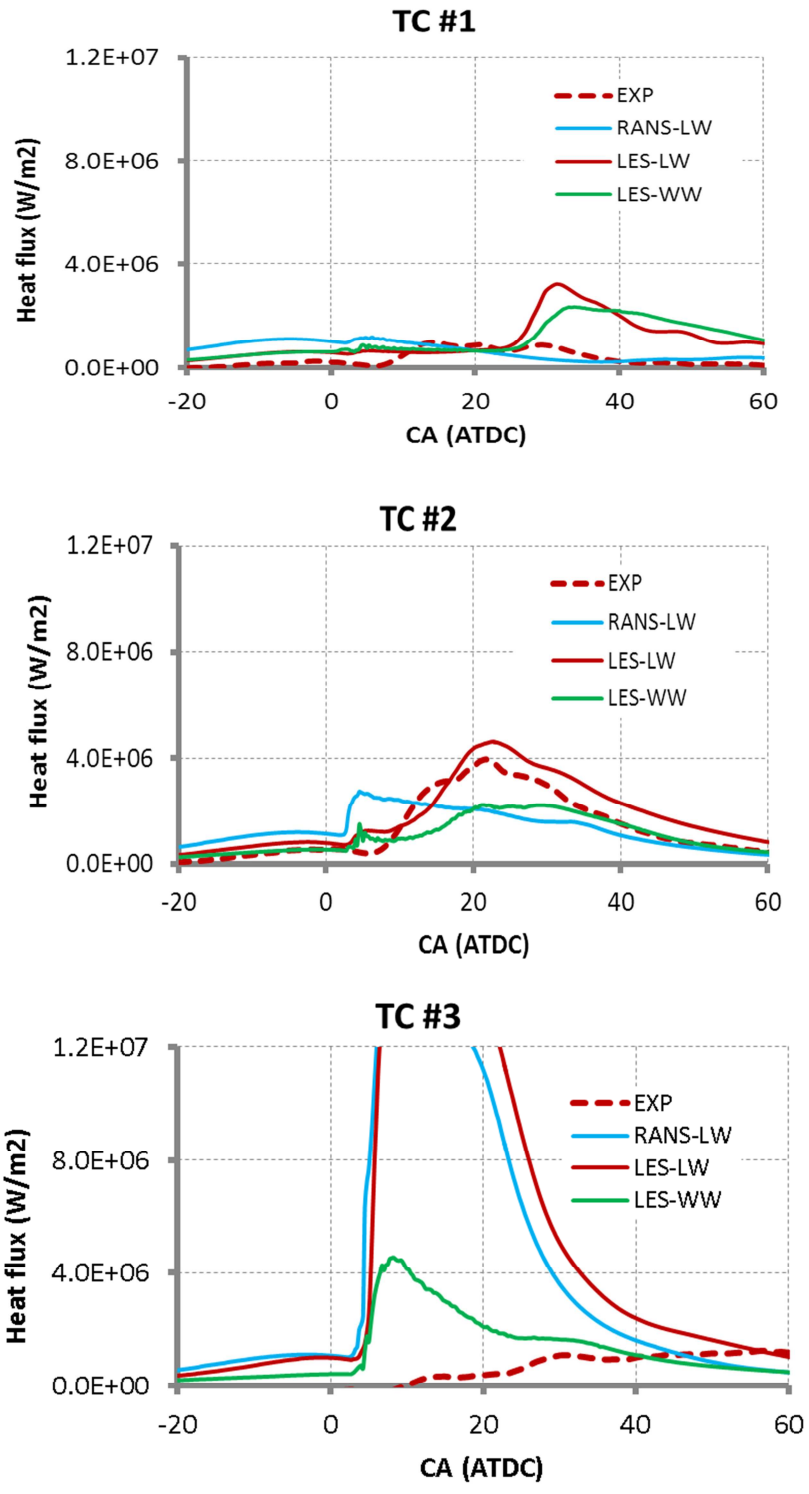

Figure C.6.1 Comparisons of heat flux on piston surface at TC#1-TC#3 (spray axis) for DOF38

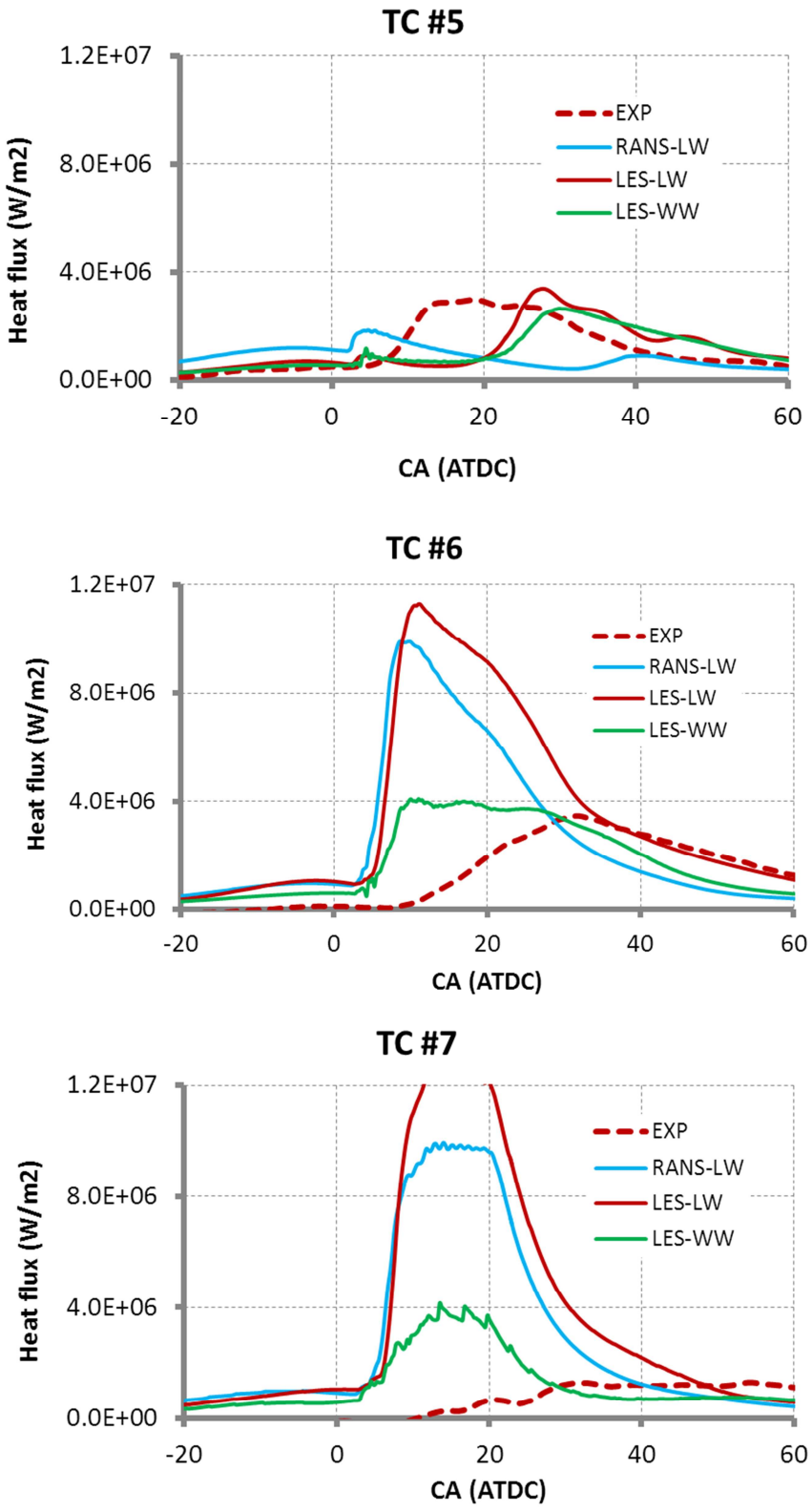

Figure C.6.2 Comparisons of heat flux on piston surface at TC#5-TC#7 (spray axis) for DOF38

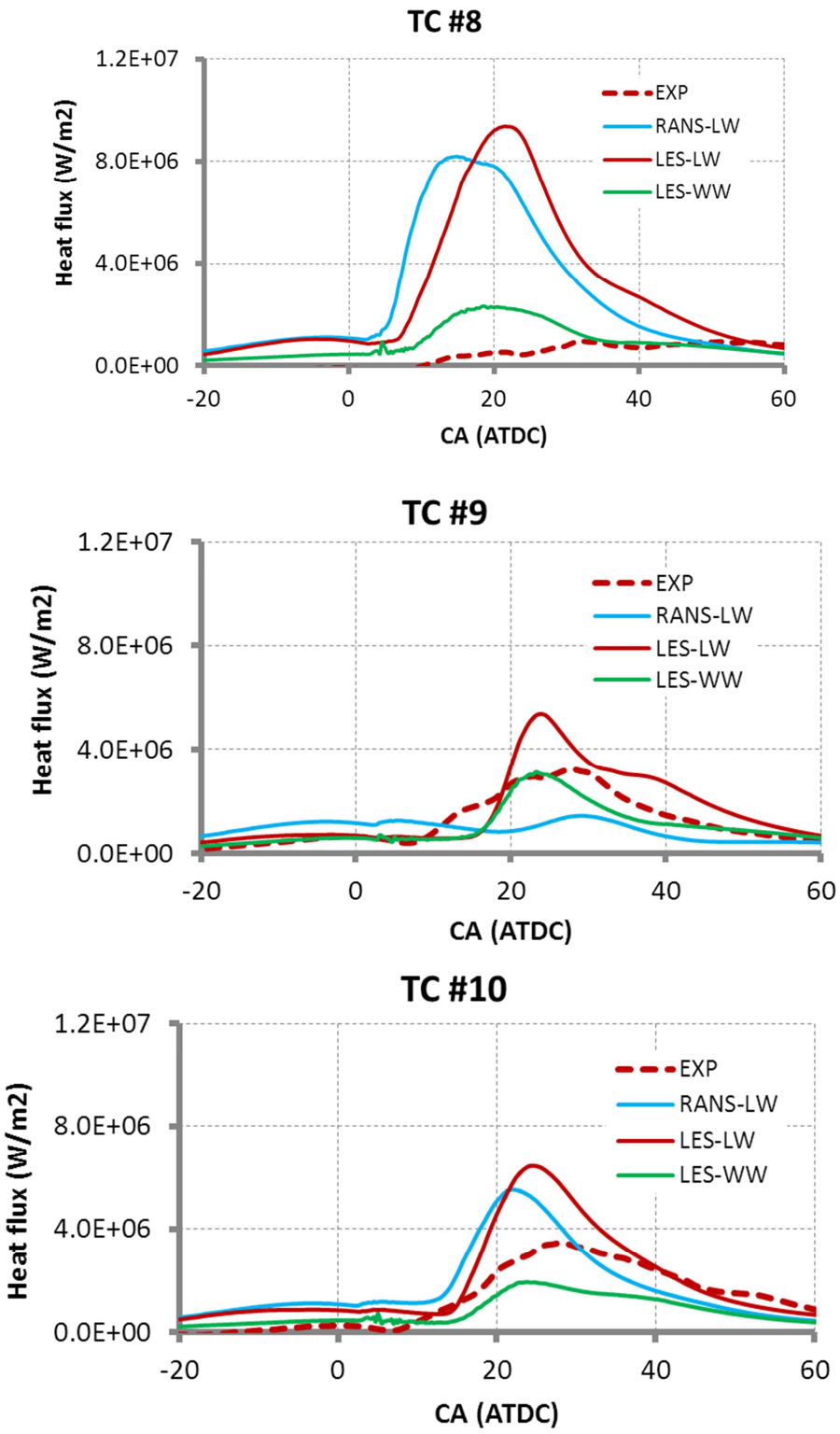

Figure C.6.3 Comparisons of heat flux on piston surface at TC#8-TC#10 (mid-way between two adjacent sprays) for DOF38

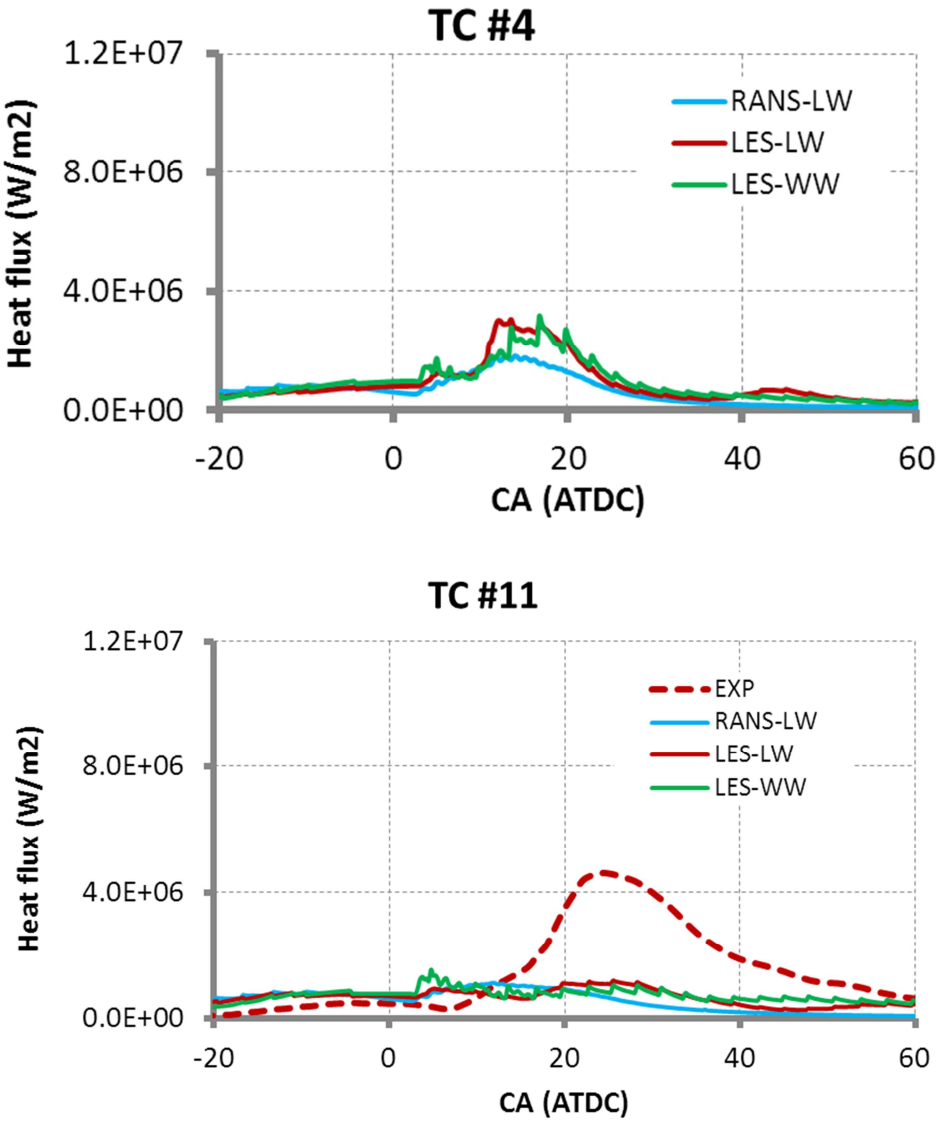

Figure C.6.4 Comparisons of heat flux on the piston surface in squish areas TC#4 and TC#11 for DOF38

C.7 DOF50

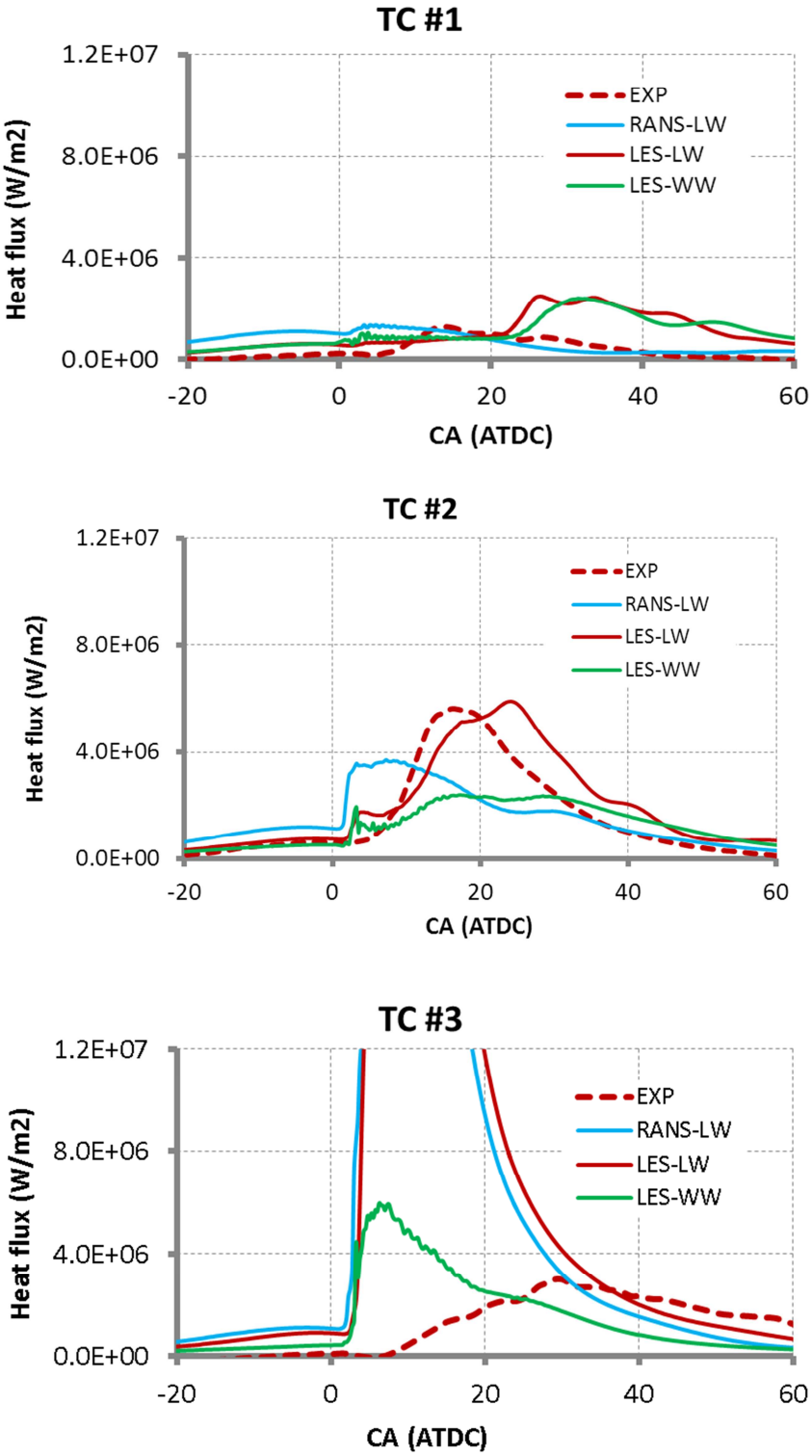

Figure C.7.1 Comparisons of heat flux on piston surface at TC#1-TC#3 (spray axis) for DOF50

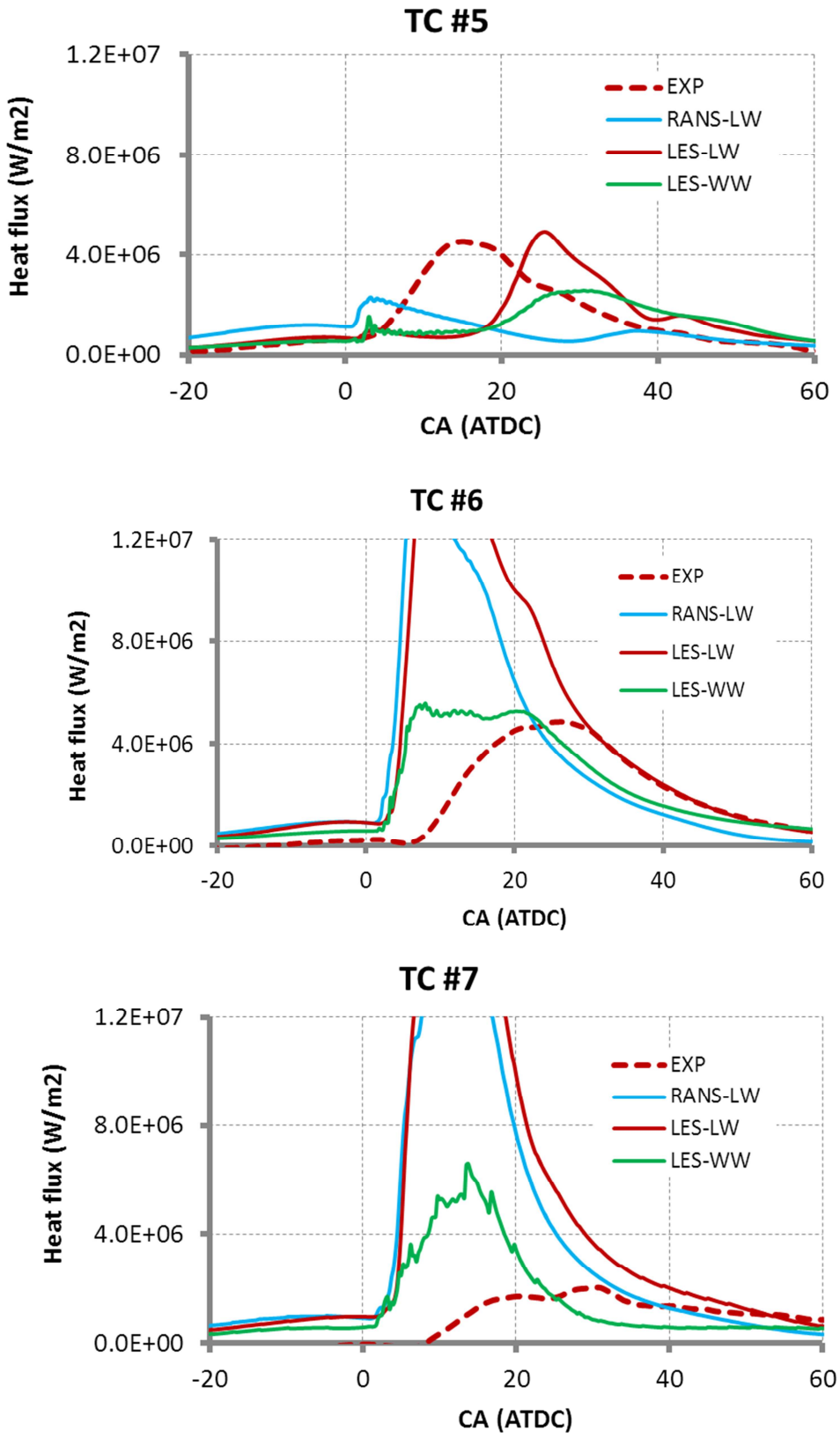

Figure C.7.2 Comparisons of heat flux on piston surface at TC#5-TC#7 (spray axis) for DOF50

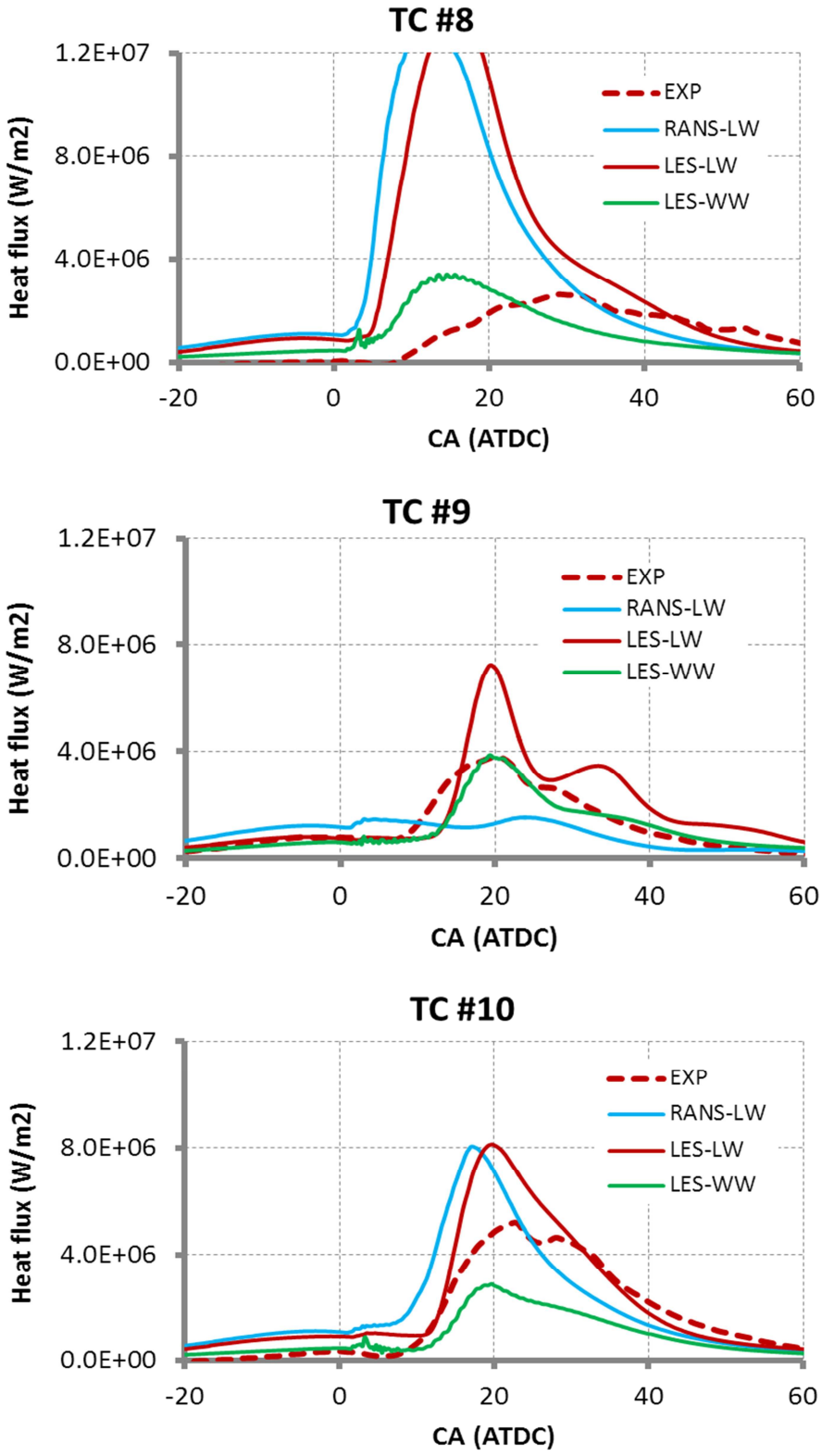

Figure C.7.3 Comparisons of heat flux on piston surface at TC#8-TC#10 (mid-way between two adjacent sprays) for DOF50

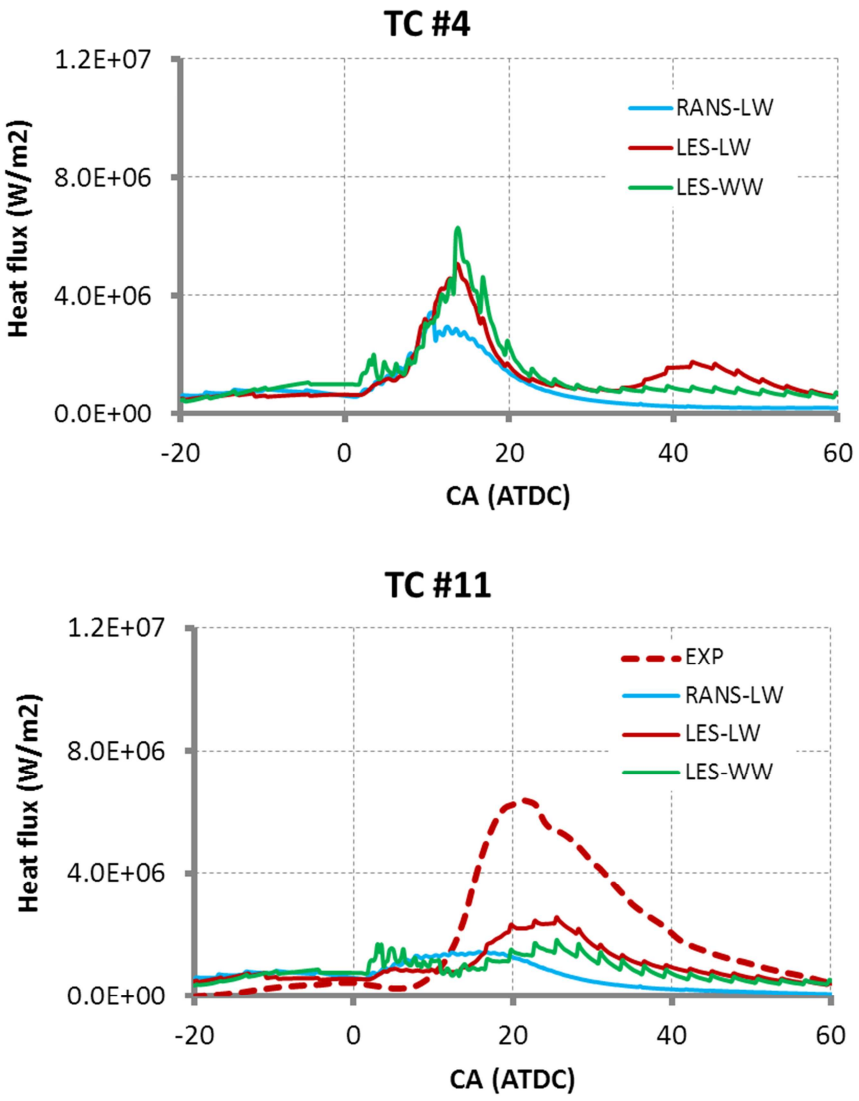

Figure C.7.4 Comparisons of heat flux on the piston surface in squish areas TC#4 and TC#11 for DOF50

C.8 Run40

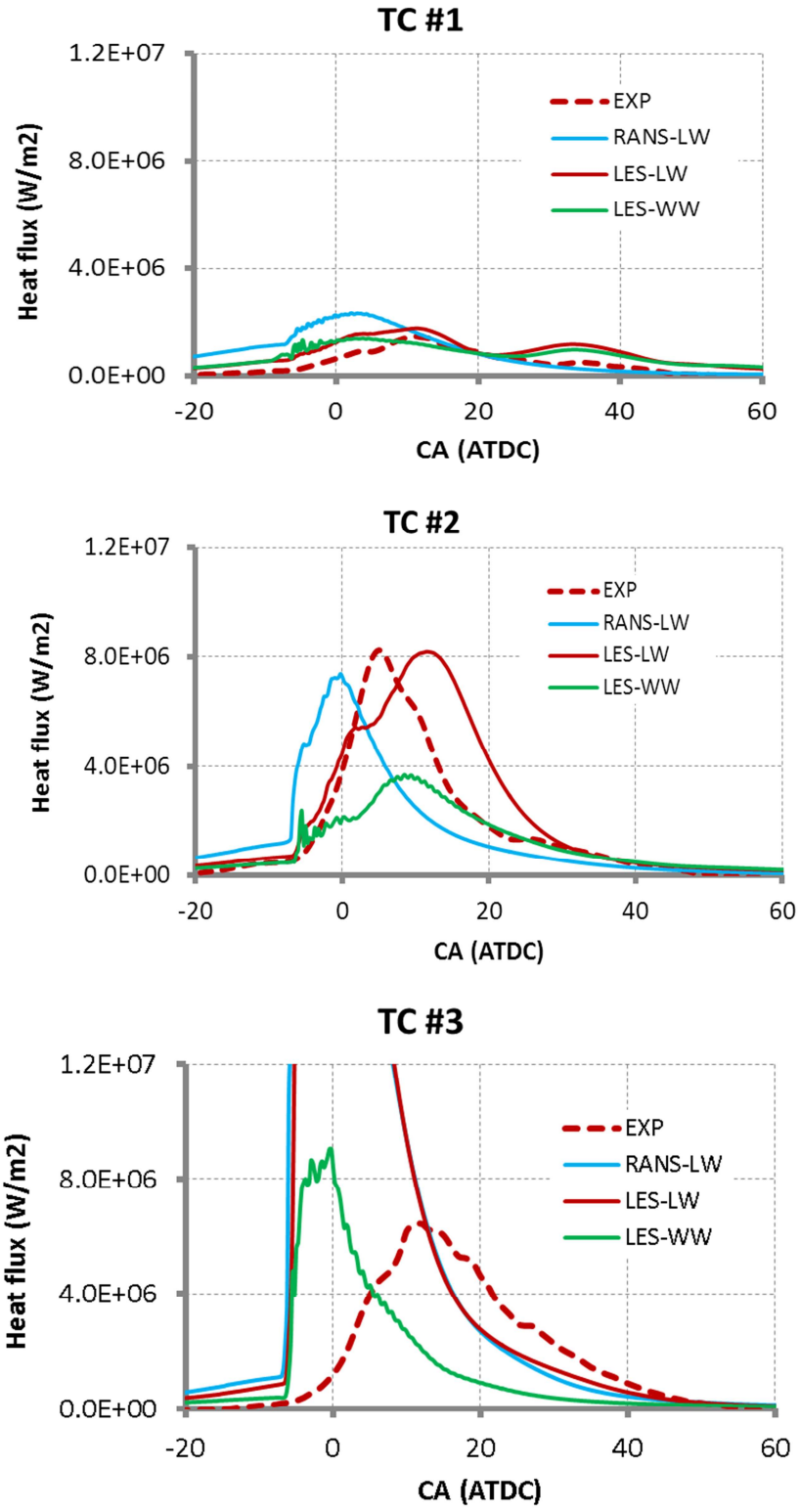

Figure C.8.1 Comparisons of heat flux on piston surface at TC#1-TC#3 (spray axis) for Run40

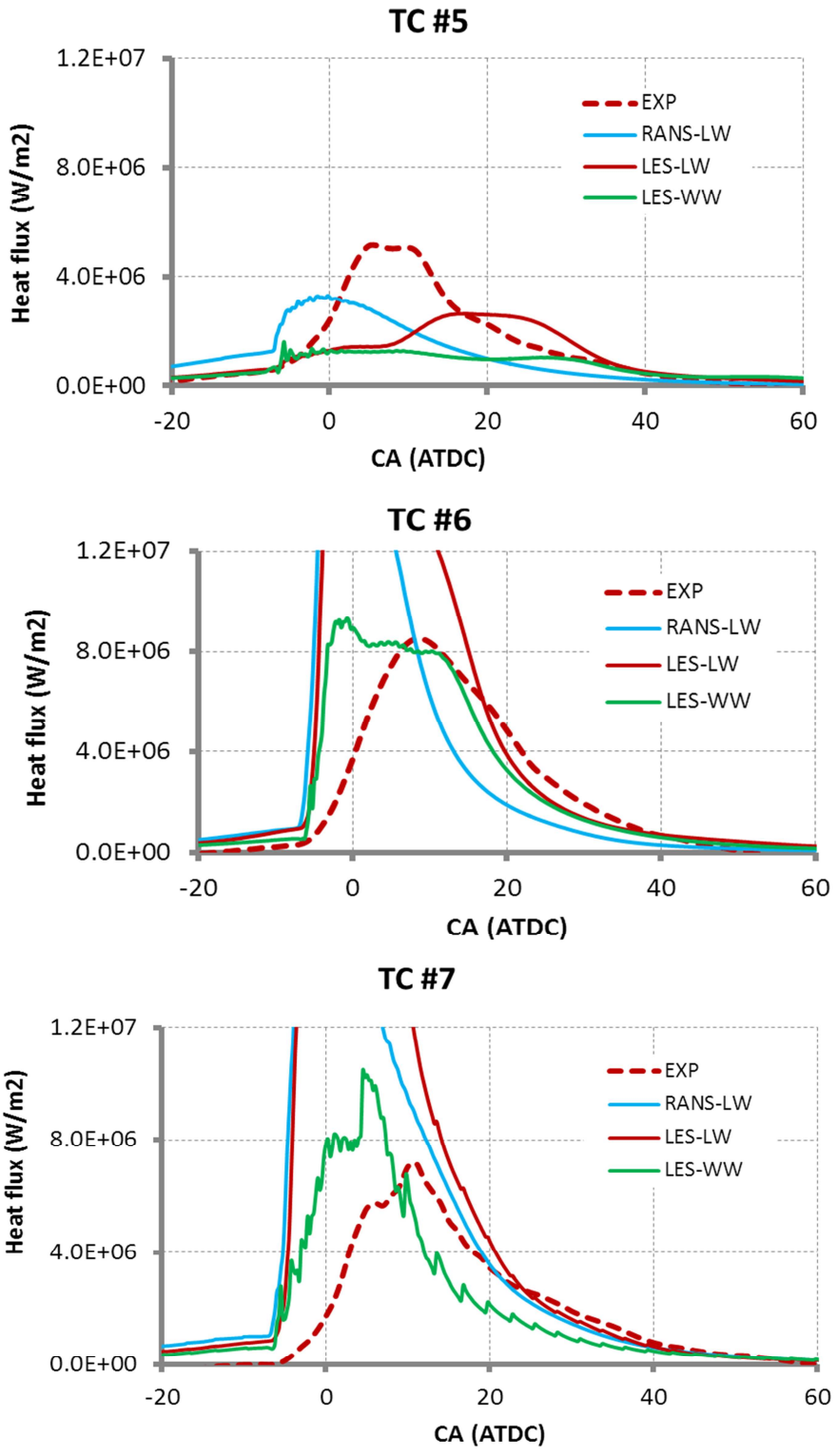

Figure C.8.2 Comparisons of heat flux on piston surface at TC#5-TC#7 (spray axis) for Run40

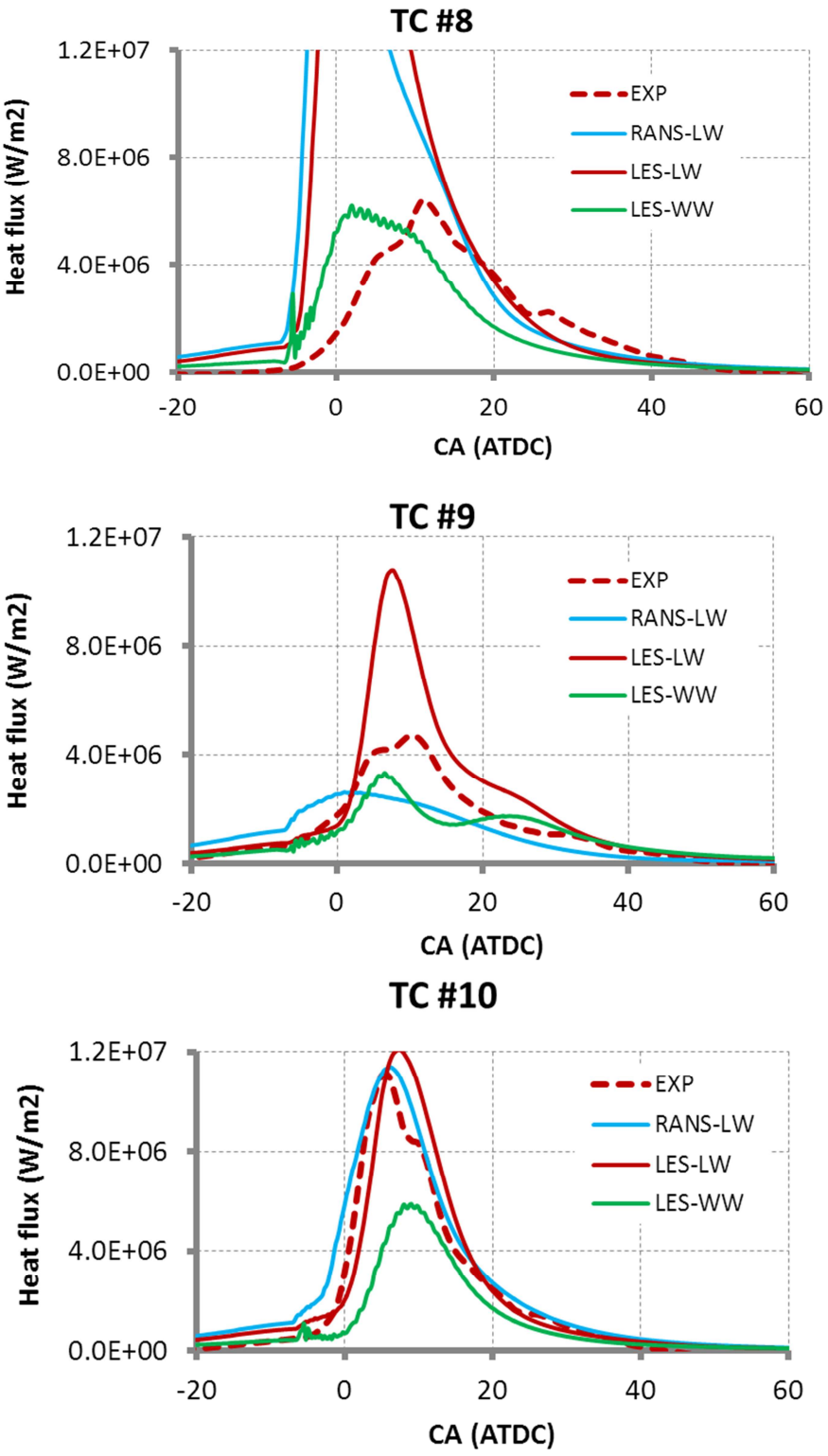

Figure C.8.3 Comparisons of heat flux on piston surface at TC#8-TC#10 (mid-way between two adjacent sprays) for Run40

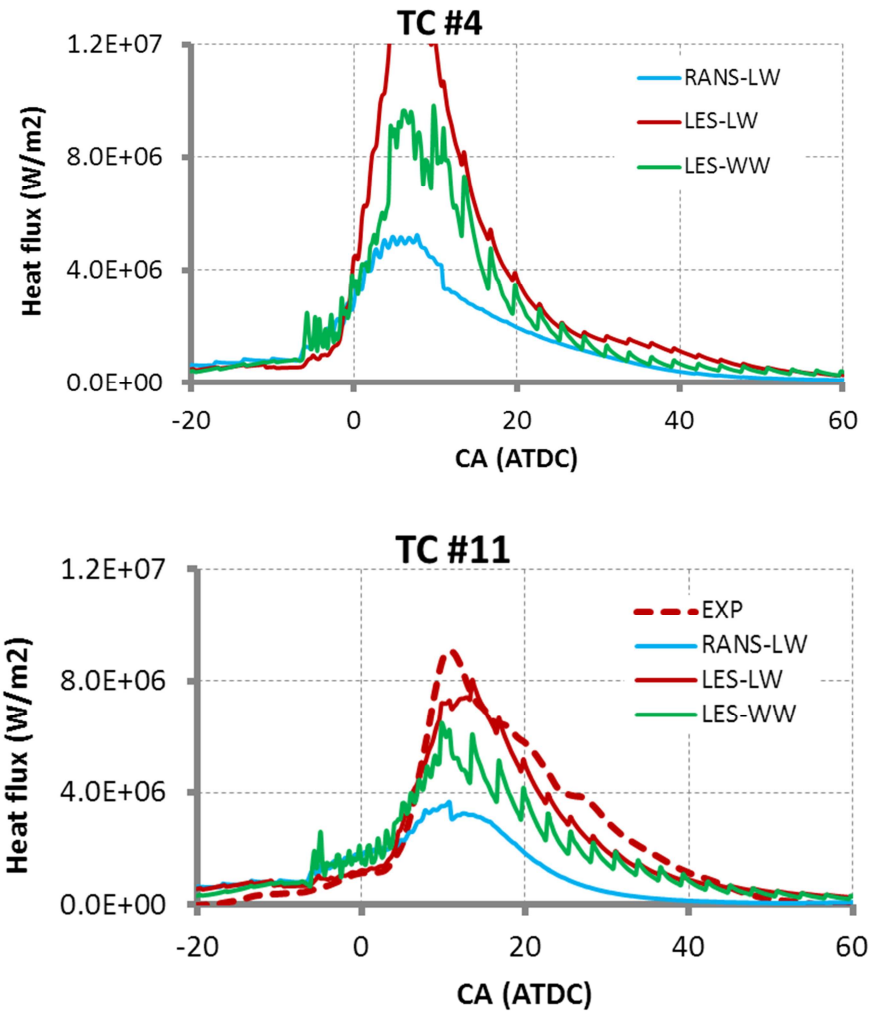

Figure C.8.4 Comparisons of heat flux on the piston surface in squish areas TC#4 and TC#11 for Run40

C.9 Run39

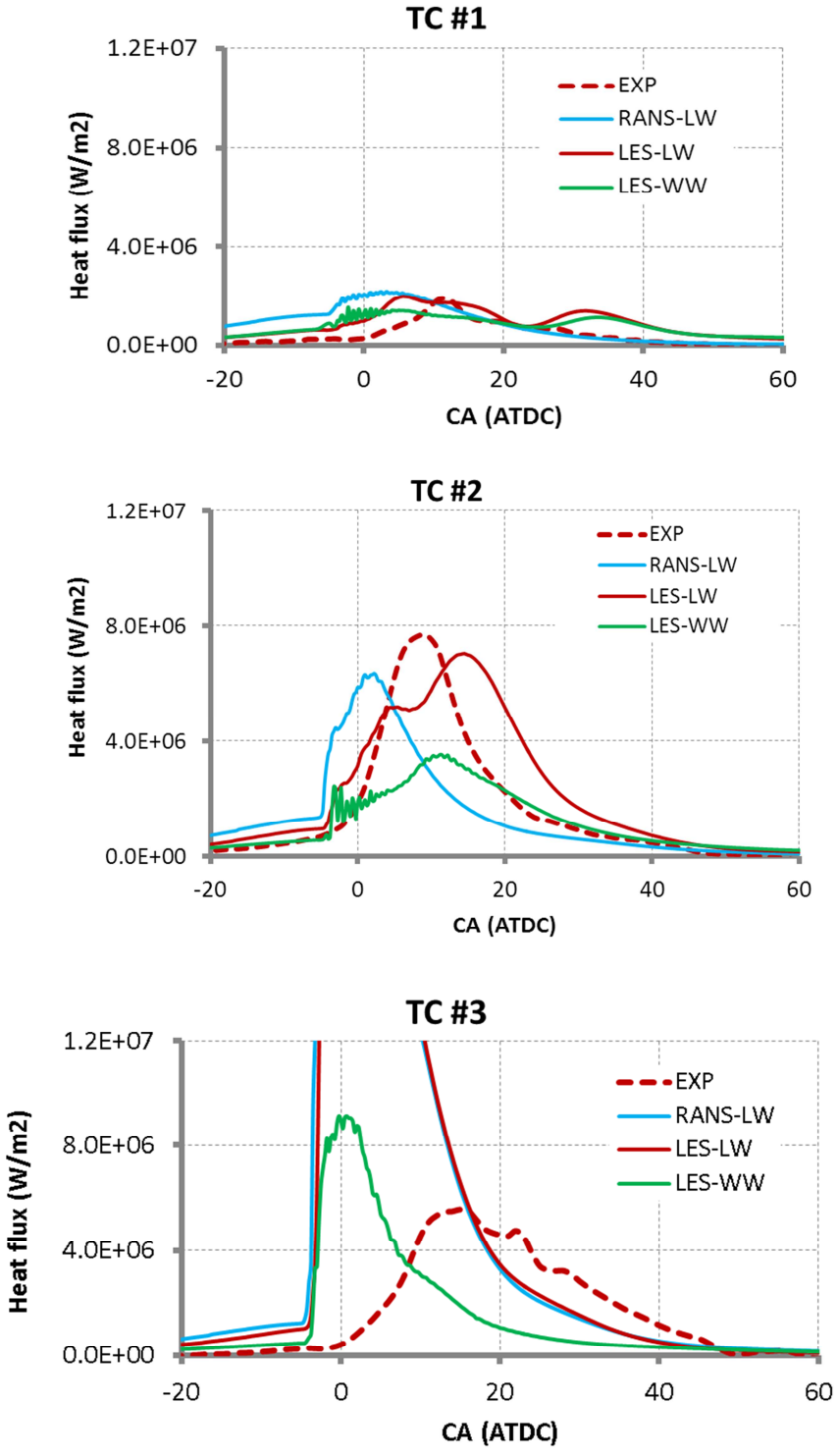

Figure C.9.1 Comparisons of heat flux on piston surface at TC#1-TC#3 (spray axis) for Run39

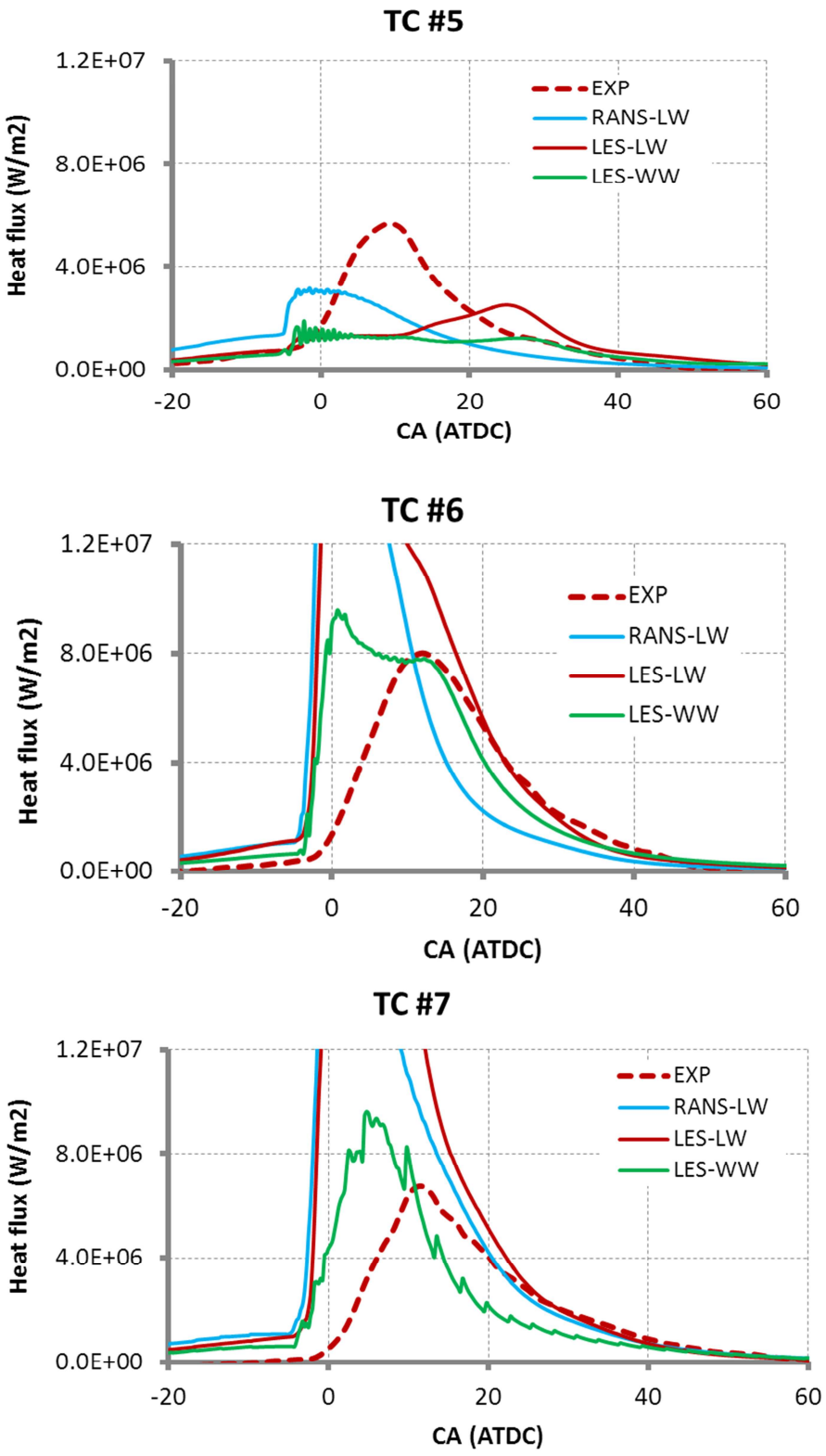

Figure C.9.2 Comparisons of heat flux on piston surface at TC#5-TC#7 (spray axis) for Run39

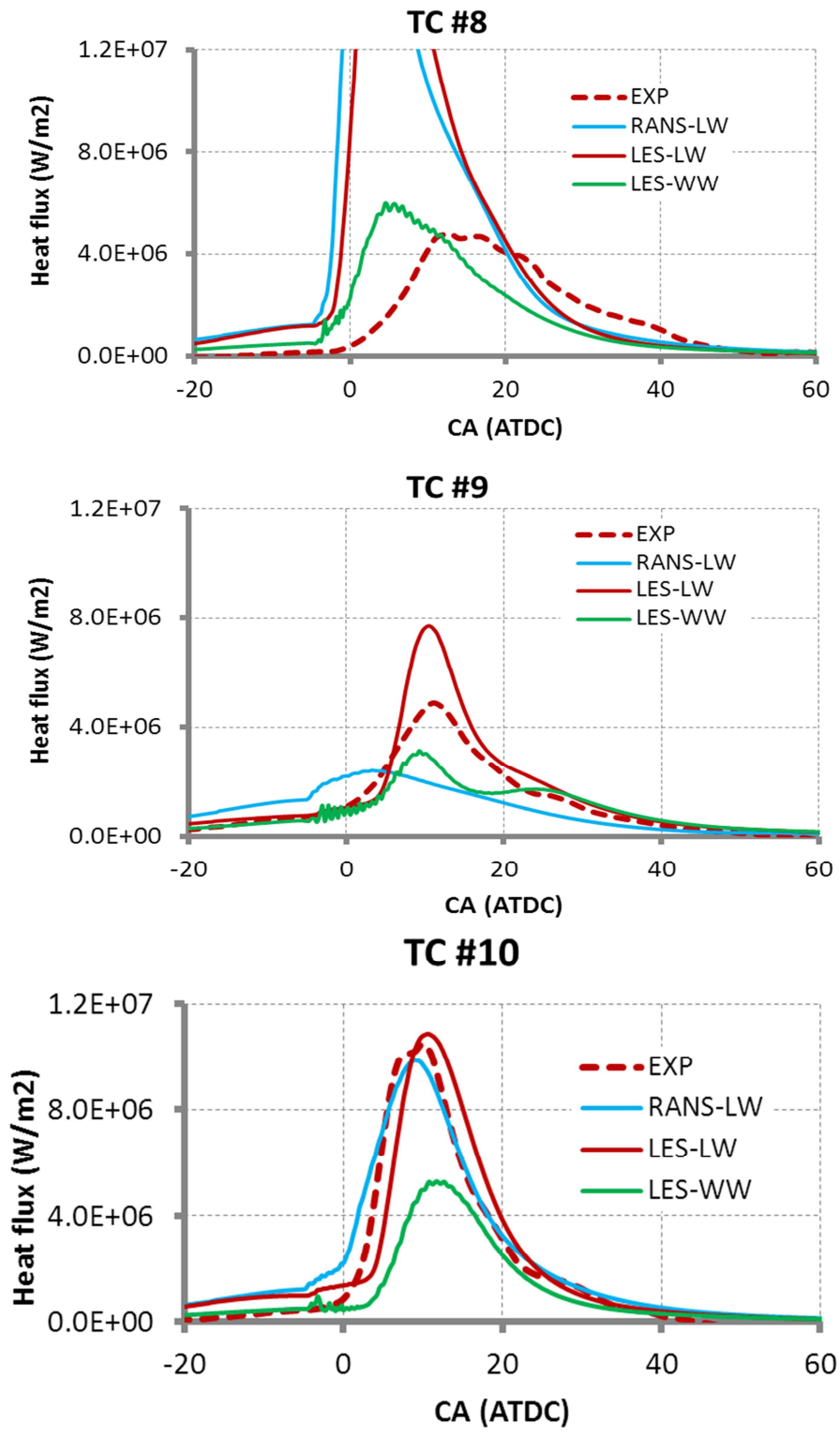

Figure C.9.3 Comparisons of heat flux on piston surface at TC#8-TC#10 (mid-way between two adjacent sprays) for Run39

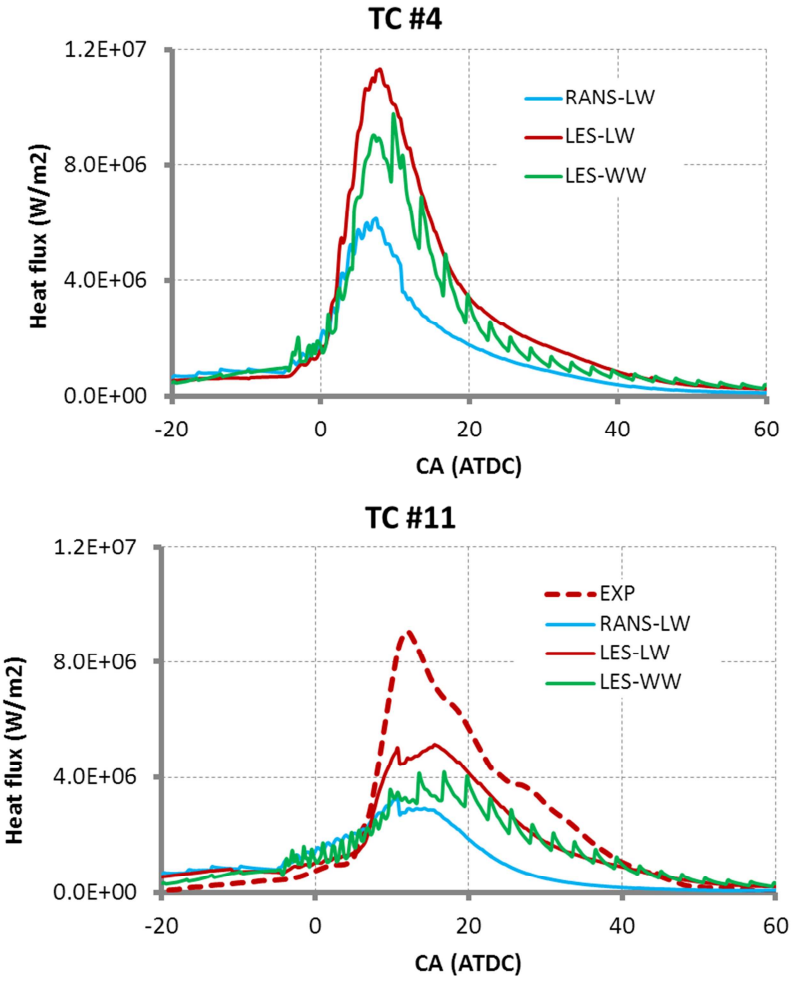

Figure C.9.4 Comparisons of heat flux on the piston surface in squish areas TC#4 and TC#11 for Run39

C.10 Run42

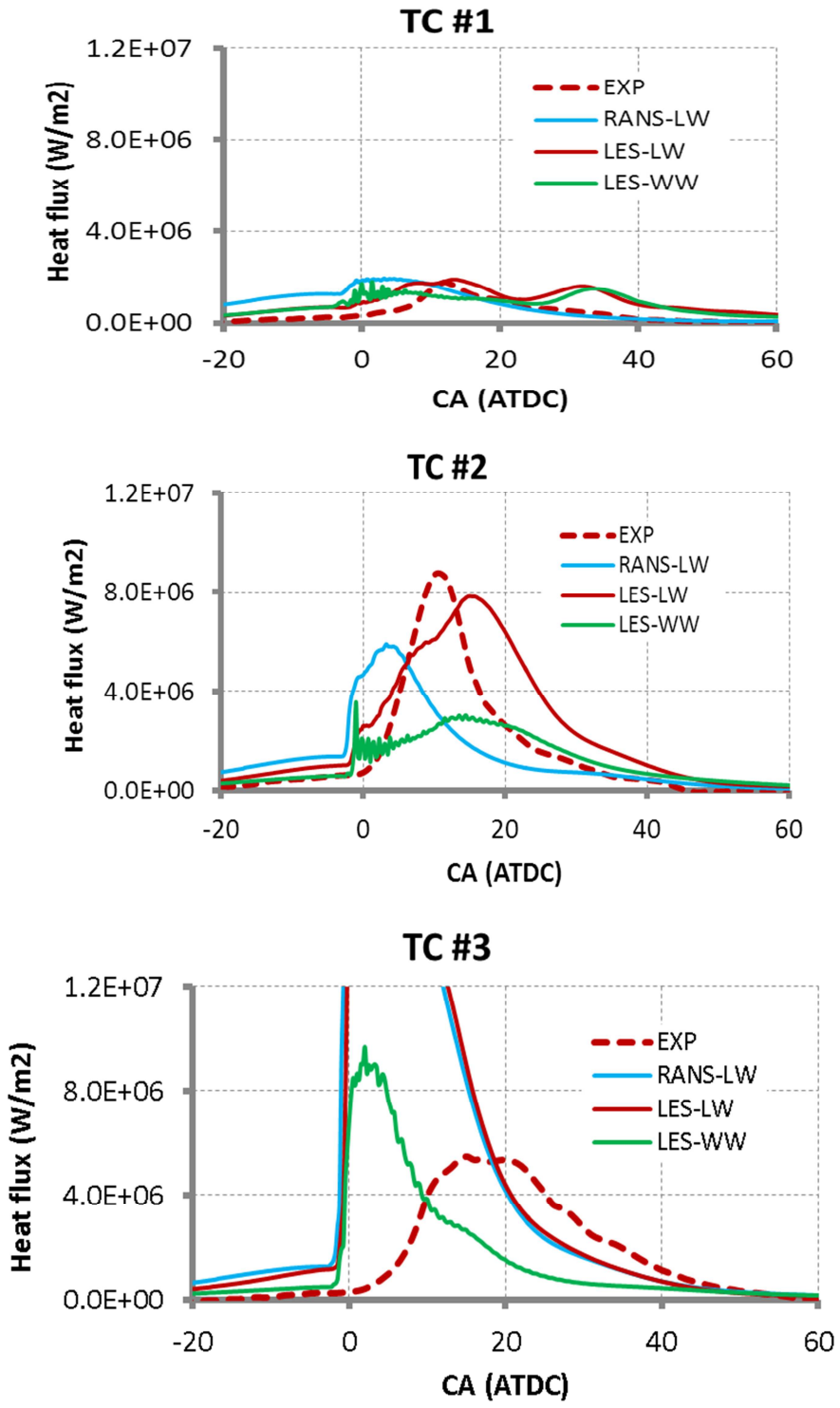

Figure C.10.1 Comparisons of heat flux on piston surface at TC#1-TC#3 (spray axis) for Run42

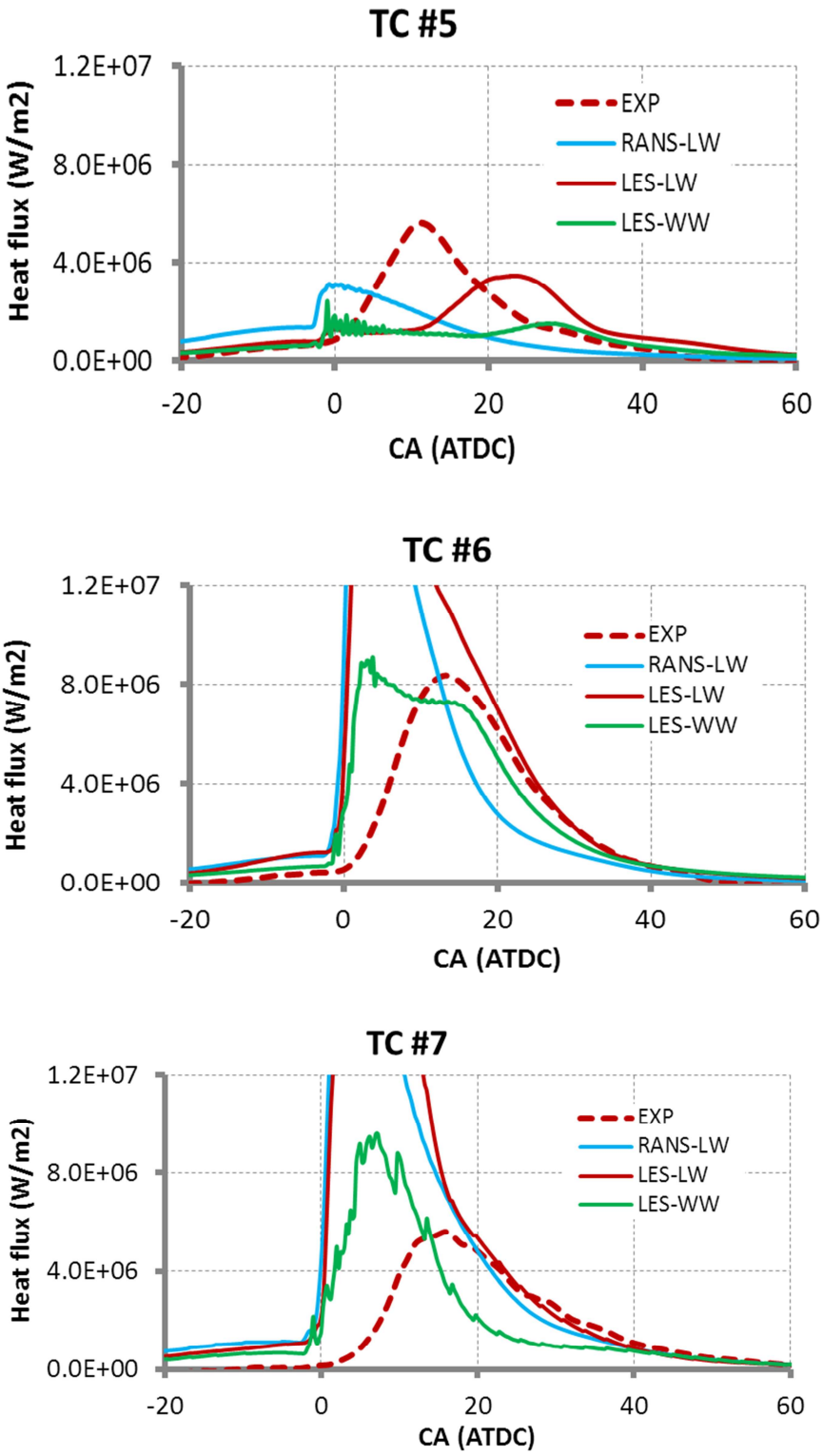

Figure C.10.2 Comparisons of heat flux on piston surface at TC#5-TC#7 (spray axis) for Run42

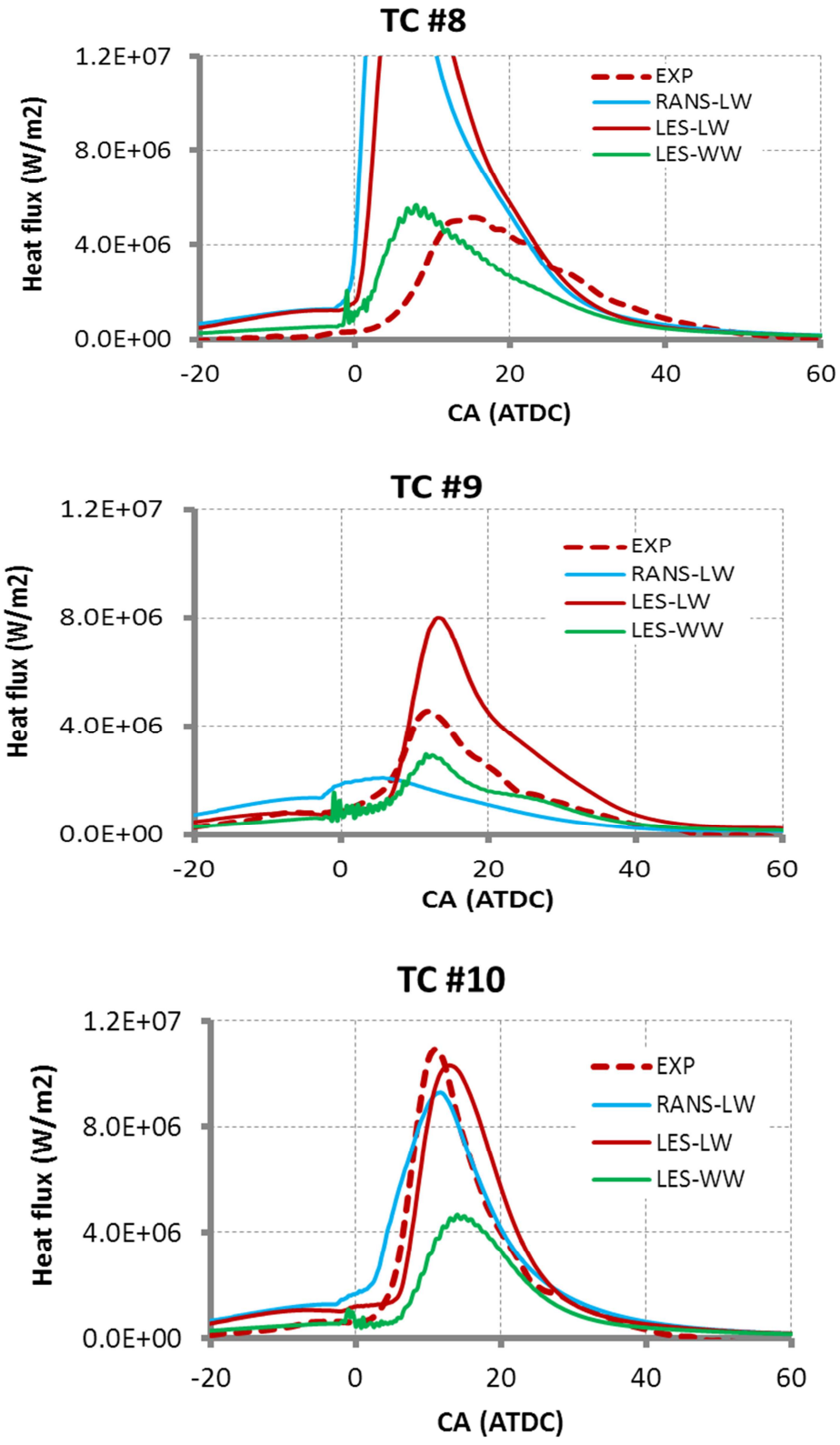

Figure C.10.3 Comparisons of heat flux on piston surface at TC#8-TC#10 (mid-way between two adjacent sprays) for Run42

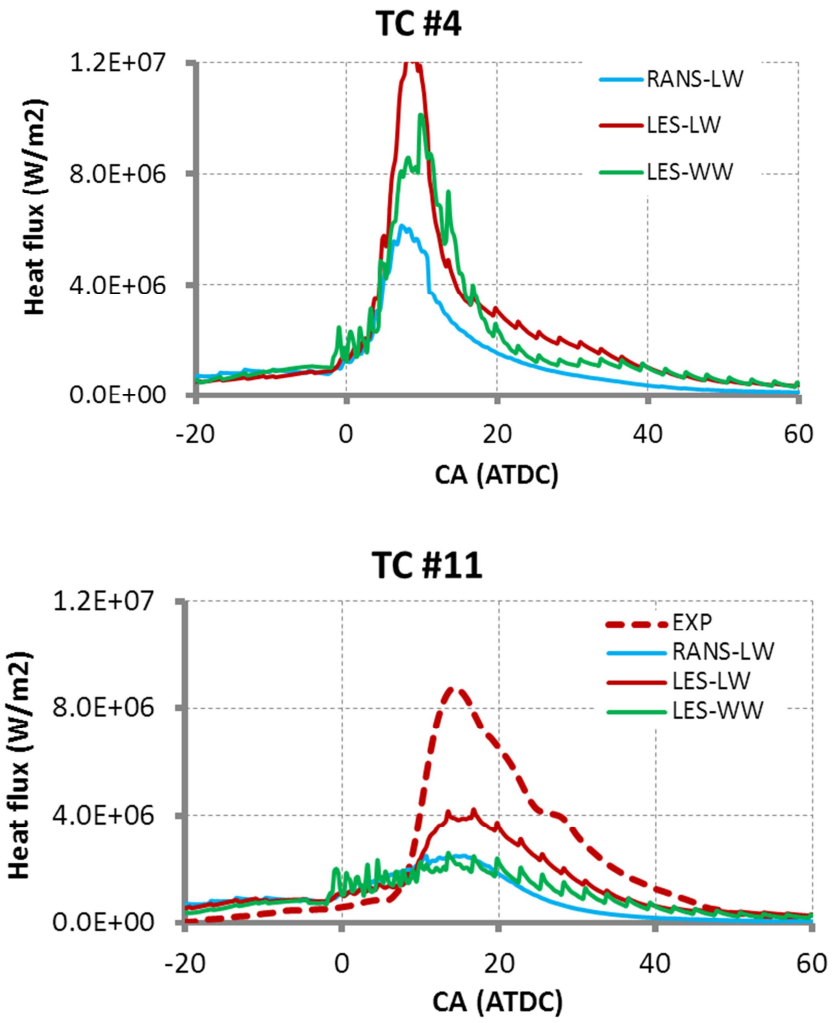

Figure C.10.4 Comparisons of heat flux on the piston surface in squish areas TC#4 and TC#11 for Run42

C.11 Run43

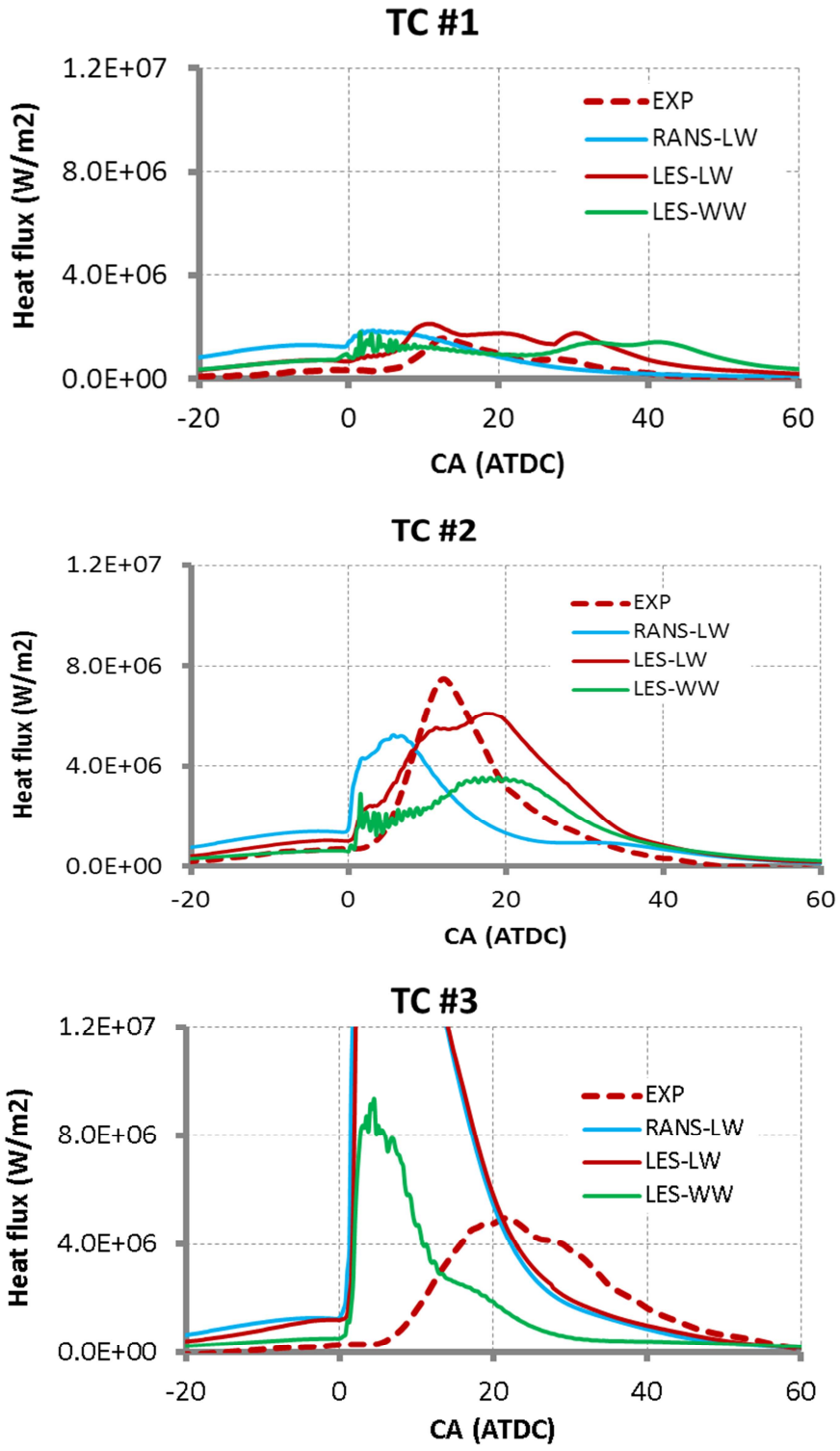

Figure C.11.1 Comparisons of heat flux on piston surface at TC#1-TC#3 (spray axis) for Run43

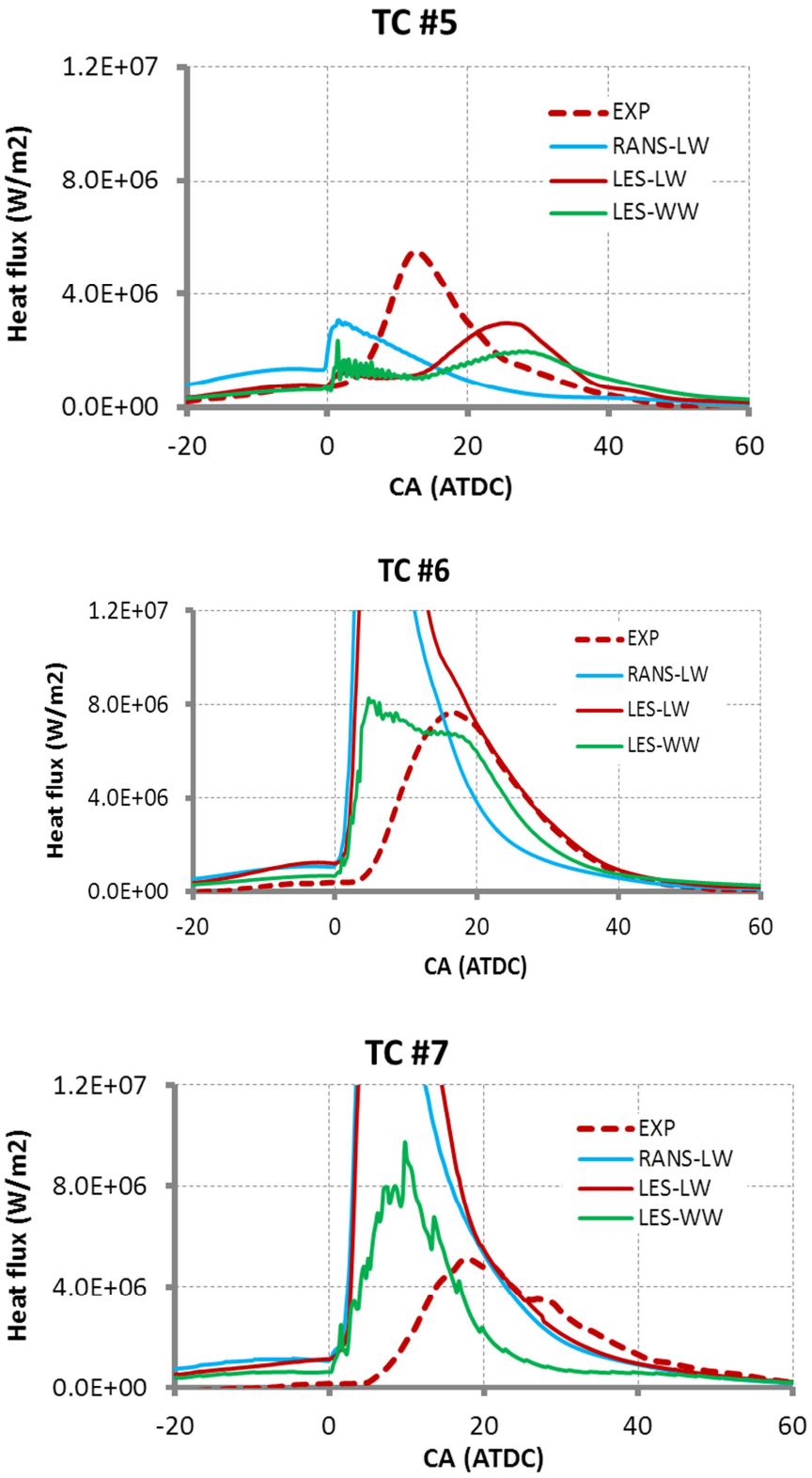

Figure C.11.2 Comparisons of heat flux on piston surface at TC#5-TC#7 (spray axis) for Run43

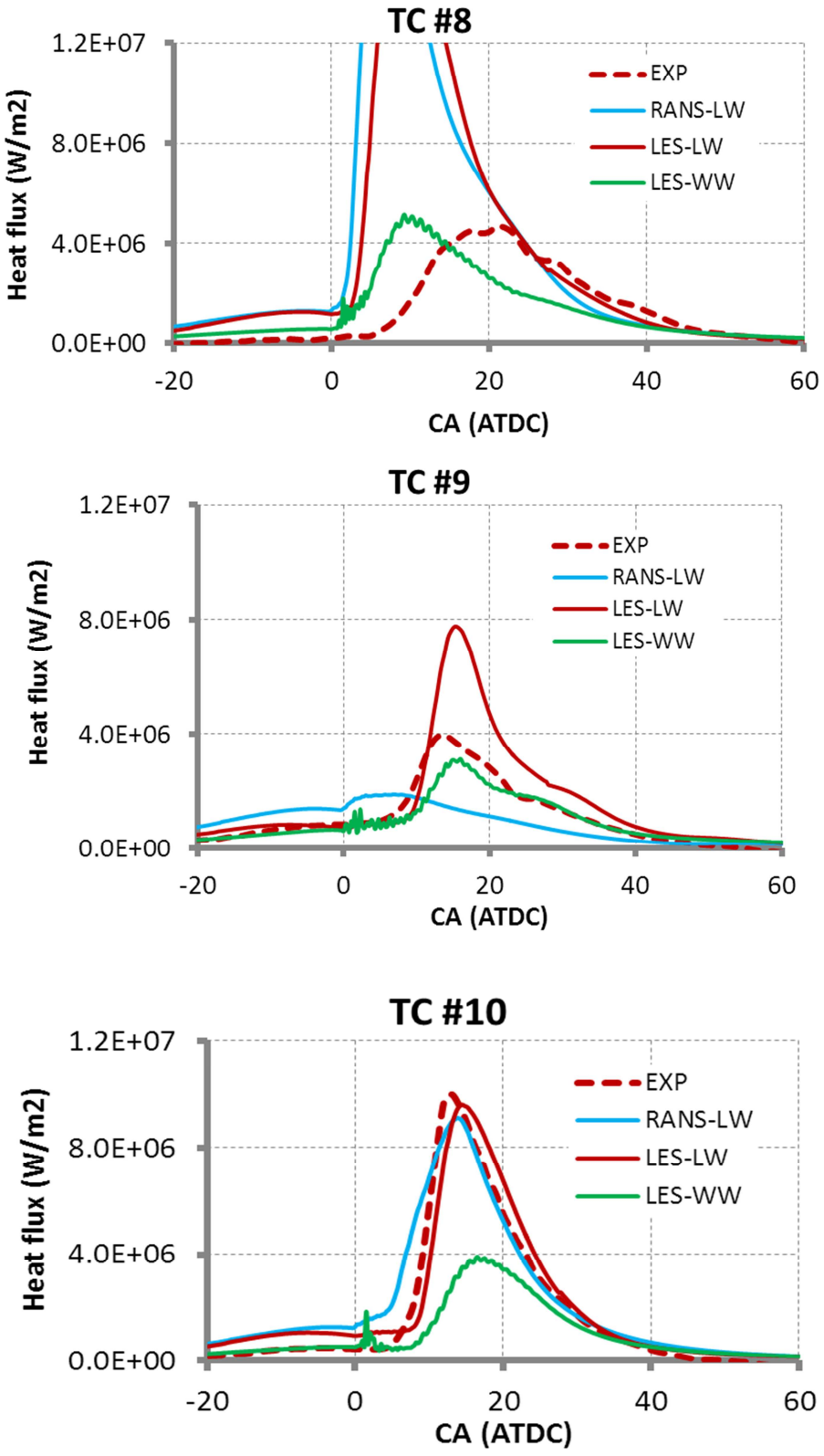

Figure C.11.3 Comparisons of heat flux on piston surface at TC#8-TC#10 (mid-way between two adjacent sprays) for Run43

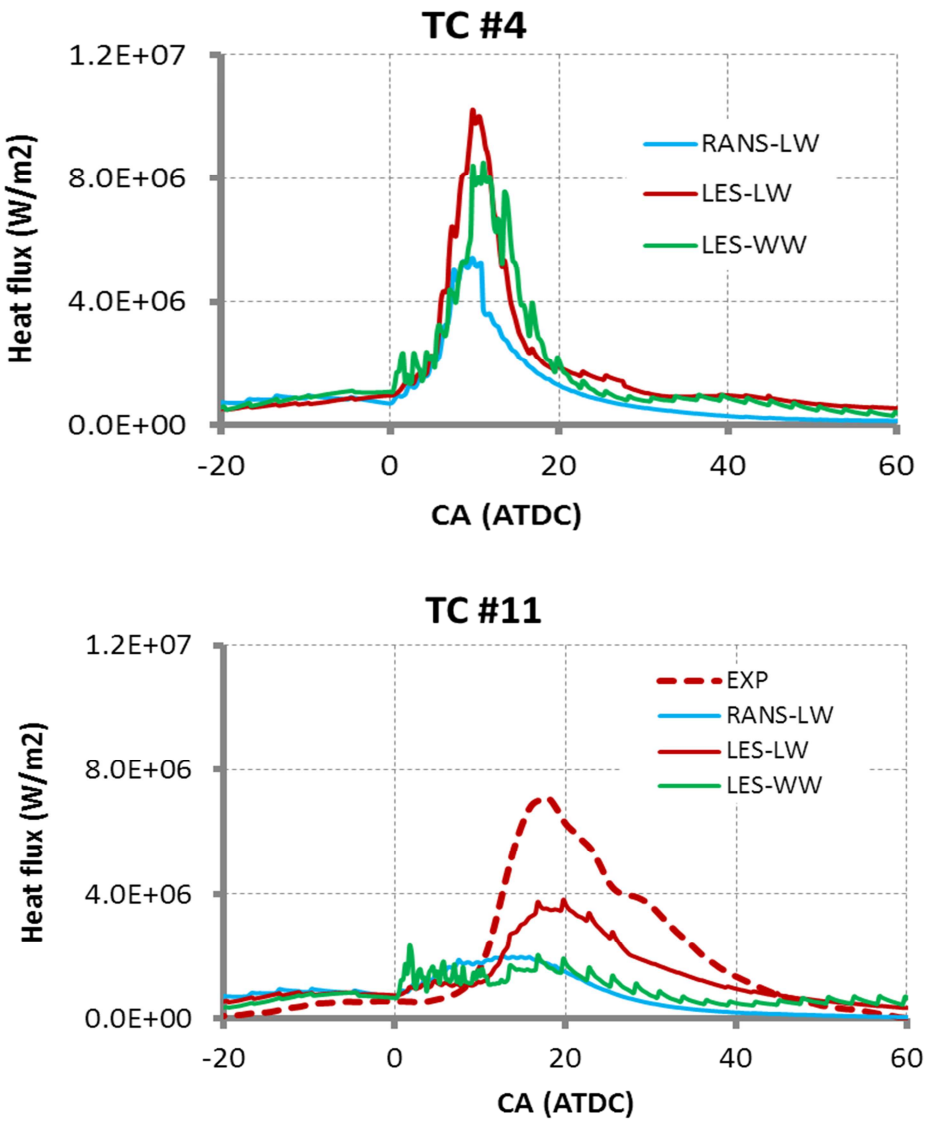

Figure C.11.4 Comparisons of heat flux on the piston surface in squish areas TC#4 and TC#11 for Run43

C.12 Run44

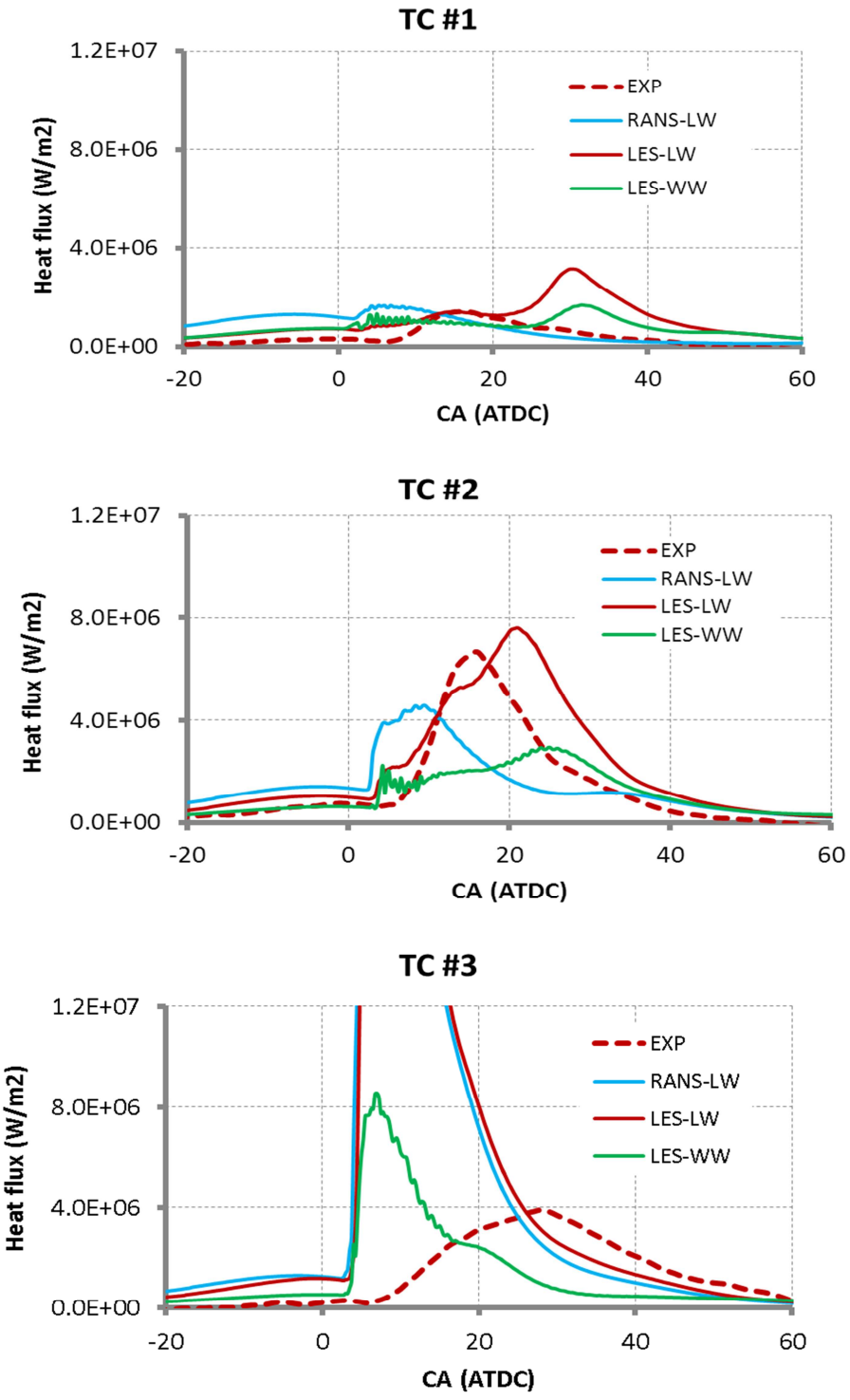

Figure C.12.1 Comparisons of heat flux on piston surface at TC#1-TC#3 (spray axis) for Run44

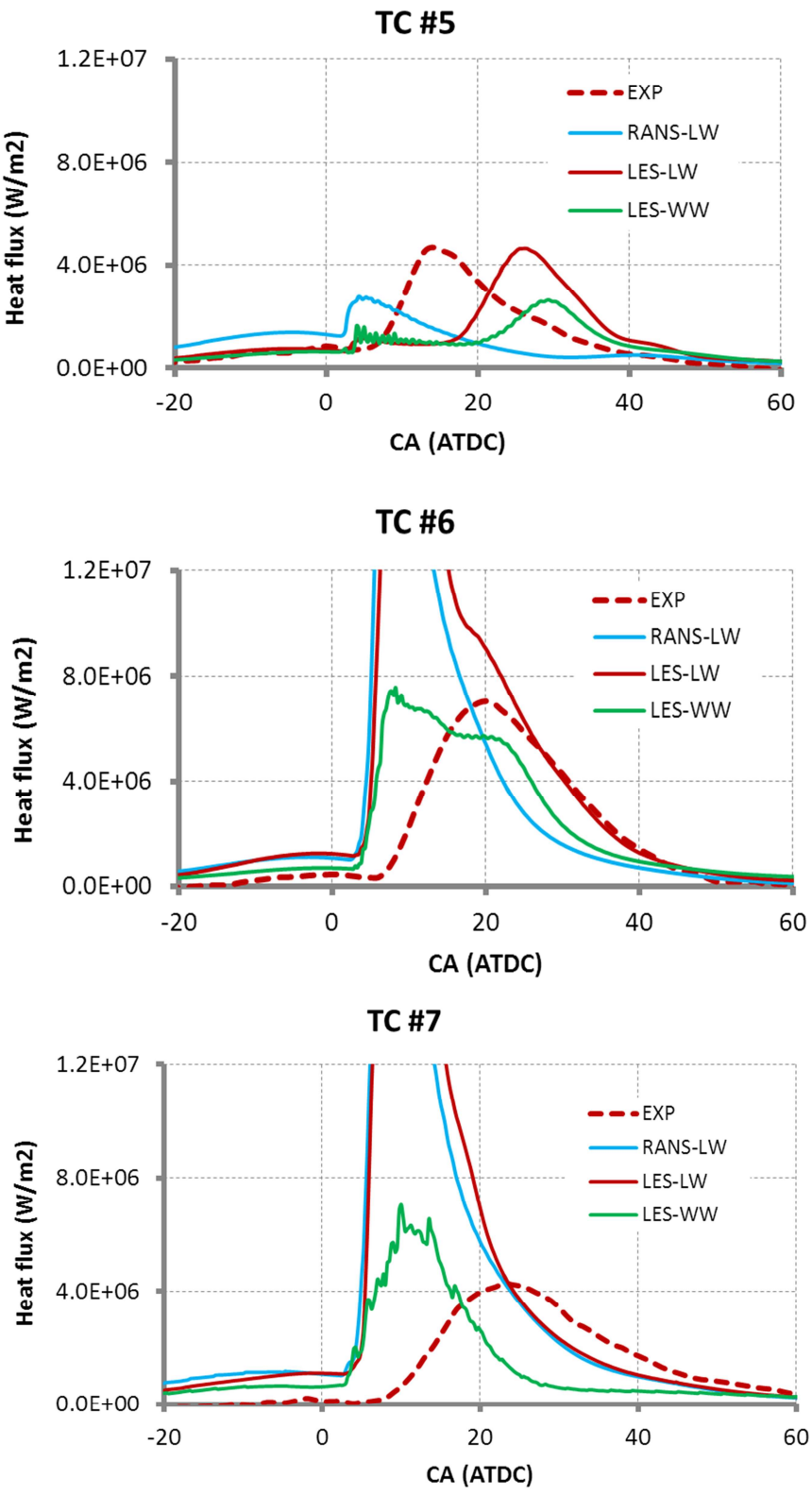

Figure C.12.2 Comparisons of heat flux on piston surface at TC#5-TC#7 (spray axis) for Run44

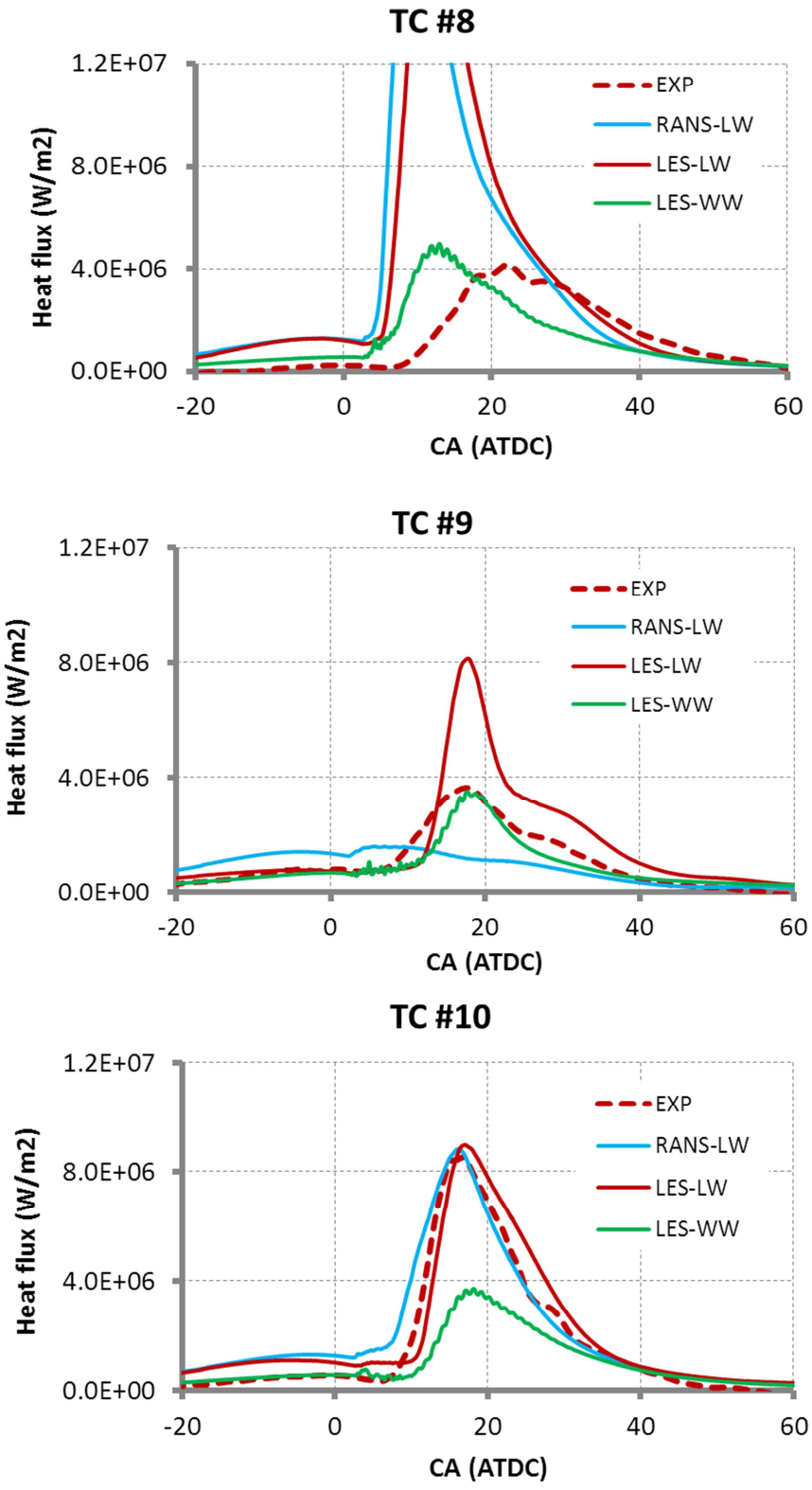

Figure C.12.3 Comparisons of heat flux on piston surface at TC#8-TC#10 (mid-way between two adjacent sprays) for Run44

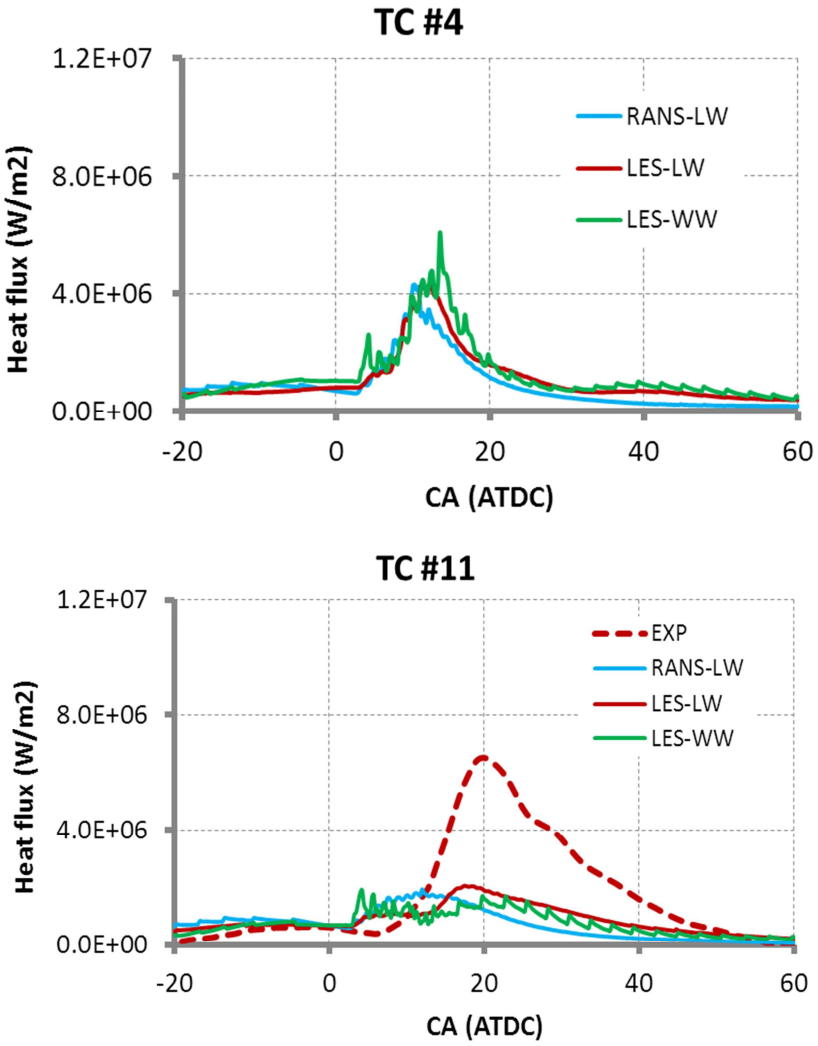

Figure C.12.4 Comparisons of heat flux on the piston surface in squish areas TC#4 and TC#11 for Run44

C.13 Run33

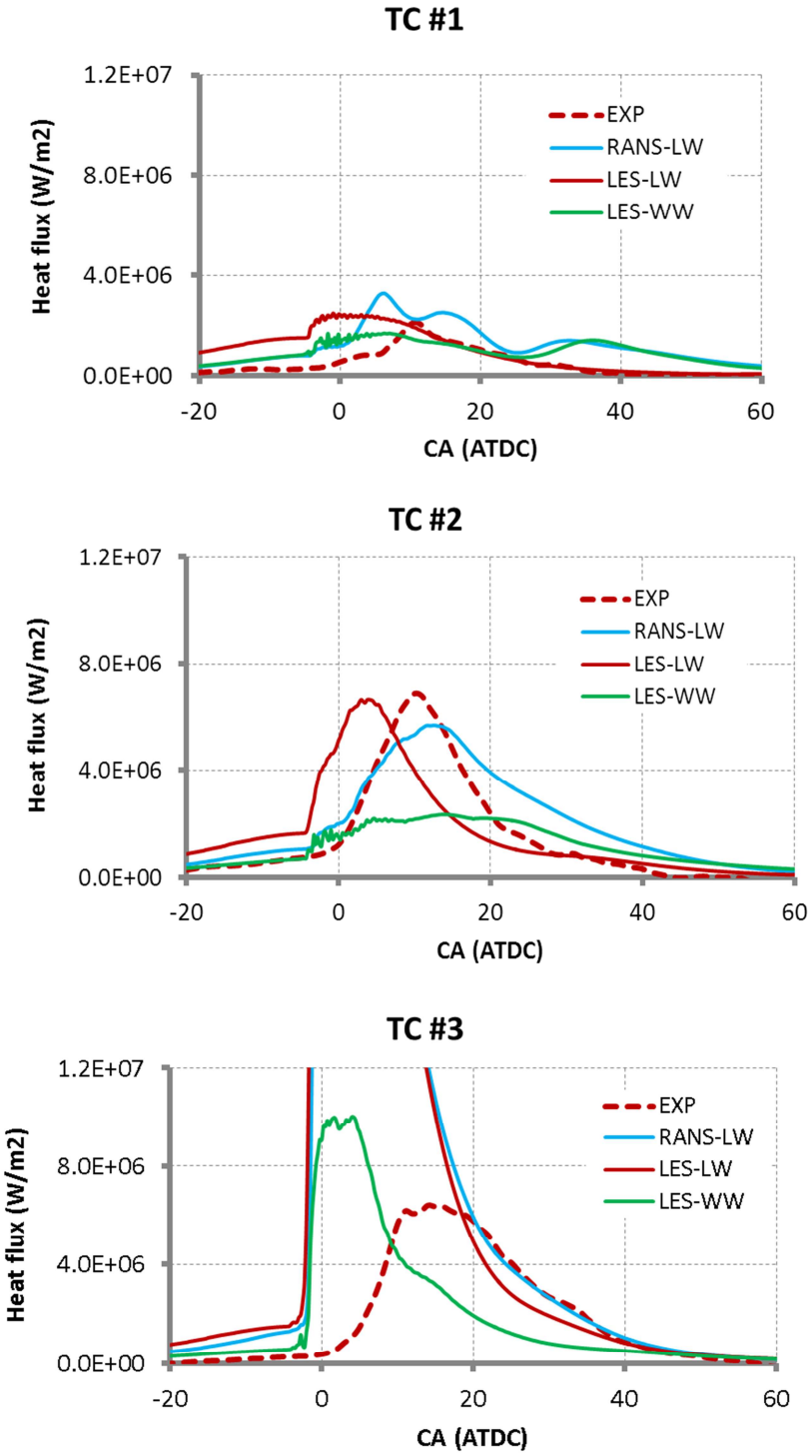

Figure C.13.1 Comparisons of heat flux on piston surface at TC#1-TC#3 (spray axis) for Run33

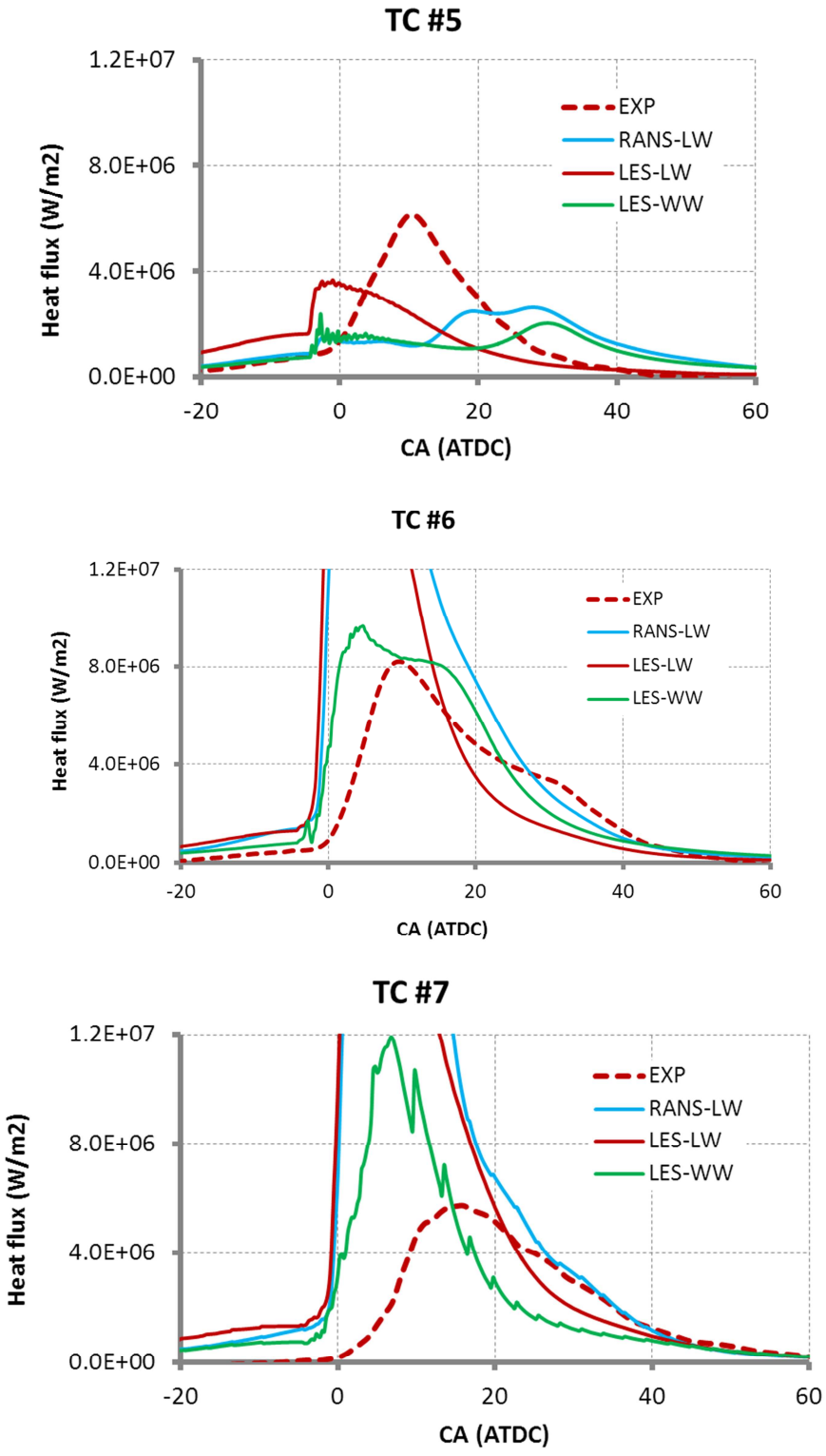

Figure C.13.2 Comparisons of heat flux on piston surface at TC#5-TC#7 (spray axis) for Run33

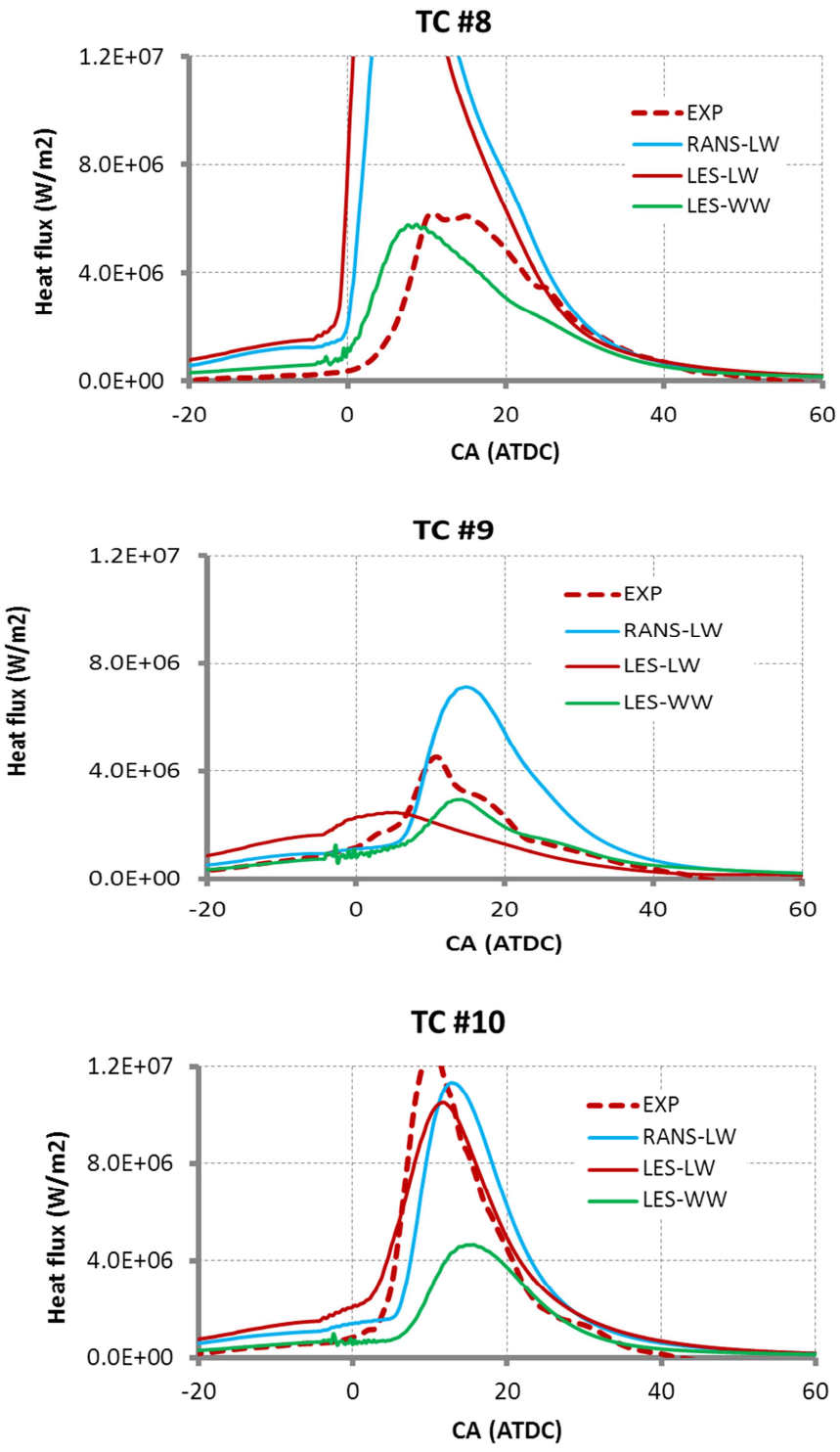

Figure C.13.3 Comparisons of heat flux on piston surface at TC#8-TC#10 (mid-way between two adjacent sprays) for Run33

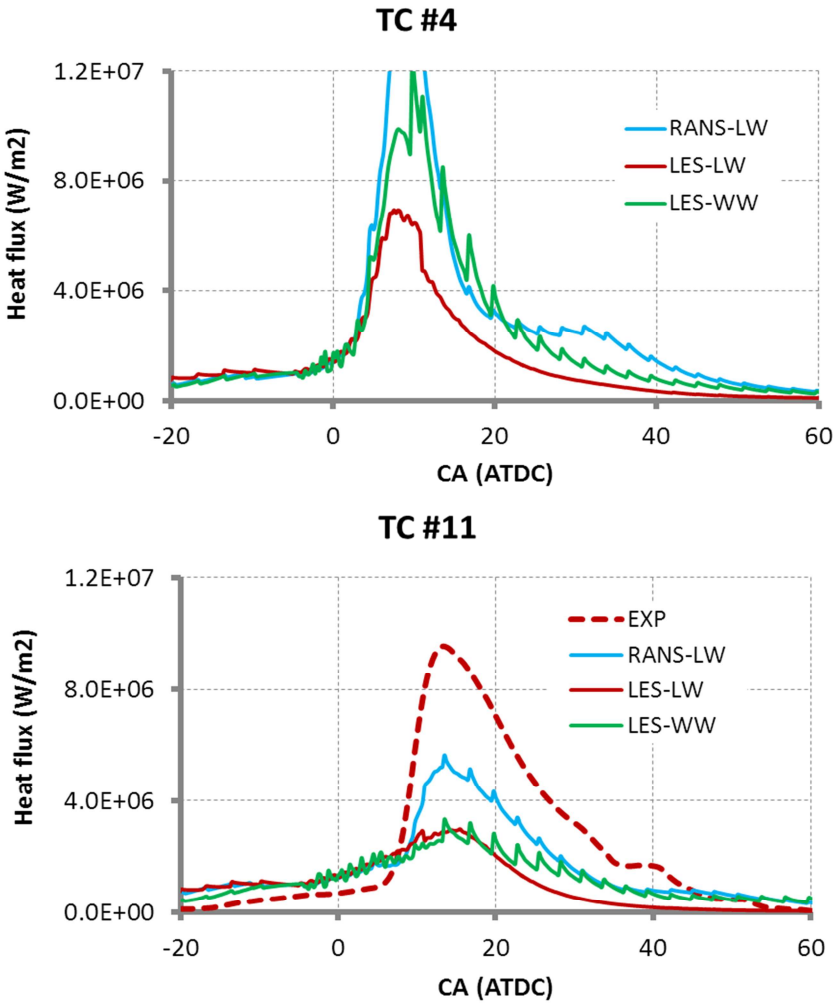

Figure C.13.4 Comparisons of heat flux on the piston surface in squish areas TC#4 and TC#11 for Run33

C.14 Run36

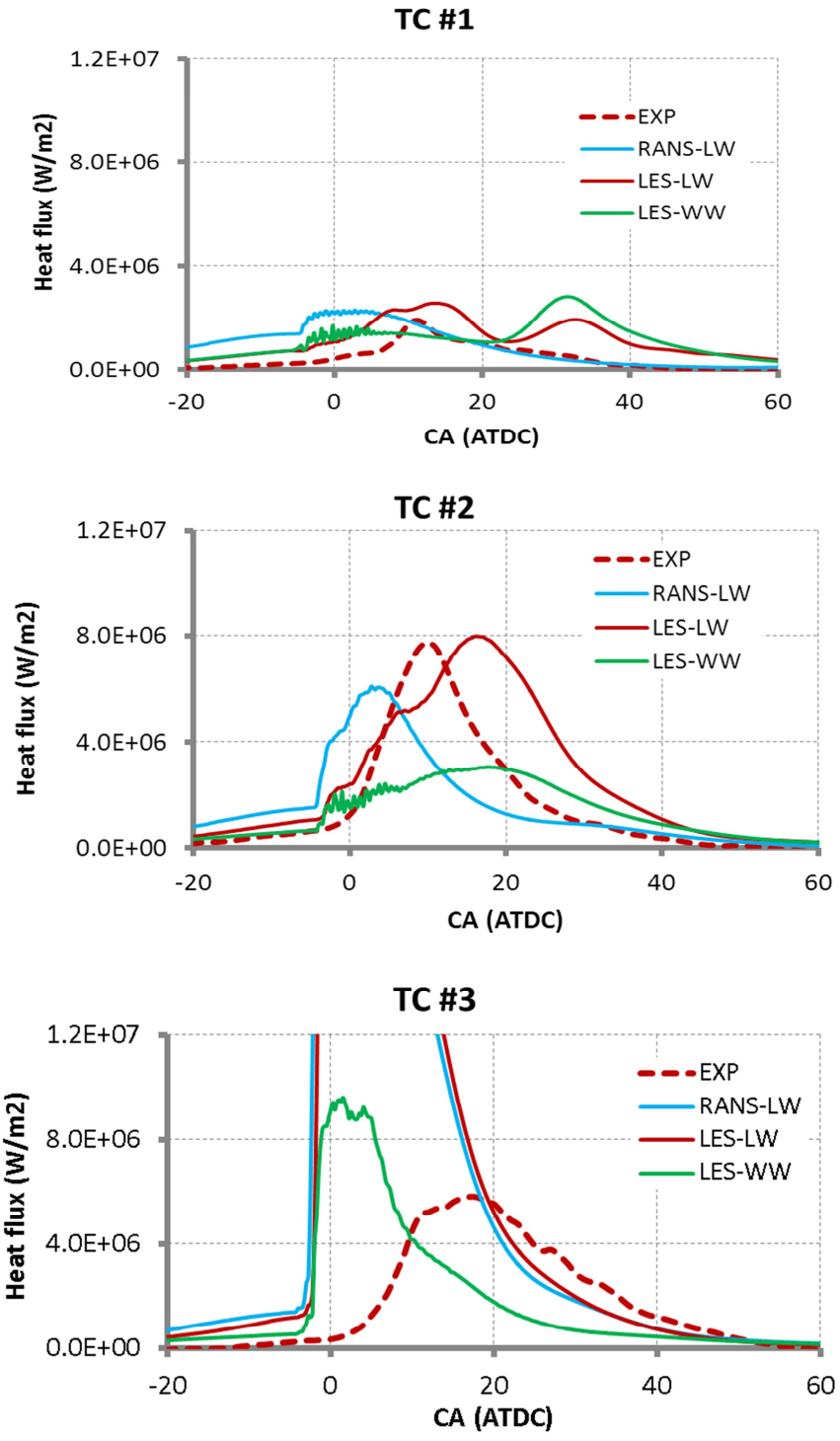

Figure C.14.1 Comparisons of heat flux on piston surface at TC#1-TC#3 (spray axis) for Run36

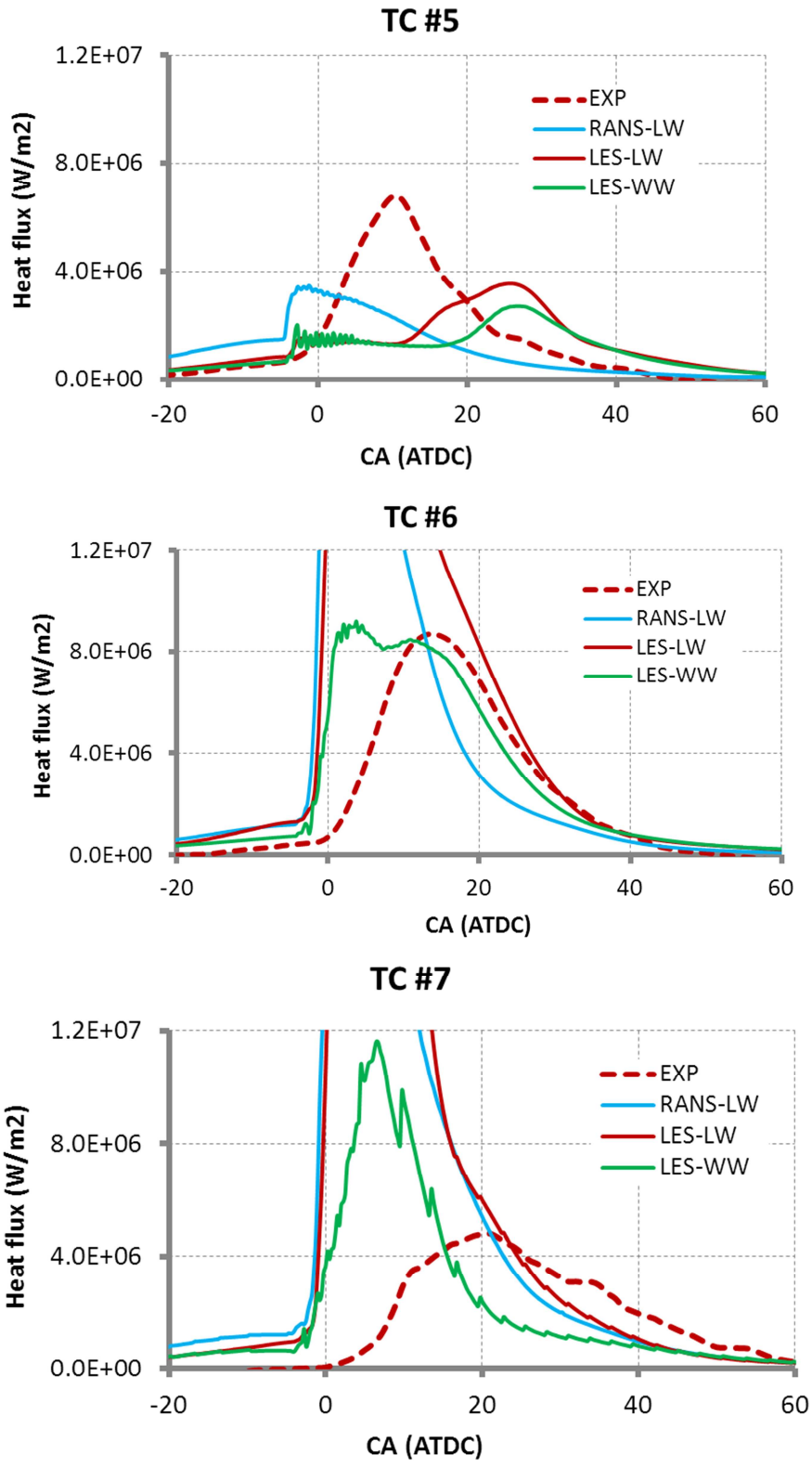

Figure C.14.2 Comparisons of heat flux on piston surface at TC#5-TC#7 (spray axis) for Run36

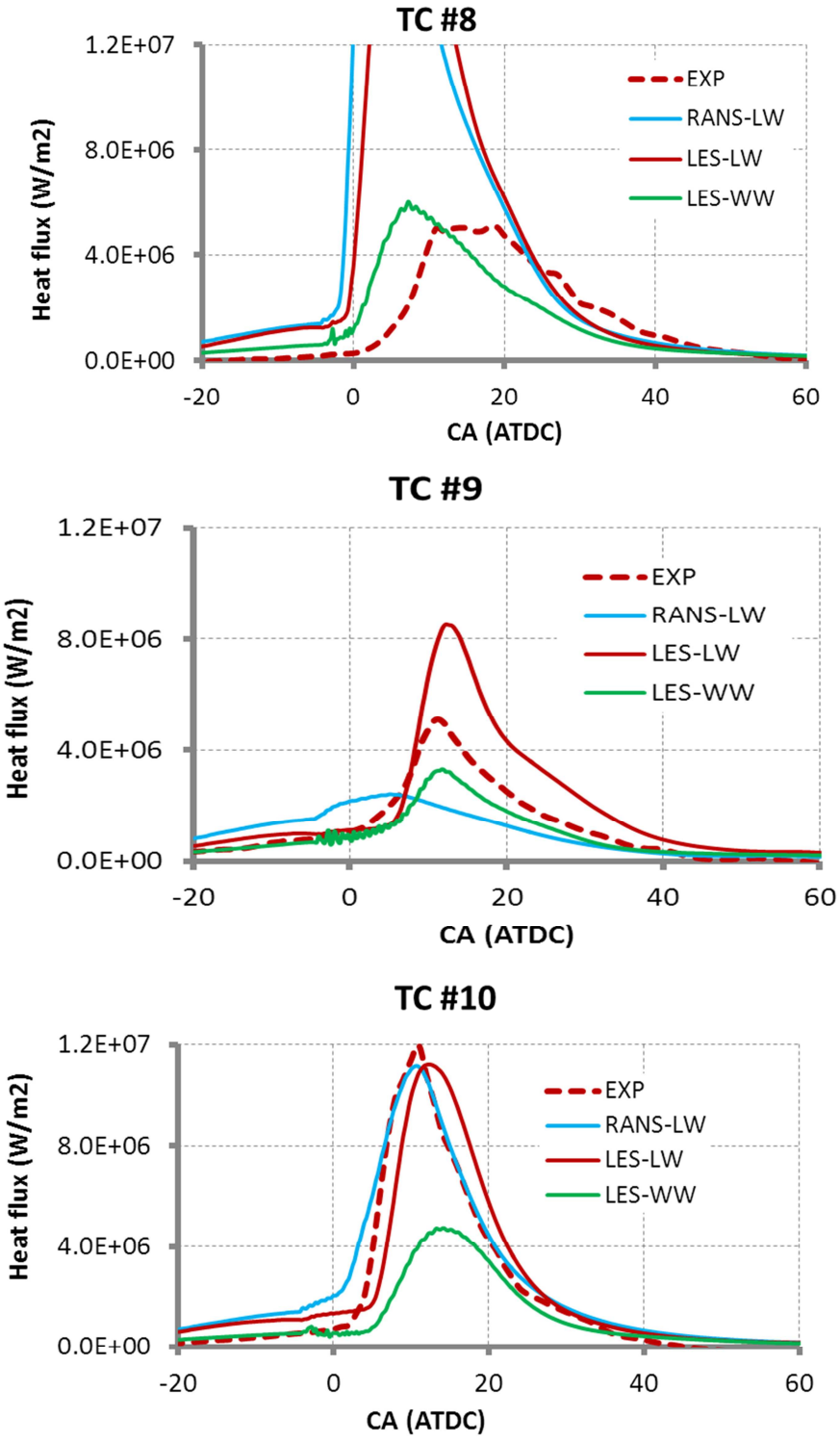

Figure C.14.3 Comparisons of heat flux on piston surface at TC#8-TC#10 (mid-way between two adjacent sprays) for Run36

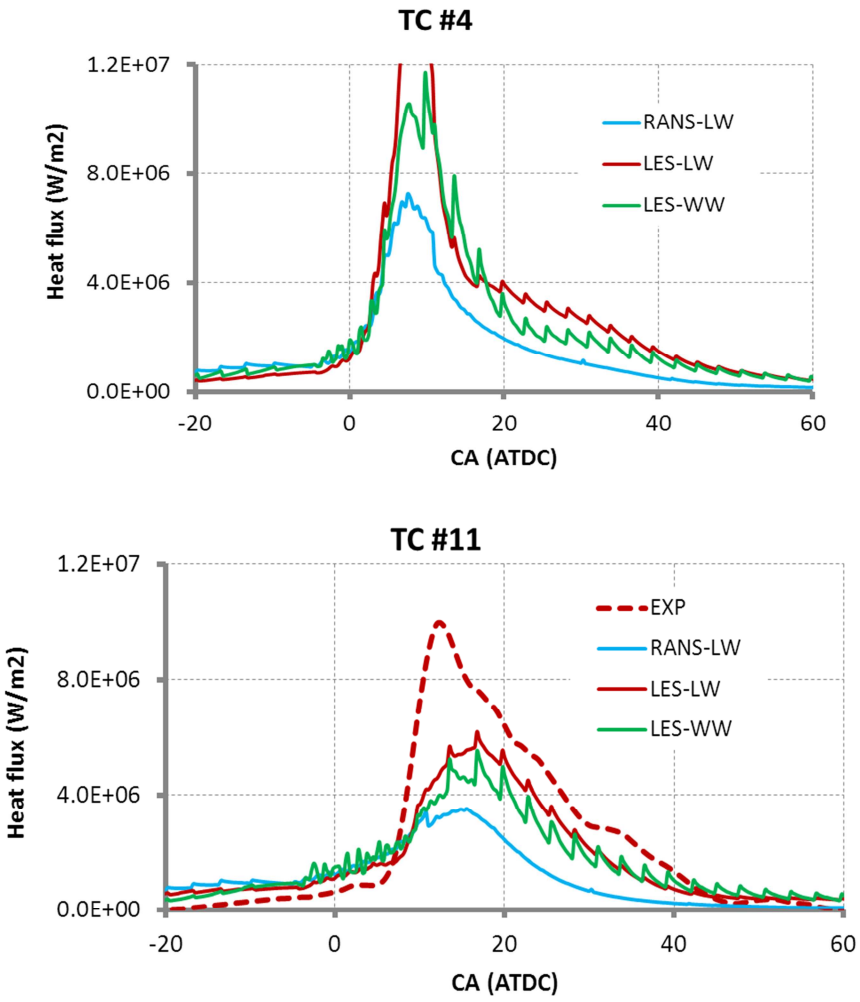

Figure C.14.4 Comparisons of heat flux on the piston surface in squish areas TC#4 and TC#11 for Run36

C.15 Run38

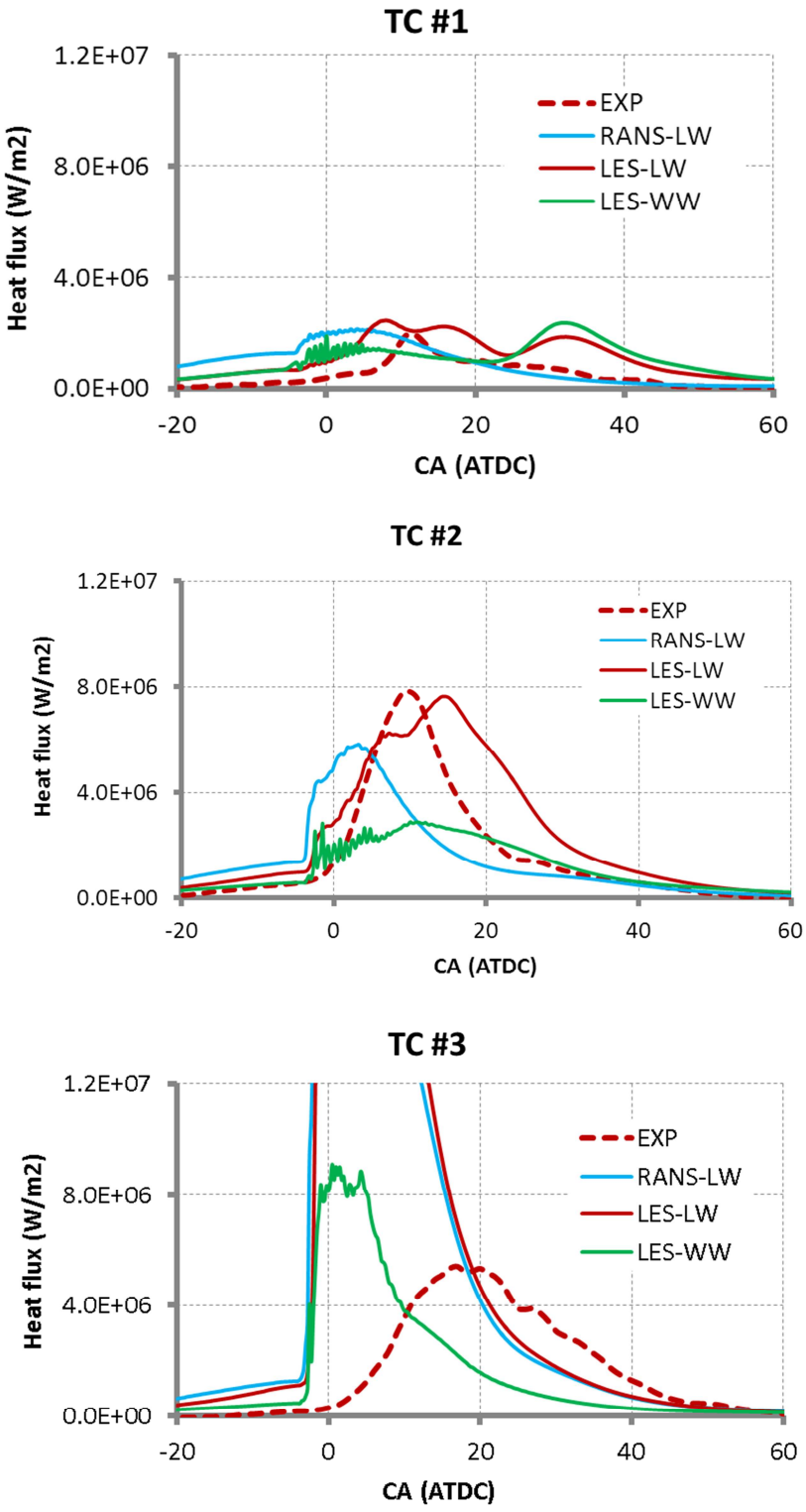

Figure C.15.1 Comparisons of heat flux on piston surface at TC#1-TC#3 (spray axis) for Run38

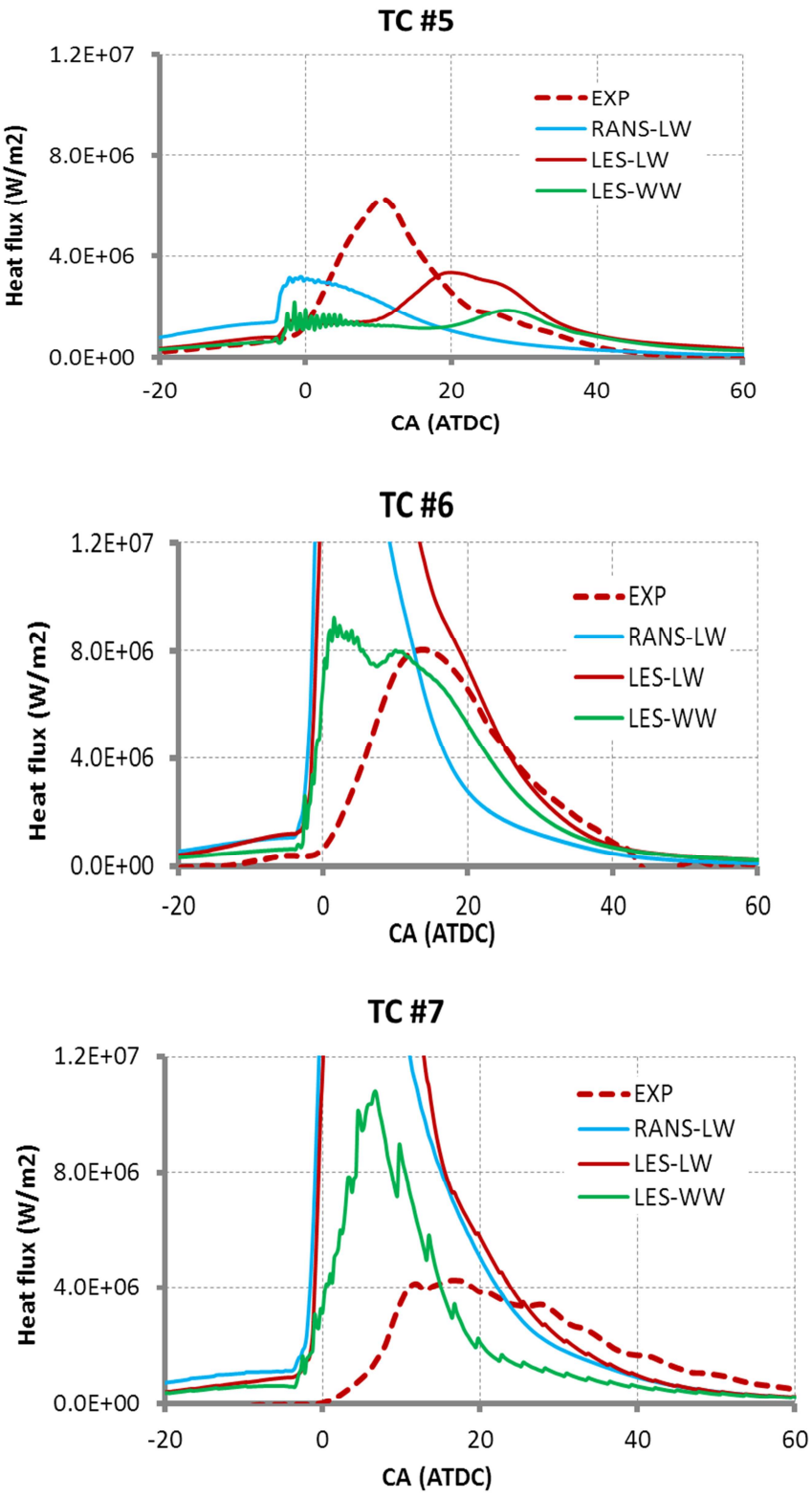

Figure C.15.2 Comparisons of heat flux on piston surface at TC#5-TC#7 (spray axis) for Run38

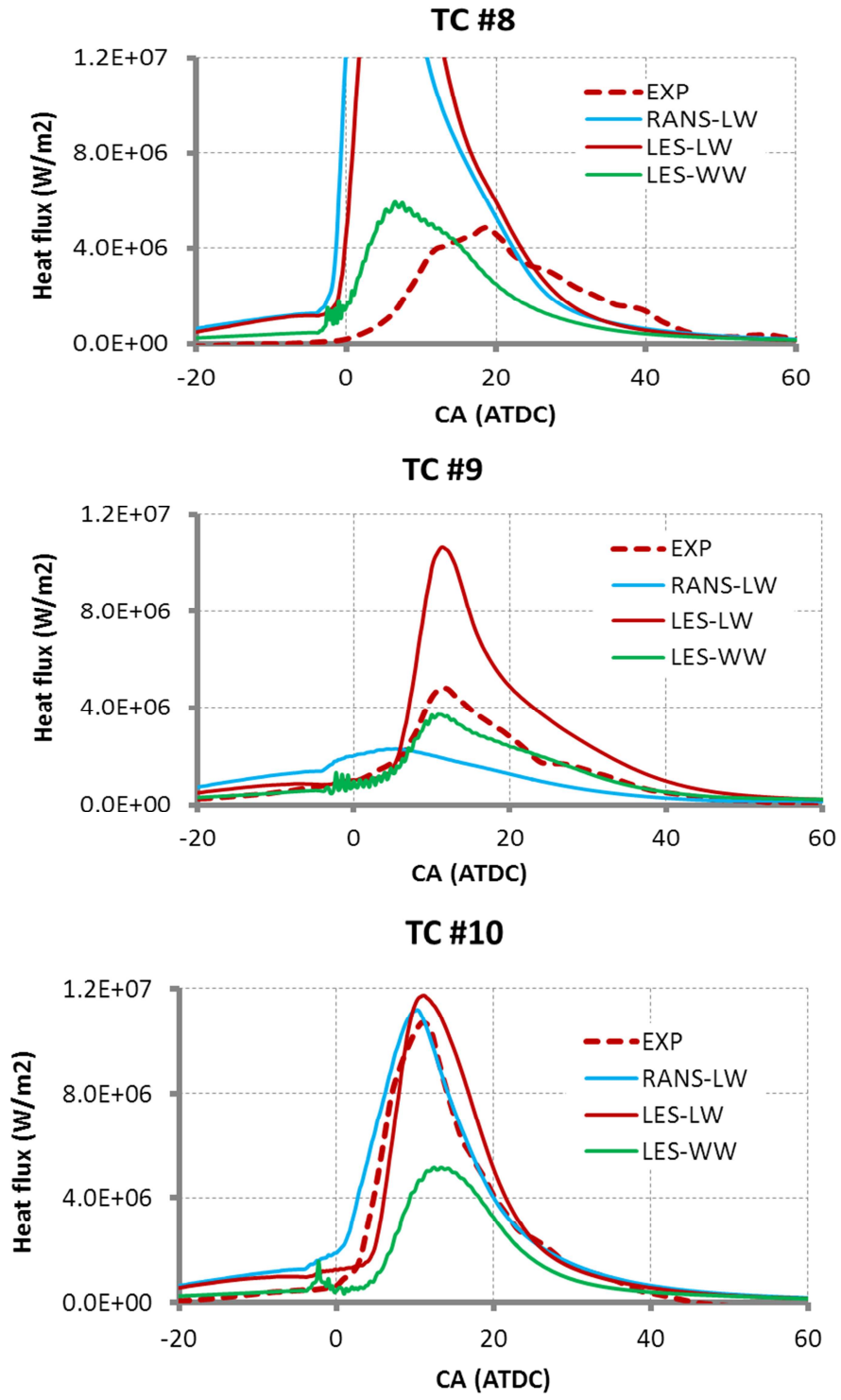

Figure C.15.3 Comparisons of heat flux on piston surface at TC#8-TC#10 (mid-way between two adjacent sprays) for Run38

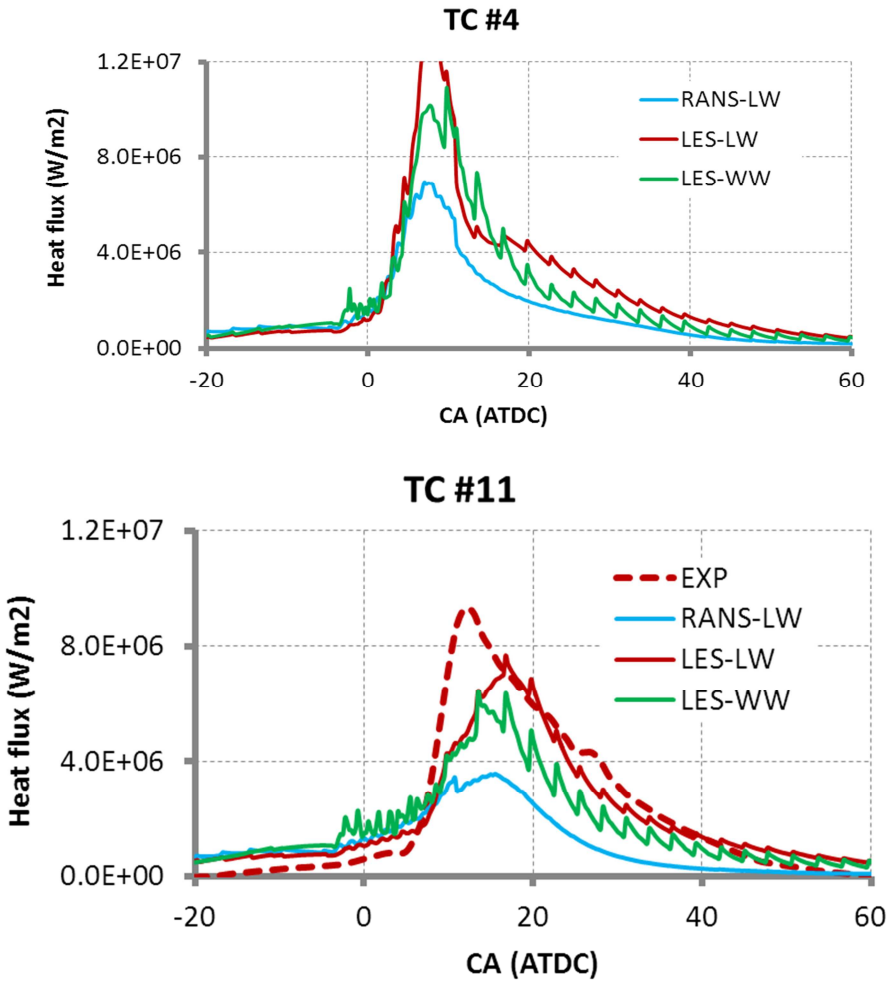

Figure C.15.4 Comparisons of heat flux on the piston surface in squish areas TC#4 and TC#11 for Run38